eXPRESS Polymer Letters Vol.9, No.11 (2015) 959
Available online at www.expresspolymlett.com
DOI: 10.3144/expresspolymlett.2015.86

Editorial corner – a personal view
Additive manufacturing of plastic and polymer composite parts: Promises and challenges of 3D-printing

*P. Krawczak**

Department of Polymers and Composites Technology & Mechanical Engineering, MINES DOUAI, 941 rue Charles Bourseul, CS 10838, 59508 Douai, France

Factories of the future are expected to implement new integrated design-manufacturing approaches to go towards 'advanced manufacturing'. Additive manufacturing (AM, or 3D-printing) actually offers new opportunities to the plastics processing industry to meet this challenge when developing applications for high-tech industrial (aerospace, medical/dental, automotive) and consumer (home, fashion and entertainment goods) markets. According to ASTM F42 Committee, AM processes can be categorized into seven areas by the type of materials used, the deposition technique, and the way the material if fused or solidified: powder bed fusion, vat photopolymerization, material extrusion, material jetting, binder jetting, sheet lamination and directed (or focused) energy deposition. Materials and processes are interconnected. As far as plastics and polymer composites are concerned, the most popular 3D-printing processes are selective laser sintering, stereolithography, fused deposition modeling, and material jetting.

The ever-growing success of 3D-printing is due to its advantages over conventional manufacturing, e.g. virtually unlimited design freedom, ability to produce parts without moulds, high degree of complexity achievable even in fine details, ability to get local texturing or functionally-graded structures when using multi-materials. However, AM is mostly employed up to now for prototypes, models for form, fit and function, and non-load bearing parts; still too rarely for the fabrication of engineering parts and final products. The reason is that the remaining issues to be addressed are still numerous. It is desirable to:

- extend the range of suitable amorphous and semi-crystalline polymers and filled/reinforced compounds, including shape-memory and liquid-crystal polymers,
- reduce the materials cost by feeding 3D-printers directly with pellets (i.e. avoid intermediate forms or semi-products such as powders or wires),
- master induced residual stresses and resulting shrinkage/warpage issues to warrant dimensional stability and accuracy over time,
- improve surface finish of parts,
- develop process modeling and simulation, topological optimization, and mechanical performance prediction to enable full virtual engineering chain,
- increase process control and monitoring, and on-line quality control (in-situ sensors for early detection of flaws),
- increase build-up rates,

… the success key being of course the development of high-value applications.

Prof. Dr. Patricia Krawczak
Member of International Advisory Board

*Corresponding author, e-mail: patricia.krawczak@mines-douai.fr

eXPRESS Polymer Letters Vol.9, No.11 (2015) 960–971
Available online at www.expresspolymlett.com
DOI: 10.3144/expresspolymlett.2015.87

Effect of rubber polarity on selective wetting of carbon nanotubes in ternary blends

H. H. Le[1,2], M. Parsaker[3], M. N. Sriharish[3], S. Henning[4], M. Menzel[4], S. Wießner[1,5], A. Das[1], Q. K. Do[6], G. Heinrich[1,5], H-J. Radusch[7]*

[1]Leibniz-Institut für Polymerforschung Dresden e.V., D-01069 Dresden, Germany
[2]Institut für Polymerwerkstoffe e.V., D-06217 Merseburg, Germany
[3]Center of Engineering Sciences, Martin Luther University Halle-Wittenberg, D-06099 Halle/S., Germany
[4]Fraunhofer IWM, D-06120 Halle/S., Germany
[5]Technische Universität Dresden, Institut für Werkstoffwissenschaft, D-01062 Dresden, Germany
[6]Institute of Chemistry, Vietnamese Academy of Science and Technology, Hanoi, Vietnam
[7]Polymer Service GmbH Merseburg, D-06217 Merseburg, Germany

Received 1 April 2015; accepted in revised form 13 June 2015

Abstract. Based on atomic force microscopy (AFM) and Fourier transform infrared spectroscopy (FTIR) analysis of the rubber-filler gel (*wetting concept*) the kinetics of selective wetting of carbon nanotubes (CNTs) in ternary styrene butadiene rubber (SBR)/butadiene rubber (BR)/natural rubber (NR) blends was qualitatively and quantitatively characterized. Almost all CNTs are found to be wetted by the non-polar NR but not by the other non-polar rubber like BR or weakly polar SBR. It was proposed that phospholipids, which are linked to the α-terminal of NR can interact with the CNT surface through cation-π interactions forming strong bonding between NR and CNTs. Using the corrected surface tension value of NR, which involves the effect of phospholipids found in our previous work the selective wetting of CNTs in ternary rubber blends can be well predicted using the *Z-model* for a thermodynamic equilibrium state. By replacing the non-polar BR by a polar rubber like nitrile butadiene rubber (NBR) as a blend component CNTs are wetted by NBR slightly more than by NR thanks to the strong interaction between CNTs and nitrile groups of NBR. SBR remains unbound to CNTs in both blends.

Keywords: *manocomposites, carbon nanotubes, rubber blends, selective filler wetting*

1. Introduction

Carbon nanotubes (CNTs) with special nanoscale structure combined with the high strength of the carbon-carbon bondings and a large aspect ratio opens up a wide range of new applications [1]. However, the physical properties of the CNT-polymer composites are often below expectations, because a sufficiently effective force transfer between the polymer matrix and CNTs has not yet been reached. In order to exploit the exceptional mechanical and electrical properties of CNTs in polymer composites, the filler wetting and dispersion as well as the filler-polymer interaction must be increased [2–4]. It is generally known, that the smaller the contact angle θ between polymer and filler, the better the wettability of the filler and the stronger the polymer-filler interaction. Although the contact angle θ can be calculated from the surface tension of the individual components of the mixture, it is not sufficient for the description of the complex wetting behavior of the filler in rubber compounding [5]. The reason is that the filler wetting is not only thermodynamically determined, but it is also a kinetic process. Due to the agglomerate structure of filler polymer chains need a certain time

*Corresponding author, e-mail: le-haihong@ipfdd.de

to wet and infiltrate into the voids and pores of the agglomerates. In addition, the evaluation of filler wetting based on the contact angle θ is always associated with a large uncertainty, because the filler surface is often absorbed by other ingredients of the mixture during the mixing process, especially in rubber processing. That leads to a significant and uncontrolled change in the surface energy of the filler and thus its wettability [6]. Different methods [7–17] were developed and used for characterization of filler wetting and polymer-filler interaction in nanocomposites containing CNTs and single polymer. Scanning electron microscopy (SEM) of cryo-fractured surfaces of the composites was used for visualization of the polymer layer bonded to the filler [7, 8]. Using dynamic mechanical analysis (DMTA) for filled rubber compounds a broad peak of the loss factor in the temperature range of the material glass transition temperature was observed and attributed to the reduced mobility of the bound polymer layer [11]. The shift of the D and G bands in the Raman spectra of the CNT composites was discussed as a result of the CNT-matrix wetting [9, 10] and cation-π bonds between ionic liquid and CNTs [11]. Analysis of rubber-filler gel after extraction experiments (bound rubber measurement) by means of nuclear magnetic resonance (NMR), pyrolysis gas chromatography (PGC) and Fourier transform infrared spectroscopy (FTIR) as well as thermogravimetric analysis (TGA) was carried out for qualitative and quantitative characterization of the physical background of the filler-polymer interaction in carbon black or silica filled rubber compounds [12–17]. If the rubber matrix consists of two or more rubber components the wetting of filler aggregates becomes much inhomogeneous because of the different affinity of filler to rubber components. Up to date, the selective wetting of filler in rubber blends has not been characterized systematically so far. In our previous works, the selective localization of carbon black (CB) [18] and silica in binary [19] and ternary rubber blends [5] were thoroughly characterized by means of the *wetting concept* based on the TGA and FTIR analysis of rubber-filler gel. Recently, the selective localization of CNTs in binary styrene butadiene rubber (SBR)/natural rubber (NR) blends was investigated [20]. An unusually high loading of CNTs localized in the NR phase was found and the strong cation-π interaction between the linked phospholipids of NR and the π electrons of CNT surface was proposed to explain this result.

In the present work we modified the *wetting concept* in order to characterize the kinetics of selective wetting of CNT surface by rubber components of ternary blends based on SBR/BR/NR and SBR/NBR/NR. The effect of strong cation-π interaction of NR and CNTs as well as the effect of rubber polarity by replacement of BR by NBR on the selective wetting of CNTs will be characterized and discussed.

2. Experimental

2.1. Materials and mixture preparation

Solution styrene butadiene rubber (S-SBR) SPRINTAN SLR-4601 (Styron Deutschland GmbH) with a styrene content of 21% and vinyl content of 63%, butadiene rubber (BR) Buna cis 132 (Styron Deutschland GmbH) and nitrile butadiene rubber (NBR) Perbunan 3445F (Lanxess) with a nitrile content of 34% as well as natural rubber (NR) Standard Malaysian Rubber (SMR10) (Weber & Schaer GmbH) were used as rubber matrix. NR was masticated by means of two-roll mill before use in order to obtain a similar Mooney viscosity value as the other blend partners. Multi-walled carbon nanotubes (CNTs) Nanocyl™ NC7000 (Nanocyl S.A., Belgium) with an average diameter of 10 nm and a broad length distribution with several nanotubes up to 10 μm were used as filler. An amount of peroxide (Peroxan DC, Pergan GmbH, Germany) of 1 phr was used as vulcanizing agent for all the mixtures.

For preparation of CNT filled compounds and blends an internal mixer (Rheocord 300p, ThermoHaake) was used by keeping the following mixing conditions: initial chamber temperature T_A of 50°C, rotor speed of 75 rpm, fill factor of 0.68. A conductivity sensor system was installed in the chamber of the internal mixer to measure the electrical signal of the conductive mixtures. CNT filled compounds were prepared by mixing 7 phr CNTs with different rubbers investigated. Two ternary blends CNT-SBR/BR/NR with a weight ratio of 33/33/34 and CNT-SBR/NBR/NR with a weight ratio of 33/33/34 containing 5 phr CNTs were prepared in one-step mixing process (*statistical blends*). For achieving ternary blends from *masterbatch mixing* a masterbatch CNT-SBR was prepared by pre-mixing CNTs in SBR and then the masterbatch was mixed with two other fresh rubbers in order to receive two masterbatch blends

(CNT-SBR)/BR/NR and (CNT-SBR)/NBR/NR with the composition corresponding to that of the *statistical blend*. For an effective dispersion of CNTs in rubber matrix an ethanol-assisted mixing process (*wet mixing*) as described in our previous work [20] was applied. CNTs were first wetted with a certain amount ethanol to a paste. Then, it was added into the mixing chamber with rubber for preparation of the composites without any additional surfactant. Ethanol was entirely vaporized during the mixing process. A weight ratio ethanol/CNT of 3.7 was chosen for a good dispersion of CNTs. Samples were taken out during the mixing process at different times for further investigation.

2.2. Determination of rubber layer *L*

An amount of 0.1 g of each uncured mixture was stored in 100 mL toluene at room temperature for seven days. The solution was cast from the flask and the rubber-filler gel was taken out and dried up in an oven with a temperature of 70°C for 3 h to a constant mass. At least two experiments were carried out for each sample. Rubber layer L was calculated using Equation (1) [18, 19]:

$$L = \frac{m_2 - m_1 \cdot c_{CNT}}{m_2} \tag{1}$$

The mass m_1 is corresponding to the rubber compound before extracting. m_2 is the mass of the rubber-filler gel, which is the sum of the undissolvable rubber part and the mass of CNTs. c_{CNT} is the mass concentration of CNTs in the composite.

2.3. Experimental determination of selective filler wetting in ternary blends

Experimental determination of filler wetting by means of the *wetting concept* was carried out according to procedure described in details in our previous work for silica filled rubber blend [19] The fraction of filler surface $S^{B(SBR)}(t)$, $S^{B(BR)}(t)$ and $S^{B(NR)}(t)$ wetted by the SBR, BR and NR phase, respectively, in ternary SBR/BR/NR blend can be determined according to Equations (2)–(4).

$$\frac{S^{B(SBR)}(t)}{S^{B(BR)}(t)} = \frac{L_P^{BR}}{L_P^{SBR}} \cdot \frac{L^{B(SBR)}(t)}{L^{B(BR)}(t)} \tag{2}$$

$$\frac{S^{B(BR)}(t)}{S^{B(NR)}(t)} = \frac{L_P^{NR}}{L_P^{BR}} \cdot \frac{L^{B(BR)}(t)}{L^{B(NR)}(t)} \tag{3}$$

$$S^{B(SBR/NBR/NR)}(t) = S^{B(SBR)}(t) + S^{B(BR)}(t) + S^{B(NR)}(t) \tag{4}$$

$S^{B(SBR/BR/NR)}(t)$ is the total filler surface wetted by the blend at the mixing time t. The plateau values L_P^{SBR}, L_P^{BR} and L_P^{NR} are the rubber layer at the end of the wetting process of SBR, BR and NR in single compounds experimentally determined (see section 3.2). $L^{B(SBR)}(t)$, $L^{B(BR)}(t)$ and $L^{B(NR)}(t)$ are the rubber layer of the blend component SBR, NBR and NR at mixing time t, respectively. Their sum is the rubber layer $L^{B(SBR/BR/NR)}(t)$, which is experimentally determined by the extraction experiment of the blend. Using FTIR analysis of the rubber-filler gel the values of $L^{B(SBR)}(t)$, $L^{B(BR)}(t)$ and $L^{B(NR)}(t)$ can be determined from $L^{B(SBR/NBR/NR)}(t)$ and the ratio of peak area A^{SBR}/A^{BR} and A^{BR}/A^{NR} according to Equations (5)–(6) as described in our previous works [19]:

$$\frac{L^{B(SBR)}(t)}{L^{B(BR)}(t)} = \frac{1}{f_{SBR/BR}} \cdot \frac{A^{SBR}(t)}{A^{BR}(t)} \tag{5}$$

$$\frac{L^{B(BR)}(t)}{L^{B(NR)}(t)} = \frac{1}{f_{BR/NR}} \cdot \frac{A^{BR}(t)}{A^{NR}(t)} \tag{6}$$

A^{SBR}, A^{BR} and A^{NR} are the areas of a characteristic peak of the SBR phase at 1494 cm^{-1} (stretching vibration of the phenyl ring) and BR phase at 3004 cm^{-1} (stretching mode C–H) as well as NR phase at 1376 cm^{-1} (bending vibration of –CH). For the system SBR/NBR/NR a characteristic peak of the NBR phase at 2238 cm^{-1} (stretching vibration of –C≡N) was used for calculation of A^{NBR}. The slope $f_{SBR/BR}$ = 0.33 and $f_{BR/NR}$ = 0.75 for SBR/BR/NR blend as well as $f_{SBR/NBR}$ = 0.31 and $f_{NBR/NR}$ = 1.1 for SBR/NBR/NR blend were determined using calibrations curves [19]. Setting $L^{B(SBR)}/L^{B(BR)}$ and $L^{B(BR)}/L^{B(NR)}$ into Equations (2)–(4) the selective wetting of CNTs in ternary rubber blend can be determined.

2.4. Structural characterization

Optical microscopy

Optical microscopy was used to characterize the CNT macrodispersion. The ratio of the surface of non-dispersed agglomerates to that of the image A/A_0 is a measure for the filler macrodispersion.

Atomic Force Microscopy

Investigations of filler distribution were carried out by an Atomic Force Microscope (AFM) Nanowizard®II (JPK-Instruments, Berlin) with a scan-head of 100×100×15 μm^3. For maximum resolution the z-scanner range was reduced to 1.5 μm. Super sharp silicon cantilever (SSS-NCHR, Nanosensors™, with tip diameter of approx. 4 nm) was used only. The AFM was operated in intermittent mode with a constant lever amplitude to keep the interaction forces in a same level to achieve a comparable phase distribution for all samples. All samples were produced by cutting in a cryo-chamber CN 30 of a rotary microtom HM 360 (Microm) with a diamond knife at –120°C.

FTIR spectroscopy analysis

The analysis of the rubber-filler gel was carried out by use of a FTIR spectrometer S2000 (Perkin Elmer) equipped with a diamond single Golden Gate ATR cell (Specac). The ATR cell was pressed on a shapeless piece of rubber-filler gel with a measuring area of 2 mm×2 mm. Five spectra were recorded for each sample.

3. Results and discussion

3.1. Online measured electrical conductance and CNT macrodispersion

The online conductance curves of two statistical blends CNT-SBR/BR/NR and CNT-SBR/NBR/NR without and with ethanol recorded during the mixing are presented in Figure 1. Without ethanol, CNT-SBR/BR/NR and CNT-SBR/NBR/NR blends show no electrical signal (curve 1 and 2), that indicates no percolated conduction filler network formed in rubbers because of the bad filler dispersion. They show several large CNT agglomerates in optical macroscopic images with a macrodispersion A/A_0 of 15 and 35%, respectively (Figure 1b and 1d). When CNT/ethanol mixture is added to SBR/BR/NR blend, a significant increase of conductance of several orders of magnitude is observed (curve 3). According to our previous work [20] the macrodispersion of filler and the online conductance correlate closely to each other. The largest change of the size of filler agglomerates, i.e. the dispersion of large filler agglomerate into smaller aggregates or even individual tubes, is determined in the period between t_{onset} and t_{Gmax}. Upon t_{Gmax} the online conductance decreases slightly that is related to the better distribution of small aggregates throughout the matrix and/or shortening of tubes. Thus, t_{onset} and t_{Gmax} have been often used for characterization of the filler dispersion kinetics. A t_{Gmax} recorded at 5 min is related to a fast dispersion of CNTs in SBR/BR/NR blend. Optical microscopic image of the sample taken out at 30 min mixing confirms the improvement of CNT dispersion in this blend with assistance of ethanol. CNT dispersion in CNT-SBR/BR/NR blend is improved markedly with a macrodispersion reducing from 15 to 3.5% (Figure 1b and 1c). In contrast, ethanol shows only moderate effect on the online conductance curve and CNT dispersion of CNT-SBR/NBR/NR blend. The macrodispersion A/A_0 decreases from 35 to 20% according to Figure 1d and 1e. The reason for the insignificant effect of ethanol in the blend containing NBR may be related to the bad compatibility between ethanol and NBR. With a surface tension of 22 mN/m ethanol shows a good compatibility with the SBR, BR and NR, however, it is not compatible with the polar NBR. Upon ethanol evaporation during the mixing CNTs will be dispersed well in NBR.

3.2. Wetting behavior of CNTs in different rubbers

The dependence of the rubber layer L on the mixing time of filled SBR, BR, NBR and NR compounds is presented in Figure 2a. With increasing mixing time the infiltration of SBR, BR, NBR and NR molecules into CNT agglomerate and the dispersion of CNTs take place simultaneously according to the *infiltration* model proposed by Manas-Zloczower [21]. The rubber layer L of investigated rubbers without ethanol assistance increases with different rates and reaches a plateau value after 50 min for both SBR and BR, 10 min for NBR and 17 min for NR, respectively. According to our previous work [5], the development of the rubber layer L can be theoretically calculated by Equation (7):

$$L = \frac{hbt^{1/2}}{hbt^{1/2} + \frac{\rho_F}{\rho_R}(1-\varepsilon)} \tag{7}$$

where ε is the porosity and ρ_F is the density of the filler. ρ_R is the density of rubber. b is a measure for wetting speed and can be described by Equation (8):

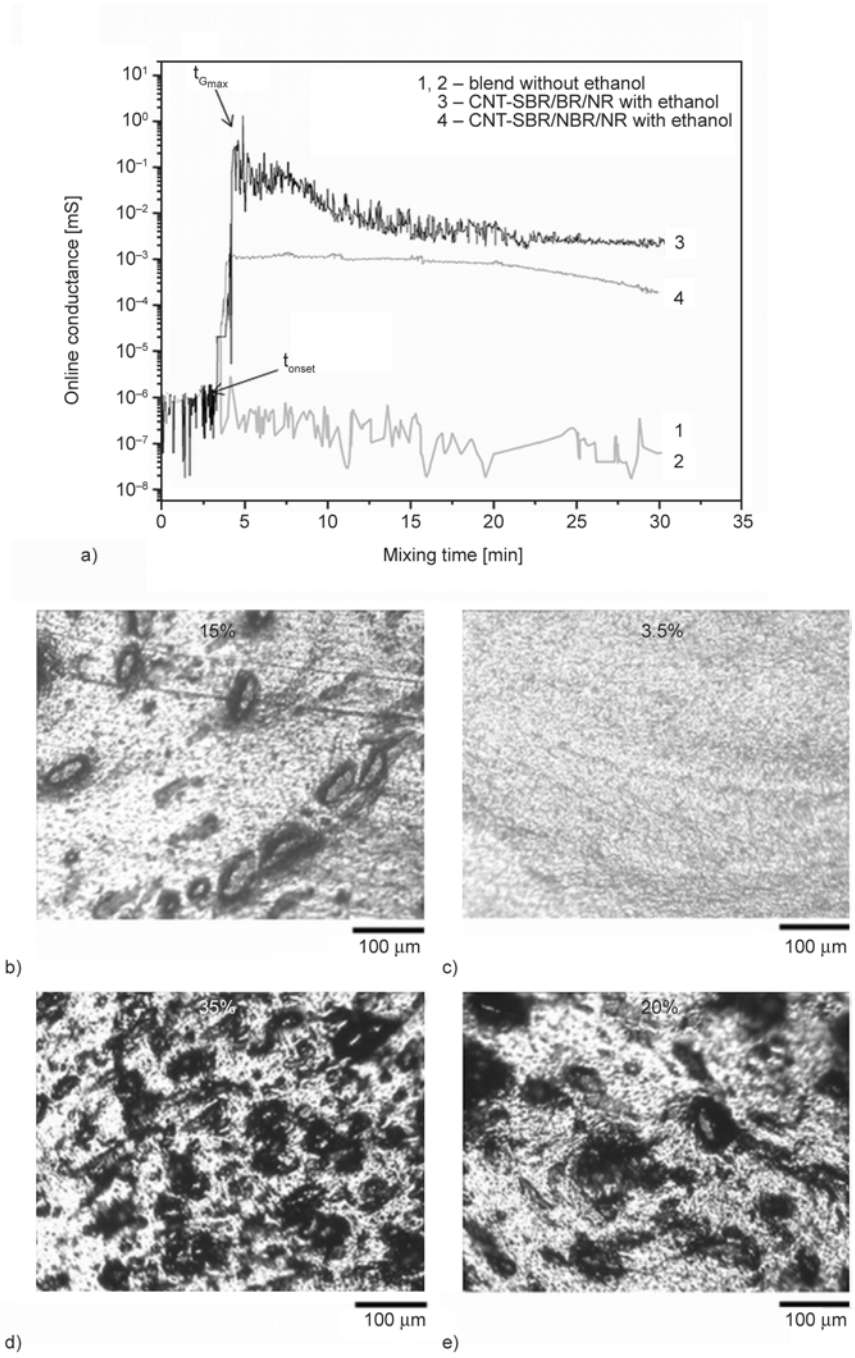

Figure 1. Online conductance curves of CNT filled blends in dependence on mixing time (a) and optical microscopic images of CNT-SBR/BR/NR without (b) and with ethanol (c) as well as CNT/NBR/NR blend without (d) and with ethanol (e) taken out at 30 min mixing

$$b = \frac{\varepsilon}{D_0}\left(\frac{S\gamma_R \cos\theta}{3\eta_R} + \frac{S^2\Delta P}{6\eta_R}\right)^{1/2} \quad (8)$$

$$L_P = \frac{\varepsilon h}{\varepsilon h + \frac{\rho_F}{\rho_R}(1-\varepsilon)} \quad (9)$$

In our model S is considered as pore size of filler, ΔP is the pressure in the mixing chamber. γ_R is the surface tension of rubber, θ is the contact angle and η_R is the rubber viscosity. D_0 is the average agglomerate diameter. The correlation between the plateau value L_P and the factor h can be described by Equation (9):

By fitting Equation (7) to the experimental data presented in Figure 2a with the average $\rho_R = 0.94$ g/cm^3 and $\rho_F = 2.0$ g/cm^3, $\varepsilon = 0.92$ [22] the wetting speed $b^{SBR} = 0.19$ min$^{-1/2}$ and $b^{BR} = 0.19$ min$^{-1/2}$ and $b^{NBR} = 0.47$ min$^{-1/2}$ as well as $b^{NR} = 0.31$ min$^{-1/2}$ can be experimentally determined for SBR, BR, NBR and NR, respectively.

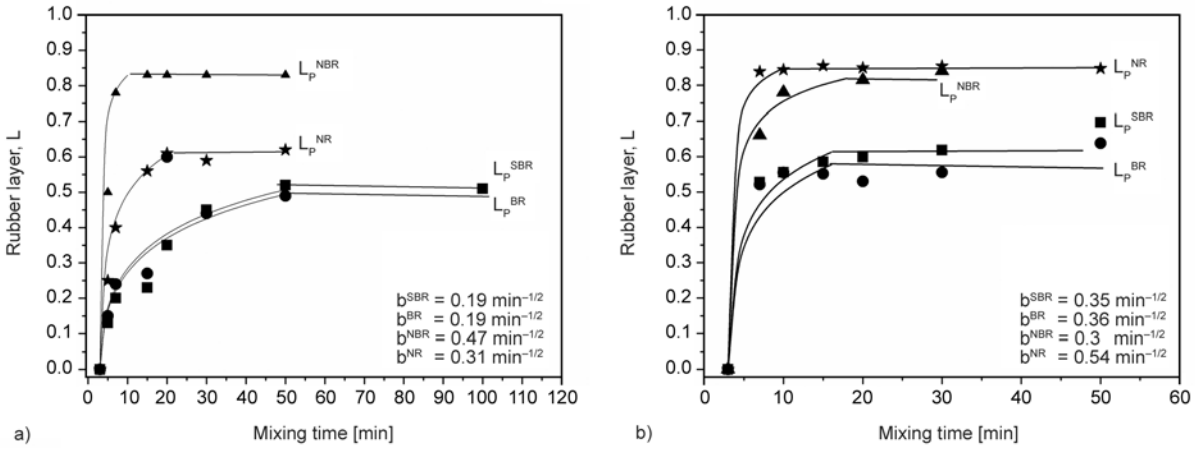

Figure 2. Development of rubber layer *L* of SBR, BR and NBR as well as NR compound during mixing process without (a) and with (b) ethanol assistance

According to Equation (8) the wetting speed *b* increases with increasing rubber surface tension. The high value of the wetting speed of NBR is corresponding to the high surface tension of NBR of 27 mN/m [23]. The good filler-rubber interaction of CNTs in NBR was evidenced by Verge *et al*. [24]. They stated that nitrile groups of NBR can be bonded with CNT surface along the mixing process through the electrostatic interactions. It comes out that the polymer bonding rate onto the CNT surface increases with the nitrile content in NBR.

Although the surface tension γ_{NR} = 22 mN/m determined by the contact angle measurement is lower than that of SBR, NR shows a higher wetting speed b^{NR} = 0.31 min$^{-1/2}$ compared to b^{SBR} = 0.19 min$^{-1/2}$. As discussed in our previous work [20] a strong rubber-filler interaction between NR and CNTs was proposed by comparing the CNT localization in SBR/NR and SBR/isoprene (IR) blend. The solid NR was proposed to consist of ω-terminal, two trans-1,4 isoprene units, about 1000–3000 cis-1,4 isoprene units, and α-terminal [25, 26]. The ω-terminal of the rubber molecule was postulated to be a modified dimethylallyl group linking to a functional group, which is associated with the proteins as cross-linking points in NR. On the other hand, the α-terminal group of NR was postulated to consist of two kinds of functional group, i.e., monophosphate and diphosphate groups, which are linked with phospholipids via hydrogen bonding as a predominant linkage. When CNTs are mixed into NR the ammonium cation N^+ of phospholipids can interact with CNT surface via cation–π interaction forming strong linkages beside the Van der Waals bondings. Based on the experimental result shown in Figure 2a it can be postulated that NR can wet CNTs faster than SBR due to the cation–π interaction. Because the amount of phospholipids in NR is very small (<1.0%) and they are associated with the chain end, the value of surface tension of NR is mainly determined by the isoprene units of the backbone. Thus, the surface tension value of NR determined by the contact angle measurement does not involve the effect of linked phospholipids and thus it cannot explain the fast wetting speed of NR *vs*. SBR. Based on our previous work [27], the strong interaction between NR and CNTs was quantified through the corrected surface tension of NR corr γ_{NR} = 26 mN/m, which was calculated by setting the stationary values of filler localization into the *Z-model*.

In Figure 2b, an addition of ethanol accelerates the CNT wetting by SBR, BR and NR due to the faster filler dispersion that eases the infiltration of rubber into filler agglomerate. In contrast, ethanol slows the wetting of CNTs by NBR because of the incompatibility between ethanol and NBR. The wetting speed b^{SBR} = 0.35 min$^{-1/2}$ and b^{BR} = 0.36 min$^{-1/2}$ and b^{NR} = 0.54 min$^{-1/2}$ are found to be increased, while b^{NBR} = 0.3 min$^{-1/2}$ is lower than that determined from Figure 2a.

3.3. Selective CNT wetting in ternary blends

On the basis of the *Z-model* proposed in our previous work [6] the selective wetting of filler in a ternary SBR/BR/NR blend at a thermodynamic equilibrium state can be predicted using Equations (10)–(12):

$$\frac{S_{eq}^{B(BR)}}{S_{eq}^{B(SBR)}} = n_{BR/SBR}\left(\frac{\gamma_{SBR}+\gamma_F-2\sqrt{\gamma_{SBR}\gamma_F}}{\gamma_{BR}+\gamma_F-2\sqrt{\gamma_{BR}\gamma_F}}\right)^2 \quad (10)$$

$$\frac{S_{eq}^{B(NR)}}{S_{eq}^{B(BR)}} = n_{NR/BR}\left(\frac{\gamma_{BR}+\gamma_F-2\sqrt{\gamma_{BR}\gamma_F}}{\gamma_{NR}+\gamma_F-2\sqrt{\gamma_{NR}\gamma_F}}\right)^2 \quad (11)$$

$$S^B = S_{eq}^{B(SBR)} + S_{eq}^{B(BR)} + S_{eq}^{B(NR)} \quad (12)$$

$S_{eq}^{B(SBR)}$, $S_{eq}^{(BR)}$ and $S_{eq}^{B(NR)}$ are the fractions of filler surface wetted by rubber component of the ternary blend at an equilibrium state. $n_{BR/SBR}$ and $n_{NR/BR}$ are the mass ratio of the rubber phase BR to SBR and NR to BR, respectively. γ_{SBR}, γ_{BR}, γ_{NR} and γ_F are the surface tension values of the blend components and filler, respectively. S^B is the total surface of filler added to the blend. Setting the surface tension values γ_{SBR} = 23.8 mN/m, γ_{BR} = 22 mN/m and corr γ_{NR} = 26 mN/m of rubber components into Equations (10)–(12) with $n_{BR/SBR}$ = 1 and $n_{NR/BR}$ = 1 for the investigated blends, three Z-shaped master curves demonstrating the selective wetting of CNTs by three blend components in dependence on the filler surface tension can be created as seen in Figure 3a. Fitting the CNT surface tension γ_F = 30 mN/m [22] into the master curves a surface fraction wetted by each phase, $S_{eq}^{B(SBR)}$ = 0.13, $S_{eq}^{B(BR)}$ = 0.07 and $S_{eq}^{B(NR)}$ = 0.8, respectively, can be predicted for a thermodynamic equilibrium state. For SBR/NBR/NR blend $S_{eq}^{B(SBR)}$ == 0.02, $S_{eq}^{B(NBR)}$ = 0.65 and $S_{eq}^{B(NR)}$ = 0.33 are theoretically determined from Figure 3b.

The CNT selective wetting determined can be qualitatively demonstrated by TGA and FTIR investigations of the rubber-filler gels. In Figure 4 the TGA curves of rubber-filler gel of CNT-SBR/BR/NR and CNT-SBR/NBR/NR blends taken out at 50 min mixing are presented. The onset of degradation temperature of NR is about 370°C, while SBR, BR and NBR start to be degraded at 430°C. Making use the different degradation temperature of NR from the other blend partners the contribution of NR is determined by means of differential thermogravimetric analysis and shown in Figure 4a. It is obvious that the contribution of the wetted NR in the rubber-filler gel of CNT-SBR/BR/NR blend is three times higher than

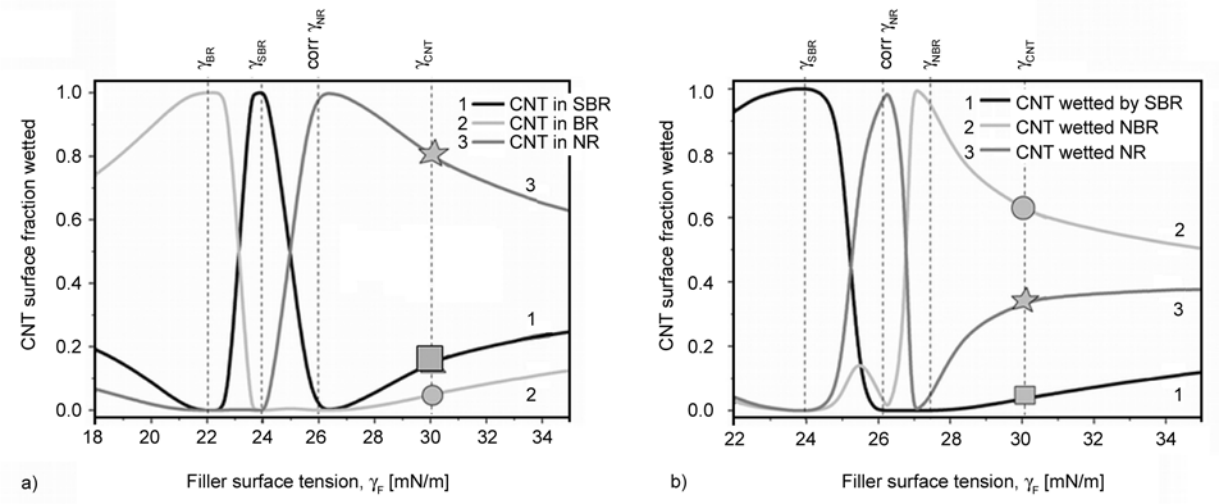

Figure 3. Master curves of selective filler wetting in 33/33/34 SBR/BR/NR (a) and 33/33/34 SBR/NBR/NR (b) blend determined by *Z-model* (symbols: ■: CNTs wetted by SBR, ●: CNTs wetted by BR or NBR, ★: CNTs wetted by NR)

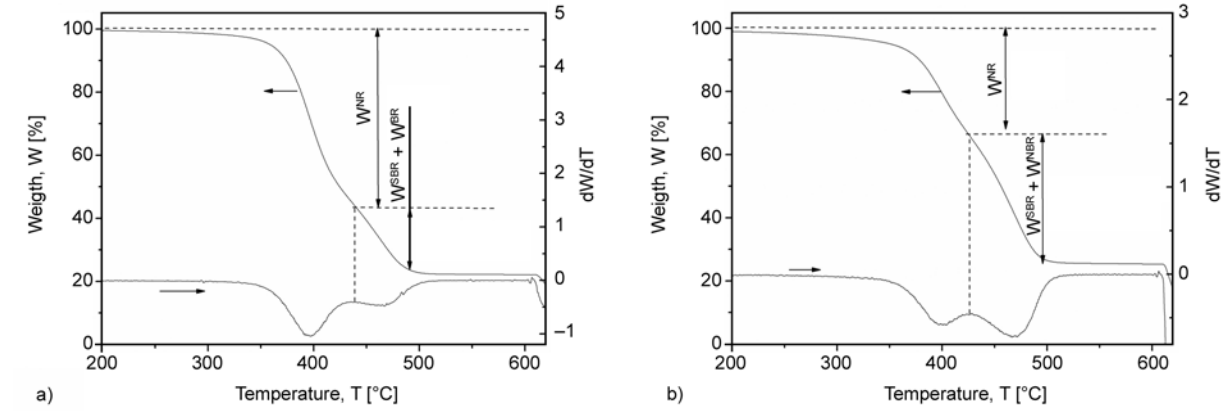

Figure 4. TGA curves of blend and its rubber-filler gel of CNT-SBR/BR/NR (a) and CNT-SBR/NBR/NR (b), respectively

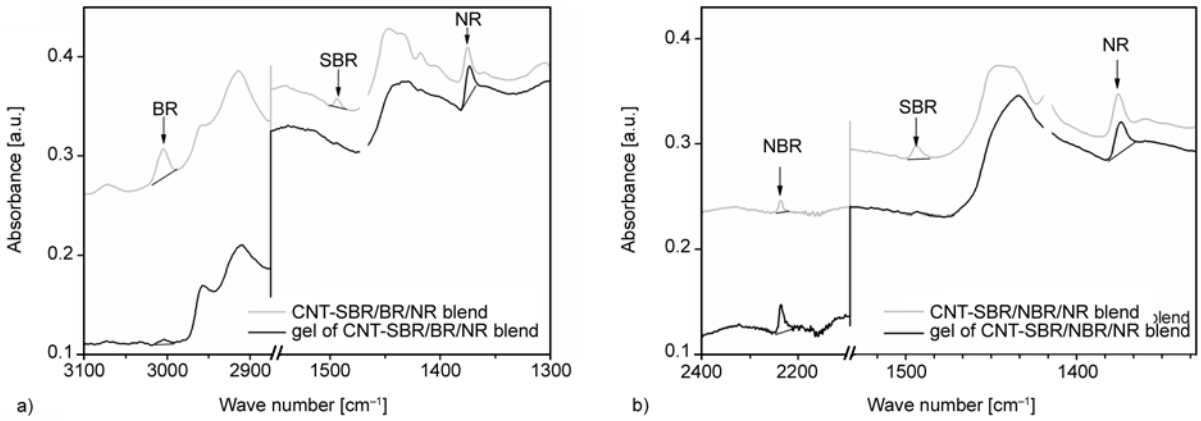

Figure 5. FTIR spectra of blend and its rubber-filler gel of CNT-SBR/BR/NR (a) and CNT-SBR/NBR/NR (b), respectively

that of SBR and BR together (Figure 4a) and it is only one third of the total wetting rubbers in the gel of CNT-SBR/NBR/NR blend (Figure 4b).

FTIR spectra of both blends and their rubber-filler gel are shown in Figure 5a and 5b. Characteristic peaks for SBR, NBR and NR as well as BR, are clearly detected in the spectra. A characteristic peak of SBR at 1494 cm^{-1} (stretching vibration of the phenyl ring) and NBR at 2238 cm^{-1} (stretching vibration of –C≡N) and NR at 1376 cm^{-1} (bending vibration of –CH) as well as BR at 3004 cm^{-1} (stretching vibration C–H) are used for evaluation of the rubber-filler gel composition. The spectral of the blend and its gel were normalized with respect to the NR peak intensity for comparison purpose. It is clearly observed for CNT-SBR/BR/NR blend that upon extraction the intensity of bound SBR and BR of the gel contributes only 10% of that of the blend (Figure 5a). It indicates that CNTs are mainly wetted by the NR phase. Comparing the spectral of CNT-SBR/NBR/NR blend with that of its gel in Figure 5b we observe that the intensity of NBR increases twice after extraction experiment, while the SBR peak nearly disappears. Thus, in this blend CNTs are significantly wetted by the NBR phase and only moderately by NR phase. Similarly to the CNR-SBR/BR/NR blend the SBR phase in CNT-SBR/NBR/NR blend seems not to wet CNTs.

The kinetics of CNT wetting in CNT-SBR/BR/NR blend in presence of ethanol was quantified by the *wetting concept*. As seen in Figure 6a the CNT surface is wetted differently after adding 5 phr CNT into the blend. It is clear that NR wets more CNT surface than SBR and BR in the first mixing stage (up to 10 min) due to the higher wetting speed as observed in Figure 2a as well as the strong cation-π interaction between NR and CNTs as discussed in [20], while CNTs are insignificantly wetted by SBR and BR phase. A CNT surface fraction of about 0.81 wetted by NR phase was found at 10 min. Both SBR and BR wet only a surface fraction of 0.19. In the second stage from 10 to 50 min, no change in the wetting kinetics of CNTs was observed, i.e. the wetting reaches its thermodynamic equilibrium state.

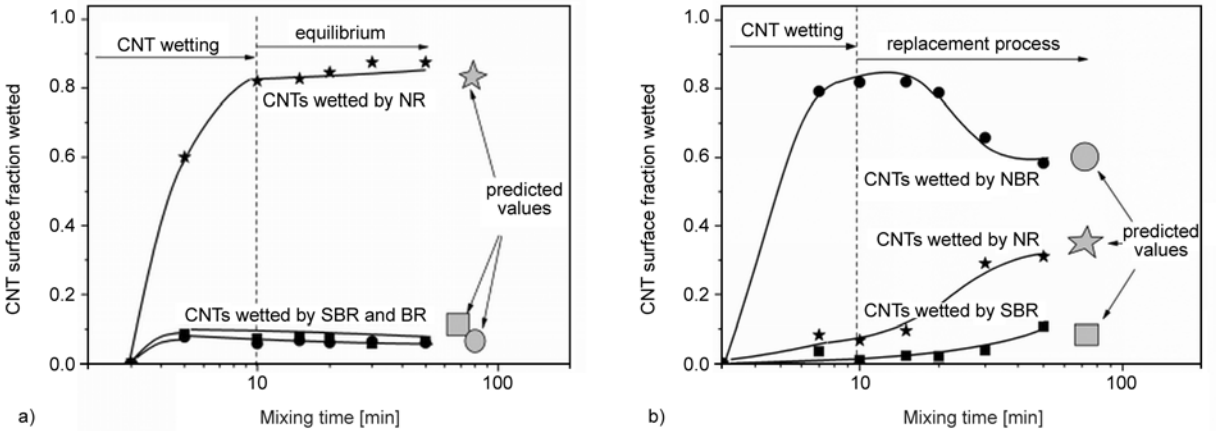

Figure 6. Kinetics of selective filler wetting in statistical blends 33/33/34 CNT-SBR/BR/NR (a) and 33/33/34 CNT-SBR/NBR/NR (b) obtained by the *wetting concept*. Values predicted by the *Z-model* are displayed (grey symbols)

By replacing the non-polar BR component by the polar NBR the kinetics of CNT wetting in CNT-SBR/NBR/NR blend is characterized and presented in Figure 6b. In the first mixing stage up to 10 min, CNTs are wetted very fast by NBR, while NR and SBR wet CNTs much slower. The fast wetting of CNTs by NBR is clearly explained by the high wetting speed b^{NBR} determined from Figure 2. A CNT surface fraction of about 0.82 was determined at 10 min, when the wetting process ends. In the second stage from 10 to 50 min, a replacement process of NBR chains by NR chains took place. A portion of bound NBR chains was replaced by NR chains on the CNT surface. Only a minor surface of CNTs is wetted by the SBR phase after long mixing time. At 50 min mixing time CNT surafce fraction wetted by each blend phase, $S^{B(SBR)} = 0.1$, $S^{B(NBR)} = 0.6$ and $S^{B(NR)} = 0.3$ are observed. These values are corresponding well to the predicted ones shown in Figure 3b. It comes out that the electrostatic interaction between nitrile groups of NBR with CNTs is stronger than the cation-π interaction between NR and CNTs.

The quantitative characterization of CNT wetting in both blends can be visualized well by AFM. In Figure 7a AFM images of CNT-SBR/BR/NR blend made by two magnifications show obviously that CNTs are encapsulated by a dark rubber phase. By taking into consideration the difference hardness of blend components the dark phase is identified as NR. SBR and BR are compatible and form a continuous phase, which seems not to wet CNTs. The morphology of CNT-SBR/NBR/NR blend presented in Figure 7b shows some unfilled domains, which can be attributed to the SBR phase. A large amount of CNTs (bright tubes) is found in the NBR continuous phase (gray continuous phase), which is surrounding the SBR and NR domains. For the CNT-SBR/NBR/NR blend, the presence of ethanol accelerates the dispersion of CNTs localized in SBR and NR phase but at the same time slowdowns the CNT dispersion in NBR phase. According to Figure 6b NBR hosts 60 wt% of CNTs used and, thus, that results in the bad dispersion of CNTs in the whole blend.

In order to investigate the replacement process of one rubber component by the other ones (desorption and adsorption) taking place on the CNT surface during *masterbatch mixing*, the kinetics of CNT wetting of (CNT-SBR)/BR/NR blend prepared by blending the CNT-SBR masterbatch with the other fresh rubbers, BR and NR, was determined and is presented in Figure 8a. It is found that SBR chains prebound to the CNT surface from *masterbatch mixing* is strongly replaced by NR and slightly by BR during the subsequent mixing process. The replacement process took place within about 5 min. Afterwards the wetting of CNTs seems to reach the stationary state

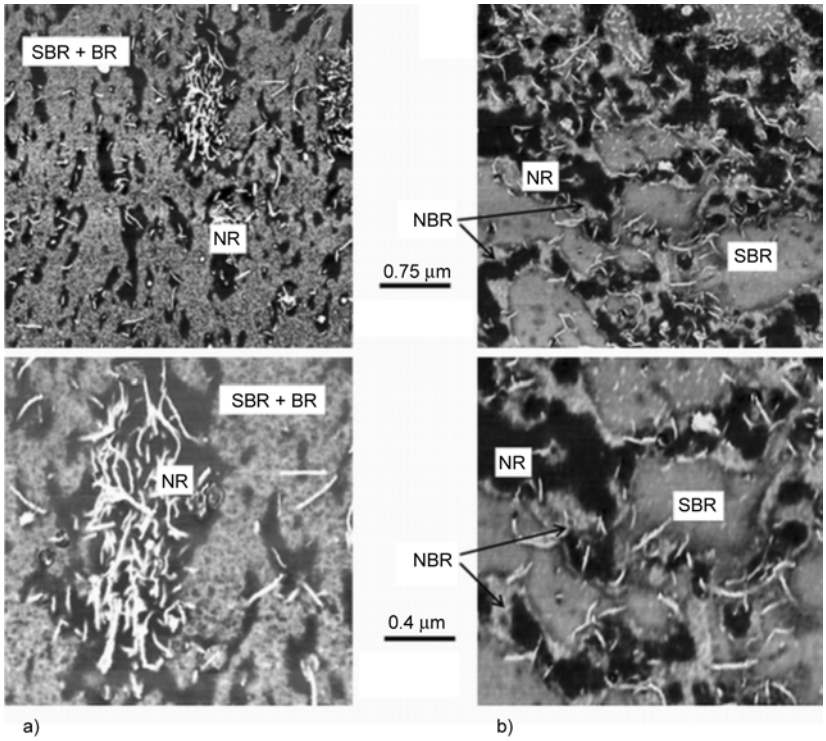

Figure 7. AFM images of CNT-SBR/BR/NR (a) and CNT-SBR/NBR/NR blend (b) at two magnifications.

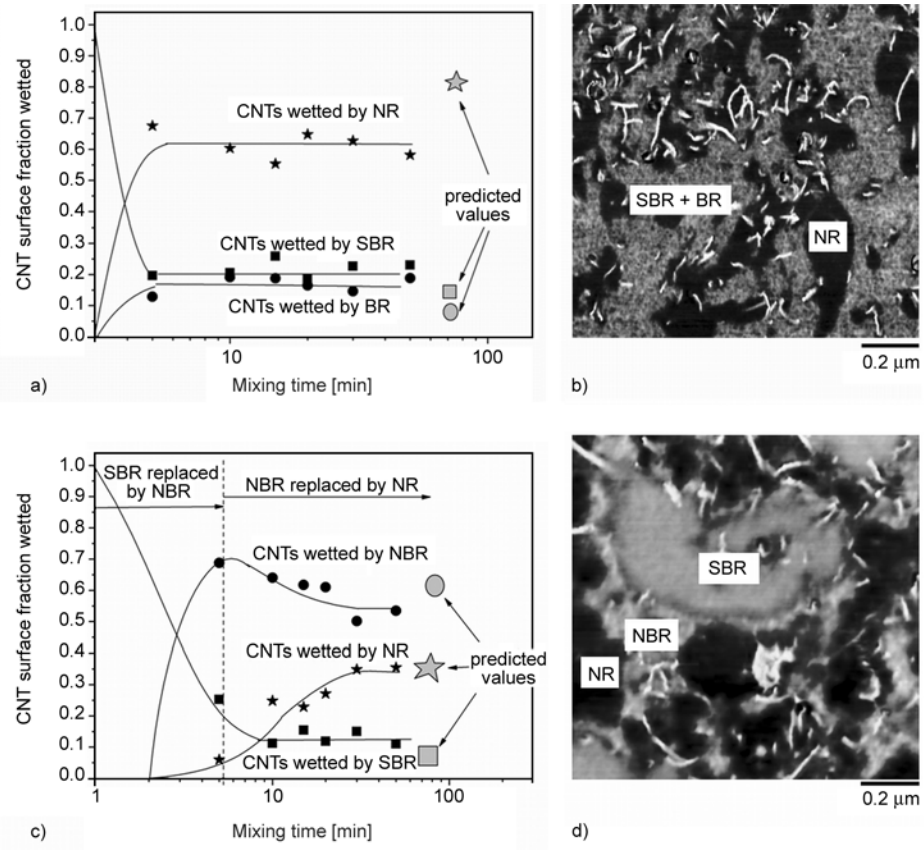

Figure 8. Kinetics of CNT selective wetting in (SBR-CNT)/BR/NR blend (a) and (CNT-SBR)/NBR/NR blend (c) as well as AFM images of samples taken out at 50 min mixing (b, d)

of CNT wetting, which is corresponding well to that of statistical blend and to the prediction. A closer look at the result from Figure 8a reveals that the experimentally determined values of CNT surface fraction wetted by SBR phase remains slightly higher than that predicted. The reason may be related to the fact that during the masterbatch mixing of CNT-SBR some radicals of SBR are formed and they can chemically interact with CNTs. Such chemical bondings are stable and cannot be replaced by NR. It is clear from AFM image of the (CNT-SBR)/BR/NR blend shown in Figure 8b that CNTs (bright tubes) are mainly wetted by the NR phase (dark domains). SBR and BR are compatible, thus they form a continuous phase (gray phase). Some individual tubes are observed in this matrix.

The effect of rubber polarity and blend morphology on the kinetics of selective wetting of CNTs can be observed in the case of (CNT-SBR)/NBR/NR blend. It is clear from Figure 8c that the pre-bound SBR chains are firstly replaced only by NBR in the first mixing stage up to 7 min, while NR seems not to take part in the replacement process. Afterwards, the CNT surface fraction wetted by NBR decreases, while the surface fraction wetted by NR increases, i.e. the bound NBR molecules are replaced by the free NR molecules. This process takes place until the predicted thermodynamic equilibrium state is reached. The obtained progression of selective wetting of CNTs is clearly understood by examining AFM images shown in Figure 8d. The SBR and NR domains are surrounded by a layer of NBR, i.e SBR has no direct contact with NR. Therefore, in the first period of mixing CNT-SBR masterbatch with NBR and NR, only NBR gets into contact with CNT-SBR masterbatch and replaces the bound SBR. At a mixing time of 15 min NBR wets the most surface of CNTs. According to the calculation by means of *Z-model* for the binary 50/50 SBR/NBR blend CNTs are entirely wetted by NBR at an equilibrium state (the result is not shown in the present work). However, according to the *Z-model* for 50/50 NBR/NR blend a CNT surface fraction of 0.6 is wetted by NBR and 0.4 by NR at an equilibrium state. Thus, after 15 min mixing the freshly bound NBR is replaced by NR until the equilibrium state is reached as seen in Figure 8c.

4. Conclusions

It was proposed that phospholipids, which are linked to the α-terminal of NR can interact with the CNT surface through cation-π interactions forming strong bonding between NR and CNTs. These strong interactions are the main reason for the favorable wetting of CNT by the NR phase in SBR/BR/NR blend. Using the corrected surface tension value of NR, which involves the effect of phospholipids found in our previous work the selective wetting of CNTs in ternary rubber blends can be well predicted for a thermodynamic equilibrium state. By replacing the non-polar BR by a polar rubber like NBR as a blend component CNTs are wetted by NBR slightly more than by NR thanks to the strong interaction between CNTs and nitrile groups of NBR. SBR remains unbound to CNTs in both blends. The sequence of replacement of the rubber molecules pre-bound to CNT surface by the other ones, for instance SBR first by NBR and then NBR by NR, is well explained by taking into consideration the blend morphology made by AFM.

Acknowledgements

The authors wish to thank the Deutsche Forschungsgemeinschaft (DFG) (Project Nr. LE 3202/1-1) and Vietnam National Foundation for Science and Technology Development (Nafosted) (Grant number 104.02-2014.90) for the financial support.

References

[1] Bokobza L.: Multiwall carbon nanotube elastomeric composites: A review. Polymer, **48**, 4907–4920 (2007). DOI: 10.1016/j.polymer.2007.06.046

[2] Rahmat M., Hubert P.: Carbon nanotube–polymer interactions in nanocomposites: A review. Composites Science and Technology, **72**, 72–84 (2011). DOI: 10.1016/j.compscitech.2011.10.002

[3] McNally T., Pötschke P.: Polymer-carbon nanotube composites: Preparation, properties and applications, Woodhead, Cambridge (2011).

[4] Alig I., Pötschke P., Lellinger D., Skipa T., Pegel S., Kasaliwal G. R., Villmow T.: Establishment, morphology and properties of carbon nanotube networks in polymer melts. Polymer, **53**, 4–28 (2012). DOI: 10.1016/j.polymer.2011.10.063

[5] Le H. H., Keller M., Hristov M., Ilisch S., Xuan T. H., Do Q. K., Pham T., Stöckelhuber K-W., Heinrich G., Radusch H-J.: Selective wetting and localization of silica in binary and ternary blends based on styrene butadiene rubber, butadiene rubber, and natural rubber. Macromolecular Materials and Engineering, **298**, 1085–1099 (2013). DOI: 10.1002/mame.201200307

[6] Le H. H., Ilisch S., Heinrich G., Radusch H-J.: Filler migration in natural rubber blends during the mixing process. in 'Natural rubber materials: Volume 1: Blends and IPNs' (Eds: Thomas S., Han C. C., Pothen L., Rajisha K. R., Maria H.) Royal Society of Chemistry, Cambridge, 132–176 (2014). DOI: 10.1039/9781849737647-00132

[7] Jiang H-X., Ni Q-Q., Natsuki T.: Design and evaluation of the interface between carbon nanotubes and natural rubber. Polymer Composites, **32**, 236–242 (2011). DOI: 10.1002/pc.21040

[8] Jiang M-J., Dang Z-M., Yao S-H., Bai J.: Effects of surface modification of carbon nanotubes on the microstructure and electrical properties of carbon nanotubes/rubber nanocomposites. Chemical Physics Letters, **457**, 352–356 (2008). DOI: 10.1016/j.cplett.2008.04.022

[9] Frogley M. D., Ravich D., Wagner H. D.: Mechanical properties of carbon nanoparticle-reinforced elastomers. Composites Science and Technology, **63**, 1647–1654 (2003). DOI: 10.1016/S0266-3538(03)00066-6

[10] Bokobza L.: A Raman investigation of carbon nanotubes embedded in a soft polymeric matrix. Journal of Inorganic and Organometallic Polymers and Materials, **22**, 629–635 (2012). DOI: 10.1007/s10904-011-9590-7

[11] Das A., Stöckelhuber K. W., Jurk R., Saphiannikova M., Fritzsche J., Lorenz H., Klüppel M., Heinrich G.: Modified and unmodified multiwalled carbon nanotubes in high performance solution-styrene–butadiene and butadiene rubber blends. Polymer, **49**, 5276–5283 (2008). DOI: 10.1016/j.polymer.2008.09.031

[12] Choi S-S.: Difference in bound rubber formation of silica and carbon black with styrene-butadiene rubber. Polymers for Advanced Technologies, **13**, 466–474 (2002). DOI: 10.1002/pat.211

[13] Kralevich M. L., Koening J. L.: FTIR analysis of silica-filled natural rubber. Rubber Chemistry and Technology, **71**, 300–309 (1998). DOI: 10.5254/1.3538486

[14] Choi S-S.: Characterization of bound rubber of filled styrene-butadiene rubber compounds using pyrolysis-gas chromatography. Journal of Analytical and Applied Pyrolysis, **55**, 161–170 (2000). DOI: 10.1016/S0165-2370(99)00095-9

[15] Sierra L., López B. L., Guth J. L.: Microstructural studies of the interactions in SB rubber and mesoporous silica mixtures. Materials Research Innovations, **5**, 268–276 (2000).
DOI: 10.1007/s10019-002-0160-z

[16] Serizawa H., Ito M., Kanamoto T., Tanaka K., Nomura A.: Structural changes during mechanical mixing in carbon black-natural rubber systems studied by pulsed NMR. Polymer Journal, **14**, 149–154 (1982).
DOI: 10.1295/polymj.14.149

[17] Ono S., Kiuchi Y., Sawanobori J., Ito M.: Structure development in silica-filled rubber composites. Polymer International, **48**, 1035–1041 (1999).
DOI: 10.1002/(SICI)1097-0126(199910)48:10<1035::AID-PI265>3.0.CO;2-5

[18] Le H. H., Ilisch S., Kasaliwal G. R., Radusch H-J.: Filler phase distribution in rubber blends characterized by thermogravimetric analysis of the rubber-filler gel. Rubber Chemistry and Technology, **81**, 767–781 (2008).
DOI: 10.5254/1.3548231

[19] Le H. H., Ilisch S., Heidenreich D., Wutzler A., Radusch H-J.: Kinetics of the phase selective localization of silica in rubber blends. Polymer Composites, **31**, 1701–1711 (2010).
DOI: 10.1002/pc.20960

[20] Le H. H., Parsekar M., Ilisch S., Henning S., Das A., Stöckelhuber K-W., Beiner M., Ho C. A., Adhikari R., Wießner S., Heinrich G., Radusch H-J.: Effect of non-rubber components of NR on the carbon nanotube (CNT) localization in SBR/NR blends. Macromolecular Materials and Engineering, **299**, 569–582 (2014).
DOI: 10.1002/mame.201300254

[21] Manas-Zloczower I.: Analysis of mixing in polymer processing equipment. Rheology Bulletin, **66**, 5–8 (1997).

[22] Puretzky A. A., Geohegan D. B., Jesse S., Ivanov I. N., Eres G.: *In situ* measurements and modeling of carbon nanotube array growth kinetics during chemical vapor deposition. Applied Physics A, **81**, 223–240 (2005).
DOI: 10.1007/s00339-005-3256-7

[23] Stöckelhuber K-W., Das A., Jurk R., Heinrich G.: Contribution of physico-chemical properties of interfaces on dispersibility, adhesion and flocculation of filler particles in rubber. Polymer, **51**, 1954–1963 (2010).
DOI: 10.1016/j.polymer.2010.03.013

[24] Verge P., Peeterbroeck S., Bonnaud L., Dubois P.: Investigation on the dispersion of carbon nanotubes in nitrile butadiene rubber: Role of polymer-to-filler grafting reaction. Composites Science and Technology, **70**, 1453–1459 (2010).
DOI: 10.1016/j.compscitech.2010.04.022

[25] Tarachiwin L., Sakdapipanich J., Ute K., Kitayama T., Tanaka Y.: Structural characterization of α-terminal group of natural rubber. 2. Decomposition of branch-points by phospholipase and chemical treatments. Biomacromolecules, **6**, 1858–1863 (2005).
DOI: 10.1021/bm058004p

[26] Tanaka Y., Mori M., Ute K., Hatada K.: Structure and biosynthesis mechanism of rubber from fungi. Rubber Chemistry and Technology, **63**, 1–7 (1990).
DOI: 10.5254/1.3538238

[27] Le H. H., Abhijeet S., Ilisch S., Klehm J., Henning S., Beiner M., Sarkawi S. S., Dierkes W., Das A., Fischer D., Stöckelhuber K-W., Wiessner S., Khatiwada S. P., Adhikari R., Pham T., Heinrich G., Radusch H-J.: The role of linked phospholipids in the rubber-filler interaction in carbon nanotube (CNT) filled natural rubber (NR) composites. Polymer, **55**, 4738–4747 (2014).
DOI: 10.1016/j.polymer.2014.07.043

eXPRESS Polymer Letters Vol.9, No.11 (2015) 972–983
Available online at www.expresspolymlett.com
DOI: 10.3144/expresspolymlett.2015.88

New eco-friendly random copolyesters based on poly(propylene cyclohexanedicarboxylate): Structure-properties relationships

L. Genovese[1], *N. Lotti*[1*], *M. Gazzano*[2], *L. Finelli*[1], *A. Munari*[1]

[1]Dipartimento di Ingegneria Civile, Chimica, Ambientale e dei Materiali, Università di Bologna, Via Terracini 28, 40131 Bologna, Italy
[2]Istituto per la Sintesi Organica e la Fotoreattività, CNR, Via Selmi 2, 40126 Bologna, Italy

Received 15 April 2015; accepted in revised form 13 June 2015

Abstract. A series of novel random copolymers of poly(propylene 1,4-cyclohexanedicarboxylate) (PPCE) containing neopentyl glycol sub-unit (P(PCExNCEy)) were synthesized and characterized in terms of molecular and solid-state properties. In addition, biodegradability studies in compost have been conducted.
The copolymers displayed a high and similar thermal stability with respect to PPCE. At room temperature, all the copolymers appeared as semicrystalline materials: the main effect of copolymerization was a lowering of crystallinity degree (χ_c) and a decrease of the melting temperature compared to the parent homopolymer. In particular, Wide Angle X-Ray diffraction (WAXD) measurements indicated that P(PCExNCEy) copolymers are characterized by cocrystallization, PNCE co-units cocrystallizing in PPCE crystalline phase. Final properties and biodegradation rate of the materials under study were strictly dependent on copolymer composition and χ_c. As a matter of fact, the elastic modulus and the elongation at break decreased and increased, respectively, as neopentyl glycol cyclohexanedicarboxylate (NCE) unit content was increased. The presence of a rigid-amorphous phase was evidenced by means of Dynamic Mechanical Thermal Analysis (DMTA) analysis in all the samples under investigation. Lastly, the biodegradation rate of P(PCExNCEy) copolymers was found to slightly increase with the increasing of NCE molar content.

Keywords: *biodegradable polymers, poly(propylene 1,4-cyclohexanedicarboxylate), neopentyl glycol, random copolymers, solid-state properties*

1. Introduction

Over the last 60 years, plastics have brought economic, environmental and social advantages; synthetic polymeric materials have found wide applications in many aspects of life and industries. This success is mainly due to their low cost, their reproducibility, and their resistance to physical aging and biological attacks [1].
In 2012, around 288 Mt of plastics have been produced worldwide, but within a short period of time almost half of them are disposed to the environment. Only in Europe, over 25 Mt of plastics ended up in the waste stream during 2012 [2].
In this scenario, the resistance of synthetic polymers to biodegradability is becoming highly disadvantageous particularly in those domains where they are used for a limited period of time before becoming wastes. It is the case in surgery, in pharmacology, in agriculture, and in packaging as well. In these fields, time-resistant polymeric wastes are no longer acceptable.
The use of polymeric materials satisfying, among all, the conditions of biodegradability and biocompati-

*Corresponding author, e-mail: nadia.lotti@unibo.it

bility is therefore clear and urgent. On the other hand, the depletion of natural resources as well as high oil and gas prices have a significant impact on increasing use of renewable raw materials in world production of polymers. The application of natural raw materials of plant origin in organic synthesis is compatible with sustainable development being a rational model of technological development including environmental aspects. In this view, in recent years both academic and industrial researchers focused their attention on the use of biodegradable materials, possibly starting from renewable sources.

Taking all these considerations into due account, aliphatic polyesters are therefore expected to be one of the most economically competitive biodegradable polymers [3]. It is also worth remembering that some of the commonly used monomers for the production of aliphatic polyesters, such as succinic acid, adipic acid, 1,3-propanediol, 1,4-butanediol, lactic acid and γ-butyrolactone can be either obtained from fossil fuels and from renewable resources [4].

Within the polyester class, poly(alkylene 1,4-cyclohexanedicarboxilate)s offer various advantages: the introduction of cycloaliphatic units to the main chain of the polymer can be a way to increase the rigidity of the macromolecular chains. Moreover, conformational transitions of cyclohexylene rings in the backbone originate secondary relaxations in dynamical mechanical spectrum, which contribute to improve the performances of the materials [5].

The synthesis and properties of polyesters and copolyesters containing these cycloaliphatic units were studied at the beginning of the eighties by Eastman Chemical Company, interested to develop materials with excellent tensile strength, stiffness and impact properties as well as materials to be used as improved hot melt adhesives.

Although 1,4-cyclohexane dicarboxylic acid is now obtained from petroleum resources, however, it can be prepared from bio-based terephthalic acid, starting from limonene and other terpenes [6]. Therefore, polymers derived, for example, from 1,4-cyclohexane dicarboxylic acid and a diol obtainable from biomass (as 1,3-propanediol, obtainable by renewable feedstocks, such as corn) can be considered as fully sustainable materials.

Moreover, the presence of the 1,4-cyclohexylene units along a macromolecule does not hinder the attack of microorganisms in some homopolymers and copolymers [7–9]. Therefore, the polyesters containing the 1,4-cyclohexylene units can be considered biodegradable materials and are very promising, environmentally friendly polyesters.

Unfortunately, homopolymers usually do not possess optimal physic-mechanical properties. As a result, many attempts are necessary to solve these issues through appropriate modification of their structure. In this view, copolymerization probably represents the most interesting tool for tailoring materials which display the right combination of properties for the desired application. Moreover, copolymerization permits to prepare novel materials possessing unique properties in that they combine the inherent nature of the parent homopolymers, improving their non-suitable characteristics without compromising those already satisfying. Finally, through this strategy, it is possible to synthesize a new class of polymers with a broad range of properties just varying the mutual amount of the comonomeric units.

The research work described in the present paper is strictly connected to these urgent necessities and is focused mainly in finding new biopolymers, in particular biopolyesters, which are obtainable from biomass and characterized by a wide range of properties, in order to potentially substitute polyolefins and aromatic polyesters. In particular, it is focused on the synthesis and characterization of new fully aliphatic Poly(propylene/neopentyl glycol cyclohexanedicarboxylate) (P(PCExNCEy)) random copolymers, with the aim of establishing structure-property relationships which are very useful to design a material for a specific application.

2. Experimental

2.1. Materials

1,4-dimethylcyclohexanedicarboxylate (DMCE), containing 99% of *trans* isomer (TCI Europe, Zwijndrecht, Belgium), 1,3-propanediol (1,3-PD), neopentyl glycol (NPG), and titanium tetrabutoxide ($Ti(OBu)_4$) (Sigma Aldrich, Milan, Italy) were reagent grade products; all reagents were used as supplied, with the exception of $Ti(OBu)_4$ which was distilled before use.

2.2. Synthesis of poly(propylene cyclohexanedicarboxylate) and poly(propylene/neopentyl glycol cyclohexanedicarboxylate) copolymers

Poly(propylene cyclohexanedicarboxylate) (PPCE) and poly(propylene/neopentyl glycol cyclohexanedi-

carboxylate) random copolymers (P(PCExNCEy)) were synthesized in bulk starting from DMCE and 1,3-PD in the case of homopolymer and different ratios PD/NPG in the case of copolymers, using 40% mol in excess of glycol with respect to dimethylester. $Ti(OBu)_4$ was employed as catalyst (about 150 ppm of Ti/g of polymer). All the syntheses were carried out in a 250 mL stirred glass reactor, with a thermostatted silicon oil bath; temperature and torque were continuously recorded during the polymerization. The polymers were prepared according to the usual two-stage polymerization procedure. In the first stage, under pure nitrogen flow, the temperature was raised to 180°C and kept constant until more than 90% of the theoretical amount of methanol was distilled off (about 120 min). In the second stage, the pressure was reduced to about 0.1 mbar to facilitate the removal of the glycol in excess, and the temperature was risen to 240°C; the polymerization was carried out until a constant torque value was measured (about 180 min).

The copolymers under investigation in this work will be indicated as P(PCExNCEy): where *x* and *y* are the mol% of propylene cyclohexanedicarboxylate (PCE) and neopentyl glycol cyclohexanedicarboxylate (NCE) co-units, respectively. The chemical structure of the copolyesters is the following:

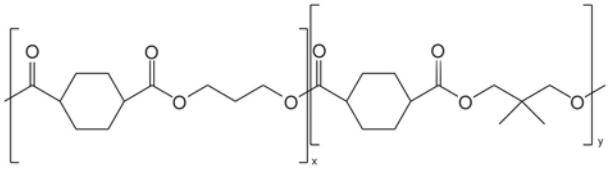

P(PCExNCEy)

2.3. Film preparation and thickness determination

Films of P(PCExNCEy) were obtained by hot pressing the polymers between Teflon sheets in an hydraulic press (Carver Inc., Wabash, Indiana USA) for 2 minutes at a temperature *T* equal to T_m + 40°C. The films were cooled in press to room temperature by running water. Before analyses the films were stored at room temperature for at least two weeks in order to attain equilibrium crystallinity.

The film thickness was determined using the Sample Thickness Tester DM-G (Brugger, Munich, Germany) consisting of a digital indicator (Digital Dial Indicator), connected to a computer. Once planted the tool on the film, the reading is made twice per second (the tool automatically performs three readings, minimum value that cannot be changed), measuring a minimum, maximum and average value of a series of measures. The reported results are an average of three experimental tests run at 10 different points on the polymer film surface, at room temperature. Measurements were performed at least in triplicate and the mean value thickness is presented.

2.4. Molecular characterization

The polymers structure and the actual copolymer composition were determined by means of ^{1}H-NMR spectroscopy. The samples were dissolved (15 mg/mL) in chloroform-d solvent with 0.03% (v/v) tetramethylsilane added as an internal standard. ^{1}H-NMR spectra were recorded at room temperature for solutions with a polymer concentration of 0.5 wt% (a relaxation delay of 0 s, an acquisition time of 1 s and up to 100 repetitions) using a Varian INOVA 400 spectrometer (Varian Inc., Palo Alto USA).

Molecular weight data were obtained by gel-permeation chromatography at 30°C using a 1100 Hewlett Packard system (Palo Alto, USA) equipped with PL gel 5 μ MiniMIX-C column (250/4.6 length/i.d., in mm) and a refractive index detector. Chloroform was used as eluent at a 0.3 mL/min flow and sample concentrations were adjusted to about 2 mg/mL. A molecular weight calibration curve was obtained by means of several polystyrene standards in the molecular weight range of 2000–100 000.

2.5. Thermal characterization

Thermogravimetric analysis was performed under nitrogen atmosphere using a Perkin Elmer TGA 4000 apparatus (Waltham, USA) at 10°C/min heating rate up to 850°C (gas flow: 30 mL/min).

Calorimetric measurements were carried out by means of a Perkin Elmer DSC7 instrument (Waltham, USA) equipped with a liquid sub ambient accessory and calibrated with high purity standards (indium and cyclohexane). With the aim of measuring the glass transition and the melting temperatures of the polymers under investigation, the external block temperature control was set at –120°C and weighed samples of c.a. 10 mg were encapsulated in aluminum pans and heated to about 40°C above fusion temperature at a rate of 20°C/min (first scan), held there for 3 min, and then rapidly quenched (about 100°C/min) to –80°C. Finally, they were reheated from –80°C to a temperature well above the melting

point of the sample at a heating rate of 20°C/min (second scan). The glass-transition temperature T_g was taken as the midpoint of the heat capacity increment Δc_p associated with the glass-to-rubber transition. The melting temperature (T_m) and the crystallization temperature (T_c) were determined as the peak value of the endothermal and the exothermal phenomena in the DSC curve, respectively. When multiple endotherms were observed, the highest peak temperature was taken as T_m. The specific heat increment Δc_p, associated with the glass transition of the amorphous phase, was calculated from the vertical distance between the two extrapolated baselines at the glass transition temperature. The heat of fusion (ΔH_m) and the heat of crystallization (ΔH_c) of the crystal phase were calculated from the total areas of the DSC endotherm and exotherm, respectively. In order to determine the crystallization rate under non-isothermal conditions, the samples were heated at 20°C/min to about 40°C above fusion temperature, kept there for 3 min and then cooled at 5°C/min. The temperature corresponding to the maximum of the exothermic peak in the DSC cooling-curve (Tcc) can be correlated to the crystallization rate. At least five replicates were run for each sample. Repeated measurements showed excellent reproducibility.

2.6. Structural characterization

X-ray diffraction (XRD) patterns of polymeric films were carried out in the wide angle region by using a PANalytical X'PertPro diffractometer (Almelo, Netherlands) equipped with a fast solid state X'Celerator detector and a copper target ($\lambda = 0.15418$ nm). Data were acquired in the 5–60° 2θ intervals, by collecting 100 sec at each 0.10° step. The indices of crystallinity (X_c) were evaluated from the XRD profiles by the ratio between the crystalline diffraction area (A_c) and the total area of the diffraction profile (A_t), $\chi_c = A_c/A_t$. The crystalline diffraction area has been obtained from the total area of the diffraction profile by subtracting the amorphous halo. The amorphous was modelled as bell shaped peak baseline. The non-coherent scattering was taken into consideration.

2.7. Stress-strain measurements

Stress-strain measurements were performed using an Instron 4465 tensile testing machine (Pianezza, (TO) Italy) equipped with a 100 N load cell, on rectangular films (40 mm high, 5 mm wide and 0.2 mm thick). The gauge length was 20 mm and the cross-head speed was 5.0 mm/min. Load-displacement curves were obtained and converted to stress strain curves. Tensile elastic modulus was determined from the initial linear slope of the stress-strain curve. At least six replicate specimens were run for each sample and the results were provided as the average value ± standard deviation.

2.8. Dynamic mechanical measurements

Suitable specimens for dynamic mechanical measurements were obtained by injection moulding in a Mini Max Molder (Custom Scientific Instruments, Easton USA), supplied with a rectangular mould (30×8×1.6 mm). Immediately after moulding, samples were quenched in liquid nitrogen and then stored in a desiccator under vacuum for 1 month prior analysis.

Dynamic mechanical measurements were performed with a dynamic mechanical thermal analyser (Rheometric Scientific, DMTA IV, New Castle USA), operated in the dual cantilever bending mode, at a frequency of 3 Hz and a heating rate of 3°C/min, over a temperature range from –150 to T_{final}, which changes according to the polyester analysed.

2.9. Composting experiments

Degradation tests were performed at 40°C. Each polyester film (diameter of 16 mm, 0.2 mm thick) was placed in a darkened vessel and sandwiched between two layers of compost (20 g each). Finally, 10 mL of deionized water were added.

Home-made compost was prepared by means of an automatic composter (NatureMill, San Francisco, USA): organic waste fraction was collected, cultured in the composter for three weeks, and then transferred in the cure chamber for at least four weeks prior to use.

Film weight loss analyses

Prior to degradation experiments, each specimen was immersed in a 70% ethanol solution for 10 min, washed repeatedly with deionized water and placed over P_2O_5 under vacuum at room temperature to constant weight (at least 24 h). Lastly, each sample was weighed to obtain the initial mass. At different time intervals, duplicate sacrificial specimens of each sample were recovered from the compost and washed according to the following procedure to remove microbial cells adhered on the film:

– immersion in a 2% sodium dodecyl sulphate (SDS) solution at 50°C for 2 h;
– repeated washing with 70% ethanol (3×);
– immersion in 70% ethanol and stirring at 120 rpm, then storing at RT for 10 min;
– repeated washing with deionized water (3×);
– drying over P_2O_5 under vacuum for 2 days to constant weight.

The mass loss was then gravimetrically determined by comparing the residual dry weight with the initial value.

Scanning electron microscopy (SEM)

SEM images were acquired on a desktop Phenom microscope (Shanghai, China) on metal sputtered film samples glued with carbon tape on aluminium stabs.

3. Results and discussion

3.1. Synthesis, molecular and thermal characterization

At room temperature the as-synthesized polyesters are opaque light yellow coloured solids. Their solubility was checked in various solvents: all the samples showed a good solubility at room temperature in the most common organic solvents, i.e. chloroform, tetrachloroethane, methylene chloride, etc. The polymers are listed in Table 1, which also collects the data of molecular characterization: as it can be seen, the polymers were characterized by relatively high and comparable molecular weights, indicating that appropriate synthesis conditions and a good polymerization control were achieved. In order to have an understanding into their chemical structure, the ^{1}H-NMR investigation was performed. The analysis confirmed the awaited structures (see as an example the ^{1}H-NMR spectrum of P(BCE70TECE30) shown in Figure 1).

The copolymer composition was calculated from the relative areas of the ^{1}H-NMR resonance peak of the 3 aliphatic proton of the propylene diol subunit located at 4.15 ppm and of the 5 protons of the methylene groups of the neopentyl diol subunit at

Table 1. Molecular characterization data of PPCE and P(PCExNCEy) random copolymers

Polymer	M_n[a]	D[b]	NCE[c] [mol%]	Thickness [µm]
PPCE	36 398	2.2	0	246±22
P(PCE95NCE5)	29 549	2.9	5	292±31
P(PCE90NCE10)	31 124	2.2	10	268±18
P(PCE85NCE15)	27 522	2.6	15	238±33
P(PCE80NCE20)	25 386	2.4	20	308±10

[a]number average molecular weight calculated by GPC analysis
[b]polydispersity index calculated by GPC analysis
[c]real copolymer composition calculated by ^{1}H-NMR

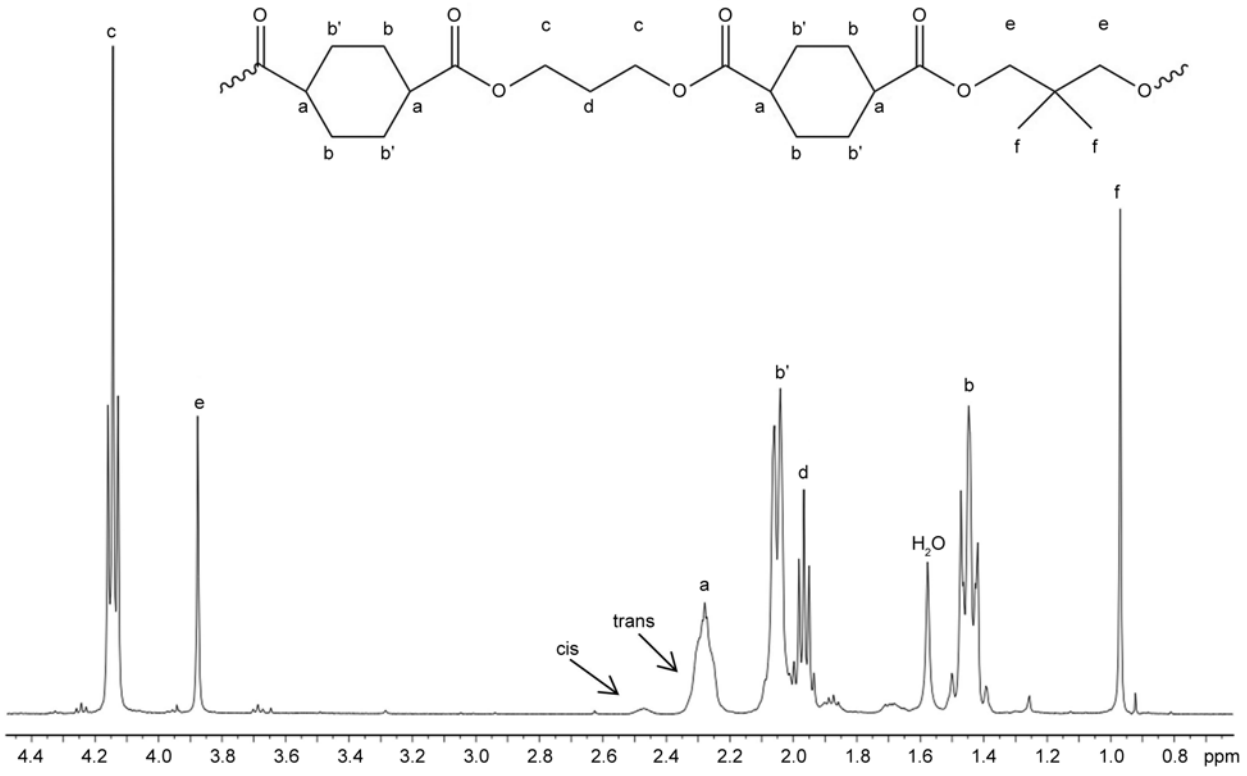

Figure 1. ^{1}H-NMR spectra of P(PCE80NCE20) with resonance assignments

3.87 ppm. From the data of Table 1, it can be seen that in all cases the actual molar composition is close to the feed one.

Previous studies [10, 22] reported that the 1,4-cyclohexylene ring present in DMCE can isomerize during polymer synthesis, due to the high temperatures employed for long times, moving toward the thermodynamically stable *cis/trans* ratio of 34–66%. Therefore, ^{1}H-NMR analysis has been also used to calculate the trans percentage in the polymers under study: in particular, the ratio of the areas of the signals centred at 2.28 ppm (*trans* isomer) and 2.44 ppm (*cis* isomer) has been considered (Figure 1). From the data obtained it can be evicted that no significant isomerization from the *trans* form to the cis one occurred during polymerization, the *cis* content being in all cases less than 5%.

Subsequently, the polymers were subjected to thermogravimetric analysis and the temperature corresponding to 5% weight loss ($T_{5\%\ w.loss}$) has been determined and collected in Table 2. As evidenced in Figure 2, where the thermogravimetric curves of the parent homopolymer and of the synthesized copolyesters are reported, the weight loss takes place in all cases in one-step.

All the copolyesters showed a high thermal stability, comparable with that of PPCE. This is due to the presence of bulky and thermally stable cyclohexylene groups, which render the polymer even more thermally stable than the corresponding aromatic polyester, i.e. Polybutylene terephthalate (PBT) and to neopentyl glycol sub-unit [10–11]. The result demonstrated that the introduction of NCE co-units along the PPCE macromolecular chain did not have any detrimental effect on thermal stability, which, as well known is crucial during polymer processing.

In order to provide the same heat treatments to all the investigated samples, prior to thermal analysis each film was kept at room temperature for two weeks.

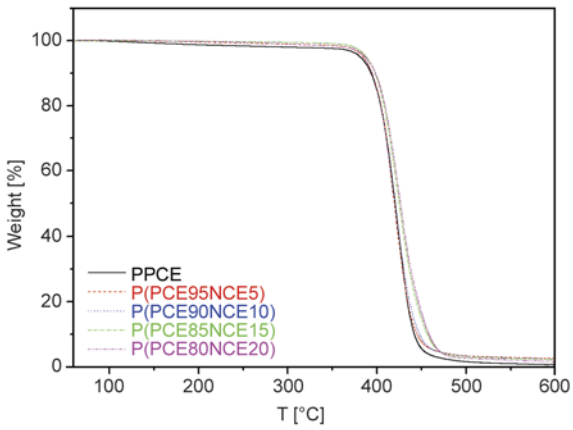

Figure 2. Thermogravimetric curves of PPCE and P(PCExNCEy) copolymers under nitrogen atmosphere (heating rate: 10°C/min)

DSC traces of so-treated samples are reported in Figure 3 and the data obtained in Table 2.

As evidenced in Figure 3, all P(PCExNCEy) copolymers presented a glass transition and a melting endotherm. The glass transition phenomenon is always not so evident, due to the high amount of crystalline phase present in these samples.

As to the melting process, the samples showed a premelting peak at low temperature (around 50°C), whose heat of fusion regularly increased as the NCE unit content is increased, which can be ascribed to the fusion of crystals with a poor degree of perfection. At much higher temperature, the main melting peak can be observed. The calorimetric results indicate that an increase in the amount of the comonomer NCE leads to a reduction in the samples both of the melting temperature and the heat of fusion, as usually found in random copolymers with the comonomeric units present in minor amount completely rejected from the crystalline phase or partially incorporated in it (see Table 2) [12, 13]. Furthermore, in the copolymers, the endotherm region is broader, suggesting the presence of a larger distribution of crystallites with different degree of perfection.

Table 2. Thermal and diffractometric characterization data for PPCE and P(PCExNCEy) copolymers

Polymer			1st scan		2nd scan							
	$T_{5\%\ w.loss}$ [°C]	T_{max} [°C]	T_m [°C]	ΔH_m [J/g]	T_g [°C]	ΔC_p [J/(°C·g)]	T_m [°C]	ΔH_m [J/g]	T_c [°C]	ΔH_c [J/g]	T_{cc} [°C]	X_c[a] [°C]
PPCE	381	413	148	58	9	0.132	148	31	63	17	91	29 (4)
P(PCE95NCE5)	385	416	142	49	11	0.183	143	26	90	26	75	26 (3)
P(PCE90NCE10)	386	420	135	43	12	0.189	135	13	97	13	–	25 (2)
P(PCE85NCE15)	387	423	125	42	13	0.262	–	–	–	–	–	25 (2)
P(PCE80NCE20)	388	425	119	39	13	0.236	–	–	–	–	–	24 (2)

[a]Estimated standard deviation (e.s.d.) in parentheses

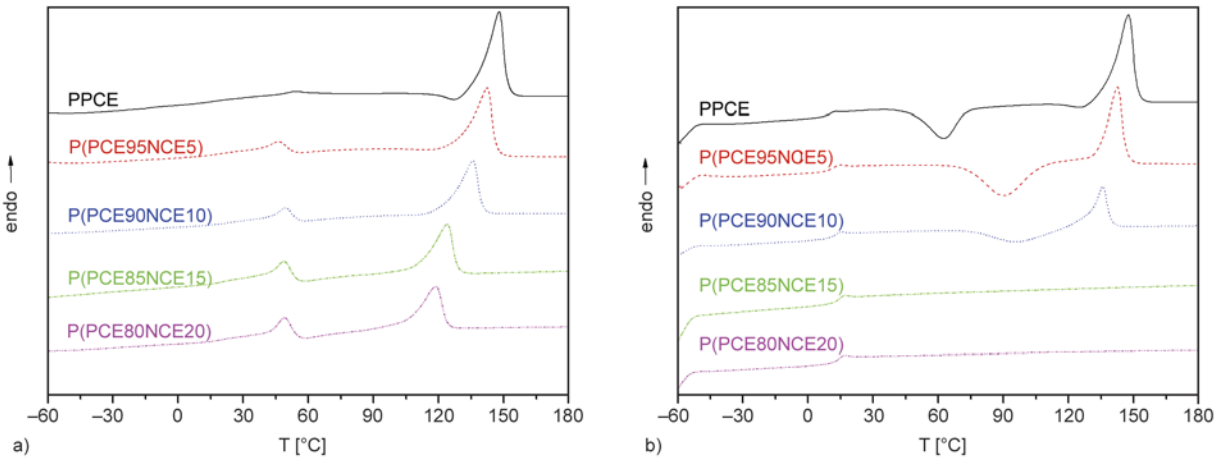

Figure 3. Calorimetric curves of PPCE and P(PCExNCEy) copolymers, (a) 1st scan; (b) 2nd scan after melt quenching

To better understand the nature of the crystalline phase present in the polymers under investigation, the structural characterization of P(PCExNCEy) copolymers was carried out by X-ray diffraction (XRD). The patterns are reported in Figure 4, together with that of PPCE added for sake of comparison. The PPCE sample shows the main reflections at 2θ values of 16.7, 17.5, 19.5, 23.3°.

As far as the copolymers are concerned, the corresponding WAXD patterns appear to be characterized by relatively intense diffraction peaks over the whole composition range.

The copolymer samples are characterized by the same XRD pattern of PPCE, indicating that the crystal structure which develops in these copolymers has the characteristics of PPCE lattice.

Nevertheless, the presence of NCE units causes the collapse of the two reflections at 16.7 and 17.5° and the reflections seems be shifted towards lower angles (higher distances, see Figure 4b panel), the shifting being higher as the content of NCE units increases. Such increases of the interplanar distances could be caused by the insertion of bigger NCE units into the PPCE crystal cell. Cocrystallization is supported by the modest decrease of crystallinity degree with copolymer composition (see Table 2), which is lower than the value expected on the basis of the complete rejection of the 'foreign' units from the

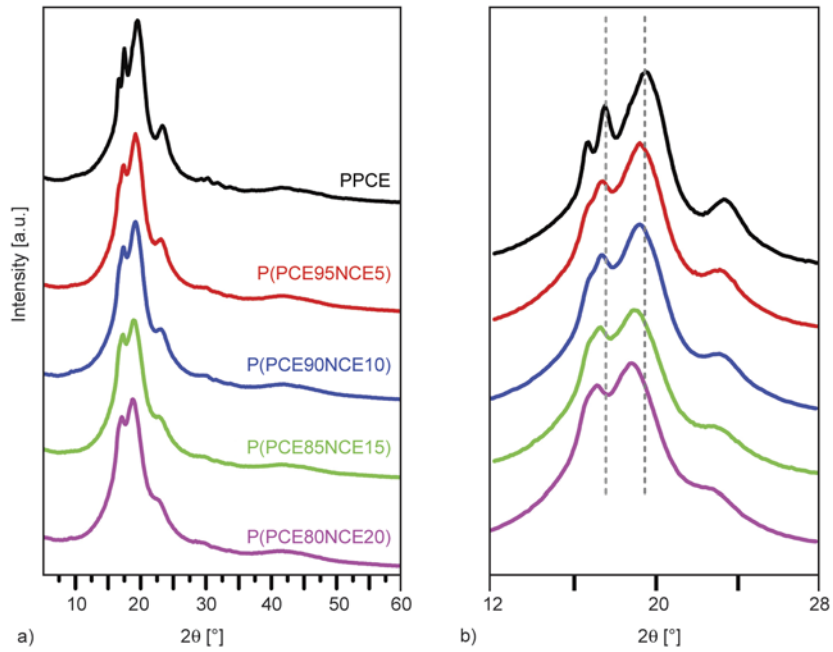

Figure 4. X-ray diffraction profiles of PPCE and P(PCExNCEy) copolymers (a). An enlarged view (b); vertical line are reference for the reader.

crystalline phase present in the sample. In conclusion, it can be plausible that at least a certain amount of comonomeric units enter into the crystal lattice.

It is well known that a partially crystalline material usually exhibits a different glass transition behavior than the completely amorphous analogs. In fact, although some conflicting results are reported in the literature, [14] crystallinity usually acts like crosslinking and raises T_g through its restrictive effect on the segmental motion of amorphous polymer chains. Therefore, in order to study the influence of chemical structure on the glass transition of random copolymers, the phenomenon should be examined in the total absence of crystallinity. In this view, all the samples under investigation were subjected to rapid cooling (quenching) from the melt. The DSC curves after melt quenching are shown in Figure 3: the calorimetric traces of PPCE and P(PCExNCEy) copolymers containing up to 10 mol% of NCE units showed a glass transition followed by an exothermal 'cold crystallization' peak and a melting endotherm at higher temperature. In particular, as concern PPCE, the enthalpy associated with the crystallization phenomenon is lower than that of the fusion endotherm, indicating that this sample cannot be frozen into a completely amorphous state by quenching. Nevertheless, a portion of amorphous material, once T_g is exceeded, acquires enough mobility to rearrange and crystallize. The DSC curves of such sample is therefore typical of partially crystalline polymers. In the case of P(PCE95NCE5) and P(PCE90NCE10) copolymers, the enthalpy of crystallization very well compares with the corresponding heat of fusion, indicating that these polymers are completely amorphous. As regards the calorimetric curves of copolymers containing from 15 to 20 mol% of NCE units, only an intense endothermal baseline deviation associated with the glass transition is observed. Therefore, the DSC scans indicate that the phase behaviour of PPCE changed even for small amount of neopentyl glycol sub-units (5 mol%). On the other hand, no effect of copolymer composition on material phase behaviour was observed.

As can be seen from the data collected in Table 2, the glass transition temperature is slightly influenced by the presence of NCE units in the chain, the T_g copolymer values being higher than that of PPCE and increasing with the molar content of NCE units. As is well known, the second-order transition temperature is affected by several factors, such as chain flexibility, steric effects, molar mass, branching and crosslinking. For high molecular weight polymers, the flexibility of the chain is undoubtedly the most important factor influencing T_g. This latter is a measure of the ability of a chain to rotate, and therefore the more flexible chains are, the lower the T_g. The increase in the glass transition temperature on introducing the two methyl side groups into the polymeric chain of PPCE can be explained as due to the steric effect of these two groups which hinder the rotation, imposing restrictions.

To evaluate the tendency of PPCE to crystallize in the copolymers under study, non-isothermal experiments were carried out, subjecting the samples to a controlled cooling rate from the melt. The temperatures of the maximum of the exothermal crystallization peak (T_{cc}) of the samples under investigation, which can be correlated to the isothermal melt crystallization rate, are collected in Table 2. As it can be observed, the crystallization rate of P(PCE95NCE5) is significantly lower than that of parent homopolymer. Moreover, amounts of NCE co-units ≥10 mol% completely undone the PPCE ability of crystallizing, indicating that the co-units act as obstacles in the regular packing of polymer chains. This result is in agreement with those obtained previously by some of us in investigating other copolymeric systems containing neopentyl glycol sub-unit [10, 15].

3.2. Dynamic mechanical characterization

The dynamical mechanical spectra of the samples under investigation are shown in Figure 5.

The upper curve of each polymer refers to the sample stored at room temperature: in the temperature range –150/100°C, all the polymers exhibits three relaxations regions denoted as γ, β and α in order of increasing temperature. In all cases, the γ relaxation was detected in the range –150/–100°C at 3 Hz, has small intensity and is rather broad. The β relaxation is approximately located at about –75°C and has a small intensity too. On the other hand, the α relaxation, detected around 40°C, has higher intensity and a certain asymmetry, being steeper on the low-temperature side and broader on the high-temperature one. Looking into more detail to the high-temperature side of α relaxation, one can see a shoulder, denoted as α′. As regards the storage modulus E', at low temperature it exhibits values typical of the glassy state (*ca*. 10^{10} Pa) and decreases slightly with increasing temperature due to thermal expansion. In

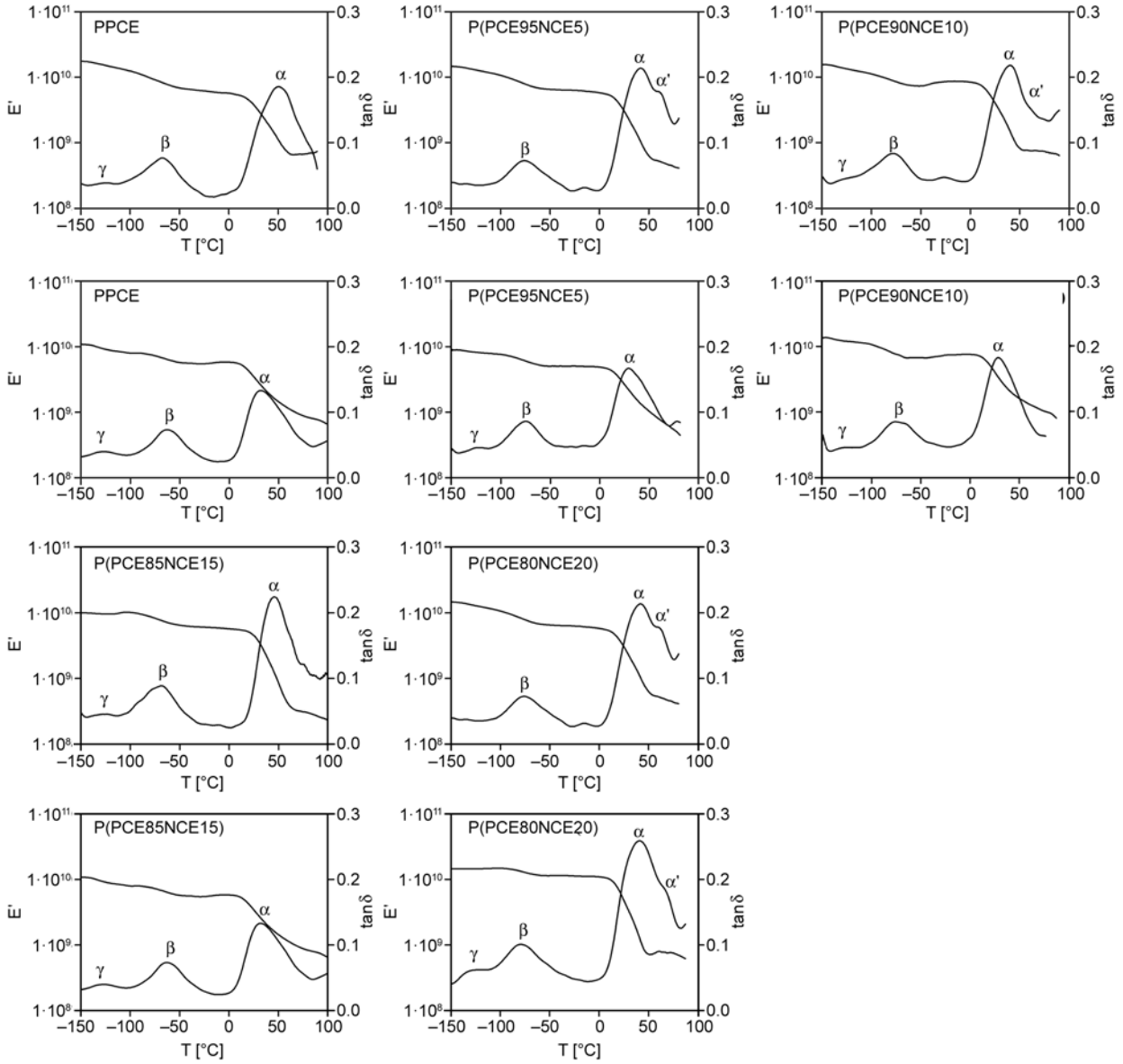

Figure 5. Dynamical mechanical curves at 3 Hz: for each sample, top row room stored sample; bottom row after cooling from high temperature under dry nitrogen flow

correspondence with α relaxation the modulus shows a steep decrease of about two orders of magnitude. As regards the assignment of these relaxations, α relaxation is confidently assigned to the glass-to-rubber transition, its temperature location being in good agreement with the calorimetric T_g. The small intensity of the peak and the high value of the modulus above the relaxation evidence the partially crystalline character of the polymer, in agreement with the calorimetric results. The location of the main relaxation shifts toward higher temperature values as the NCE unit content is increased (see Table 3), in agreement with calorimetric results. This can be explained on the basis of the progressive decrease in chain flexibility as the amount of NCE units increases. The α′ process can be related to a rigid confined amorphous phase, analogously to another similar copolymeric systems previously investigated by some of us [16].

Table 3. Dynamical mechanical data

Polymer	1st scan			2nd scan[a)]		
	T_α [°C]	T_β [°C]	T_γ [°C]	T_α [°C]	T_β [°C]	T_γ [°C]
PPCE	40	–74	–130	23	–73	–125
P(PCE95NCE5)	40	–76	–133	27	–75	–123
P(PCE90NCE10)	42	–78	–132	29	–76	–125
P(PCE85NCE15)	43	–78	–133	32	–77	–123
P(PCE80NCE20)	46	–79	–131	40	–75	–123

[a)]2nd scan after cooling from high temperature under nitrogen flow

Concerning the identification of the molecular origin of the γ relaxation, it can be traditionally associated with restricted motions of the chain in polymers with aliphatic sequences: in particular, the relaxation is generally attributed to rotations of the methylene units of glycol sub-unit which is the flexible part of the repeating unit [5].

As regards the attribution of the β relaxation to a molecular motion, as reported in the literature [5], this relaxation originates from the chair-boat-chair conformational transition of the cyclohexylene ring. Indeed, the cyclohexylene rings in chair conformations can transform form chair to chair via an intermediate twist boat conformation [17].

In the second scan after cooling from high temperature under dry nitrogen gas, the shoulder α′ disappeared, the α peak keeping anyway a certain asymmetry. Moreover, α intensity decreases indicating that during the cooling crystallization occurs in the samples under investigation. Surprisingly, however, the α relaxation moves to lower temperature: taking into account that α′ shoulder disappears, such result can be explained as due to a significant improving of crystal phase perfection that reduces significantly the rigid-amorphous phase fraction.

The copolymer with the highest content of NCE co-unit, P(PCE80NCE20), is characterized by a different behaviour: as a matter of fact, the α′ relaxation does not disappear in 2nd scan after cooling from high temperature under dry nitrogen flow and the intensity of α relaxation doesn't decrease in magnitude. This last result clearly indicates that no significant crystallization occurred on cooling, due to slow crystallization kinetic of this copolymer. As it is well known, the amount of rigid amorphous phase depend upon the area of the crystalline-amorphous boundary, the degree of irregularity of the crystalline phase and the molecular mobility [11]. In the case of P(PCE80NCE20), the non-crystallizable comonomer hinders significantly the crystallization process, leading to small and imperfect crystallites. The crystalline phase turns out to be highly dispersed, and the increase in crystal surface results into extensive constraints on the amorphous phase.

As to elastic modulus E' in second scan, also the steepness and intensity of the modulus drop in the α transition region show a great reduction as the crystallinity increases, reflecting the typical behaviour of partially crystalline polymers [18].

3.3. Mechanical characterization

In an application perspective, the analysis of the mechanical properties of the polymers under study is of primary importance. Therefore, P(PCExNCEy) copolymers were subjected to stress-strain measurements. In Table 4 their elastic modulus (E), stress at break (σ_b), and deformation at break (ε_b) are shown, together with the data of PPCE and Polypropylene terephthalate (PPT) added for sake of comparison.

As it can be seen, the elastic modulus regularly decreased as NCE unit content was increased; on the contrary, the elongation at break, increased with the increasing of the molar amount of NCE co-unit. Since all the investigated polymers display a soft amorphous phase (T_g values are in all cases below room temperature), the observed trend can be ascribed to crystallinity degree (Table 2).

It is in fact well known [19, 20] that crystallinity degree has a considerable effect on the mechanical properties of a polymer: in particular high X_c results in harder, stiffer and less ductile behaviour. As therefore expected, the higher the PCE content, the higher the elastic modulus and the lower the elongation ability of the investigated polymers. Moreover, it is worth emphasizing that the copolymer containing the 20 mol% of NCE is characterized by an elastomeric behaviour.

In conclusion, a new class of aliphatic polyesters with tunable mechanical properties has been here presented. Indeed, by just varying the molar composition of the copolymers, even for modest changes of crystallinity degree, it is possible to synthesize a new material which can be used for rigid plastic containers or soft wrapping films.

Last but not least, substituting the aromatic ring with the aliphatic one, the modulus changes dramatically (see Table 4): it is lower in aliphatic sample. In particular, PPT, due to the presence of the aromatic ring has a very high modulus and a brittle behavior.

Table 4. Mechanical characterization data of PPT, PPCE and P(PCExNCEy) copolymers

Polymer	E [MPa]	σ_b [MPa]	ε_b [%]
PPCE	435±26	15±2	11±1
P(PCE95NCE5)	381±29	20±1	150±14
P(PCE90NCE10)	338±20	12±1	190±32
P(PCE85NCE15)	248±12	12±2	332±32
P(PCE80NCE20)	232±20	20±1	559±18
PPT	942±85	42±5	5±1

3.4. Composting studies

The biodegradability of P(PCExNCEy) copolymers was monitored by subjecting them to composting, which is a particularly useful technique to biodegrade a polymeric material which has been contaminated by organic matter. Biodegradation rate was investigated by weight loss measurements.

After 140 days of incubation the highest weight loss value was of 11%, measured for P(PCE80NCE20). Degradation rate was found dependent on composition: the higher the NCE content, the higher the weight loss. As a matter of fact, weight losses were equal to 3, 4, 6 and 8% for PPCE, P(PCE95NCE5), P(PCE90NCE10) and P(PCE85NCE15), respectively.

As expected, the higher the crystallinity degree of the polymers under study, the lower the biodegradation rate in compost; in fact they are well known factors influencing the biodegradation rate of a polymer [21–23].

The morphology of the polymer films was analysed by SEM. As an example, micrographs of PPCE and P(PCExNCEy) films after 140 days of incubation in compost are reported in Figure 6.

All the samples under investigation showed a smooth and homogenous surface before incubation. After incubation, SEM analyses highlighted results in agreement with weight loss measurements: PPCE film presented only a surface roughening after 140 days of incubation in compost, while in the copolymer large damaged areas appeared, with numerous cracks and channels, whose intensity depended on the degree of degradation.

4. Conclusions

The introduction of neopentyl glycol along the PPCE macromolecular chain has been carried out by the polycondensation reaction of 1,4-dimethylcyclohexanedicarboxylate with 1,3-propanediol and neopentyl glycol. This easy synthesis strategy allowed the preparation of a new class of aliphatic polyesters with improved properties with respect to the parent homopolymer. Moreover, the final material properties can be effectively tailored simply varying the copolymer composition.

As expected, the introduction of neopentyl glycol sub-unit in the PPCE resulted in a decrease of the crystallinity degree and melting point, due to a decrement of chain symmetry and regularity. The higher the mol% of NCE co-units, the greater the effect on these properties. As a consequence, the mechanical properties and the biodegradation rate turned out to be influenced. As a matter of fact it has been observed a decrease in the elastic modulus and an increase in the elongation to break till to an elastomeric behaviour.

The biodegradation rate in compost resulted in all cases higher than that of PPCE, and once again dependent on the copolymer composition: the higher the NCE mol%, the higher the weight losses of the copolymers under study.

It is notable all the new materials are potentially bio-based and biodegradable, and can be candidates

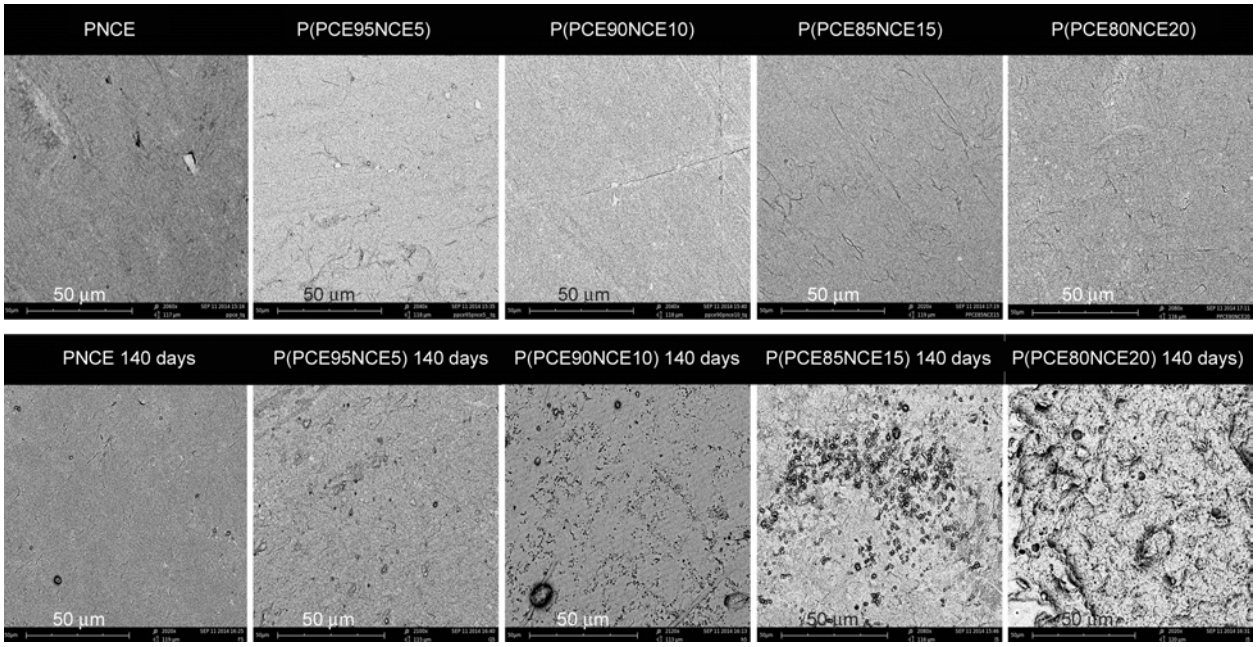

Figure 6. SEM micrographs of PPCE and P(PCExNCEy) before composting (top) and after 140 days of incubation (bottom)

for substituting some traditional petroleum-based polymers in specific applications.

References

[1] Vert M.: Aliphatic polyesters: Great degradable polymers that cannot do everything. Biomacromolecules, **6**, 538–546 (2005).
DOI: 10.1021/bm0494702

[2] PlasticsEurope: Plastics – the Facts 2013, An analysis of European latest plastics production, demand and waste data (2013).

[3] Tserki V., Matzinos P., Pavlidou E., Vachliotis D., Panayiotou C.: Biodegradable aliphatic polyesters. Part I. Properties and biodegradation of poly(butylene succinate-*co*-butylene adipate). Polymer Degradation and Stability, **91**, 367–376 (2006).
DOI: 10.1016/j.polymdegradstab.2005.04.035

[4] Luckachan G. E., Pillai C. K. S.: Biodegradable polymers – A review on recent trends and emerging perspectives. Journal of Polymers and the Environment, **19**, 637–676 (2011).
DOI: 10.1007/s10924-011-0317-1

[5] Berti C., Celli A., Marchese P., Marianucci E., Barbiroli G., Di Credico F.: Influence of molecular structure and stereochemistry of the 1,4-cyclohexylene ring on thermal and mechanical behavior of poly(butylene 1,4-cyclohexanedicarboxylate). Macromolecular Chemistry and Physics, **209**, 1333–1344 (2008).
DOI: 10.1002/macp.200800125

[6] Berti C., Binassi E., Colonna M., Fiorini M., Kannan G., Kanaram S., Mazzacurati M.: Bio-based terephthalate polyesters. U.S. Patent 20100168461 A1, USA (2010).

[7] Gigli M., Lotti N., Gazzano M., Siracusa V., Finelli L., Munari A., Dalla Rosa M.: Fully aliphatic copolyesters based on poly(butylene 1,4-cyclohexanedicarboxylate) with promising mechanical and barrier properties for food packaging applications. Industrial and Engineering Chemistry Research, **52**, 12876–12886 (2013).
DOI: 10.1021/ie401781d

[8] Gigli M., Lotti N., Vercellino M., Visai L., Munari A.: Novel ether-linkages containing aliphatic copolyesters of poly(butylene 1,4-cyclohexanedicarboxylate) as promising candidates for biomedical applications. Materials Science and Engineering: C, **34**, 86–97 (2014).
DOI: 10.1016/j.msec.2013.08.013

[9] Gigli M., Lotti N., Gazzano M., Siracusa V., Finelli L., Munari A., Dalla Rosa M.: Biodegradable aliphatic copolyesters containing PEG-like sequences for sustainable food packaging applications. Polymer Degradation and Stability, **105**, 96–106 (2014).
DOI: 10.1016/j.polymdegradstab.2014.04.006

[10] Soccio M., Lotti N., Finelli L., Gazzano M., Munari A.: Neopenthyl glycol containing poly(propylene azelate)s: Synthesis and thermal properties. European Polymer Journal, **43**, 3301–3313 (2007).
DOI: 10.1016/j.eurpolymj.2007.06.011

[11] Soccio M., Lotti N., Finelli L., Gazzano M., Munari A.: Neopenthyl glycol containing poly(propylene terephthalate)s: Structure–properties relationships. Journal of Polymer Science Part B: Polymer Physics, **46**, 170–181 (2008).
DOI: 10.1002/polb.21352

[12] Mandelkern L.: Crystallization of polymers. McGraw-Hill, New York (1954).

[13] Mandelkern L.: Crystallization and melting. in 'Comprehensive polymer science' (eds.: G. Allen, J. C. Bevington) Pergamon Press, Oxford, Vol 2, 363–414 (1989).

[14] Boyer R. F.: The relation of transition temperatures to chemical structure in high polymers. Rubber Chemistry and Technology, **36**, 1303–1421 (1963).
DOI: 10.5254/1.3539649

[15] Soccio M., Lotti N., Finelli L., Munari A.: Crystallization behavior and morphology of Poly(propylene terephthalate) copolymers containing neopenthyl glycol moieties. Journal of Polymer Science Part B: Polymer Physics, **46**, 818–830 (2008).
DOI: 10.1002/polb.21420

[16] Soccio M., Nogales A., Ezquerra T. A., Lotti N., Munari A.: Effect of copolymerization in the dynamics of poly (trimethylene terephthalate). Macromolecules, **45**, 180–188 (2012).
DOI: 10.1021/ma202361r

[17] Vanhaecht B., Rimez B., Willem R., Biesemans M., Koning C. E.: Influence of stereochemistry on the thermal properties of partially cycloaliphatic polyamides. Journal of Polymer Science Part A: Polymer Chemistry, **40**, 1962–1971 (2002).
DOI: 10.1002/pola.10284

[18] McCrum N. G., Read B. E., Williams G.: Anelastic and dielectric effects in polymeric solids. Wiley, London (1967).

[19] Robertson G. L.: Food packaging: Principles and practice. CRC Press, London (1993).

[20] Lee D. S., Yam K. L., Piergiovanni L.: Food packaging: Science and tecnology. CRC Press, London (2008).

[21] Gigli M., Negroni A., Soccio M., Zanaroli G., Lotti N., Fava F., Munari A.: Influence of chemical and architectural modifications on the enzymatic hydrolysis of poly (butylene succinate). Green Chemistry, **14**, 2885–2893 (2012).
DOI: 10.1039/C2GC35876J

[22] Gigli M., Negroni A., Zanaroli G., Lotti N., Fava F., Munari A.: Environmentally friendly PBS-based copolyesters containing PEG-like subunit: Effect of block length on solid-state properties and enzymatic degradation. Reactive and Functional Polymers, **73**, 764–771 (2013).
DOI: 10.1016/j.reactfunctpolym.2013.03.007

[23] Gigli M., Negroni A., Soccio M., Zanaroli G., Lotti N., Fava F., Munari A.: Enzymatic hydrolysis studies on novel eco-friendly aliphatic thiocopolyesters. Polymer Degradation and Stability, **98**, 934–942 (2013).
DOI: 10.1016/j.polymdegradstab.2013.02.019

eXPRESS Polymer Letters Vol.9, No.11 (2015) 984–1000
Available online at www.expresspolymlett.com
DOI: 10.3144/expresspolymlett.2015.89

Macroporous materials by self-assembly of linear oligo(phenylsilsesquioxanes)

A. Kowalewska[*], *M. Nowacka, T. Makowski*

Centre of Molecular and Macromolecular Studies, Polish Academy of Science, Sienkiewicza 112, 90-363 Lodz, Poland

Received 27 January 2015; accepted in revised form 26 June 2015

Abstract. Materials with macroporous architecture were prepared in a template-free system using linear oligo(phenylsilsesquioxanes) (Ph-LPSQ), obtained in a two-step, one-pot, acid/base sol-gel method. The spontaneous self-assembly of silsesquioxane chains is governed by π-π interactions between side substituents and facilitated by the backbone rigidity of the polymer. The porous structure of the material can be changed on adjusting the processing conditions (concentration of Ph-LPSQ solution, the ratio solvent/nonsolvent and rate of stirring during precipitation). Ph-LPSQ oligomers can be also used for modification of silica particles and preparation of interesting macro-mesoporous materials of narrow pore size. Morphology and properties of the polymer and self-assembled particles were characterized by nuclear magnetic resonance (NMR) and Fourier transform infrared (FTIR) spectroscopies, wide angle X-ray scattering (WAXS), scanning electron microscopy SEM, mercury intrusion porosimetry, fluorescence spectroscopy and dynamic light scattering.

Keywords: *molecular engineering, ladder phenylsilsesquioxanes, sol-gel, self-assembly, micropspheres*

1. Introduction

Nano- and microstructured polymeric materials of well-defined composition, morphology and function are of general scientific importance and technological interest. For example, solid or hollow polymeric spheres can be applied for controlled storage and release, in catalysis, as photonic crystals and templates to macroporous materials [1]. Several types of mesoporous silica [2] have also found many technological applications due to their morphological characteristics [3–6]. Monolithic silica or silsesquioxane gels with hierarchical well-defined macropores and shape-controlled mesopores exhibit low or no shrinkage during drying. They attract large interest in separation techniques, in catalysis, micro- and optoelectronics (e.g. chromatographic stationary phases for HPLC and UPLC flexible aerogels, superhydrophobic materials, insulating coatings, biomedical entrapment materials) [7].

Macroporous structure of silica monoliths can be generated in the course of hydrolytic polycondensation of alkoxysilanes, due to coexisting phase separation and gelation phenomena [8]. Macroporous materials were also obtained by aggregation and gelation of PEG-stabilized silica particles [9] or in silicone oil dispersions [10]. Macroporous poly (methylsilsesquioxanes) (MSQ) were prepared by micellar nanoscale templating combined with polymerization-induced phase microseparation [11, 12] in a two-step process of all-acidic hydrolytic polycondensation [13] or using an acid/base two step processing method [7, 14]. Macro-mesoporous silica materials can also be prepared by dual templating using supramolecular systems [15–17]. However, to our best knowledge there are no reports on macroporous structures based on poly(phenylsilsesquioxanes). Such materials would be of special interest owing to their low polarity and possible

[*]Corresponding author, e-mail: anko@cbmm.lodz.pl

interactions with biological systems. However, the literature reports concern poly(phenylsilsesquioxane) microparticles obtained in a modified Stöber route [18, 19] emulsion polymerization [20], a template-free two-step acid–base catalyzed sol–gel process [21, 22] and base catalyzed oil-in-water emulsion polycondensation [19]. Phenylsilsesquioxane particles of 'core-shell' structure show both thermoplastic and thermosetting properties [23, 24]. Ladder-like polysilsesquioxanes structurally differ from polyhedral oligomeric silsesquioxanes (POSS) and random silsesquioxane networks (Figure 2). They gain a growing interest due to their unique physiochemical properties (good solubility, film-forming properties, morphological-stability, excellent thermochemical resistance) [25–27]. Poly(phenylsilsesquioxanes) show high thermal stability (degradation onset temperatures about 793 K in air) and good mechanical properties [28]. For most of the poly(phenylsilsesquioxanes), the characteristic tensile strength value is in the range of 20–40 MPa and the elongation 3–20% [29]. They are less hard and brittle than poly(methylsilsesquioxanes) [30]. It was found that rheological properties of organic polymer blends (strain hardening/softening under dynamic shear and uniaxial elongation) can change on addition of Ph-LPSQ [31].

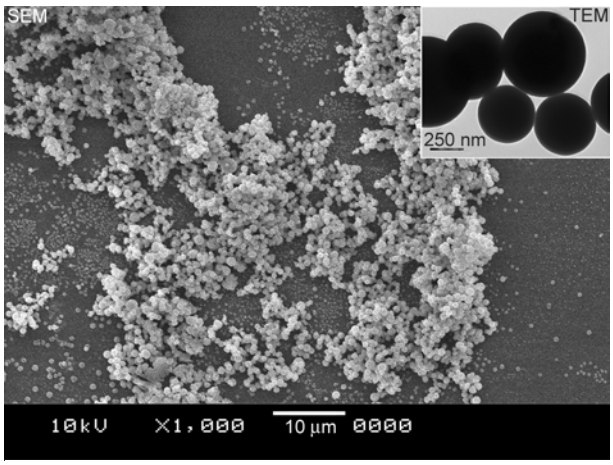

Figure 1. Spherical particles obtained by self-assembly of oligomeric Ph-LPSQ (polymer concentration in CH_2Cl_2 = 50 mg/cm^3, hexane/CH_2Cl_2 v/v = 1000, the insert contains a TEM micrograph of the formed microspheres)

The application of poly(phenylsilsesquioxane)-based materials encompasses membranes [32], interlayer dielectrics [33], protective coating films in electronics [34] optical devices [35] and thermostable superhydrophobic coatings [36]. Poly(phenylsilsesquioxane)-derived materials were also used as pre-ceramic precursors for hierarchically porous silicon oxycarbide-derived carbons for supercapacitor electrodes [37] and low dielectric constant porous matrix [38]. Composite materials based on Ph-LPSQ include well-defined inorganic–organic hybrid block copolymers of enhanced thermal properties [39], materials of improved the elongation at break, flexural strength and flame-retardancy [40], fibers [41]. Other applications include their use in carbon fiber/ceramic matrix composites [42], and also drug delivery [43].

We have found that linear oligosilsesquioxanes bearing side phenyl groups (Ph-LPSQ) can self-assemble and form spherical nano- and microstructures in template-free systems (Figure 1). Such microparticles made of Ph-LPSQ oligomers can be used for preparation of mesoporous materials and also for modification of silica microspheres. Morphology and properties of the self-assembled objects were studied using SEM microscopy, mercury intrusion porosimetry, fluorometry and dynamic light scattering.

Formation of macropores in the reported system, conversely to MSQ monoliths, is not governed by polymerization-induced phase separation. Instead, a

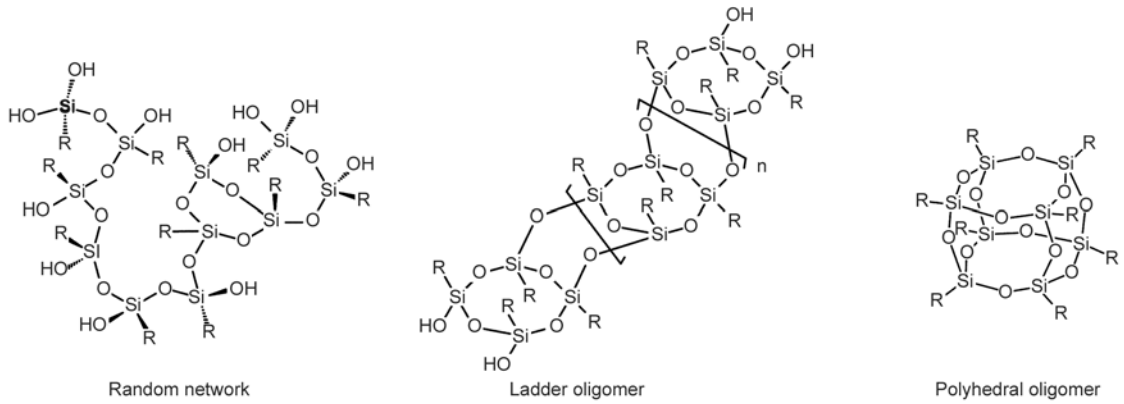

Figure 2. Various structural types of silsesquioxane polymers and oligomers

spontaneous self-assembly of oligomeric silsesquioxanes takes place, owing to π-π interactions between side substituents and the backbone rigidity. It is known that π–π aromatic interactions can play an important role in the organization of Ph-LPSQ systems (including their crystallization [44, 45] and co-crystalization [46]). π–π templating with ladder-like Ph-LPSQ was also used for controlled, one-dimensional (linear) chain growth in the sol–gel polymerization of phenyltrimethoxysilane [47].

It is expected that such structured particles could possibly find an application as precursors to ceramic silicon-oxycarbide microspheres with high C/Si ratio, macroporous templates and chromatographic stationary phases.

2. Experimental section

2.1. Materials and methods

2.1.1. Reagents

Triethoxyphenylsilane (98%, Aldrich, Poznan, Poland), tetraethylorthosilicate (TEOS, 98%, Aldrich, Poznan, Poland), hydrochloric acid (aqueous solution 35–38 wt%, POCh, Gliwice, Poland) and ammonium hydroxide aqueous solution (25 wt%, POCh, Gliwice, Poland) were used as received. Model linear Ph-LPSQ of regular structure was prepared as earlier reported [48]. Solvents were purified according to literature procedures [49].

2.1.2. Instrumentation

Solid-state ^{13}C and ^{29}Si CPMAS NMR spectra were recorded on an AV-400 Bruker spectrometer (Billerica, MA, USA) at 59.627 MHz. The peak positions were referenced to the signal of Q_8M_8 (trimethylsilyl ester of cubic octameric silicate) as standard. Wide-angle X-ray scattering (WAXS) measurements were performed using source of CuKα radiation (Philips), operating at 30 kV and 50 mA X-ray beam. The diffraction patterns were recorded in the 2θ range from 3 to 45° and are presented as functions of the scattering vector d, where $d = 1/s$; $s = 2\sin(\pi 2\theta/360)/0.154$, where 2θ is the scattering angle. Typical time of acquisition was 30 sec. The samples were prepared as powder and were irradiated at the incident angle (α_i) of 0.05°.

Mass spectrometric measurements (MALDI-TOF) were recorded on a Voyager-Elite (PerSeptive Biosystems, Framingham, MS, USA) time-of-flight instrument equipped with a pulsed N_2 laser (337 nm, 4-ns pulse width) and time-delayed extraction ion source. An accelerating voltage of 20 kV was applied. Mass spectra were recorded in the linear positive ion mode using 1,8-dihydroxy-9-anthracenone (ditranol, DT) as the matrix and LiCl, $KO(O)CCF_3$ or $AgO(O)CCF_3$ as cationization agents. For size exclusion chromatography (SEC) an Agilent 1100 series chromatograph (Agilent, Santa Clara, CA, USA) composed of degasser, pump, and autosampler was used. Two PL Gel 5 μm MIXED-C columns (7.8×300 mm) were employed in a series (temperature 300 K). RI (OPTILAB T-rex, Wyatt, Santa Barbara, CA, USA) and MALLS (λ = 682 nm, DAWN HEOS, II, Wyatt, Santa Barbara, CA, USA) were used as detectors. The mobile phase was dichloromethane at a flow rate of 0.8 cm^3/min. Samples (concentration of polymers: 7 mg/cm^3) were dissolved in CH_2Cl_2 and passed through 0.2 μm pore size SRP membrane filters. Injection volumes of the sample solutions were 100 μL. Molecular masses were derived from a calibration curve based on polystyrene standards and Astra 4.90.07 software was used to treat the data.

Phase transitions of polymers were studied by differential scanning calorimetry (DSC) technique [DuPont 2000 thermal analysis system (TA Instruments, New Castle, DE, USA)]. Thermograms were taken for samples (sealed in aluminium pans) quenched from the amorphous phase (room temperature) and then heated (10 K/min) from 273 to 523 K. The sample was kept at 523 K for 3 min to erase any thermal history. Subsequently, it was cooled to 273 K and heated again to 523 K. Thermogravimetric analysis (TGA) was performed using a Hi-Res TGA 2950 Thermogravimetric Analyzer (TA Instruments, New Castle, DE, USA). The analysis was performed under nitrogen from room temperature to 1173 K. The heating rate was 10 K/min.

Diameters of microspheres and micelles formed during the precipitation in nonsolvents were measured at 298 K using a Zetasizer Nano ZEN3600, (Malvern, UK) equipped with a quartz cell. Fluorescence spectra of Ph-LPSQ (in solution and as a suspension) were recorded at room temperature by means of a Horiba Jobin Yvon, Fluorolog-3 spectrofluorometer (Kyoto, Japan) using indicated excitation wavelengths.

Diameters and shape of the precipitated particles were determined by analysis of scanning electron microscopy (SEM) microphotographs. Microstructured samples were dispersed in hexanes and placed on a silicon wafer. They were left for drying at room

temperature. SEM images were taken with a JEOL JSH 5500 LV scanning electron microscope (Tokyo, Japan) in high-vacuum mode at the accelerated voltage of 10 kV. Samples were sputter coated with a fine gold layer, about 20 nm thick using ion coating JEOL JFC 1200 apparatus (Tokyo, Japan). For Transmission Electron Microscopy (TEM) analysis [micrographs were taken with Tesla BS 512 with YAG camera (TESLA, Czechoslovakia)] a small drop of not stained dispersion of micelles in a non-solvent was deposited on a copper grid.

Macropore intrusion volumes and macropore size distributions were measured by mercury intrusion porosimetry on an AutoPore 9220 (Micromeritics Instruments, Norcross, GA, USA) over a pressure range of 4136.8 Pa – 345 MPa and analyzed using the Washburn equation. Before the analysis, all samples were dried [Memmert 200 dryer (Memmert GmbH, Germany)] to constant weight at 308 K for at least 24 h to remove air, and directly measured thereafter.

Nitrogen sorption data were collected with a Micromeritics ASAP 2020 instrument (Micromeritics Instruments, Norcross, GA, USA). Before each nitrogen adsorption–desorption measurement, the samples were degassed at ambient temperature overnight and directly measured thereafter. The isotherms were measured at liquid nitrogen temperature. Specific surface area and pore size distributions were determined using, respectively, the BET (Brunauer-Emmett-Teller) and the BJH (Barrett-Joyner-Halenda) model.

2.2. Synthesis

2.2.1 Preparation of Ph-LPSQ by polycondensation of oligomeric silanols pre-formed by acidic hydrolysis of $PhSi(OEt)_3$

Hydrochloric acid was added drop-wise to a stirred mixture of $PhSi(OEt)_3$ and deionised H_2O. The mixture was left at a given temperature with stirring for a given time (Table 1). The reaction mixture became transparent, indicating complete hydrolysis of alkoxysilyl groups. NH_4OHaq was then added drop-wise with stirring to the obtained sol. The reaction mixture was allowed to solidify at a given temperature for a given time. The polymeric product was dissolved in a small amount of CH_2Cl_2 and precipitated into large volumes of MeOH. Precipitation was repeated trice and polymer fractions differing by their molar mass and molar mass distribution were separated.

^{13}C NMR; δ [ppm]: 134.8, 131.0, 130.3, 127.8 (Ph)
^{29}Si NMR; δ [ppm]: –62 [$PhSi(OH)_2O_{1/2}$] (T^1), –70 [$PhSi(OH)O_{2/2}$] (T^2), –79 ($PhSiO_{3/2}$) (T^3).

2.2.2. Formation of micelles and structured materials in nonsolvents

Ph-LPSQ (M_w(MALLS) = 2500, M_w/M_n = 1.3) was dissolved in dry dichlorometane at a given concentration, and added drop-wise to a stirred nonsolvent (hexanes or EtOH). The microstructured precipitate was filtered and washed with a copious volume of the nonsolvent, then dried to constant weight at room temperature in a vacuum desiccator.

Samples for DLS experiments were prepared using a solution of Ph-LPSQ in CH_2Cl_2 filtered through 0.2 μm PTFE membrane. A given volume was added with stirring (1000 rpm) to the nonsolvent and immediately transferred to a quartz cuvette and placed in the sample compartment of Zetasizer Nano ZEN3600.

2.2.3. Preparation of Ph-LPSQ-SiO_2 composites by condensation of oligomeric Ph-LPSQ onto silica microspheres

Silica microspheres were obtained following the procedure: ethanol (54 cm^3), NH_4OH (2.6 cm^3 26 wt%) and H_2O (1.0 cm^3) were mixed and heated at 323 K for 30 minutes. Tetraethoxysilane (1.9 g, 0.009 mol) was added slowly dropwise to the solution stirred at 1000 rpm and the resulting mixture was heated at 323 K for 24 h. The mixture becomes turbid after about 5 minutes due to the formation of SiO_2 particles (φ = 0.2–0.5 μm by SEM).

Ph-LPSQ (0.19 g; M_w(MALLS) = 2500, M_w/M_n = 1.3) was dissolved in 4 cm^3 of CH_2Cl_2 and added drop-wise to the suspension over 10 minutes. The mixture was heated at 323 K for 24 hours and then admixed with 15 cm^3 of dry toluene and refluxed at 383 K for 8 hours using a Dean-Stark apparatus. The volume of the reaction mixture was reduced by 70% and the residue was precipitated by addition to hexanes (100 cm^3). It was dried to a constant weight (0.7 g), then dissolved in CH_2Cl_2 (14 cm^3) (a turbid solution was formed) and precipitated again in hexanes (1400 cm^3).

3. Results and discussion

3.1. Synthesis, structure and physiochemical properties of Ph-LPSQ

Polymeric Ph-LPSQs were prepared by one-pot, two-step, acid-base catalyzed hydrolytic polycondensation of phenyltriethoxysilane carried out in bulk. The method does not yield highly cross-linked resins but soluble polymeric materials, which can be explained on the basis of two different mechanisms that can occur during a sol-gel process, depending on pH of the reaction mixture [50]. Rapid protonation of ethoxide groups is the first step in acid catalysed hydrolysis of $PhSi(OEt)_3$, which makes it more susceptible to hydrolysis. Under such conditions the hydrolysis of alkoxy groups is nearly complete before the beginning of the condensation of silanols (Figure 3). Primary silanols become preferentially protonated and thus more prone to nucleophilic attack. Unprotonated silanols present in the reaction mixture operate as basic species and react with their protonated counterparts yielding siloxane bonds. Basicity of silanol groups decreases with increasing number of siloxane bonds at the respective silicon atom. Therefore, under acidic conditions monomeric species tend to react with oligomers of the least degree of condensation. Consequently, linear or weakly branched structures are mostly formed. Secondary silanols are activatied for condensation in alkaline conditions, by deprotonation of SiOH groups and formation of silanolate anions. These strong nucleophiles tend to deprotonate most acidic silanols in the oligomeric chain (the side ones). The preferential activation of side silanols in linear oligomers in the two-step, acid-base catalyzed sol-gel process, as well as steric and electronic factors caused by side phenyl groups, result in formation of Ph-LPSQ of ladder-like structure. Obviously, the silsesquioxane backbone of the obtained products is statistically more branched than that prepared by stepwise coupling polycondensation method [48]. The influence of synthetic conditions ($[SiOEt]_0/[H_2O]_0$, $[NH_4OH]_0/[SiOEt]_0$, time and temperature of the process at constant $[HCl]_0/[SiOEt]_0 = 2.2\cdot10^{-4}$) on the structure of product was studied (Table 1). Polymers of M_w(MALLS) 2500–23000 u. were obtained. Their purification by precipitation into MeOH allowed for fractionation of oligomers by their molecular mass.

MALDI TOF spectroscopy was applied to elucidate the structure of Ph-LPSQ obtained with the two-step method (Figures 4 and 5). Tentative assignment of peaks in MALDI-TOF spectra (Figure 4) suggests that the oligomers can indeed be linear. Species containing completely condensed $PhSiO_{2/2}$ units and additionally incompletely condensed groups [$PhSiO_{2/2}(OH)$ and $PhSiO_{1/2}(OH)_2$] dominate in the mixture. Oligosilsesquioxanes of low molecular mass ($m/_z < 1000$ u) can fold and form cage-like architectures [51, 52]. However, only a very small number of the obtained Ph-LPSQ species can be assigned to cyclic structures (along their linear-branched counterparts) which can be attributed to the synthetic method (polycondensation in bulk). Only those, that can correspond to incompletely closed silsesqioxane cages [$(T^3)_8(T^2)_2$ and $(T^3)_{10}(T^2)_2$; m/z 1316.9 u and 1575.0 u] are more abundant. Microstructural analysis of oligo(phenylsilsesquioxanes) obtained under various reaction conditions (Figure 5) proved the propensity of the system to form linear oligomers at low temperatures, with high amount of H_2O and at increased time of condensation under acidic conditions. Branched species are more easily formed at higher temperatures.

Regularity of the structure of Ph-LPSQ chains cannot be proved by a MALDI spectrum alone. Wide angle X-ray diffraction (WAXS) data collected for the prepared materials (Figure 6) were compared with the diffraction pattern of cis-isotactic Ph-LPSQ obtained following the reported stepwise coupling polycondensation procedure [48]. WAXS diffractograms of both amorphous polymers are almost identical and suggest the presence of ladder segments (d_1). However, there are discernible differ-

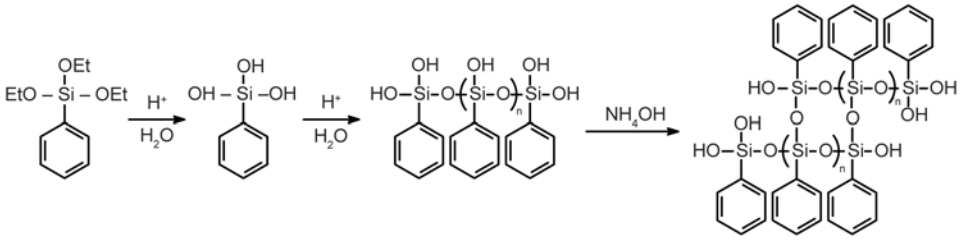

Figure 3. Preparation of Ph-LPSQ by two-step, acid-base catalyzed hydrolytic polycondensation of $PhSi(OEt)_3$

1	$(T^3)_{12}(T^2)_3Li^+$	7	$(T^3)_{14}(T^2)_4Li^+$	13	$1+(T^3)_2$	19	$7+(T^3)_2$
2	$(T^3)_{11}(T^2)_3(T^1)_1Li^+$	8	$(T^3)_{12}(T^2)_4Li^+$	14	$2+(T^3)_2$	20	$8+(T^3)_2$
3	$(T^3)_{10}(T^2)_3(T^1)_2^+$	9	$(T^3)_{10}(T^2)_6Li^+$	15	$3+(T^3)_2$	21	$9+(T^3)_2$
4	$(T^3)_9(T^2)_3(T^1)_3^+$	10	$(T^3)_{10}(T^2)_6Li_2^+$	16	$4+(T^3)_2$	22	$10+(T^3)_2$
5	$(T^3)_8(T^2)_3(T^1)_4^+$	11	$(T^3)_8(T^2)_8Li_2^+$	17	$5+(T^3)_2$	23	$11+(T^3)_2$
6	$(T^3)_7(T^2)_5(T^1)_3Li^+$	12	$(T^3)_6(T^2)_{10}Li_2^+$	18	$6+(T^3)_2$	24	$12+(T^3)_2$

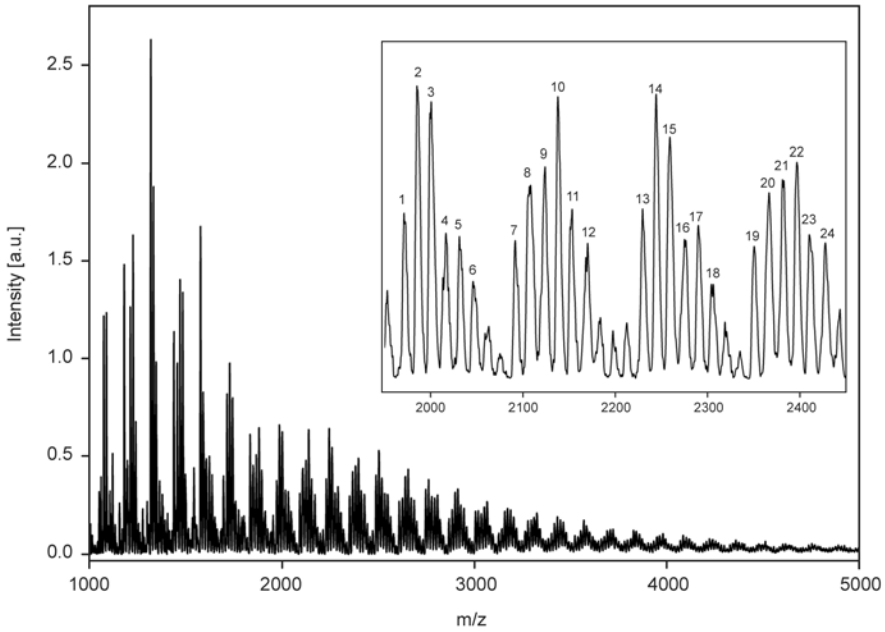

Figure 4. MALDI TOF spectrum (DT, Li^+) of Ph-LPSQ [sample 1a, M_w(MALLS) = 2500, M_w/M_n = 1.3 (Table 1)]

Table 1. Reaction conditions applied for the synthesis of Ph-LPSQ ($[HCl]_0/[SiOEt]_0 = 2.2\cdot10^{-4}$, $[NH_4OH]_0/[SiOEt]_0 = 1.7\cdot10^{-3}$, temperature of the post-condensation treatment T_3 = 333 K, time of the post-condensation treatment t_3 =8 h)

No.	$\frac{[SiOEt]_0}{[H_2O]_0}$	T_1 [K]	t_1 [h]	T_2 [K]	t_{2a} [min]	t_{2b} [h]	fraction	Y [%]	M_n RI	PDI RI	M_w MALLS	PDI MALLS
1*							1a	58	1000	1.6	2500	1.3
							1b	3	1300	1.4	3200	1.2
							1c	6	2000	1.4	4500	1.2
							1d	31	2100	1.4	5000	1.2
2	0.833	294	3	338	1	6	–	61	3400	2.2	13000	2.1
3	0.833	294	18.5	338	1	6	–	61	3400	2.1	12000	1.9
4	0.833	294	27	338	1	6	–	48	3700	1.9	11400	1.7
5	0.833	294	42.5	338	1	6	–	52	2900	1.9	8300	1.8
6*	0.335	303	48	303	1	24	–	58	2800	2.1	11000	1.8
7	0.334	303	48	303	1	24	–	61	2800	2.1	11000	1.8
8	0.333	303	48	303	1	24	–	58	2900	2.1	11000	1.6
9	0.329	303	48	303	1	24	–	51	2900	2.0	10400	1.6
10	1.674	303	24	303	1400	24	–	52	1200	1.9	3100	1.3
11	1.116	303	24	303	160	24	–	56	3100	1.8	9500	1.3
12	0.837	303	24	303	30	24	–	56	1050	1.8	2900	1.2
13	0.833	318	2	318	15	24	–	70	1700	3.9	18500	2.1
14	0.833	318	4	318	15	24	–	71	1400	3.9	15700	2.0
15	0.833	318	6	318	15	24	–	69	2200	3.8	22800	2.2
16	0.833	318	24	318	15	24	–	78	1100	4.9	15700	2.3

* – large scale synthesis
T_1 – temperature of the acidic hydrolysis and oligomerization
t_1 – time of the acidic hydrolysis and oligomerization
T_2 – temperature of the basic condensation
t_{2a} – time of formation of turbidity in the mixture
t_{2b} – time of basic condensation

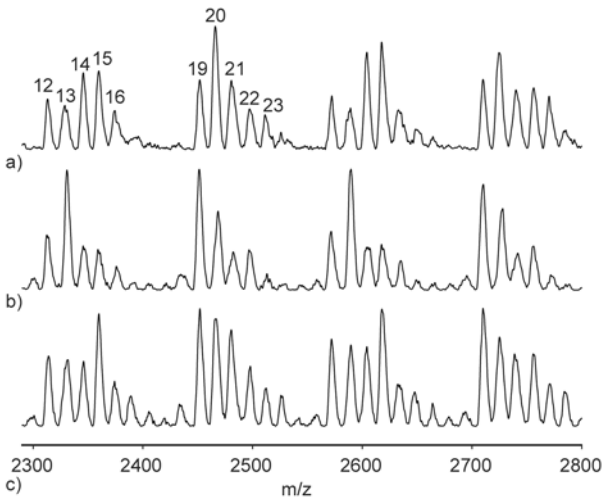

Figure 5. Microstructure (MALDI-TOF, DT, Ag^+) of Ph-LPSQ prepared under different experimental conditions (a) 1d, (b) 6, (c) 2 (Table 1)

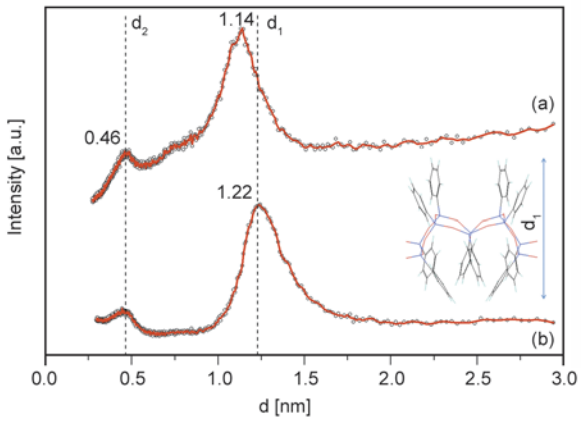

Figure 6. WAXS diffractograms of Ph-LPSQ (a) sample 1a and (b) model linear Ph-LPSQ

ences pointing to defects in the structure of sol-gel product (an additional, diffuse diffraction peak at about 0.77 nm and a decrease of the width of ladder segment d_1 owing to less regular arrangement of siloxane bonds in the polymer backbone). ^{29}Si NMR CPMAS traces (Figure 7) clearly show an incomplete condensation of Ph-LPSQ (a broad peak at –70 ppm corresponds to silanolated silsesquioxane groups T^2, that were revealed by MALDI-TOF, along with all-siloxane condensed silsesquioxane units T^3 at –79 ppm). Vibrational spectra can be also very useful for the characterization of ladder silsesquioxanes. Theoretical studies [53] have proved that stretching vibrations of siloxane bonds in ladder LPSQ are represented by two peaks at about 1150 (ring-asym) and 1050 cm^{-1} (ring-sym). The more organized species, the more defined and separate Si–O–Si peaks should be. FTIR data (Figure 7) recorded for the obtained Ph-LPSQ are coherent with the theory. The structure of poly(phenylsilsesquioxanes) was found to be, typically for sol-gel reactions, dependent on the ratio [SiOEt]/[H_2O] and the reaction temperature.

Thermal characteristics of the prepared Ph-LPSQ were obtained using DSC and TGA techniques. The polymers are amorphous and phase transitions that could possibly stem from their rigid structure were not recorded. Devitrification was not observed for

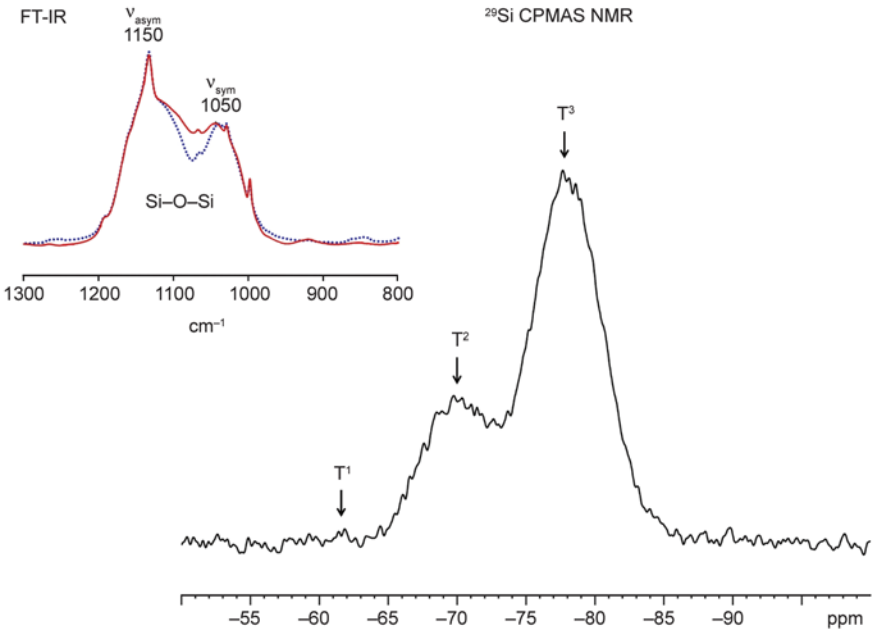

Figure 7. ^{29}Si CPMAS NMR of Ph-LPSQ (sample 5, Table 1) and FTIR spectra (insert) of Ph-LPSQ sample 1a (solid line) and model linear Ph-LPSQ (dot line)

Ph-LPSQ of M_w > 5000). Double chain silsesquioxane backbone surrounded by phenyl groups is rigid (a certain amount of branching in Ph-LPSQ can additionally hinder the polymer mobility) and the T_g effect can be difficult to notice. However, less branched oligomers of low molecular mass (M_w < 3000) exhibit a glass transition at 360 K (Figure 8). An endothermic change in a similar temperature range was observed for cross-linked poly(phenysilsesquioxane) particles obtained by a two-step acid-base catalysed sol-gel process [21, 22, 54]. T_g transition was not sensitive to the thermal treatment during DSC analysis. The reported value also did not change after an attempt to increase the cross-linking density by thermal condensation and azeotropic distillation of water with toluene.

The mechanism of thermal degradation of the obtained Ph-LPSQ was studied under an inert and oxidative atmosphere. The material was found to be thermally stable under both conditions (Figure 8). The main decomposition process in N_2 takes place at 833 K, irrespectively of the molecular mass. Minor transitions occur at 763 K (only for samples of low M_w) and 953 K. Residue left in N_2 at 1173 K (71%) is larger than the calculated one (41%), which suggests entrapment of carbon in the structure during the process [55]. TGA traces in N_2 show also a small increase of sample weight above 1073 K that can be related to the formation of silicon nitride in the process of carbothermal reduction of Si–O structures in the residue [56, 57]. Two step (833 and 923 K) thermooxidative decomposition of Ph-LPSQ in air by release of benzene and combustion of the organic part results in the formation of silica (residue of 46%, calculated 46.5%). An analogous thermal behavior was reported for octahedral phenylsilsesquioxane, both in N_2 and air [55].

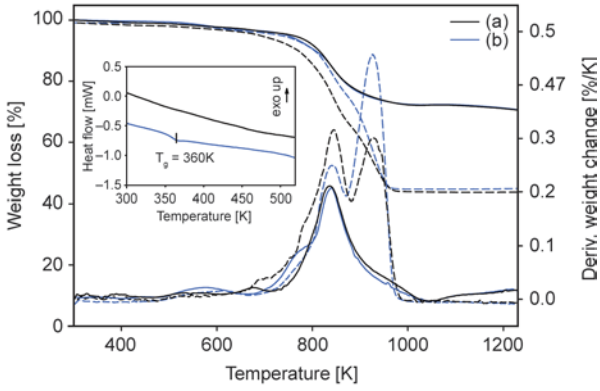

Figure 8. Thermal behavior of Ph-LPSQ of high and low M_w in N_2 (solid lines) and in air (dashed lines) (TGA, 10 K/min) (a) M_w(MALLS) 5000, M_w/M_n = 1.2, (b) Mw(MALLS) 2500, M_w/M_n = 1.3. The insert presents DSC traces (10 K/min, 2nd heating) of Ph-LPSQ of high and low M_w.

3.2. Dynamic light scattering studies of Ph-LPSQ micelles

The size and structure of nanometric objects formed during precipitation of Ph-LPSQ [sample 1a, M_w(MALLS) = 2500, M_w/M_n = 1.3] into a nonsolvent were studied using dynamic light scattering. Their time- and concentration-dependent behavior was monitored. The results demonstrate that Z-average diameter of nano-micelles and nano-spheres increases with the increasing concentration of oligomer solution and high concentration favours the formation of larger aggregates. The studies showed that in the case of a nonpolar nonsolvent (hexanes) the size of micelles reproducibly depends on the ratio between the polymer, solvent and nonsolvent (Figure 9). Micelles of about 200 nm, that were formed at low concentrations of Ph-LPSQ (a < 4 mg/cm^3), tend to adsorb hexanes and swell slowly with time in a linear mode. At larger concentrations of Ph-LPSQ, the micelles tend to rapidly increase (a = 5 mg/cm^3) and then precipitate (a > 5 mg/cm^3), which effectively decrease the amount of the polymer in suspension and leads to the formation of residual micelles of smaller size. An increase in the amount of hexanes caused formation of larger objects (Figure 10a) due to increased hydrostatic pressure. It augments the solvent flux through the wall of a micelle and destabilizes the system. Polar protic solvents (EtOH) rapidly swell the micelles, especially

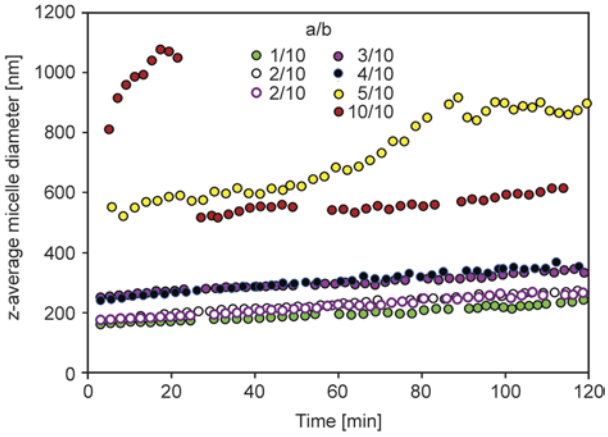

Figure 9. The behavior of Ph-LPSQ micelles in hexanes (a – concentration of Ph-LPSQ in CH_2Cl_2 [mg/cm^3], b – volume ratio: hexanes/CH_2Cl_2 [cm^3/cm^3])

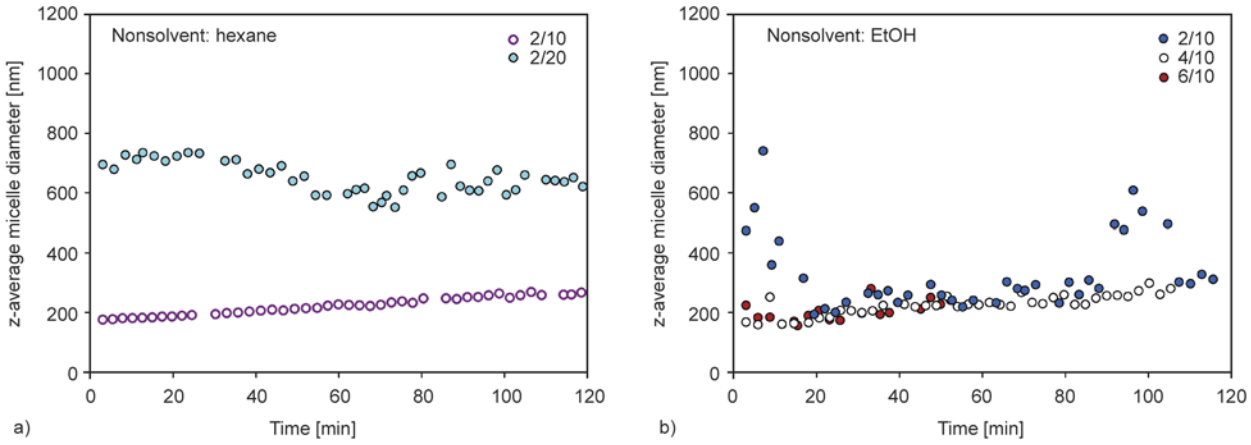

Figure 10. The effect of the amount of hexanes (a) and ethanol (b) on the change of size of micelles of Ph-LPSQ

at low polymer concentrations (Figure 10b). That low stability can be attributed to hydrogen bonding interactions between alcohol molecules and residual hydrophilic silanol moieties in the material.

The literature reports evidence similar phenomena, leading to the formation of spherical structures with a random-coil backbone conformation, for oligomers with large aromatic [58, 59], dendritic [60] or amphiphilic [61, 62] side groups. Analogously, rigid rod–flexible coil block copolymers can self-assemble in selective solvents into specific nanostructures with morphology governed by the geometric disparity between the rod and coil segments and anisotropic interactions between rod blocks (formation of liquid crystalline or crystalline structures) [63, 64]. The process described herein is not typical, since microparticles are formed by rigid molecules with relatively small side substituents. The possible mechanism of micellization of Ph-LPSQ seems to resemble the one proposed for self-assembly of oligoacrylates bearing sterically hindered 1,10-bi-2-naphthalene side groups interacting through π–π stacking [58, 59]. The micelle walls are made of densely packed molecular chains and the affinity among side groups helps in the formation of nanometer-scale spheres with minimum free energy. The structure of the forming micelles is stabilized by π-π inter- and intramolecular interactions between phenyl groups that belong to the neighboring silsesquioxane chains. Such π-π conjugation in rigid segments can affect remarkably optical properties of the formed vesicles which can display e.g. switchable optical characteristics by external triggers [65].

3.3. Fluorescence of Ph-LPSQ

Chromophoric side groups can offer a good way to study polymer dynamics and structure, providing there are appropriate and effective interactions between aromatic molecules [66, 67]. Hindered rotation about siloxane bonds in the double silsesquioxane chain of poly(phenylsilsesquioxanes) [48] prevents its folding and coil aggregation in solution that could result in fluorescence quenching. Fluorescence studies were thus carried out at room temperature for the prepared Ph-LPSQ (sample 1a, Table 1) both in solution and as micelles suspended in hexanes.

Emission spectra were recorded at λ_{ex} = 260 nm (Figure 11). Ph-LPSQ dissolved in dichloromethane

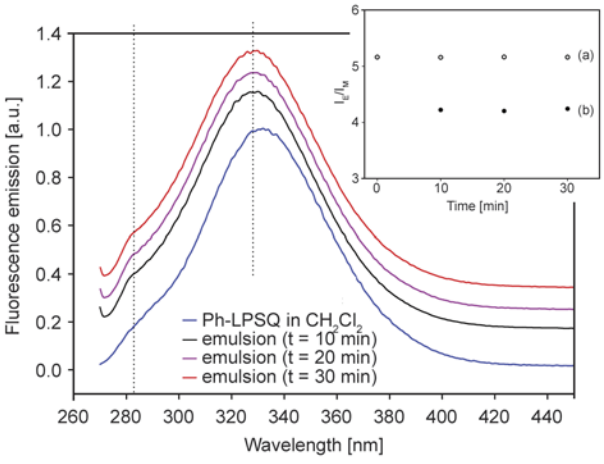

Figure 11. Emission fluorescence spectra (λ_{ex} = 260 nm) and I_E/I_M ratio plotted against the time of experiment (insert) for (a) Ph-LPSQ dissolved in dichloromethane (polymer concentration a = 0.18 mg/cm^3); or (b) suspended as micelles (a = 0.18 mg/cm^3; hexanes/CH_2Cl_2 v/v = 20/1)

show a weak emission peak of the single (monomeric) phenyl group (286 nm) and much stronger one for an excimer of sandwich geometry (331 nm). Samples of micellar structure exhibit a negligible blue shift (3 nm for both monomer and excimer), which can be caused by the change in solvent composition in the studied system. Fluorescence of micelles is stable over the experiment timescale. I_E/I_M ratio for dissolved polymers is bigger than that for micelles (Figure 11, insert) which can be caused by fluorescence quenching due to the aggregation effect and increase of local concentration of phenyl groups in micelles.

Interesting effects were noted on increasing λ_{ex} with energies close to the monomer emission (λ_{ex} = 280 and 290 nm) (Figure 12a). For the studied polymers the shape of emission bands at higher excitation wavelengths is different for microsuspension and the solution. In solution excitation at 280 and 290 nm give similar fluorescence profiles with quenched dimeric excimers (331 nm) and exposed small emission peaks. Possible ways leading to the emissions at wavelengths longer than that of an excimer nearest to the excitation wavelength include energy transfer and formation of excited multimers by interaction of an excited single phenyl with surrounding phenyl groups. Both paths require large density of phenyl aggregates of proper geometry to produce noticeable emissions. Polystyrene can be to some extent regarded as a model system for the studied Ph-LPSQ. It was found that formation of intramolecular excimers in polystyrenes of diverse structure and various sequence length of phenyl groups occurs primarily by interactions between vicinal chromophores in the polymer chain [68] and depends upon the polymer molecular weight [69].

The analogous emission profile for Ph-LPSQ in suspension is different and changes with λ_{ex} (Figure 12b). Fluorescence quenching at λ_{ex} = 280 nm is less efficient than that in the solution. Intense Rayleigh scattering peaks can be observed, with maxima depending on the excitation wavelength, which points to the presence of defined particles in the studied mixture.

3.4. Morphology of self-assembled structures

Owing to the backbone rigidity and π-π interactions between side substituents, oligomeric Ph-LPSQ can self-assemble spontaneously in template-free systems and form symmetrical, nonporous, nano- and microstructures (φ < 1 μm) in nonsolvents (polar protic alcohols and nonpolar nonprotic alkanes). Molecular mass is the restricting factor and only Ph-LPSQ oligomers of M_w < 3000 formed suspensions on precipitation into a nonsolvent from their concentrated solutions in CH_2Cl_2. The stability of suspensions and the shape of particles that aggregated and precipitated under the studied conditions varied depending on the concentration ratio between Ph-LPSQ, solvent and non-solvent (Table 2). Spherical micelles are always formed in the initial stages of the process. It was proven by the structure of the sample presented on Figure 1, that was prepared in a small scale and under specific conditions (concentration of Ph-LPSQ in CH_2Cl_2 = 50 mg/cm^3, volume ratio hexanes/CH_2Cl_2 = 1000 cm^3/cm^3). Under more concentrated conditions the micelles tend to stick to each other and collapse into particles of irregular

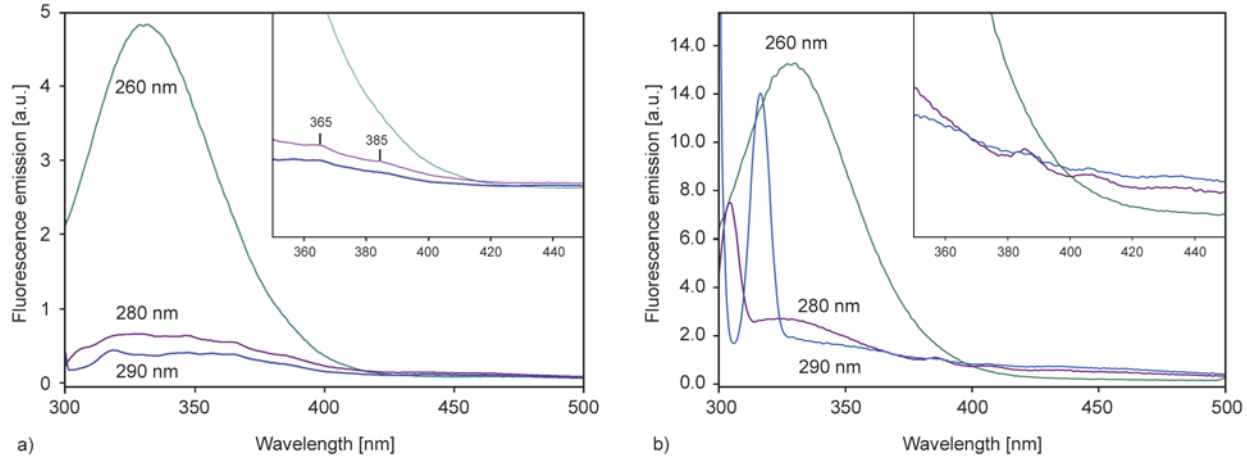

Figure 12. Fluorescence [not normalized spectra registered at λ_{ex} = 260 (green), 280 (violet) and 290 nm (blue)] of Ph-LPSQ (a) in solution in CH_2Cl_2 (a = 0.18 mg/cm^3) and (b) as a micro-suspension (a = 0.18 mg/cm^3; hexanes/CH_2Cl_2 v/v = 20/1)

Table 2. Conditions applied for the preparation of microstructured Ph-LPSQ in a template free system

Sample	1-A	1-B	1-C	1-D	1-E	1-F	1-G	1-H	1-I	1-J
Polymer [g]	1.0	1.0	1.0	1.0	1.0	0.10	0.10	0.05	0.025	1.0
a [mg/cm^3]	1000	200	50	500	330	100	100	50	25	50
b [cm^3/cm^3]	100	100	100	50	33	50	50	50	50	100
Rotation [rpm]	1000	1000	1000	1000	1000	1000	500	1000	1000	1000

a – concentration of Ph-LPSQ in CH_2Cl_2
b – volume ratio: hexanes/CH_2Cl_2

shape. The residual particles dispersed in non-solvent have spherical shapes.

The shape, size of microspheres and material distribution within the micelles were analyzed using scanning and transmission electron microscopy. TEM micrographs of precipitated Ph-LPSQ microspheres (not stained) show both isolated and aggregated units of spherical shape (diameters ranging from 50–200 nm) and dense internal packing. SEM images show that the obtained materials contain irregular but rather monodisperse particles. However, morphology of aggregated structures (Figure 13) varies depending on the oligomer precipitation conditions. The materials prepared with larger amounts of Ph-LPSQ (1-A and 1-D) have monolithic porous structure. Sample 1-D contains also a share of separated particles, which suggest formation of monoliths by aggregation and collapse of micelles. Other specimens display irregular particles, and their size differs with the quantity of polymer used (e.g. samples 1-F and 1-D). The rate of rotation in the system plays an important role for the particle shape. The lower the rate the more regular particles were formed (samples 1-F and 1-G).

3.5. Porosity measurements

A study was carried out to find a correlation between system parameters [polymer concentration (a) and the ratio of solvent and nonsolvent (b)] and the porous structure of the structured assemblies (Table 3). Specific surface area and pore size distributions of selected samples (1-A, 1-D, 1-E) were calculated using, respectively, the Brunauer-Emmett-Teller (BET) and Barrett-Joyner-Halenda (BJH) methods (Table 3). Nitrogen sorption data show that all samples exhibit low surface area (<7 m^2/g) due to the presence of pores of average diameter in the range 7–13 nm. However, their number is low and adsorption isotherms (Figure 14a) do not exhibit hysteresis loop typically associated with capillary condensation in mesoporous materials. Mercury intrusion was also used to characterize the obtained materials. The method is more suitable for macroporous samples and it can provide information about porosity in a wide pore range (<4 nm to 0.4 mm). The estimated porosity (Table 3) is larger than 60% for all specimens but their total pore area is moderate (between 27 and 70 m^2/g; average pore diameter 85–600 nm), depending on precipitation parameters. The comparison of the ratio of macropores/mesopores in the total porosity of the sample (Table 3) shows that the samples containing higher ratio of mesopores exhibit higher surface areas. However, if the general porosity of the sample is low (monolithic samples 1-A and 1-D) then their total surface area is low.

A significant difference concerning the average pore diameter can be observed between materials of irregular micellar structure and porous monoliths. A

Table 3. Nitrogen adsorption and Hg intrusion data summary

Method	Sample	1-A	1-D	1-E	1-B	1-C	1-J
	a [mg/cm^3]	**1000**	**500**	**330**	**200**	**50**	**50**
N_2 adsorption	BET surface area [m^2/g]	1.53	2.52	6.19	–	–	–
	BJH adsorption average pore diameter (4V/A) [nm]	13.16	11.82	7.10	–	–	–
	BJH desorption average pore diameter (4V/A) [nm]	8.99	7.79	6.64	–	–	–
Hg intrusion	total pore area [m^2/g]	69.95	60.39	27.36	27.09	64.40	162.74
	average pore diameter (4V/A) [μm]	0.085	0.155	0.595	0.557	0.266	0.103
	bulk density [g/cm^3]	0.43	0.29	0.19	0.20	0.20	0.21
	apparent (skeletal) density [g/cm^3]	1.16	0.90	0.84	0.78	1.20	1.39
	porosity [%]	63.14	67.89	77.41	74.56	83.68	85.30
	macropores [%]	54.05	62.92	76.68	74.34	80.35	70.88
	mesopores [%]	9.09	4.97	0.73	0.22	3.33	14.42

a – concentration of Ph-LPSQ in CH_2Cl_2

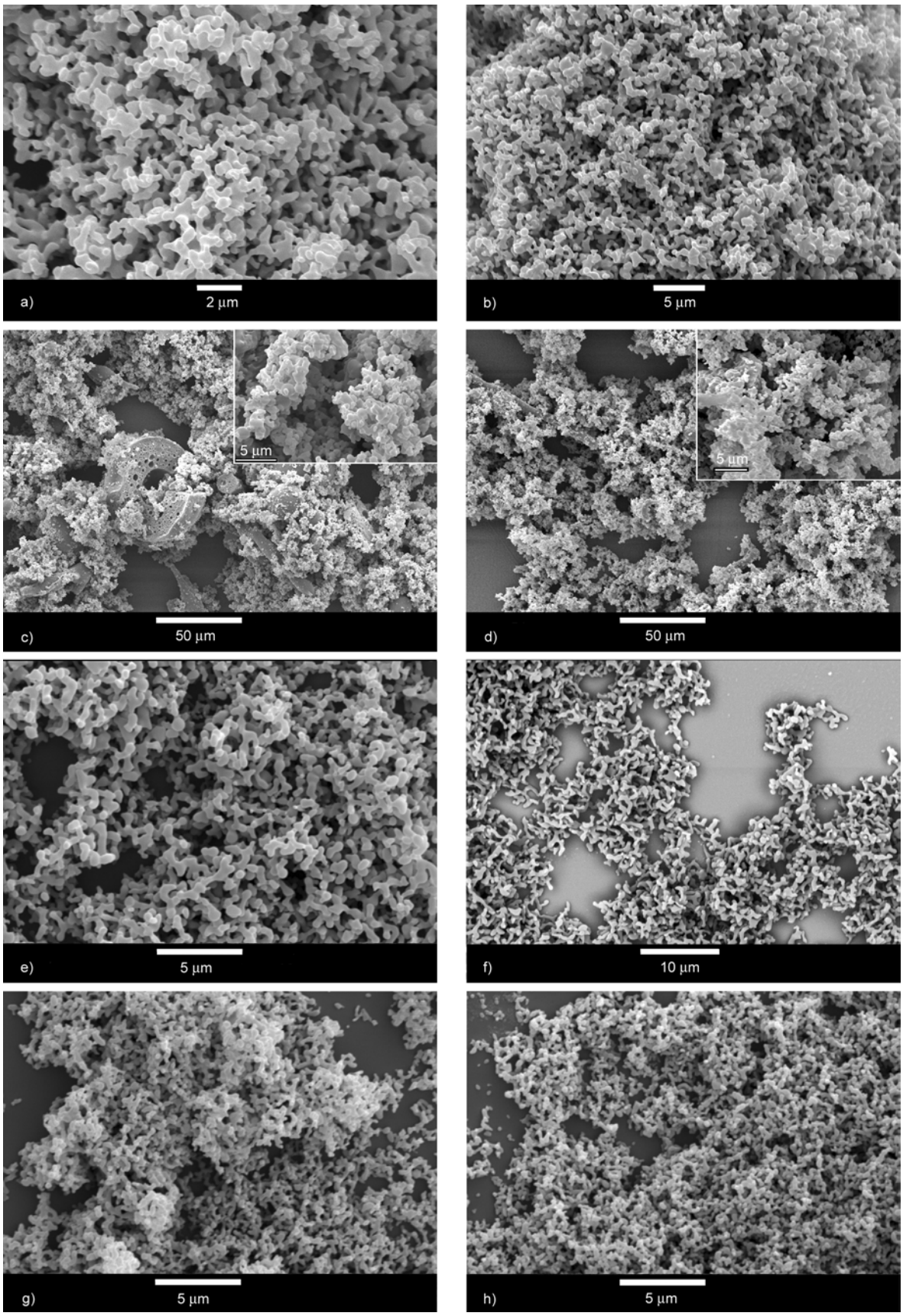

Figure 13. Scanning micrographs of samples a) 1-B, b) 1-C, c) 1-D, d) 1-E, e) 1-F, f) 1-G, g) 1-H, h) 1-I

change of cumulative Hg intrusion volume in different ranges of pore diameters can be observed in the studied materials (Figure 14b). Two types of porosity, corresponding to SEM micrographs, can also be distinguished. All samples were evacuated to remove air and residual moisture from the pore system and mercury penetrates first all inter-particle voids and largest pores to reach a plateau intrusion at about 10 μm. Comparing to porous monoliths 1-A and 1-D, the increase of intrusion volume in samples 1-B, 1-C and 1-E suggests formation of large macropores as the micelles are linked on precipitation. Sample 1-D, that contains a larger share of micellar structures than 1-A, exhibits additional intrusion slope for pores of φ about 1 μm. Both, 1-A and 1-D exhibit also a small increase of the volume of intruded Hg at about 20 nm that can be related to the size of pores detected by nitrogen adsorption. Cumulative pore area analysis (Figure 14b) shows that in samples 1-A and 1-D it is due only to small pores (φ < 50 nm).

Species 1-B, 1-C and 1-E display multimodal pore size distribution. Apart from macrovoids patterned on linking of the precipitating micelles, pores of φ about 1 μm and smaller (15 and 25 nm) are also formed during the process. Their size depends on the precipitation conditions. It suggests that such pores can be due to inter-granular voids formed by primary particles [70]. Sample 1-C, prepared with the lowest concentration of polymer solution and large volume of the nonpolar solvent have quite peculiar Hg intrusion characteristics. The presence of such a large amount of small pores (φ < 100 nm) along with the macropores can be possibly related to the formation of empty vessels during the precipitation. Such objects can collapse more easily.

3.6. Formation of porous silica-silsesquioxane hybrid materials using Ph-LPSQ

Oligomeric Ph-LPSQ was also used for the modification of silica particles prepared in Stöber process. Materials of irregular structure (Figure 15) with particle surface covered with fine microfilaments were obtained using the precipitation procedure. Mercury intrusion data indicate that the material 1-J is porous (Figure 16), but its structure differs from the previously discussed macroporous samples. The pores are smaller (average φ about 20–30 nm) but much more regular. The ratio mesopores/macropores, surface area and sample porosity are highest among the studies samples (Table 3) while the sample bulk density is comparable to that of macroporous materials (1-B, 1-C, 1-E).

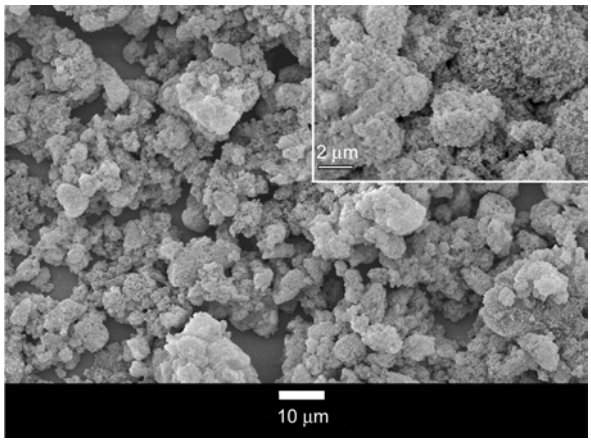

Figure 15. SEM micrograph Ph-LPSQ-SiO_2 hybrid (1-J)

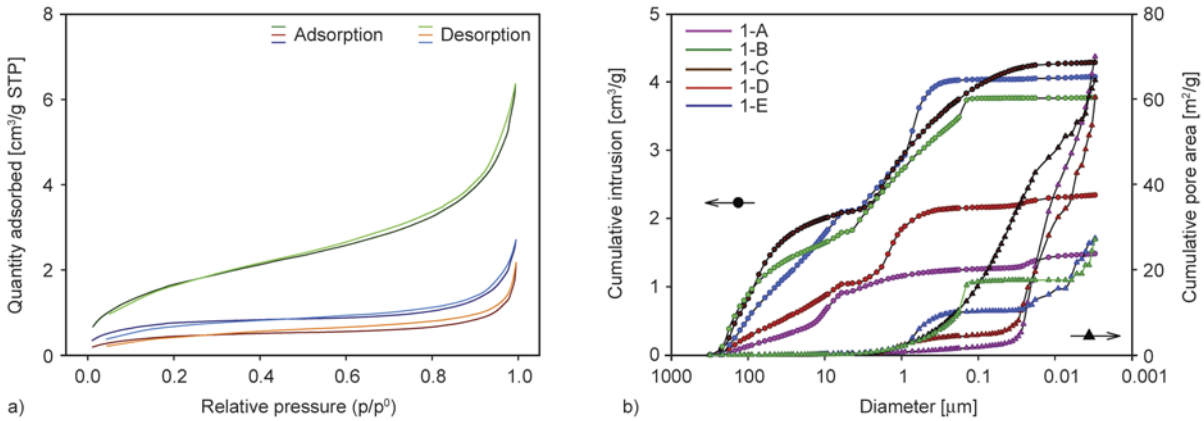

Figure 14. Porosity analysis of the structured Ph-LPSQ materials (a) N_2 adsorption isotherms for samples 1-A (red), 1-D (blue) and 1-E (green), (b) pore size distribution and cumulative pore area estimated by mercury intrusion porosimetry

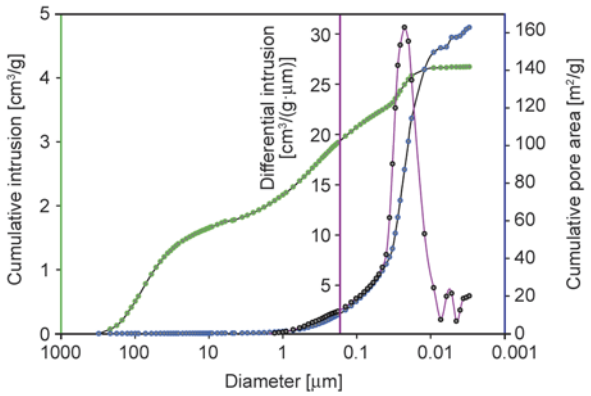

Figure 16. Porosity and surface parameters of Ph-LPSQ-SiO_2 hybrid (1-J)

4. Conclusions

Linear, oligomeric phenylsilsesquioxanes (Ph-LPSQ) can be obtained by a two-step, one-pot, acid/base sol-gel method carried out in bulk. MALDI-TOF analysis revealed that the oligomers are not defect-free, but the composition of the products can be adjusted with duration and temperature of the reaction stages. Oligomeric Ph-LPSQ and hybrid materials based on them are capable of formation of micro- and nanostructures due to morphology of silsesquioxane chain and spontaneous π-π inter- and intramolecular associative interactions between side phenyl substituents. Micellar structures with minimum free energy are formed due to π–π stacking of side phenyl groups in densely packed macromolecular chains. The size and shape of the formed particles and macropores is determined by the parameters of the process (concentration of Ph-LPSQ, solvent/nonsolvent ratio and rate of stirring).

The described method can be used for the preparation of polymeric microspheres in template-free systems. The formed macroporous materials can possibly have an applicative potential as chromatographic stationary phases or interesting precursors for silicon-oxycarbide glasses with high C/Si ratio.

Acknowledgements

The authors thank Polish National Science Centre for the financial support within grant DEC-2011/03/B/ST5/02672 'Studies on preparation and structurization of new hybrid materials'. We are also grateful for analytic data provided by Mrs Beata Wiktorska (CMMS PAS – MALLS analysis) Mr. Marcin Florczak (CMMS PAS – MALDI-TOF), Mr. Przemysław Sowiński (CMMS PAS – TEM micrographs) and Dr. Marcin Kempiński (Kazimierz Wielki University in Bydgoszcz – mercury intrusion porosimetry measurements).

References

[1] Fu G-D., Li G. L., Neoh K. G., Kang E. T.: Hollow polymeric nanostructures – Synthesis, morphology and function. Progress in Polymer Science, **36**, 127–167 (2011).
DOI: 10.1016/j.progpolymsci.2010.07.011

[2] Wu S-H., Mou C-Y., Lin H. P.: Synthesis of mesoporous silica nanoparticles. Chemical Society Reviews, **42**, 3862–3875 (2013).
DOI: 10.1039/c3cs35405a

[3] Giraldo L. F., López B. L., Pérez L., Urrego S., Sierra L., Mesa M.: Mesoporous silica applications. Macromolecular Symposia, **258**, 129–141 (2007).
DOI: 10.1002/masy.200751215

[4] Argyo C., Weiss W., Bräuchle C., Bein T.: Multifunctional mesoporous silica nanoparticles as a universal platform for drug delivery. Chemistry of Materials, **26**, 435–451 (2014).
DOI: 10.1021/cm402592t

[5] Tang F., Li L., Chen D.: Mesoporous silica nanoparticles: Synthesis, biocompatibility and drug delivery. Advanced Materials, **24**, 1504–1534 (2012).
DOI: 10.1002/adma.201104763

[6] Colilla M., González B., Vallet-Regí M.: Mesoporous silica nanoparticles for the design of smart delivery nanodevices. Biomaterials Science, **1**, 114–134 (2013).
DOI: 10.1039/c2bm00085g

[7] Guo X., Yu H., Yang H., Kanamori K., Zhu Y., Nakanishi K.: Pore structure control of macroporous methylsilsesquioxane monoliths prepared by *in situ* two-step processing. Journal of Porous Materials, **20**, 1477–1483 (2013).
DOI: 10.1007/s10934-013-9733-z

[8] Nakanishi K., Shikata H., Ishizuka N., Koheiya N., Soga N.: Tailoring mesopores in monolithic macroporous silica for HPLC. Journal of High Resolution Chromatography, **23**, 106–110 (2000).
DOI: 10.1002/(SICI)1521-4168(20000101)23:1<106::AID-JHRC106>3.0.CO;2-1

[9] Cademartiri R., Brook M. A., Pelton R., Brennan J. D.: Macroporous silica using a 'sticky' Stöber process. Journal of Materials Chemistry, **19**, 1583–1592 (2009).
DOI: 10.1039/b815447c

[10] Rajendra V., Brook M. A.: Controlled formation of macroporous or hollow silica particles in non-aqueous silicone dispersions. RSC Advances, **3**, 22229–22238 (2013).
DOI: 10.1039/c3ra45182h

[11] Nakanishi K., Amatani T., Yano S., Kodaira T.: Multi-scale templating of siloxane gels via polymerization-induced phase separation. Chemistry of Materials, **20**, 1108–1115 (2008).
DOI: 10.1021/cm702486b

[12] Nakanishi K., Kanamori K.: Organic–inorganic hybrid poly(silsesquioxane) monoliths with controlled macro- and mesopores. Journal of Materials Chemistry, **15**, 3776–3786 (2005).
DOI: 10.1039/b508415f

[13] Dong H., Brennan J. D.: Macroporous monolithic methylsilsesquioxanes prepared by a two-step acid/acid processing method. Chemistry of Materials, **18**, 4176–4182 (2006).
DOI: 10.1021/cm060509e

[14] Dong H., Brennan J. D.: Controlling the morphology of methylsilsesquioxane monoliths using a two-step processing method. Chemistry of Materials, **18**, 541–546 (2006).
DOI: 10.1021/cm051900n

[15] Stein A., Li F., Denny N. R.: Morphological control in colloidal crystal templating of inverse opals, hierarchical structures, and shaped particles. Chemistry of Materials, **20**, 649–666 (2008).
DOI: 10.1021/cm702107n

[16] Loiola A. R., da Silva L., Cubillas P., Anderson M. W.: Synthesis and characterization of hierarchical porous materials incorporating a cubic mesoporous phase. Journal of Materials Chemistry, **18**, 4985–4993 (2008).
DOI: 10.1039/B806674D

[17] Wang Z. Y., Stein A.: Morphology control of carbon, silica, and carbon/silica nanocomposites: From 3D ordered macro-/mesoporous monoliths to shaped mesoporous particles. Chemistry of Materials, **20**, 1029–1040 (2008).
DOI: 10.1021/cm0717864

[18] Arkhireeva A., Hay J. N.: Synthesis of sub-200 nm silsesquioxane particles using a modified Stöber sol–gel route. Journal of Materials Chemistry, **13**, 3122–3127 (2003).
DOI: 10.1039/b306994j

[19] Jiang K., Chi F., Li B., Jiang B.: A facile method for preparation of hollow polyphenylsilsesquioxane microspheres. Chemistry Letters, **37**, 492–493 (2008).
DOI: 10.1246/cl.2008.492

[20] Ma C., Kimura Y.: Preparation of nano-particles of poly(phenylsilsesquioxane)s by emulsion polycondensation of phenylsilanetriol formed in aqueous solution. Polymer Journal, **34**, 709–713 (2002).
DOI: 10.1295/polymj.34.709

[21] Takahashi K., Tadanaga K., Hayashi A., Matsuda A., Tatsumisago M.: Glass transition and thermal softening of poly(phenylsilsesquioxane) particles prepared using two-step acid–base catalyzed sol–gel process. Journal of Non-Crystalline Solids, **354**, 700–704 (2008).
DOI: 10.1016/j.jnoncrysol.2007.07.073

[22] Takahashi K., Tadanaga K., Hayashi A., Matsuda A., Katagiri K., Tatsumisago M.: Structure of polyphenylsilsesquioxane particles prepared by two-step acid-base catalyzed sol–gel process and formation of hollow particles. Journal of Nanoscience and Nanotechnology, **7**, 3307–3312 (2007).
DOI: 10.1166/jnn.2007.659

[23] Matsuda A., Sasaki T., Hasegawa K., Tatsumisago M., Mianmi T.: Thermal softening behavior of poly(phenylsilsesquioxane) and poly(benzylsilsesquioxane) particles. Journal of the Ceramic Society of Japan, **108**, 830–835 (2000).
DOI: 10.2109/jcersj.108.1261_830

[24] Takahashi K., Tadanaga K., Matsuda A., Hayashi A., Tatsumisago M.: Thermoplastic and thermosetting properties of polyphenylsilsesquioxane particles prepared by two-step acid-base catalyzed sol-gel process. Journal of Sol-Gel Science and Technology, **41**, 217–222 (2007).
DOI: 10.1007/s10971-006-1501-y

[25] Lee A. S. S., Choi S-S., Jang S-H., Hwang S. S., Baek K-Y.: Preparation of high modulus thin films based on photocurable azido-functionalized ladder-like structured polysilsesquioxanes. Macromolecular Research, **22**, 1109–1114 (2014).
DOI: 10.1007/s13233-014-2152-4

[26] Kaneko Y., Toyodome H., Mizumo T., Shikinaka K., Iyi N.: Preparation of a sulfo-group-containing rod-like polysilsesquioxane with a hexagonally stacked structure and its proton conductivity. Chemistry – A European Journal, **20**, 9394–9399 (2014).
DOI: 10.1002/chem.201402011

[27] Lee S-H., Lim J-H., Kim K-M.: Fabrication of hybrid ladderlike polysilsesquioxane-grafted multiwalled carbon nanotubes. Journal of Applied Polymer Science, **124**, 3792–3798 (2012).
DOI: 10.1002/app.35389

[28] Baney R. H., Itoh Maki I., Sakakibara A., Suzuki T.: Silsesquioxanes. Chemical Reviews, **95**, 1409–1430 (1995).
DOI: 10.1021/cr00037a012

[29] Brown J. F.: Double chain polymers and nonrandom crosslinking. Journal of Polymer Science Part C: Polymer Symposia, **1**, 83–97 (1963).
DOI: 10.1002/polc.5070010106

[30] Ainuddin A. R., Hakiri N., Muto H., Sakai M., Matsuda A.: Mechanical properties comparison of phenylsilsesquioxane–methylsilsesquioxane hybrid films by indentation. Journal of the Ceramic Society of Japan, **119**, 490–493 (2011).
DOI: 10.2109/jcersj2.119.490

[31] Li G. Z., Matsuda T., Nishioka A., Miyata K., Masubuchi Y., Koyama K., Pittman C. U. Jr.: Rheological properties of polystyrene blends with rigid ladderlike polyphenylsilsesquioxane. Journal of Applied Polymer Science, **96**, 706–713 (2005).
DOI: 10.1002/app.21503

[32] Prado L. A. S. A., Sforça M. L., de Oliveira A. G., Yoshida I. V. P.: Poly(dimethylsiloxane) networks modified with poly(phenylsilsesquioxane)s: Synthesis, structural characterisation and evaluation of the thermal stability and gas permeability. European Polymer Journal, **44**, 3080–3086 (2008).
DOI: 10.1016/j.eurpolymj.2008.07.002

[33] Lee A. S., Baek K-Y., Hwang S. S.: Synthesis of a photocurable ladder-like poly(phenyl-co-mercaptopropyl) silsesquioxane as gate dielectric material. Molecular Crystals and Liquid Crystals, **580**, 88–94 (2013). DOI: 10.1080/15421406.2013.807720

[34] Hong-Ji C., Meng F.: Core–shell-shaped organic–inorganic hybrid as pore generator for imprinting nanopores in organosilicate dielectric films. Macromolecules, **40**, 2079–2085 (2007). DOI: 10.1021/ma062471x

[35] Chen W-C., Liu W-C., Wu P-T., Chen P-F.: Synthesis and characterization of oligomeric phenylsilsesquioxane-titania hybrid optical thin films. Materials Chemistry and Physics, **83**, 71–77 (2004). DOI: 10.1016/j.matchemphys.2003.09.039

[36] Yang H., Cheng Y., Xiao F.: Thermal stable superhydrophobic polyphenylsilsesquioxane/nanosilica composite coatings. Applied Surface Science, **258**, 1572–1580 (2011). DOI: 10.1016/j.apsusc.2011.09.137

[37] Meier A., Weinberger M., Pinkert K., Oschatz M., Paasch S., Giebeler L., Althues H., Brunner E., Eckert J., Kaskel S.: Silicon oxycarbide-derived carbons from a polyphenylsilsequioxane precursor for supercapacitor applications. Microporous and Mesoporous Materials, **188**, 140–148 (2014). DOI: 10.1016/j.micromeso.2013.12.022

[38] Kang D. W., Kim S. T., Kim Y. M.: Preparation and characteristics of polyphenylsilsesquioxane-*b*-polyurethane copolymer as a dielectric material. Journal of Inorganic and Organometallic Polymers, **13**, 157–170 (2003). DOI: 10.1023/A:1025836316494

[39] Lee A. S., Choi S-S., Lee H. S., Jeon H. Y., Baek K-Y., Hwang S. S.: Synthesis and characterization of organic–inorganic hybrid block copolymers containing a fully condensed ladder-like polyphenylsilsesquioxane. Journal of Polymer Science Part A: Polymer Chemistry, **50**, 4563–4570 (2012). DOI: 10.1002/pola.26269

[40] Jiang Y., Li X., Yang R.: Polycarbonate composites flame-retarded by polyphenylsilsesquioxane of ladder structure. Journal of Applied Polymer Science, **124**, 4381–4388 (2012). DOI: 10.1002/app.35428

[41] Ren Z., Zhang R., Wang F., Yan S.: A study on the hydrogen bonding interaction of the electrospun ladder polyphenylsilsesquioxane/polyisophthalamide composite fibers by ATR FT-IR. Polymer Chemistry, **2**, 608–613 (2011). DOI: 10.1039/c0py00274g

[42] de Omena Pina S. R., Pardini L. C., Yoshida I. V. P.: Carbon fiber/ceramic matrix composites: Processing, oxidation and mechanical properties. Journal of Materials Science, **42**, 4245–4253 (2007). DOI: 10.1007/s10853-006-0688-1

[43] Kummari S. V. K. R., Kummara M. R., Palem R. R., Nagellea S. R., Shchipunov Y., Ha C-S.: Chitosan–poly(aminopropyl/phenylsilsesquioxane) hybrid nanocomposite membranes for antibacterial and drug delivery applications. Polymer International, **64**, 293–302 (2015). DOI: 10.1002/pi.4789

[44] Li P-F., Yan S-K., Ren Z-J.: An optical microscopy study on the solvent-induced crystalline morphology of ladder polyphenylsilsesquioxane. Acta Physico-Chimica Sinica, **28**, 494–498 (2012). DOI: 10.3866/PKU.WHXB201111233

[45] Li G. Z., Yamamoto T., Nozaki K., Hikosaka M.: Studies on morphology of single crystals of ladder-like polyphenylsilsesquioxane (PPSQ) by polarized optical microscopy. Macromolecular Chemistry and Physics, **201**, 1283–1285 (2000). DOI: 10.1002/1521-3935(20000801)201:12<1283::AID-MACP1283>3.0.CO;2-1

[46] Li G., Yamamoto T., Nozaki K., Hikosaka M.: Crystallization of ladderlike polyphenylsilsesquioxane (PPSQ)/isotactic polystyrene (i-PS) blends. Polymer, **42**, 8435–8441 (2001). DOI: 10.1016/S0032-3861(01)00326-3

[47] Kim K-M., Ogoshi T., Chujo Y.: Controlled polymer hybrids with ladderlike polyphenylsilsesquioxane as a template via the sol–gel reaction of phenyltrimethoxysilane. Journal of Polymer Science Part A: Polymer Chemistry, **43**, 473–478 (2005). DOI: 10.1002/pola.20571

[48] Liu C., Liu Y., Shen Z., Xie P., Zhang R., Yang J., Bai F.: Study of the steric tacticity of novel soluble ladder-like poly(phenylsilsesquioxane) prepared by stepwise coupling polymerization. Macromolecular Chemistry and Physics, **202**, 1581–1585 (2001). DOI: 10.1002/1521-3935(20010601)202:9<1581::AID-MACP1581>3.0.CO;2-5

[49] Armarego W. L. F., Chai Ch. L. L.: Purification of laboratory chemicals. Elsevier Science (2003).

[50] Brinker C. J.: Hydrolysis and condensation of silicates: Effects on structure. Journal of Non-Crystalline Solids, **100**, 31–50 (1988). DOI: 10.1016/0022-3093(88)90005-1

[51] Kim H-J., Lee J-K., Park S-J., Ro H. W., Yoo D. Y., Yoon D. Y.: Observation of low molecular weight poly(methylsilsesquioxane)s by graphite plate laser desorption/ionization time-of-flight mass spectrometry. Analytical Chemistry, **72**, 5673–5678 (2000). DOI: 10.1021/ac0003899

[52] Ro H. W., Park E. S., Soles C. L., Yoon D. Y.: Structure–property relationships for methylsilsesquioxanes. Chemistry of Materials, **22**, 1330–1339 (2010). DOI: 10.1021/cm901771y

[53] Park E. S., Ro H. W., Nguyen C. V., Jaffe R. L., Yoon D. Y.: Infrared spectroscopy study of microstructures of poly(silsesquioxane)s. Chemistry of Materials, **20**, 1548–1554 (2008). DOI: 10.1021/cm071575z

[54] Takahashi K., Tadanaga K., Matsuda A., Hayashi A., Tatsumisago M.: Effects of phenyltriethoxysilane concentration in starting solutions on thermal properties of polyphenylsilsesquioxane particles prepared by a two-step acid-base catalyzed sol-gel process. Journal of the Ceramic Society of Japan, **115**, 131–135 (2007). DOI: 10.2109/jcersj.115.131

[55] Fina A., Tabuani D., Carniato F., Frache A., Boccaleri E., Camino G.: Polyhedral oligomeric silsesquioxanes (POSS) thermal degradation. Thermochimica Acta, **440**, 36–42 (2006). DOI: 10.1016/j.tca.2005.10.006

[56] Shi Y., Wan Y., Zhao D.: Ordered mesoporous non-oxide materials. Chemical Society Reviews, **40**, 3854–3878 (2011). DOI: 10.1039/c0cs00186d

[57] Kapoor M. P., Inagaki S.: Synthesis of mesoporous silicon oxynitrides via direct nitridation with nitrogen. Chemistry Letters, **32**, 94–95 (2003). DOI: 10.1246/cl.2003.94

[58] Liu N., Wang X., Cao H., Chen C., Zhang W., Wei Y.: Concentration-dependent self-assembly of a novel comb oligomer having rigid binaphthyl macrocyclic pendants. Macromolecular Rapid Communications, **26**, 1925–1930 (2005). DOI: 10.1002/marc.200500570

[59] Liu N., Wang X., Jin E., Chen C., Zhang W., Wei Y.: Synthesis and self-assembly of comb oligomers having rigid racemic or chiral binaphthyl macrocyclic pendant groups. Polymer, **47**, 3021–3027 (2006). DOI: 10.1016/j.polymer.2006.03.018

[60] Percec V., Ahn C-H., Ungar G., Yeardley D. J. P., Möller M., Sheiko S. S.: Controlling polymer shape through the self-assembly of dendritic side-groups. Nature, **391**, 161–164 (1998). DOI: 10.1038/34384

[61] Basu S., Vutukuri D. R., Shyamroy S., Sandanaraj B. S., Thayumanavan S.: Invertible amphiphilic homopolymers. Journal of the American Chemical Society, **126**, 9890–9891 (2004). DOI: 10.1021/ja047816a

[62] El Kadib N. A., Finiels A., Marcotte N., Brunel D.: Self-templating amphiphilic polysiloxanes to design nanostructured silica-based architectures. Chemical Communications, **49**, 5168–5170 (2013). DOI: 10.1039/c3cc41943f

[63] Chen L., Shen H., Eisenberg A.: Kinetics and mechanism of the rod-to-vesicle transition of block copolymer aggregates in dilute solution. Journal of Physical Chemistry B, **103**, 9488–9497 (1999). DOI: 10.1021/jp9913665

[64] Zhang J., Chen X-F., Wei H-B., Wan X-H.: Tunable assembly of amphiphilic rod–coil block copolymers in solution. Chemical Society Reviews, **42**, 9127–9154 (2013). DOI: 10.1039/c3cs60192g

[65] Liu C-L., Lin C-H., Kuo C-C., Lin S-T., Chen W-C.: Conjugated rod–coil block copolymers: Synthesis, morphology, photophysical properties, and stimuli-responsive applications. Progress in Polymer Science, **36**, 603–637 (2011). DOI: 10.1016/j.progpolymsci.2010.07.008

[66] Hunter C. A., Sanders J. K. M.: The nature of π-π interactions. Journal of the American Chemical Society, **112**, 5525–5534 (1990). DOI: 10.1021/ja00170a016

[67] Snyder S. E., Huang B-S., Chu Y. W., Lin H-S., Carey J. R.: The effects of substituents on the geometry of π–π interactions. Chemistry – A European Journal, **18**, 12663–12671 (2012). DOI: 10.1002/chem.201202253

[68] Lindsell W. E., Robertson F. C., Soutar I.: Intramolecular excimer formation in macromolecules – V. Head-to-head polystyrene, block copolymers of styrene and butadiene and regular condensation polymers of α-methylstyrene. European Polymer Journal, **17**, 203–208 (1981). DOI: 10.1016/0014-3057(81)90154-3

[69] Abuin E., Lissi E., Gargallo L., Radic D.: Polystyrene fluorescence spectra. Molecular weight dependence in different solvents. European Polymer Journal, **20**, 105–107 (1984). DOI: 10.1016/0014-3057(84)90233-7

[70] Giesche H.: Mercury porosimetry: A general (practical) overview. Particle and Particle Systems Characterization, **23**, 9–19 (2006). DOI: 10.1002/ppsc.200601009

eXPRESS Polymer Letters Vol.9, No.11 (2015) 1001–1014
Available online at www.expresspolymlett.com
DOI: 10.3144/expresspolymlett.2015.90

Effect of polydimethylsiloxane incorporation on the properties of polyimides synthesized from newly designed α,α′-bis(2-aminophenoxy)-p-xylene

A. R. Ashraf[1], *Z. Akhter*[1*], *V. McKee*[2], *M. Siddiq*[1]

[1]Department of Chemistry, Quaid-i-Azam University, 45320 Islamabad, Pakistan
[2]School of Chemical Sciences, Dublin City University, Glasnevin, Dublin 9, Ireland

Received 7 April 2015; accepted in revised form 26 June 2015

Abstract. A novel diamine monomer α,α′-bis(2-aminophenoxy)-p-xylene (2APX) was synthesized and condensed with four different dianhydrides to prepare a series of polyimides. Aminopropyl terminated polydimethylsiloxane (PDMS) was incorporated within the backbone of polyimides for the preparation of poly(imide siloxane) copolymers. Fourier transform infrared (FTIR), ^{1}H and ^{13}C nuclear magnetic resonance (NMR) spectroscopic studies accompanied by elemental and single crystal X-ray analysis were performed for structure elucidation of 2NPX and 2APX. The crystal system of the 2NPX was found to be monoclinic, belonging to space group $P2_1/n$ while 2APX was triclinic with space group $P\bar{1}$. The structural elucidation of polymers was carried out by FTIR and ^{1}H NMR spectroscopy and their properties were studied by solubility testing, wide angle X-ray diffraction (WAXRD), thermogravimetric analysis (TGA) and viscosity measurement along with laser light scattering technique (LLS). WAXRD pattern showed the semicrystalline nature of polyimides which was decreased in case of copolymers. The poly(imide siloxane) copolymers displayed slightly lower temperature resistance but improved solubility as compared to polyimides. Maximum degradation temperature (T_{max}) of polyimides was in the range of 523–570°C while that of copolyimides, ranged between 483–525°C. Similarly, a decline in inherent viscosities and increase in molecular weight was noticed while moving from polyimides to copolyimides.

Keywords: *polymer synthesis, molecular engineering, 2APX, single crystal, poly(imide siloxane) copolymers, laser light scattering*

1. Introduction

The advances in the field of high performance materials demand a unique combination of properties i.e. good oxidative and thermal stability, high glass transition temperature, excellent mechanical properties, good adhesion along with chemical, wear, fire and radiation resistance for diverse range of applications including aerospace, automotive and microelectronic industries, as films, adhesives, sealants, coatings, insulators, gas separation membranes etc. In this regard, large number of polymeric materials such as polyamides, polyimides, poly(amide-imide)s polybenzimidazoles, polyethers, polyketones, polysulphones, and polyesters have been developed in order to replace metal, ceramic or glass and reduce the cost of present day industrial processes [1–7]. Polyimides especially aromatic polyimides have attracted the attention of scientists and engineers more than any other polymer as they have great potential to serve this purpose due to favorable combination of aforementioned sought properties [8]. At present time, polyimides are considered as versatile polymers with an almost unlimited spectrum of applications in advanced technologies. The

*Corresponding author, e-mail: zareenakhter@yahoo.com

exceptional properties displayed by the polyimides are reliant on their chemical structure, composition, molecular aggregation and intra or interchain molecular interactions, hence can be tailored to desired ones through changing the chemical structure and molecular composition of polyimides. In this respect, various strategies can be applied i.e. modification of monomers in order to endow the polymer chain with new functionalities, composite engineering or copolymerization etc. Therefore, the curiosity of academic and industrial research is the production of new polyimide based materials so as to further enhance their properties and diversify applications. Much research has been carried out in last few years to improve certain properties of polyimides for specific applications. For instance, main disadvantage associated with the application of polyimide films in optoelectronic industry is their yellowish nature. This is attributed to the intra or intermolecular charge transfer complex (CTC) formation between the alternating electron-acceptor dianhydride and electron-donor diamine moieties in the polymer chain [9]. It was prophesied that use of weak electron-accepting dianhydrides or electron-donating diamines will suppress these charge transfer (CT) interactions. Keeping this in mind Haixia Yang and coworkers prepared fluorinated polyimides from diamines bearing electron withdrawing trifluoromethyl substituents (lowering its electron-donating ability) and observed significantly enhanced optical transparency [10]. Semi-aromatic polyimides derived from alicyclic dianhydride i.e. 1,2,4,5-cyclohexanetetracarboxylic dianhydride (weak electron-accepting) and different aromatic diamines also produced alike results [11]. Likewise, introduction of flexible spacers (–O–, –CO–, –SO_2–) [12], kink in structure through *ortho* or *meta* catenation instead of *para* [13], bulky pendant groups or hinge atoms [14] or trifluoromethyl groups (–CF_3) [15] in the structure of either diamine or dianhydride led to improvement in processability and solubility of polyimides while upholding their beneficial properties. Polyimides with significantly enhanced thermal and mechanical properties were produced by the incorporation of heterocyclic rings of benzimidazole, benzoxazole, pyrimidine and benzoxadiazole into the backbone of polyimides [16]. Juntao Wu studied the influence of nano-sized Al_2O_3 content on various properties of PI/Al_2O_3 nanocomposites and found that the incorporation of Al_2O_3 in the polyimide triggered an increase in thermal stability, Young's modulus and electrical aging performance of hybrid films as compared to pure polyimide [17]. Copolymerization strategy i.e. synthesis of polymers from two different diamines or dianhydrides is also applied to modify the properties of polyimides [18–20]. In this regard, aminopropyl terminated polydimethylsiloxane (PDMS) is often covalently incorporated within the polyimide chain. Polydimethylsiloxane is a flexible inorganic elastomer having very low glass transition temperature (–123°C) and imparts several beneficial properties to the polymeric system into which it is co-reacted e.g. improved solubility and flame resistance, increased permeability, permselectivity, adhesive ability and impact resistance, reduced water absorption and dielectric constant, modified surface properties, superior electrical properties etc. [21–27]. Therefore, silicone containing polyimides have attracted significant attention recently and studies are mainly focused on investigating the effects of polydimetylsiloxane incorporation on the aforementioned properties of polyimides. In this context, Othman reported a series of poly(siloxane-imide) block copolymers and concluded that incorporation of silicon units into the polyimide chains significantly reduced the refractive index and dielectric constant with reasonably low dielectric loss [28]. Similarly, Ku and coworkers observed that pyridine-containing poly(imide-siloxane)s showed stronger adhesion to copper foils along with lower moisture absorption as compared to conventional aromatic polyimides [29].

While improving a particular property of polyimide, it has to be remembered that their thermal and mechanical properties for which these are known for, must not be compromised. Therefore, an adjusted degree of structural modification should be applied so as to optimize the balance of properties.

This article reports the synthesis of polyimides and siloxane-containing copolyimides derived from a newly designed ether based diamine monomer i.e. α,α′-bis(2-aminophenoxy)-p-xylene. This new diamine was characterized by FTIR and NMR spectroscopic techniques along with elemental and single crystal X-ray diffraction analysis. FTIR and NMR spectroscopy, solubility, WAXRD, thermal, viscometric and laser light scattering analysis were carried out for the synthesized polymers and copolymers. The emphasis of the study was to evaluate the properties of polyimides derived from diamine hav-

ing amino group at ortho position with respect to ether linkage and monitor the influence of polydimethylsiloxane incorporation on solubility, crystallinity, thermal stability, viscosity, and molecular weight of parent polyimides.

2. Experimental

2.1. Materials

All chemicals and reagents used for the synthesis of diamine, polyimides and poly(imide siloxane) copolymers were of highest purity and were used as received. 2-nitrophenol (2NP), potassium carbonate anhydrous (K_2CO_3), pyromellitic dianhydride (PMDA), 3,3′,4,4′-benzophenonetetracarboxylic dianhydride (BTDA) and oxydiphthalic anhydride (ODPA) were purchased from Fluka Chemie GmbH (Buchs, Switzerland). While 2,2-bis(3,4-dicarboxyphenyl)hexafluoropropane dianhydride (6FDA), 1,4-bis(chloromethyl) benzene (CMB), 5% palladium on activated carbon (Pd/C) and aminopropyl terminated polydimethylsiloxane (PDMS) of M_n = 2500 were obtained from Sigma Aldrich Chemie GmbH (Schnelldorf, Germany). Hydrazine monohydrate was procured from Merck (Darmstadt, Germany). Solvents, N-methylpyrrolidone (NMP), N,N-dimethylacetamide (DMAc), N,N-dimethylformamide (DMF), tetrahydrofuran (THF) ethanol, were acquired from various commercial sources and were dried before use [30].

2.2. Instrumentation and measurements

Melting temperatures of the aromatic dinitro and diamine compounds were determined in a capillary tube using Gallenkamp electrothermal melting point apparatus (Staffordshire, UK). The solid state Fourier transform infrared (FTIR) spectra (400–4000 cm^{-1}) were obtained using Thermo Nicolet-6700 spectrophotometer (Madison, USA). Nuclear magnetic resonance (NMR) spectra were recorded in deuterated DMSO-d_6 using Bruker spectrometer (Bruker NMR Instruments) operating at 300 MHz for ^1H NMR and at 75 MHz for ^{13}C NMR using tetramethylsilane (TMS) as internal reference. The elemental analyses were performed using CHNS-932 LECO instrument (Michigan, USA). Single crystal X-ray data of α,α′-bis(2-nitrophenoxy)-p-xylene and α,α′-bis(2-aminophenoxy)-p-xylene were obtained on a Bruker Apex II CCD diffractometer (Bruker XRD Instruments) at 150 K. Wide-angle X-ray diffractograms were obtained using PANalytical PW 3040/60 X'Pert PRO diffractometer (Almelo, Netherlands). Thermogravimetric analysis (TGA) were carried out using Perkin-Elmer Pyris instrument (Waltham, USA) at a heating rate of 20°C/min in a nitrogen atmosphere up to a maximum temperature of 800°C. The inherent viscosities of the polyimides were determined using Ubbelohde's viscometer at 25°C by dissolving 0.2 g/dL of sample in DMSO. Molecular weights and radius of gyration (R_g) of polymers were determined by dissolving 0.8 g/dL of sample in DMSO through static laser light scattering technique using Brookhaven's BI-200 SM instrument (Holtsville NY, USA) fitted with Argon-Ion laser (Coherent Innova) with vertically polarized incident light of wavelength 637 nm and a BI 900 At digital correlator.

2.3. Monomer synthesis

2.3.1. Synthesis of α,α′-bis(2-nitrophenoxy)-p-xylene (2NPX)

2NPX was synthesized by the Williamson's etherification reaction of 2-nitrophenol with 1,4-bis(chloromethyl)benzene according to Figure 1. For this purpose, a 250 mL two neck round-bottom flask fitted with reflux condenser and nitrogen tube was charged with 11.12 g of 2-nitrophenol (80 mmol), 7.00 g of 1,4-bis(chloromethyl)benzene (40 mmol), 11.00 g of potassium carbonate (anhydrous) and 60 mL of

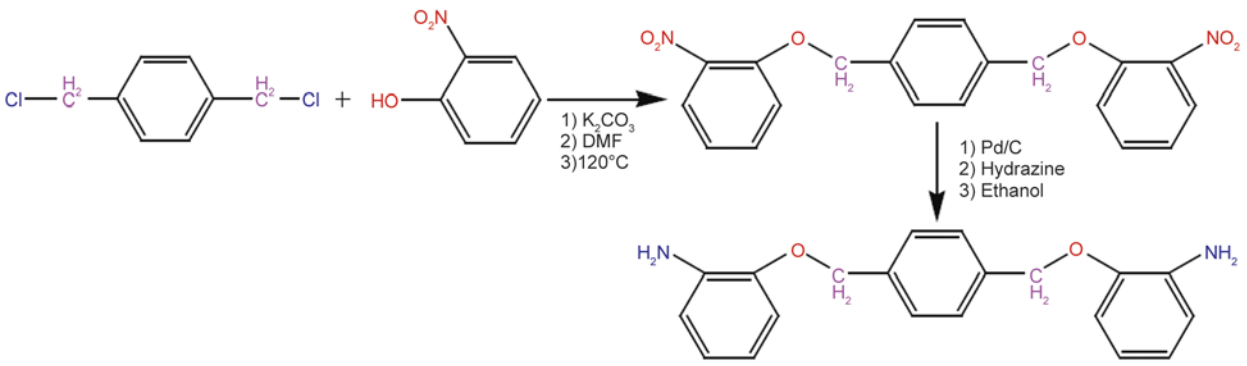

Figure 1. Scheme for synthesis of 2APX

DMF. The resulting mixture was heated at 120°C for 16 hrs. The color of solution was changed from yellow to dark brown. It was then cooled to room temperature and poured into 800 mL of ice cold water. Light yellow precipitates were formed which were filtered, washed with ethanol and dried. The yield of reaction was found to be 78% and melting point of the product determined was 165°C.

2.3.2. Synthesis of α,α′-bis(2-aminophenoxy)-p-xylene (2APX)

For the synthesis of 2APX, 3.0 g of the obtained dinitro compound (2NPX) (7.89 mmol), 0.10 g of 5% Pd/C and 50 mL ethanol were introduced in a two neck round-bottom flask, to which 10 mL of hydrazine monohydrate was added dropwise. After the addition was complete, the reaction was continued at reflux temperature for 12 hrs. Then the mixture was filtered in hot form to remove Pd/C and solvent was rotary evaporated to get the solid product. The crude product was washed with water to remove any trapped hydrazine and finally recrystallized from ethanol. White colored diamine was obtained in 69% yield having melting point at 124°C.

2.4. Synthesis of polyimides

Polyimides were synthesized from diamine 2APX and dianhydrides via a two-step route as shown in Figure 2a. The synthesis of polyimide PMDA-2APX is used as an example to illustrate the general synthetic procedure: a 50 mL two neck round-bottom flask (prebaked on vacuum to exclude any moisture) was charged with 0.320 g of 2APX (1 mmol) and 4 mL DMF. After the complete dissolution of diamine, 0.218 g of PMDA (1 mmol) was added to this solution by dissolving it in 4 mL DMF. The mixture was allowed to stir at room temperature under the inert atmosphere of nitrogen for 24 hrs. The resulting poly(amic acid) solution was thermally imidized by casting it on a clean glass plate followed by curing with a programmed procedure in a vacuum oven: 18 hrs. at 80°C, 1 hr at 150°C, 1 hr at 200°C, 1 hr at 250°C and 2 hrs at 300°C to produce a fully imidized polyimide. Similarly, 2APX was condensed with 3,3′,4,4′-benzophenone tetracarboxylic dianhydride (BTDA), oxydiphthalic anhydride (ODPA) and 2,2-bis(3,4-dicarboxyphenyl) hexafluoropropane dianhydride (6FDA) for the preparation of BTDA-2APX, ODPA-2APX and 6FDA-2APX polyimides.

2.5. Synthesis of poly(imide siloxane) copolymers

The poly(imide siloxane) copolymers were synthesized by one-step condensation polymerization reactions of equimolar amounts of diamine 2APX and different dianhydrides in the presence of aminopropyl terminated polydimethyl siloxane (PDMS). The synthesis of PMDA-2APX-PDMS is presented as an example to describe the synthetic procedure: a 50 mL two neck round-bottom flask (prebaked on vacuum to exclude any moisture) equipped with nitrogen tube, reflux condenser, magnetic stirrer and Dean-Stark trap was charged with 0.218 g of PMDA (1 mmol) and 3 mL of NMP/THF (1:1) mixture. Then 0.250 g of PDMS (0.1 mmol) dissolved in 2 mL of THF was added slowly to the dianhydride solution. After stirring the mixture for 1 hr, 0.288 g of 2APX (0.9 mmol) dissolved in 2 mL NMP was added and allowed to stir at room temperature for 16 hrs. The resulting poly(amic acid) solution was imidized by heating in a mixture of toluene/NMP (2:5) at reflux temperature for 8 hrs. The toluene was distilled off under vacuum, the solution was cooled to room temperature and poured in a large quantity of water to give a rubbery material, which was filtered and dried in vacuum oven at 80°C for 24 hrs. In the same way BTDA-2APX-PDMS, ODPA-2APX-PDMS and 6FDA-2APX-PDMS copolyimides were synthesized by using BTDA, ODPA and 6FDA respectively according to Figure 2b.

3. Results and discussion

3.1. Synthesis and characterization of monomer

The ether-based diamine α,α′-bis(2-aminophenoxy)-p-xylene (2APX) was synthesized via a two-step approach according to scheme shown in Figure 1. Firstly, dinitro compound α,α′-bis(2-nitrophenoxy)-p-xylene (2NPX) was synthesized by the Williamson's etherification of 2-nitrophenol with 1,4-bis(chloromethyl)benzene in dimethylformamide catalysed by anhydrous potassium carbonate. Then the 2NPX was reduced to corresponding diamine 2APX with hydrazine monohydrate and Pd/C in ethanol. The structures of 2NPX and 2APX were confirmed by FTIR, ^{1}H NMR, ^{13}C NMR spectroscopic studies, elemental and single crystal X-ray analysis. Data obtained from these techniques is presented in Table 1. The FTIR spectrum of 2NPX

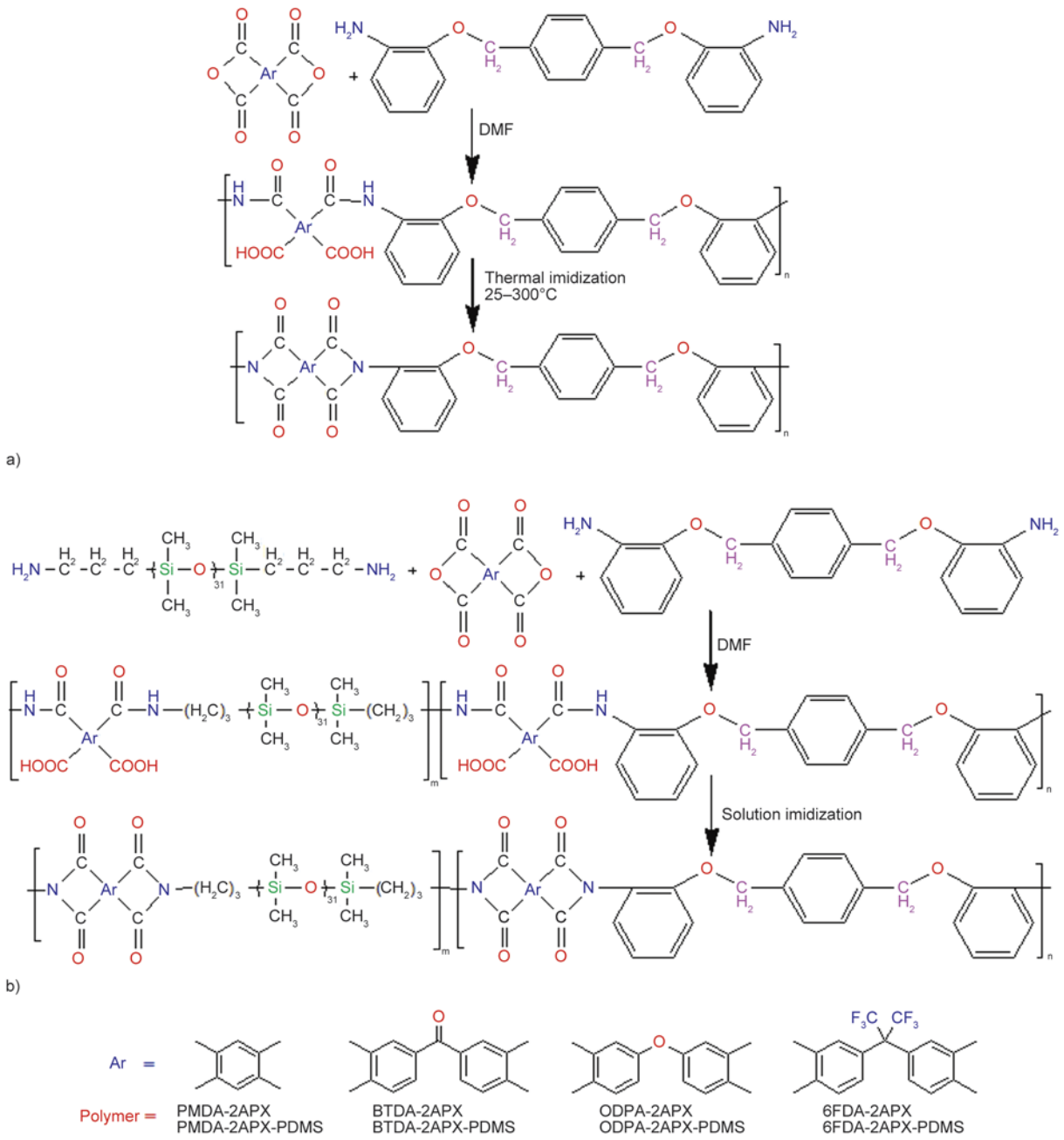

Figure 2. Scheme for synthesis of polyimides (a) and poly(imide siloxane) copolymers (b)

Table 1. FTIR, NMR and elemental analysis data of 2NPX and 2APX

Technique	2NPX	2APX
FTIR	3114 (Ar–H), 2879 (CH_2), 1580 (NO_2 asym), 1342 (NO_2 sym), 1253 (C–O–C)	3460, 3435 (NH_2), 3056 (Ar–H), 2865 (CH_2), 1275 (C–O–C)
^{1}H NMR	7.90 (1H, m, H^3), 7.68–7.63 (1H, m, H^5), 7.50–7.44 (3H, m, H^4, H^9,$H^{9'}$), 7.16–7.11 (1H, m, H^6), 5.33 (2H, s, $H^{7,7'}$)	7.51 (2H, s, H^9,$H^{9'}$), 6.89–6.86 (1H, m, H^4), 6.70–6.68 (2H, m, H^5,H^6), 6.55–6.49 (1H, m, H^3), 5.09 (2H, s, $H^{7,7'}$), 4.74 (2H, s, –NH_2)
^{13}C NMR	151.2 (C_1), 140.2 (C_8), 136.3 (C_5), 135.2 (C_2), 128.7 (C_9), 125.5 (C_3), 121.3 (C_4), 116.4 (C_6), 70.50 (C_7)	145.7 (C_1), 138.4 (C_8), 137.4 (C_2), 128.2 (C_9), 121.6 (C_4), 116.6 (C_5), 114.6 (C_3), 112.6 (C_6), 69.5 (C_7)
Elemental	% Calcd: C = 63.16, H = 4.21, N = 7.37 % found: C = 62.93, H = 4.18, N = 7.25	% Calcd: C = 75.00, H = 6.25, N = 8.75 % found: C = 74.60, H = 6.35, N = 8.50

displayed the characteristic absorption bands of ether linkage (C–O–C) at 1253 cm^{-1} and nitro functionality (NO_2) at 1580 and 1342 cm^{-1} corresponding to asymmetric and symmetric stretches respectively. The reduction of 2NPX to 2APX was confirmed by disappearance of NO_2 absorptions and

advent of typical N–H stretching bands for primary amines at 3460 and 3435 cm^{-1} in the FTIR spectrum of 2APX. Structures of 2NPX and 2APX were also elucidated by ^{1}H NMR spectroscopic technique. Phenyl protons were verified by the appearance of signals in the characteristic region between 6–8 ppm according to substituents attached. The protons of aromatic ring at ortho and para positions of nitro group ($H^{3\&5}$) resonated at the farthest downfield (7.90–7.63 ppm) in the ^{1}H NMR spectrum of 2NPX which is attributed to the deshielding engendered by electron withdrawing effect of NO_2 group. However, in case of 2APX resonance signals for these protons were shifted to upfield region (6.70–6.49 ppm) which is clear evidence in favor of nitro group reduction to amine. Moreover, presence of amine functionality in the structure of 2APX was also certified by the advent of two protons singlet at 4.74 ppm in the ^{1}H NMR spectrum as shown in Figure 3a. Appearance of two protons singlets at 5.33 and 5.09 ppm for 2NPX and 2APX respectively due to methylene protons (H^{7}) proves the formation of ether linkage. ^{13}C NMR spectroscopic study also supported the structures of compounds as the characteristic signals for all the carbon atoms were observed as shown in ^{13}C NMR spectrum of 2APX presented in Figure 3b. Like the proton NMR, a slight upfield shift observed for carbon atoms at ortho and para positions of NH_2 group ($C_{3\&5}$) in the ^{13}C NMR spectrum of 2APX as compared to 2NPX

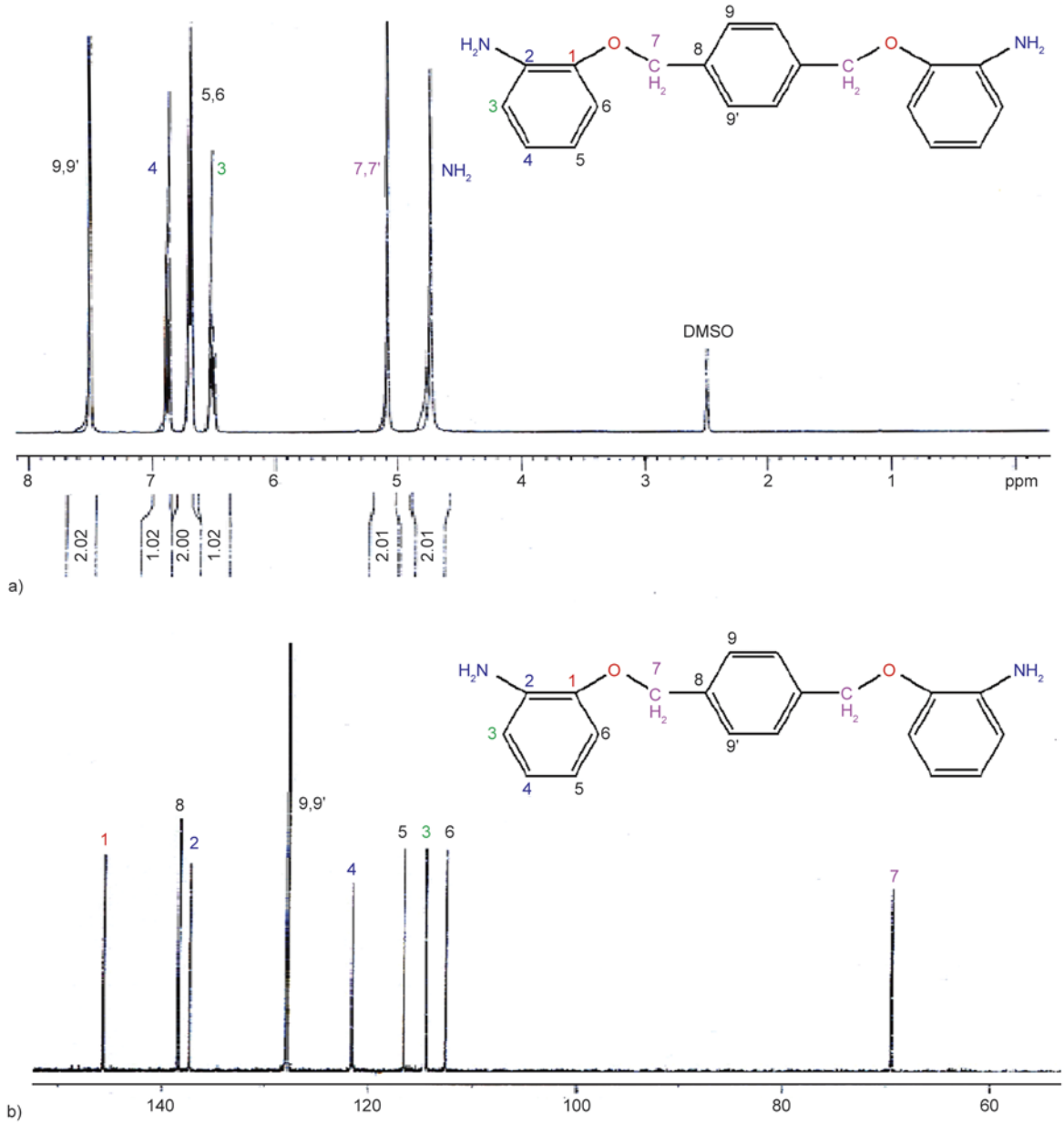

Figure 3. ^{1}H NMR (a) and ^{13}C NMR (b) spectra of 2APX

is attributed to the electron donating effect of amine group. This also supports the successful conversion of NO_2 group to NH_2 moiety. Elemental analysis shows that found and calculated ratios of carbon (C), hydrogen (H) and nitrogen (N) are in good agreement with each other. It also supports the successful synthesis of monomers.

Single crystal X-ray analysis also confirmed the structure of 2NPX and 2APX. Crystals of compounds suitable for single crystal X-ray analysis were developed by slow evaporation of DMSO and ethanol respectively at room temperature to identify their structures. Crystallographic data was collected at 150(2) K on a Bruker Apex II CCD diffractometer using Mo-Kα radiation (α = 0.71073 Å). The structure was solved by direct methods and refined on F^2 using all the reflections [31]. All the non-hydrogen atoms were refined using anisotropic atomic displacement parameters and hydrogen atoms bonded to carbon were inserted at calculated positions using a riding model. The amine hydrogens in 2APX were located from difference maps and their coordinates refined. Parameters for data collection and refinement are summarised in Table 2. The structures of 2NPX and 2APX are shown in Figure 4 and 5 respectively. The dinitro molecule (2NPX) is centrosymmetric having no obvious π-π stacking interactions in the lattice although there are some weak

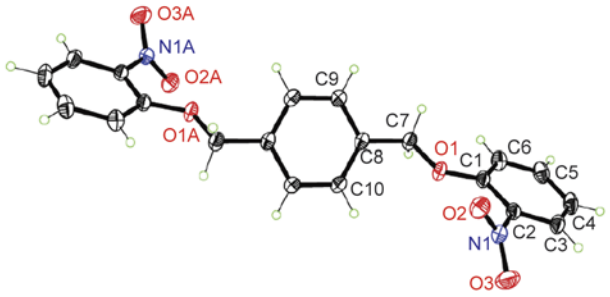

Figure 4. Molecular structure of 2NPX. Non-hydrogen atoms shown with 50% probability ellipsoids. Atoms with suffix 'A' generated by symmetry operation 1-x, 1-y, 1-z.

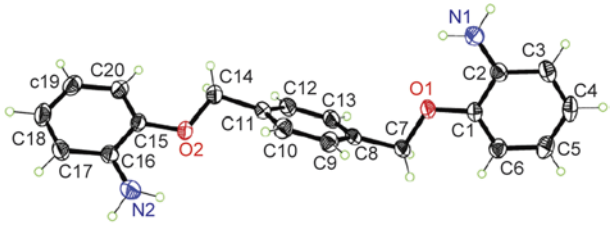

Figure 5. Molecular structure of 2APX. Non-hydrogen atoms shown with 50% probability ellipsoids.

CH····O interactions. The central ring makes an angle of 52.41(5)° with the outer rings. The molecule of 2APX has no internal symmetry since the terminal rings are at different angles to the central phenyl group (78.87(4) and 34.52(4)° for rings containing N1 and N2, respectively). No convincing hydrogen bonding was observed in the structure,

Table 2. Crystal data and structure refinement for 2NPX and 2APX

Parameter	2NPX	2APX
Empirical formula	$C_{20}H_{16}N_2O_6$	$C_{20}H_{20}N_2O_2$
Formula weight	380.35	320.38
Temperature	150(2) K	150(2) K
Wavelength	0.71073 Å	0.71073 Å
Crystal system	Monoclinic	Triclinic
Space group	$P2_1/n$	$P\bar{1}$
Unit cell dimensions	a = 7.4203(4) Å α = 90° b = 11.7771(6) Å β = 90.8180(10)° c = 9.7275(5) Å γ = 90°	a = 8.7516(6) Å α = 64.8160(10)° b = 10.1550(7) Å β = 68.0410(10)° c = 11.0313(8) Å γ = 77.8430(10)°
Volume	850.00(8) Å^3	821.28(10) Å^3
Z	2	2
Density (calculated)	1.486 Mg/m^3	1.296 Mg/m^3
Absorption coefficient	0.112 mm^{-1}	0.084 mm^{-1}
F(000)	396	340
Crystal size	0.37×0.21×0.17 mm^3	0.60×0.24×0.21 mm^3
Crystal description	orange block	colourless rhomb
Theta range for data collection	2.72 to 30.56°	2.15 to 28.34°
Reflections collected	9717	8491
Independent reflections	2583 [R(int) = 0.0224]	4059 [R(int) = 0.0196]
R [$F^2 > 2\sigma(F^2)$]	0.042	0.043
$wR(F^2)$	0.119	0.113
GooF	1.06	1.07
CCDC number	1056786	1056787

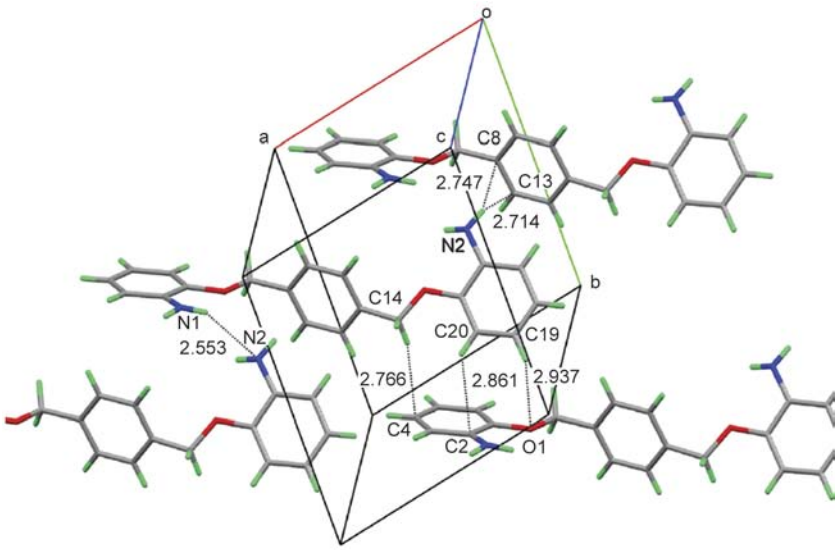

Figure 6. Weak intermolecular interactions in the lattice of 2APX

although there are some NH····π and CH····π interactions as shown in Figure 6 and these seem to be the most significant intermolecular effects.

3.2. Synthesis and characterization of polyimides and copolyimides

The newly designed diamine 2APX was condensed with four commercially available dianhydrides i.e. PMDA, BTDA, ODPA, 6FDA to synthesize simple polyimides. Then this diamine was polymerized with same dianhydrides along with aminopropyl terminated polydimethylsiloxane (PDMS) oligomer of M_n = 2500 to synthesize poly(imide siloxane) copolymers. The synthesis of the polyimides and copolyimides was confirmed by FTIR and ^{1}H-NMR spectroscopic techniques. FTIR spectra of polyimides displayed characteristic absorption bands associated with five membered imide ring around 1780 and 1715 cm^{-1} attributed to asymmetric and symmetric C=O stretches respectively, along with C–N stretching absorptions around 1375 cm^{-1}. The completion of the reaction i.e. conversion of polyamic acid to fully cyclized polyimide was confirmed by disappearance of: carboxyl and NH bands in the region of 3100–3500 cm^{-1} (at the polyamic acid stage) and the appearance of the characteristic absorption bands of the imide ring accompanied by shifting of carbonyl stretching vibrations towards higher frequency i.e. from 1650 to 1715 cm^{-1}. However, polyimide derived from BTDA displayed absorption bands around 1645 cm^{-1} along with typical peaks of imide group even after imidization which is attributed to the presence of ketonic carbonyl moiety in its structure. Similarly appearance of characteristic peaks for siloxane moieties i.e. Si–O–Si and Si–CH_3 around 1080 and 792 cm^{-1} respectively along with typical peaks of imide structure in the FTIR spectra of PDMS containing copolyimides confirmed the synthesis of poly(imide siloxane) copolymers. FTIR data of polyimides and copolyimides is listed in Table 3. Representative FTIR spectra of polyimide PMDA-2APX at poly(amic acid) stage and after imidization are shown in Figure 7.

Table 3. FTIR data of polyimides and copolyimides

Polymer	Before imidization		After imidization					
	OH, NH	C=O (amide)	OH, NH	C=O (imide)	C–N (imide)	Si–O–Si	Si–CH_3	CH_3
PMDA-2APX	3524	1627	–	1704, 1779	1349	–	–	–
PMDA-2APX-PDMS	3435	1643	–	1722, 1778	1376	1088	792	2961
BTDA-2APX	3432	1655	–	1716, 1779	1373	–	–	–
BTDA-2APX-PDMS	3446	1652	–	1717, 1780	1378	1087	794	2961
ODPA-2APX	3465	1660	–	1715, 1777	1374	–	–	–
ODPA-2APX-PDMS	3462	1637	–	1717, 1780	1377	1078	792	2961
6FDA-2APX	3496	1655	–	1716, 1786	1378	–	–	–
6FDA-2APX-PDMS	3458	1648	–	1716, 1785	1380	1094	793	2962

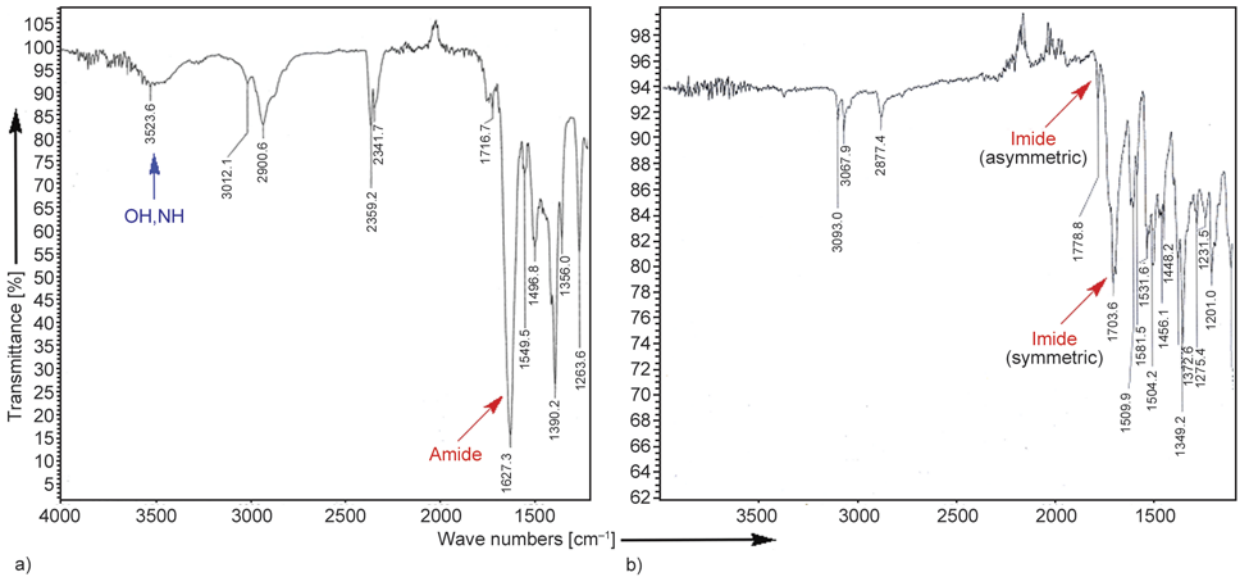

Figure 7. FTIR spectra of PMDA-2APX at poly(amic acid) stage (a) and after imidization (b)

Soluble polymers i.e. 6FDA-2APX, 6FDA-2APX-PDMS and ODPA-2APX-PDMS were also characterized by ^{1}H NMR spectroscopy and data obtained is presented in Table 4. Appearance of characteristic signals of aromatic protons along with methylene protons supported the proposed structures of polymers. Representative ^{1}H NMR spectrum of the 6FDA-2APX with the assignment of protons is shown in Figure 8 which is in complete agreement with the proposed structure of polyimide. In case of

Table 4. ^{1}H NMR data of polymers

Polymer	^{1}H NMR (DMSO-d_6) chemical shifts in ppm					
	Ar–H	O–CH_2	CH_2			Si–CH_3
			H^{10}	H^{11}	H^{12}	
6FDA-2APX	8.38–7.03 (9H, m, $H^{1,2,3,4,5,6,7,9,9'}$)	5.08	–	–	–	–
6FDA-2APX-PDMS	8.43–7.18 (9H, m, $H^{1,2,3,4,5,6,7,9,9'}$)	5.23	3.58	1.60	0.47	–0.001
ODPA-2APX-PDMS	8.16–7.35 (9H, m, $H^{1,2,3,4,5,6,7,9,9'}$)	5.12	3.62	1.59	0.48	–0.053

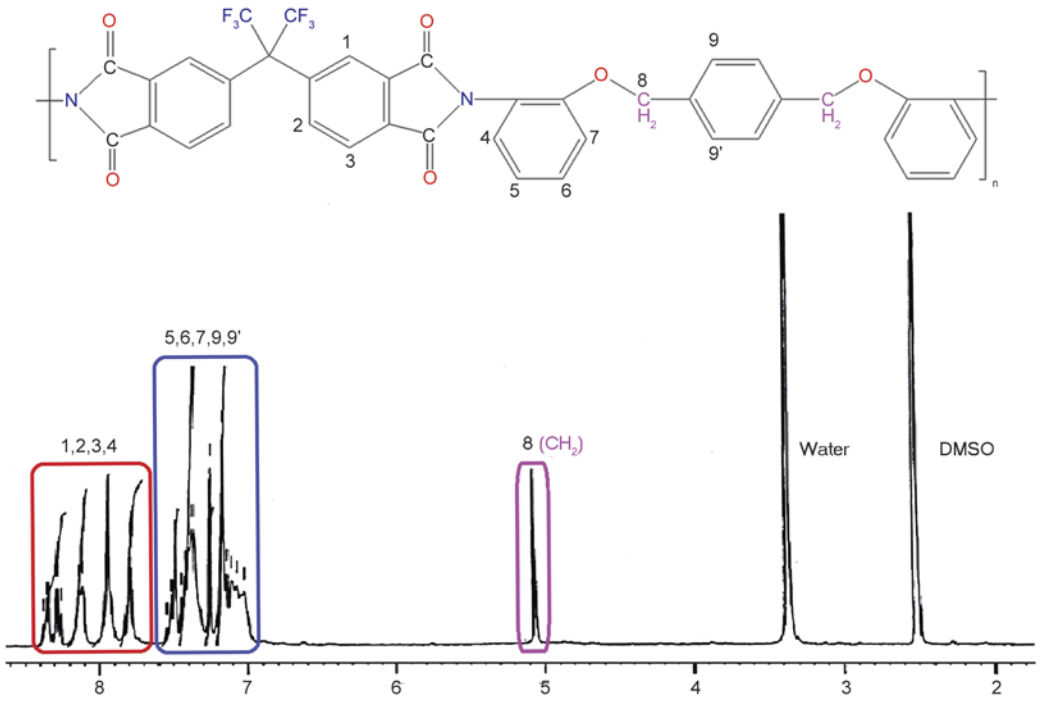

Figure 8. ^{1}H NMR Spectrum of 6FDA-2APX

6FDA-2APX, resonance signals in the range of 8.38–7.74 ppm are assigned to the phenyl protons of dianhydride segment i.e. H^1, H^2 and H^3 in the polymer chain. This downfield shift is attributed to electron withdrawing nature of carbonyl groups present in it. Aromatic protons of the diamine fragment appeared slightly upfield between 7.48–7.03 ppm. Two proton singlet signal present at 5.08 ppm in spectrum is ascribed to methylene group present in structure inherited from diamine. The disappearance of signals for amine protons and downfield shift observed for phenyl proton adjacent to $–NH_2$ functionality (H^3 in diamine and H^4 in polymer) from 6.52 to 7.74 ppm (owing to electron withdrawing effect of dianhydride segment) as compared to ^{1}H NMR spectrum of 2APX, validated the establishment of imide linkage from amine and dianhydride. Moreover, imidization of poly(amic acid) was also confirmed by the fact that ^{1}H NMR spectra of polymer showed no signals in the characteristic region of amide protons i.e. between 9–11 ppm. In addition to aforementioned peaks, ^{1}H NMR spectra of 6FDA-2APX-PDMS and ODPA-2APX-PDMS displayed resonance signals around 3.60, 1.60, 0.47 and 0.00 ppm which are characteristic peaks for: methylene protons adjacent to imide ring (H^{10}), central methylene of propyl (H^{11}), methylene next to Si (H^{12}) and methyl protons adjacent to Si (H^{13}) respectively. These signals suggest that aminopropyl terminated polydimethylsiloxane (PDMS) segments have been incorporated successfully into the polyimide chain.

3.3. Organosolubility of polymers

The solubility of polymers was tested quantitatively (0.1 g/5 mL) in organic solvents like DMSO, DMF, DMAc, NMP and also in H_2SO_4. It was found that the simple polyimides except that synthesized from 4,4′-(hexafluoroisopropylidene) diphthalic anhydride i.e. 6FDA-2APX were insoluble in these solvents. This is attributed to ultra-strong intermolecular interactions and good packing ability of the polymer chains which suggests their semi-crystalline behavior and it is also proved by their WAXRD analysis. Under normal circumstances, intermolecular interactions in the polyimide chains occur between electron-donating diamine segments and electron-withdrawing dianhydride moieties in the polymer chain. But in case of polyimides under discussion, in addition to these interactions, there are some other intermolecular effects responsible for enhancing chain packing ability. Luckily, we got the single crystal of 2APX and it was observed during X-ray analysis that CH$\cdots\pi$ interactions are present between the 2APX molecules as shown in Figure 6. Therefore, polyimides synthesized from this diamine displayed insolubility in spite of having ether linkage in their structure. Moreover, the existence of a large number of benzene rings in polymer backbone without bulky side groups tremendously improved the structure regularity and consequently reduced the solubility. The solubility of 6FDA-2APX is attributed to steric hindrance of bulky CF_3 groups. These groups increased the disorder in the chains and hindered compact chain stacking thus reducing the chain-chain interactions. This resulted in increase of free volume and consequently better penetration of solvent molecules into the polymer chains that enhanced solubility. However, solubility of other polyimides was improved by the incorporation of flexible PDMS segment in the backbone as it reduced the packing ability of polymer chains. Solubility data of simple polyimides and poly(imide siloxane) copolymers is given in Table 5 and results show that polyimides which were insoluble, have shown partial solubility after copolymerization. Also the polyimide ODPA-2APX which was partially soluble before copolymerization, completely

Table 5. Solubility data of polymers

Polymer	DMSO	DMF	DMAc	NMP	H_2SO_4
PMDA-2APX	–	–	–	–	+
PMDA-2APX-PDMS	+	+	+	+	++
BTDA-2APX	–	–	–	–	+
BTDA-2APX-PDMS	+	+	+	+	++
ODPA-2APX	+	+	+	+	+
ODPA-2APX-PDMS	++	++	++	++	++
6FDA-2APX	++	++	++	++	++
6FDA-2APX-PDMS	++	++	++	++	++

++: (soluble on heating), +: (slightly soluble on heating), −: (insoluble)

solubilized after introduction of flexible PDMS segment in the backbone. This improvement in solubility of copolyimides was expected as reported in literature [32, 33].

3.4. Wide angle X-ray diffraction analysis (WAXRD)

The crystallinity of the polyimides and copolyimides was examined by wide angle X-ray diffraction analysis with 3040/60 X'Pert PRO diffractometer in the region of 2θ = 5–50° at room temperature using the polyimide powder obtained as samples. WAXRD diffractograms shown in Figure 9 illustrate the semi-crystalline nature of polyimides and almost amorphous morphology of copolymers. Among the polyimides, the least crystalline behavior was observed for 6FDA-2APX which is attributed to reduction in chain packing efficiency due to bulky CF_3 groups. Incorporation of flexible PDMS segment led to decline in crystallinity of polyimides as it discouraged the chain symmetry thus making it harder for them to pack into the crystal lattice hence reveals a large decrease in crystallinity [34]. These results also support the observed insolubility of polyimides and partial solubility of copolyimides as the amorphous nature of the resulting polymers endows them a good solubility [35].

3.5. Thermal properties of polymers

The thermal properties of the polyimides were evaluated by means of TGA. It was observed that copolyimides are thermally less stable as compared to corresponding polyimides. The temperature at 10% weight loss (T_{10}), an important criterion for evaluation of thermal stability was in the range of 386–405°C for polyimides while for poly(imide siloxane) copolymers, it ranged between 368–403°C. Temperature range of maximum weight loss (T_{max}) was 523–570°C and 483-525°C for polyimides and copolyimides respectively. Residual mass (wt%) at 800°C (R_{800}) was also measured and found between 47–52% for polyimides and 31–39% for siloxane-containing copolyimides. This decrease in thermal stability of coployimides is ascribed to the presence of thermally less stable aliphatic portion in the form of PDMS within the copolymer backbone. Representative thermograms of polyimide ODPA-2APX and copolyimide ODPA-2APX-PDMS are shown in Figure 10. Thermal stability data for polyimides and copolyimides is listed in the Table 6 and results reveal that these polymers exhibit good thermal stability with a slight weight loss up to 400°C. This could be attributed to phenylation of the backbone and formation of imide units in the structure of polymers.

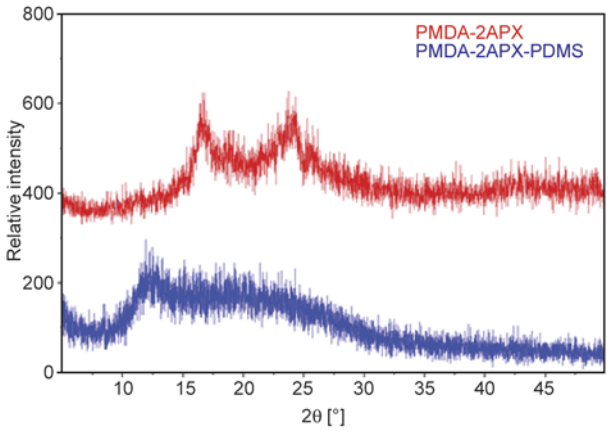

Figure 9. WAXRD diffractograms of polyimides and copolyimides

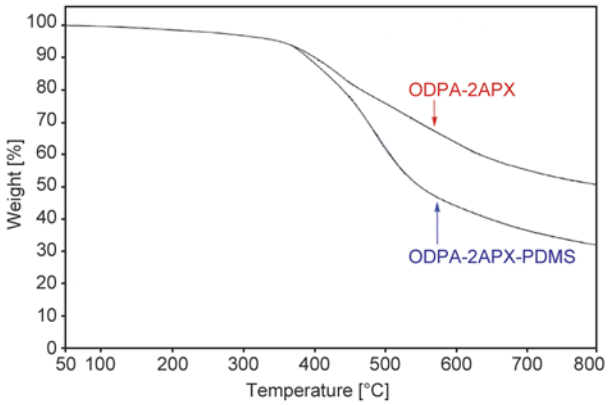

Figure 10. Thermograms of ODPA-2APX and ODPA-2APX-PDMS

Table 6. Thermal analysis data of polymers

Polymer	T_{10} [°C][a]	T_{max} [°C][b]	R_{800} [°C][c]
PMDA-2APX	395	565	48
PMDA-2APX-PDMS	386	525	34
BTDA-2APX	405	570	51
BTDA-2APX-PDMS	403	515	39
ODPA-2APX	400	540	52
ODPA-2APX-PDMS	390	495	32
6FDA-2APX	386	523	47
6FDA-2APX-PDMS	368	483	31

[a]temperature at 10% weight loss
[b]temperature at which maximum degradation occurs
[c]residual mass (wt%) at 800°C

3.6. Viscometric analysis

The inherent viscosities of the soluble polyimides and copolyimides synthesized were determined by

Table 7. Viscometric and light scattering data

Polymer	η_{inh} [dL/g]	M_w [g/mole]	R_g [nm]
6FDA-2APX	0.29	3.52×10^5	53
6FDA-2APX-PDMS	0.11	8.48×10^5	85
ODPA-2APX-PDMS	0.15	3.29×10^6	78

d*n*/d*c* = 0.165 mL/g
Relative errors: M_w = ±5%, R_g = ±5%

dissolving 0.2 g/dL of sample in DMSO at 25°C using Ubbelohde's Viscometer and data obtained is given in Table 7. Inherent viscosity of polymer 6FDA-2APX was found to be 0.29 dL/g. Since the inherent viscosity is a good criterion for estimation of molecular weight, hence polyimide 6FDA-2APX is expected to show reasonable molecular weight. This supposition was supported by laser light scattering analysis as molecular weight of 3.52×10^5 was determined. The η_{inh} was declined to 0.11 dL/g for copolyimide 6FDA-2APX-PDMS as incorporation of PDMS segment, decreased the rigidity and stiffness of polymer chains owing to its flexible nature. The inherent viscosities of 0.11 and 0.15 dL/g are reasonable for this kind of copolymers as reported in the literature [36].

3.7. Laser light scattering analysis

Molecular weights of polymers were determined using static laser light scattering (SLLS) analysis technique by dissolving 0.8 g/dL of sample in DMSO. SLLS measures light intensity as a function of scattering angle and solute concentration and the relationship between the light scattering from a dilute polymer solution and the weight-average molecular weight can be described by the Zimm formalism. This allows the determination of weight-average molecular weight, radius of gyration and shape information of the solute [37]. The results revealed that copolyimide 6FDA-2APX-PDMS have higher molecular weight than corresponding polyimides (6FDA-2APX). This increase in weight is understandable as high molecular weight PDMS segment (M_n = 2500) is introduced in the polymer chain. Moreover, incorporation of PDMS segment imparts flexibility to chain, hence it can grow to a longer length and consequently molecular weight of polymer increases. Like the molecular weight (M_w), radius of gyration (R_g) of copolymers is also longer than simple polymers, which is again attributed to reduction in chain rigidity by PDMS. These results of molecular weight suggest that synthesized diamine has good tendency to react with dianhydrides. Results obtained from viscometric and laser light scattering of polymers are listed in Table 7 and representative Zimm plot for ODPA-2APX-PDMS is shown in Figure 11.

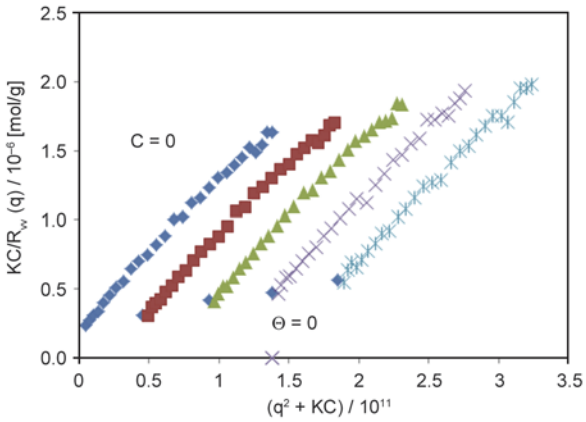

Figure 11. Zimm plot for ODPA-2APX-PDMS at 20°C

4. Conclusions

Polyimides and poly(imide siloxane) copolymers were synthesized successfully from newly designed diamine monomer 2APX. The structures of diamine and polymers were verified by different techniques. The main objective of the research was to study the properties of polyimides derived from diamine having amino group at ortho position with respect to ether linkage and monitor the influence of aminopropyl terminated polydimethylsiloxane (PDMS) segment on properties of the parent polyimides. In this regard main emphasis was on solubility, crystallinity, thermal stability, viscosity and molecular weight of polymers. Polyimides, except that synthesized from 6FDA, were insoluble in organic solvents, however their solubility was improved after incorporation of siloxane units in the polymer chains. WAXRD pattern showed that polyimides are semi-crystalline in nature that was decreased in case of copolyimides. Comparison of data obtained from the thermal study of these polymers showed that poly(imide siloxane) copolymers are thermally less stable than corresponding polyimides. Viscometric analysis revealed that siloxane-containing polyimides are less viscous than simple polymers. Finally, high molecular weight polymers were synthesized successfully by introduction of PDMS segment in the backbone of polymer chain. The observed behavior of polymers suggests that the synthesized polyimides can be used as high temperature and solvent

resistant materials for applications under severe conditions where excellent thermal stability and resistivity is desired. However poly(imide siloxane) copolymers can be used in applications where improved processability is of prime importance while sacrificing some of thermal stability.

Supplementary Data

CCDC 1056786 and 1056787 contain the supplementary crystallographic data for this paper. These data can be obtained free of charge from The Cambridge Crystallographic Data Centre via
www.ccdc.cam.ac.uk/data_request/cif.

Acknowledgements

The author would like to acknowledge the Higher Education Commission of Pakistan for providing financial support under Indigenous 5000 Ph.D. Fellowship Program (Phase II). The financial support from University Research Funds (URF) is also greatly acknowledged.

References

[1] García J. M., García F. C., Serna F., de la Peña J. L.: High-performance aromatic polyamides. Progress in Polymer Science, **35**, 623–686 (2010).
DOI: 10.1016/j.progpolymsci.2009.09.002

[2] Gao Y., Zhou Y., He M., Wang H., Cui Y., Zhang T.: Synthesis and characterization of fluorinated polyimides derived from 1,4-bis-[4-amino-2-(trifluoromethyl)-phenoxy] benzene/tetrafluoride benzene. Designed Monomers and Polymers, **17**, 590–600 (2014).
DOI: 10.1080/15685551.2014.907615

[3] Kim S. D., Lee S., Heo J., Kim S. Y., Chung I. S.: Soluble polyimides with trifluoromethyl pendent groups. Polymer, **54**, 5648–5654 (2013).
DOI: 10.1016/j.polymer.2013.08.057

[4] Dodda J. M., Kovářík T., Kadlec J., Kullová L.: Preparation, characterization and thermal degradation study of poly(amide imide)s based on tri-component mixture of PMDA/BTDA, diamines and acid chloride. Polymer Degradation and Stability, **98**, 2306–2316 (2013).
DOI: 10.1016/j.polymdegradstab.2013.08.010

[5] Banihashemi A., Atabaki F.: Synthesis and characterization of new thermally stable polybenzimidazoles and poly(amide-benzimidazole)s. European Polymer Journal, **38**, 2119–2124 (2002).
DOI: 10.1016/S0014-3057(02)00081-2

[6] Banihashemi A., Akhlaghinia B.: New heat stable polyethers, polyketones and polysulfones. Macromolecular Chemistry and Physics, **200**, 2284–2293 (1999).
DOI: 10.1002/(SICI)1521-3935(19991001)200:10<2284::AID-MACP2284>3.0.CO;2-X

[7] Honkhambe P. N., Bhairamadgi N. S., Biyani M. V., Wadgaonkar P. P., Salunkhe M. M.: Synthesis and characterization of new aromatic polyesters containing cardo decahydronaphthalene groups. European Polymer Journal, **46**, 709–718 (2010).
DOI: 10.1016/j.eurpolymj.2009.12.028

[8] Liaw D-J., Wang K-L., Huang Y-C., Lee K-R., Lai J-Y., Ha C-S.: Advanced polyimide materials: Syntheses, physical properties and applications. Progress in Polymer Science, **37**, 907–974 (2012).
DOI: 10.1016/j.progpolymsci.2012.02.005

[9] Mathews A. S., Kim I., Ha C-S.: Synthesis, characterization, and properties of fully aliphatic polyimides and their derivatives for microelectronics and optoelectronics applications. Macromolecular Research, **15**, 114–128 (2007).
DOI: 10.1007/BF03218762

[10] Tao L., Yang H., Liu J., Fan L., Yang S.: Synthesis and characterization of highly optical transparent and low dielectric constant fluorinated polyimides. Polymer, **50**, 6009–6018 (2009).
DOI: 10.1016/j.polymer.2009.10.022

[11] Zhai L., Yang S., Fan L.: Preparation and characterization of highly transparent and colorless semi-aromatic polyimide films derived from alicyclic dianhydride and aromatic diamines. Polymer, **53**, 3529–3539 (2012).
DOI: 10.1016/j.polymer.2012.05.047

[12] Chen J-C., Wu J-A., Li S-W., Chou S-C.: Highly phenylated polyimides containing 4,4′-diphenylether moiety. Reactive and Functional Polymers, **78**, 23–31 (2014).
DOI: 10.1016/j.reactfunctpolym.2014.02.010

[13] Huang M., Wang L., Li X., Yan S., Yeung K. W., Chu P. K., Xu Z., Yi C.: Design and preparation of novel fluorescent polyimides containing *ortho*-linked units and pyridine moieties. Designed Monomers and Polymers, **15**, 389–404 (2012).
DOI: 10.1080/1385772X.2012.686691

[14] Zhang K., Niu H., Wang C., Bai X., Lian Y., Wang W.: Novel aromatic polyimides with pendent triphenylamine units: Synthesis, photophysical, electrochromic properties. Journal of Electroanalytical Chemistry, **682**, 101–109 (2012).
DOI: 10.1016/j.jelechem.2012.06.018

[15] Wang C., Chen W., Chen Y., Zhao X., Li J., Ren Q.: New fluorinated poly(ether sulfone imide)s with high thermal stability and low dielectric constant. Materials Chemistry and Physics, **143**, 773–778 (2014).
DOI: 10.1016/j.matchemphys.2013.10.012

[16] Liu J., Zhang Q., Xia Q., Dong J., Xu Q.: Synthesis, characterization and properties of polyimides derived from a symmetrical diamine containing bis-benzimidazole rings. Polymer Degradation and Stability, **97**, 987–994 (2012).
DOI: 10.1016/j.polymdegradstab.2012.03.010

[17] Wu J., Yang S., Gao S., Hu A., Liu J., Fan L.: Preparation, morphology and properties of nano-sized Al_2O_3/polyimide hybrid films. European Polymer Journal, **41**, 73–81 (2005).
DOI: 10.1016/j.eurpolymj.2004.08.014

[18] Deligöz H., Vatansever S., Öksüzömer F., Koç S. N., Özgümüş S., Gürkaynak M. A.: Synthesis and characterization of sulfonated homo- and *co*-polyimides based on 2,4 and 2,5-diaminobenzenesulfonic acid for proton exchange membranes. Polymers for Advanced Technologies, **19**, 1792–1802 (2008).
DOI: 10.1002/pat.1196

[19] Yang C-P., Yang H-W.: Preparation and characterization of organosoluble copolyimides based on a pair of commercial aromatic dianhydride and one aromatic diamine, 1,4-bis(4-aminophenoxy)-2-*tert*-butylbenzene, series. Journal of Applied Polymer Science, **75**, 87–95 (2000).
DOI: 10.1002/(SICI)1097-4628(20000103)75:1<87::AID-APP10>3.0.CO;2-R

[20] Yang C-P., Chen R-S.: Preparation and characterization of organosoluble copolyimides based on a pair of commercial aromatic dianhydride and one aromatic diamine, 1,2-bis(4-aminophenoxy)-4-*tert*-butylbenzene, series. Colloid and Polymer Science, **279**, 736–744 (2001).
DOI: 10.1007/s003960000479

[21] Feng L., Iroh J. O.: Polyimide-*b*-polysiloxane copolymers: Synthesis and properties. Journal of Inorganic and Organometallic Polymers and Materials, **23**, 477–488 (2013).
DOI: 10.1007/s10904-012-9795-4

[22] Adhikari R., Dao B., Hodgkin J., Mardel J.: Synthesis, structures and membrane properties of siloxane-imide co-polymers produced by aqueous polymerization. European Polymer Journal, **47**, 1328–1337 (2011)
DOI: 10.1016/j.eurpolymj.2011.02.018

[23] Ghosh A., Banerjee S.: Synthesis, characterization, and comparison of properties of novel fluorinated poly (imide siloxane) copolymers. Journal of Applied Polymer Science, **107**, 1831–1841 (2008).
DOI: 10.1002/app.27241

[24] Ghosh A., Banerjee S.: Thermal, mechanical, and dielectric properties of novel fluorinated copoly(imide siloxane)s. Journal of Applied Polymer Science, **109**, 2329–2340 (2008).
DOI: 10.1002/app.28298

[25] Ghosh A., Banerjee S., Häußler L., Voit B.: New fluorinated poly(imide siloxane) random and block copolymers with variation of siloxane loading. Journal of Macromolecular Science Part A: Pure and Applied Chemistry, **47**, 671–680 (2010).
DOI: 10.1080/10601325.2010.483364

[26] Ghosh A., Sen S. K., Dasgupta B., Banerjee S., Voit B.: Synthesis, characterization and gas transport properties of new poly(imide siloxane) copolymers from 4,4′-(4,4′-isopropylidenediphenoxy)bis(phthalic anhydride). Journal of Membrane Science, **364**, 211–218 (2010).
DOI: 10.1016/j.memsci.2010.08.015

[27] Kang J. H., Cho K., Park C. E.: Adhesion strength of poly(imide-siloxane) with Alloy 42 lead frame and silicon dioxide. Polymer, **42**, 2513–2520 (2001).
DOI: 10.1016/S0032-3861(00)00548-6

[28] Othman M. B. H., Ramli M. R., Tyng L. Y., Ahmad Z., Akil H. M.: Dielectric constant and refractive index of poly (siloxane–imide) block copolymer. Materials and Design, **32**, 3173–3182 (2011).
DOI: 10.1016/j.matdes.2011.02.048

[29] Ku C-K., Ho C-H., Chen T-S., Lee Y-D.: Synthesis and characterization of pyridine-containing poly(imide-siloxane)s and their adhesion to copper foil. Journal of Applied Polymer Science, **104**, 2561–2568 (2007).
DOI: 10.1002/app.24719

[30] Perrin D. D., Armarego W. L. F., Perrin D. R.: Purification of laboratory chemicals. Pergamon, Oxford (1988).

[31] Sheldrick G. M.: Crystal structure refinement with SHELXL. Acta Crystallographica Section C, **71**, 3–8, 2015.
DOI: 10.1107/S2053229614024218

[32] Simionescu M., Marcu M., Cazacu M.: New poly(amide-imide) siloxane copolymers by polycondensation. European Polymer Journal, **39**, 777–784 (2003).
DOI: 10.1016/S0014-3057(02)00290-2

[33] Hamciuc E., Hamciuc C., Cazacu M., Ignat M., Zarnescu G.: Polyimide–polydimethylsiloxane copolymers containing nitrile groups. European Polymer Journal, **45**, 182–190 (2009).
DOI: 10.1016/j.eurpolymj.2008.10.028

[34] Ma T., Zhang S., Li Y., Yang F., Gong C., Zhao J.: Synthesis and characterization of novel polyimides derived from 4-phenyl-2, 6-bis [3-(4-aminophenoxy)-phenyl]-pyridine diamine and aromatic dianhydrides. Polymer Degradation and Stability, **95**, 1244–1250 (2010).
DOI: 10.1016/j.polymdegradstab.2010.03.026

[35] Bu Q., Zhang S., Li H., Li Y., Gong C., Yang F.: Preparation and properties of thermally stable polyimides derived from asymmetric trifluoromethylated aromatic diamines and various dianhydrides. Polymer Degradation and Stability, **96**, 1911–1918 (2011).
DOI: 10.1016/j.polymdegradstab.2011.07.003

[36] Simionescu M., Marcu M., Cazacu M., Racleş C.: Poly(siloxaneimide)s 2. Polycondensation of some imidic diacid chlorides with aminoalkylsiloxanes. European Polymer Journal, **38**, 229–233 (2002).
DOI: 10.1016/S0014-3057(01)00184-7

[37] Khan M. S. U., Akhter Z., Naz T., Bhatti A. S., Siddiqi H. M., Siddiq M., Khan A.: Study on the preparation and properties of novel block copolymeric materials based on structurally modified organometallic as well as organic polyamides and polydimethylsiloxane. Polymer International, **62**, 319–334 (2013).
DOI: 10.1002/pi.4305

eXPRESS Polymer Letters Vol.9, No.11 (2015) 1015–1026
Available online at www.expresspolymlett.com
DOI: 10.3144/expresspolymlett.2015.91

Devulcanization of ground tire rubber: Physical and chemical changes after different microwave exposure times

P. S. Garcia[1], *F. D. B. de Sousa*[1], *J. A. de Lima*[1], *S. A. Cruz*[1], *C. H. Scuracchio*[2*]

[1]Center of Engineering, Modeling and Applied Social Science (CECS), Universidade Federal do ABC (UFABC), Santa Adelia 166, 09210-170 Santo André, SP, Brazil
[2]Materials Engineering Department (DEMa), Universidade Federal de São Carlos (UFSCar), Washington Luís (SP-310), Km 235, 13565-905 São Carlos, SP, Brazil

Received 6 April 2015; accepted in revised form 28 June 2015

Abstract. Microwave devulcanization is known to be a promising and an efficient rubber recycling method which makes possible for the rubber to regain its fluidity, and makes it capable of being remolded and revulcanized. The focus of this work is to understand the physical and chemical changes that occur in the ground tire rubber after different microwave exposure periods. For this purpose chemical, thermal, rheological and morphological analyses were performed on the tire rubber, which contains natural rubber (NR) and styrene-butadiene rubber (SBR) as polymeric material. The results showed that the microwave treatment promoted the breaking of sulfur cross-links and consequently increased the rubber fluidity. However, long periods of exposure led to degradation and modification of some properties. At nanoscale, the deformation of the devulcanized NR domain under stress was observed, and the morphology obtained appears to be a droplet dispersion morphology. The most exposed samples presented only one glass transition temperature, and from this it was concluded that the treatment may have played an important role in the compatibilization of the elastomeric blend. Based on the results, it is required to control the microwave exposure time and polymeric degradation in order to achieve a regenerated rubber with satisfactory properties.

Keywords: *recycling, ground tire rubber, devulcanization, microwaves, degradation*

1. Introduction

The lack of recycling programs for vulcanized elastomers, such as scrap tire rubber, has become an environmental, social and economic problem. The rubber tires in landfills and dumps can create serious problems to the entire municipal solid waste (MSW) management system because of their low degradability and large volume. These scrap tires can also be responsible for the proliferation of mosquitoes and other disease-carrying vectors, besides potential soil contamination due to the presence of stabilizers, plasticizers and of other chemical substances leached from rubber [1, 2]. This situation could also impact the economic sphere due to higher sanitation and health system costs. Furthermore, if the rubbers were reused without incorporating technological solutions, the resulting materials would present low economic benefit, which would result in the depreciation of their final properties [3, 4].

However, there are methods that can be used to obtain recycled materials with enhanced properties, so that the rubber becomes processable and moldable. Once the rubber can flow, it can be revulcanized as the virgin rubber [5] or it can also be incorporated into thermoplastics to produce high toughness materials [6–9]. The technique known as devulcanization is used for regaining this fluidity. It is a physical or chemical method which has the objec-

*Corresponding author, e-mail: carlos.scu@ufscar.br

tive to break the three-dimensional network, such as monosulfide, disulfide, and polysulfide present in the vulcanized rubber [10–12]. However, it should also be noted that the breaking of the main polymer chains might occur, leading to polymer degradation [13, 14].

Regarding devulcanization processes, there are currently many techniques available, such as chemical, thermal, mechanical, thermomechanical, microbial and by irradiation (ultrasound and microwaves) [1, 10–12, 15, 16]. The microwave devulcanization, used in this study, has proved to be an efficient technique. This method enables to apply large amounts of energy rapidly and uniformly to the rubber, without using chemical reagents during the process [17, 18], which makes it an eco-friendly process [19]. The energy used to heat the rubber promotes the breaking of sulfur cross-links [13]. However, nonpolar elastomers, such as tire rubber, are unable to absorb the microwave energy due to their low absorption and scattering, which requires adding some particles to absorb the energy, such as carbon black [13]. This filler is known to absorb electromagnetic radiation through a phenomenon known as Maxwell-Wagner polarization, and the devulcanization process can only be achieved through it [20–22]. According to Pistor *et al*. [23] the greater the presence of carbon black in the rubber, the more uniform and selective will be the devulcanization process.

Some studies have reported the use of microwave devulcanization in different types of elastomers. Zanchet *et al*. [24] noted that the microwave devulcanization enhanced the interfacial adhesion between devulcanized styrene-butadiene rubber (SBR) in a virgin SBR matrix. The results showed that this mixture can be used in automotive profiles obtained by compression molding. Other papers analyzed the influence of the amount of carbon black in the rubber during the microwave devulcanization and concluded that the degree of devulcanization increases as a function of the increase in the amount of carbon black [23, 25]. Paulo *et al*. [26] verified that the microwave devulcanization, using inorganic salts and nitric acid, promoted the breakup of sulfur cross-links and the oxidation in the SBR. Pistor and coworkers [23, 27, 28] evaluated the influence of the microwave devulcanization process in ethylene-propylene-diene (EPDM). As expected, the radiation was able to promote the breakage of the elastomeric three-dimensional network. The authors also noticed that oil and additives present into EPDM influenced directly in the efficiency of the devulcanization process.

Despite the fact that microwave devulcanization is a known method, there are few studies addressing the chemical and physical aspects of the GTR after being exposed to radiation for different periods. Scuracchio and coworkers [13, 29] evaluated only the thermal and rheological aspects of the devulcanized GTR. According to the authors, with the technique, they were able to create a material with properties quite different from the original vulcanized rubber, due to the changes in the tire rubber structure and composition during the treatment.

The present study deals with these issues by proposing an in-depth study to better understand the chemical and physical changes occurred in the GTR structure after the microwave devulcanization process. The results of the chemical, morphological, thermal and rheological analysis were correlated with: (1) microwave exposure periods; (2) structural changes in GTR; (3) and the quantity of each element present in the GTR structure before and after the devulcanization process, such as natural rubber, synthetic rubber, carbon black, oils and additives.

2. Materials and methods

2.1. Materials

GTR from tread layers of truck tires, separated from non elastomeric components (as received), of 60 mesh particle size (about 75%) was supplied by Pirelli Ltda. (Brazil). The real composition of this rubber is unknown; however, the GTR usually contains polyisoprene (natural rubber – NR), synthetic rubber, which may contain styrene-butadiene rubber (SBR) and/or polybutadiene (BR), and other materials added during the tire manufacturing process, such as vulcanization additives, softeners and fillers. Interestingly, carbon black is the most widely used filler [18].

2.2. Recycling of ground tire rubber: Devulcanization process

Vulcanized ground tire rubber (GTRv) samples were recycled by devulcanization using microwaves. This system is comprised of a conventional microwave oven adapted with a motorized speed-control stirring system. It is very similar to the system used by Scuracchio [13, 29]. In this work, the microwave

oven used (Brastemp BMS35) has dimensions of approximately 0.35×0.22×0.34 m. The power of the magnetron was set up at 820 W and 60 g of the sample was put in a 250 mL glass beaker with a stirring speed of 100 rpm. The devulcanization process was conducted using different periods, where GTRv samples were exposed to the microwaves for: 3 min (GTR3); 5 min (GTR5); 6 min (GTR6); and 7 min (GTR7). Then, each sample was homogenized in an open two-roll mill, which was operated at a friction ratio of 1:1.4 with a nip gap of 1 mm. The total mixing time was approximately 10 min for each sample at room temperature. It should be pointed out that all samples were exposed to the same treatment conditions and they were prepared the same way.

2.3. Characterization

In order to characterize the changes in the GTR structure after the devulcanization process, the chemical, thermal, rheological and morphological analysis were carried out.

2.3.1. Chemical analysis

The soluble (sol) and insoluble (gel) fractions of each sample, after the devulcanization process, were determined by Soxhlet extraction, by using toluene (Vetec – 99.5%; RJ, Brazil) as solvent. In the analysis, about 4 g of GTR was immersed in toluene for 6 h at 80°C. After extraction, the samples were dried for 24 h at 80°C to remove the solvent and their masses were measured. The gel content was calculated as the ratio of the dry weight of the samples after extraction to the weight of the samples before extraction.

Attenuated total reflectance Fourier transform infrared (ATR-FTIR) spectroscopy analyses were performed on all the samples to obtain information about chemical modifications on the GTR structure as a result of the devulcanization process. The spectra were recorded on a Perkin Elmer Frontier FTIR (Perkin Elmer, Waltham, MA, USA) with ATR accessory, from 4000 to 700 cm^{-1} at resolution of 4 cm^{-1} over 20 scans.

2.3.2. Thermal analysis

Thermogravimetric (TGA) analyses were conducted to provide information about thermo-oxidative degradation of the samples after devulcanization. The analyses were performed on a TGA Q500 (TA Instruments, New Castle, DE, USA) device. About 10–15 mg of each sample was heated from room temperature to 560°C under nitrogen atmosphere at heating rate of 10°C/min to monitor the weight loss of oil and elastomers. At 560°C, the gas flow was changed to oxygen atmosphere and the samples were heated from 560 to 800°C in order to observe the carbon black degradation.

The glass transition temperatures of each sample were determined by using the differential scanning calorimetry (DSC; Q200, TA Instruments, New Castle, DE, USA). The experiments were performed according to the following program: (A) Initial temperature of 30°C; (B) Cooling: cooling rate of 30°C min^{-1} to –90°C; (C) Heating: heating rate of 30°C min^{-1} to 250°C. The results reported in this work correspond to the heating runs. All DSC curves were normalized according to the sample mass.

2.3.3. Rheological analysis

The rheometric measurements were determined at 190°C in an Oscillating Disk Rheometer (ODR; TechPro Rheotech, RheoTech MDpt, Akron, USA), according to ASTM D-2084-11. ODR was operated at the frequency of 1.67 Hz and 1° arc. This technique was a useful tool to monitor the rubber curing characteristics, as well as to verify the existence of revulcanization at high temperatures after microwave treatment.

The melt-viscosity of the devulcanized materials was measured by using a high pressure capillary rheometer Instron Ceast SR20 (SmartRHEO 2000, Pianezza, TO, Italy) with a capillary die of 1 mm and L/D ratio of 20. Measurements were performed at 190°C over a shear rate range between 300 and 15 000 s^{-1}. The data were corrected according to Rabinowitsch corrections for non-Newtonian behavior, however the Bagley correction was neglected due to the high L/D ratio.

It should be pointed out that both rheological tests were conducted using rubber sheets obtained from the homogenizing and mixing process in the two-roll mill. For the capillary rheometer test, the sheets were cut in small pieces to facilitate their filling in the barrel.

2.3.4. Morphological analysis

The analysis of the surface morphology of the devulcanized samples, after being homogenized in a two-roll mill, was carried out using Scanning Electron Microscopy (SEM; JEOL, JSM-6010LA, Tokyo,

Japan) at an acceleration voltage of 5 kV. Surface sheets were coated with a thin layer of gold to attain some information about the flow behavior of each sample.

Atomic force microscopy (AFM; NX10, Park systems, Suwon, Korea) was applied to investigate the surface morphology of the devulcanized samples. Phase images were recorded in the tapping mode using a silicon tip. The probe oscillated at a resonance frequency of approximately 320 KHz with spring constant of 48 N/m.

3. Results and discussion

Before approaching the tests some preliminary observations were made about the texture samples. Figure 1 shows that the long exposure times to microwave caused drastic changes in their textures, and this observation was noted only after the mixing process. In the case of GTR3, small agglomerates were obtained, while in the GTR5 sample a tacky rubber sheet was formed. After these first observations, it was necessary to understand in depth the structural changes that occurred after the treatment, and their effects on the properties of the GTR.

3.1. Chemical properties

The percentage of soluble (sol) and insoluble (gel) contents after the devulcanization are shown in Table 1. The results show that longer microwave exposure times led to lower gel content. As described in the literature [12, 13], the devulcanization process can modify the chemical structure of vulcanized elastomers, mainly with the breaking of C–S and S–S bonds, forming materials with lower insoluble portions, as observed in this present study. Regarding the GTRv sample, a small amount of soluble materials could also be measured due to two possible reasons:

Table 1. Percentage of gel and sol contents

Samples	Gel content [%]	Sol content [%]
GTRv	86.0	14.0
GTR3	83.5	16.5
GTR5	73.0	27.0
GTR6	71.2	28.7
GTR7	69.0	31.0

either the oils/additives from rubber were solubilized in toluene, as described by Scuracchio *et al*. [29], and/or there were small amounts of polymer chains that were not cured.

To better understand how the microwaves may have altered the chemical structures of the GTR, the ATR-FTIR technique was used. According to spectra (Figure 2), the intensities of some bands were altered with the devulcanization process. Previous studies have attributed these IR bands to: (1) 1537 cm^{-1}: stretching vibration of a methyl-assisted conjugated double bond ($\nu_{-(C=C)_n-}$, where $n > 6$) from both NR [30, 31] and SBR [32]; (2) 1435 and 1376 cm^{-1}: δ_{CH_2}

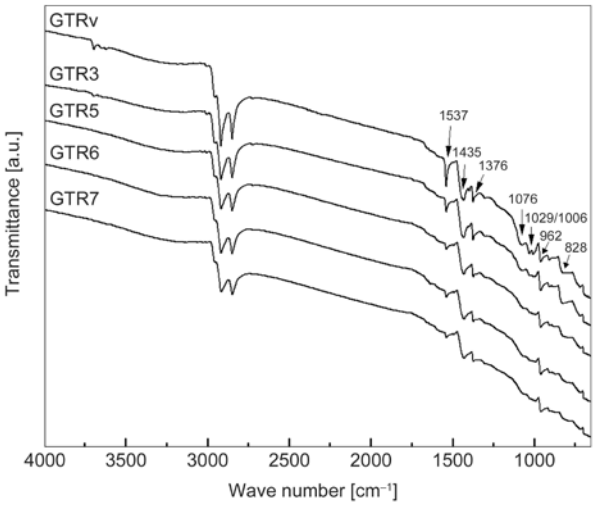

Figure 2. FTIR spectra of vulcanized and devulcanized GTR samples

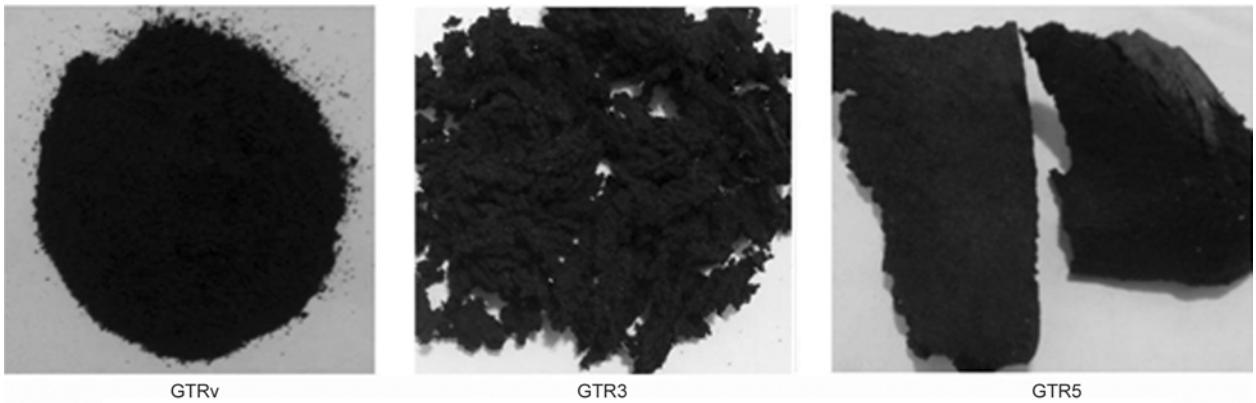

Figure 1. Photos of the GTRv, GTR3 and GTR5 samples after mixing process

deformation from NR rubber [31]; (3) 1076 cm^{-1}: symmetric C–S–C group stretching vibrations in the two C–S bonds [33]; (4) 1029 and 1006 cm^{-1}: C–S bonds [25]; (5) 962 cm^{-1}: –CH=CH– group vibrations of butadiene present in SBR [33, 34]; and (6) 828 cm^{-1}: γ_{C-H} bending from NR rubber [31]. The results reveal that the samples most exposed to microwaves had lower intensity bands, which was more evident in the GTR7 sample. It is also interesting to notice that the bands at 1076, 1029 and 1006 cm^{-1}, which are related to C–S bonds, are seen mainly in the GTRv and GTR3 samples. Hirayama and Saron [25] also noticed changes in the intensity bands in the SBR samples most exposed to microwaves. The authors observed that polysulfidic bonds were broken, however the monosulfidic bonds remained preserved.

So, the results obtained from both chemical techniques proved the existence of structural changes in GTR molecules when exposed to microwaves, especially with the breaking of C-S bonds. Moreover, it is expected that other GTR properties were also altered as a result of the chemical changes observed. Accordingly, an in-depth study of the thermal, rheological and morphological properties of the GTR was performed.

3.2. Thermal properties

The TGA-DTGA results shown in Figure 3 represent the events that occurred in the GTR3 sample, and the other samples presented similar behavior. Based on this, the following events are observed: (1) volatilization of processing oils and additives, or any other element with low molar mass and low boiling temperature; (2) decomposition of the polymeric material present in the tire rubber, where the first and the second peaks belong to the NR and synthetic rubber (SBR and/or BR) decomposition,

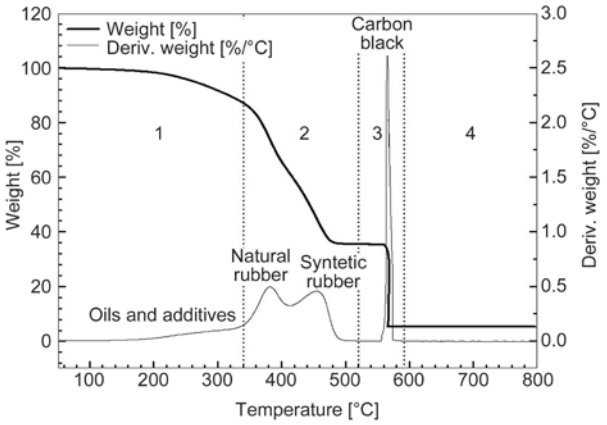

Figure 3. TGA-DTGA curves of the GTR3 sample

respectively [13, 35, 36]; (3) consumption of carbon black, and (4) the residual materials that correspond to the inorganic materials found after the pyrolysis process [35–37].

From the analyses, the temperature range (ΔT) and the weight loss percentage (Δm) of each element were measured (Table 2). According to the results, the longer the microwave exposure times, the lower the weight loss of processing oil, additives and NR, as previously observed by Scuracchio *et al*. [13]. During the devulcanization process, the samples were able to reach the thermal degradation temperatures of processing oils and additives, and these temperatures provided higher decomposition and scission of the NR chains. Therefore, the most degraded materials had smaller amounts of processing oils, NR and additives to be consumed during the thermogravimetric tests. Regarding the carbon black and residual materials, the samples most exposed to microwaves showed greater weight loss of these elements due to the degradation process. The samples most exposed also showed slight increase in the weight loss percentage of synthetic rubber. This indicates that the molecules of the synthetic rubbers were slightly consumed or not consumed at all.

Table 2. Parameter values obtained from TGA curves for vulcanized and devulcanized GTR

Samples	Data	Oils and additives	Natural rubber	Synthetic tubber	Carbon black	Residues
	ΔT [°C]	**~ 35 to 320**	**320 to 410**	**410 to 520**	**520 to 600**	**600 to 800**
GTRv	Δm [%]	10.31	28.35	26.05	29.88	5.41
	T_{max} [°C]	~253	381.02	454.60	569.65	–
GTR3	Δm [%]	10.37	27.91	26.24	30.20	5.28
	T_{max} [°C]	~253	382.03	456.40	565.59	–
GTR5	Δm [%]	10.08	25.36	26.67	32.36	5.52
	T_{max} [°C]	~256	384.55	453.30	566.99	–
GTR6	Δm [%]	9.97	22.47	28.26	33.62	5.65
	T_{max} [°C]	~256	387.46	449.05	566.98	–
GTR7	Δm [%]	8.84	19.41	28.63	36.92	6.20
	T_{max} [°C]	~256	391.03	447.78	567.94	–

It can also be observed that the temperatures at the maximum weight loss rate (T_{max}) of both elements (NR and synthetic rubber) were shifted (Table 2). The NR peaks of the most devulcanized samples shifted to higher temperatures. This phenomenon may have occurred due to the presence of higher amounts of carbon black. These fillers may have played the role of a physical barrier to the output of volatiles, increasing the tortuous and mean free path of these gases, as illustrated in Figure 4a [38]. Like the carbon black, the residual materials may have also played a part in delaying the output of gases. Shih and Jeng [39] reported that the structure of the carbon black pores can adsorb volatiles and liquid, all of them resulting from the pyrolysis process. Thus, in this work it is assumed that the carbon black could have acted as barrier (Figure 4a) and/or could have also adsorbed volatile products (Figure 4b). Fernandez-Berridi *et al*. [35] also observed an increase in the thermostability of the NR with the addition of the SBR in the blend. Once more, it is important to emphasize that the large amount of carbon black in GTR increased its thermostability, as seen in Figure 5.

Although all these factors contributed to the shift of T_{max}, the effect of the breaking of cross-links on the thermostability should be considered. This breakage can thermally destabilize the rubber, promoting its degradation at lower temperatures. However, the effect of the presence of carbon black was still more intense.

Regarding the thermostability of the synthetic rubber, the samples with longer microwave exposure times shifted their T_{max} to lower temperatures (Table 2). Although there is the effect of carbon black on the material, it is believed that the effect of the breaking of cross-links stood out. Another possibility is that the devulcanization process played a role in improving the adhesion between the mixture phases. Karger-Kocsis *et al*. [12] reported that this treatment can act on the compatibility of devulcanized molecular structures. Zanchet *et al*. [24] noted that the microwave treatment enhanced the interfacial adhesion between devulcanized SBR and virgin SBR matrix.

So, in this work, molecular entanglements could have occurred between the devulcanized molecules of the NR and synthetic rubber, and it would result in the shift of this T_{max} to lower values.

The DSC technique was employed to determine the T_g of each elastomeric phase, as shown in Table 3. In general, two distinct glass transitions can be observed, called T_{g1} and T_{g2}, which are related to the presence of the NR and SBR in the GTR, respec-

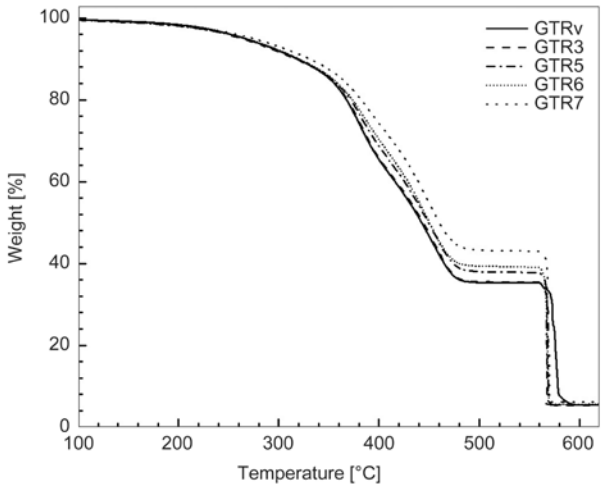

Figure 5. TGA curves of the vulcanized and devulcanized samples

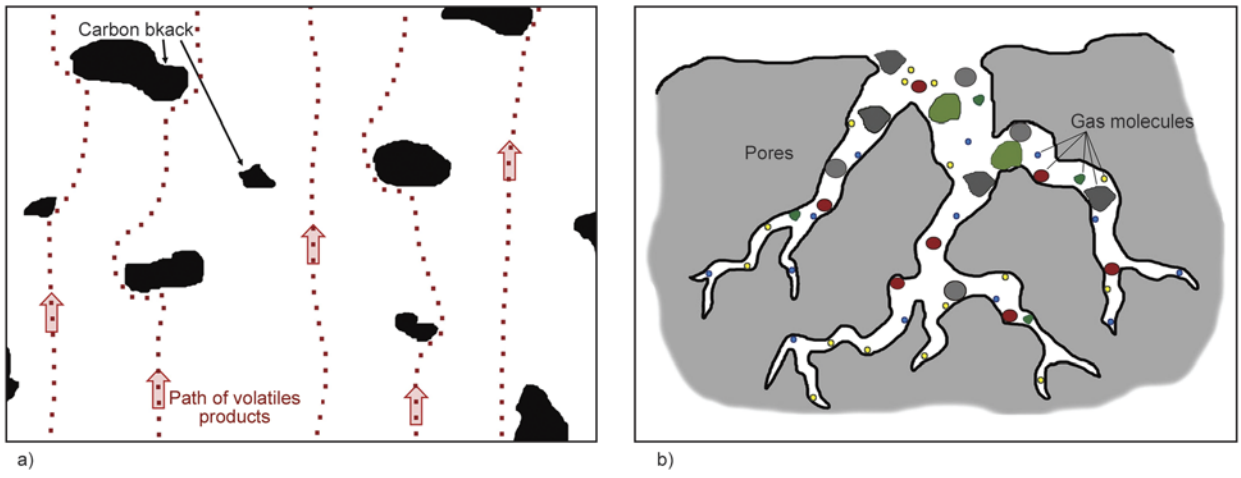

Figure 4. Schema of barrier effect and increase of mean free path of volatiles (a) and adsorption of gas molecules in the carbon black pores (b)

Table 3. Glass transition temperature (T_g) and glass transition width (ΔL) of the samples

Sample	T_{g1}	ΔL_1	T_{g2}	ΔL_2
GTRv	–57	5.7	–46	8.1
GTR3	–56	7.2	–44	9.0
GTR5	–65	10.5	–44	11.4
GTR6	–64	12.4	–	–
GTR7	–62	15.7	–	–

tively [40]. The results shown in Table 3 indicate that the T_{g1} values of the most degraded samples were shifted to lower values, since the cross-links were broken and the polymer chains gained mobility. Pistor *et al*. [23] also noted the same tendency toward lower T_g values with the increase in the exposure time of the ethylene-propylene-diene rubber (EPDM) to microwaves. The authors related these results to the rupture of covalent bonds.

It was also expected that the GTR7 sample had the lowest T_{g1} value. However, in this case, it is likely that the carbon black acted by restricting the segmental motion of the NR molecules, increasing the T_{g1} value, as reported by Scuracchio *et al*. [13]. The literature [13, 29, 41] also showed that the devulcanization process, in these case, by ultrasound, can lead to the formation of cyclic sulphur structures in the polymer chains of the devulcanized SBR, increasing the T_g.

Thus, these factors (breaking of cross-links and carbon black) are expected to counterbalance themselves.

GTR5, GTR6 and GTR7 samples had only a single glass transition in their DSC curves, so that the T_{g2} could not be determined by this technique in this particular case. There are two factors that can explain what took place: (1) the largest amount of carbon black found in these samples could have restricted the segmental motion of the SBR molecules, and/or (2) the devulcanization process might have acted as a compatibilizing agent through molecular entanglement of the devulcanized molecular structures, as previously mentioned.

Table 3 also shows the width values of the glass transition (ΔL), which is defined as the difference between the initial and final temperatures of the transition. These values reflect the number or the distribution modes and relaxation times associated with the transition temperature. For the polymer blends, it can be related to the concentration gradient, also called microheterogeneity. According to Table 3, the ΔL_1 and ΔL_2 values increase with devulcanization, indicating an increase in the relaxation numbers that may be associated to different microenvironments (regions with dimensions of the order of a few chain segments with different neighborhoods). Pistor *et al*. [27] also noticed the width values of glass transition (ΔL) in the most exposure samples to microwaves. These results were associated to the break of the three-dimensional network, where some molecules could acquire mobility at lower temperatures.

3.3. Rheological properties

Table 4 shows the rheometric measurements obtained in the ODR. Scorch time (t_{s1}, the starting time of the vulcanization reaction) and minimum torque (M_L, parameter related to the Mooney viscosity of the material prior to the reaction) were evaluated. According to the results, the absence of revulcanization in the devulcanized samples was observed during analysis (5 min), since the torque did not exceed the minimum of 1 lbf·in (= 0.113 Nm). In relation to M_L values, the decrease of this parameter in the samples GTR5 and GTR6 showed the decrease of the three-dimensional network generated by devulcanization (since M_L value is related to the viscosity and, consequently, to the cross-link density), as shown earlier. The increase of this parameter for the GTR7 sample is probably related to the increasing amount of carbon black and the lowest amount of oil in its structures, as shown by thermogravimetric data (Table 2). So, the increasing in the torque during analysis indicates its flow difficulty in these shear rates.

To determine the storage modulus (G') and the loss modulus (G'') as a function of time (min), the ODR analysis was also used, as seen in Figure 6. Before analyzing the results, it should be noted that both G′ and G'' are dependent on the length and on the level of entanglement of the polymer chains [42]. Furthermore, the higher the cross-link density, the higher the G' values. According to Figure 6, the devulcanized samples show three distinct behaviors. Sample GTR3 had the highest G' value due to its elevated

Table 4. Rheological parameters of the devulcanized samples

Samples	t_{s1} [min]	M_L [lbf·in]
GTR3	>5	6.3
GTR5	>5	4.1
GTR6	>5	4.1
GTR7	>5	6.2

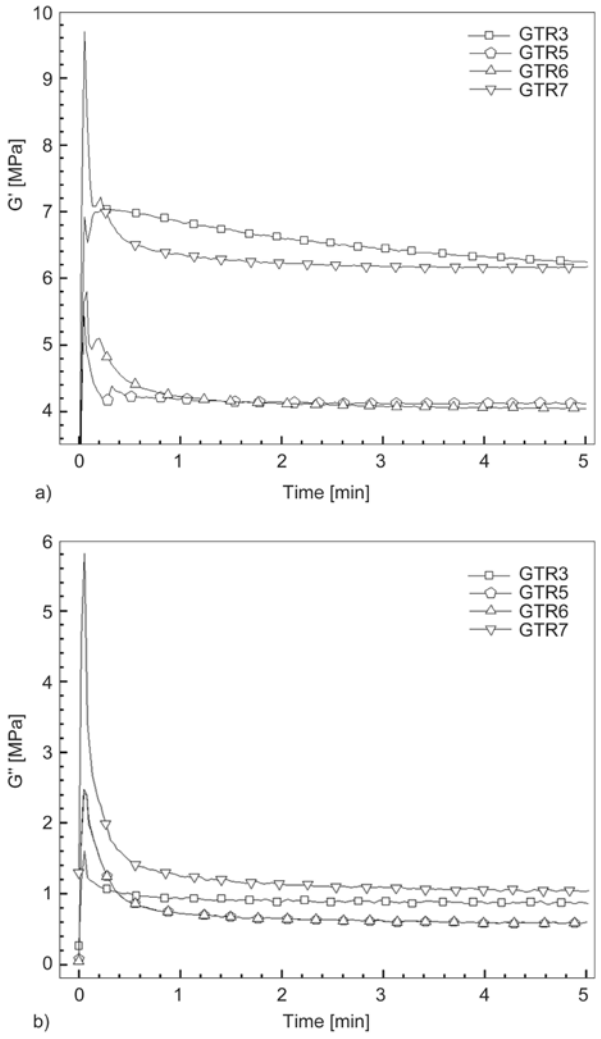

Figure 6. Storage (a) and loss modulus (b) as a function of the time [min] for devulcanized samples

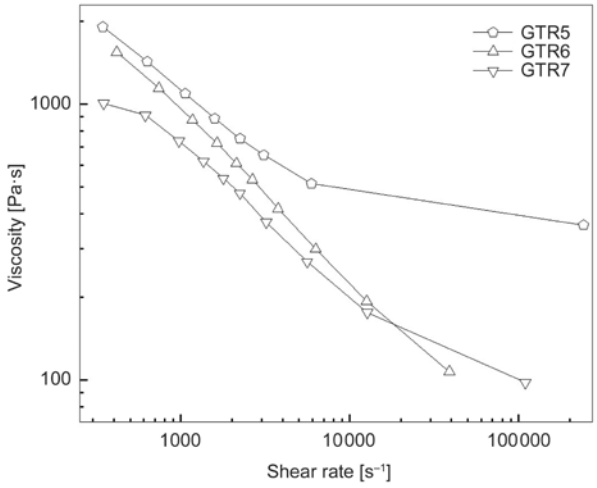

Figure 7. Viscosity versus shear rate for devulcanized samples

cross-link density. GTR5 and GTR6 had the lowest G' values due to its decreasing stiffness by increasing the mobility of the polymer chains, as a result of the devulcanization process. However, sample GTR7 exhibited values very close to those of GTR3. As mentioned before, GTR7 was the sample with the highest amount of carbon black and inorganic residues in its structure, and considered as fillers, its stiffness increased. This sample also presented a low concentration of oils, which also favored the increase of G'. Note that the values G″ followed the same trend observed for G'. The breaking of the cross-links increased the G'' value, especially for GTR7. However, GTR3 displayed distinct behaviors during the test. The G'' values varied between the values of GTR7 and GTR5/GTR6. It is possible that the large amount of oil benefited the sliding of its polymer chains, which were not cross-linked or were broken during the treatment. Thus, G'' was higher than the G'' of the GTR5 and GTR6 samples. It is also a possibility that this result may not be reliable. It is known that the G' and G'' values strongly depend on the sample morphology, and in this case, probably, GTR3 morphology may not be uniform. As mentioned earlier, after the mixing process, GTR3 presented small agglomerates, whereas GTR5, GTR6 and GTR7 presented tacky rubber sheets.

Regarding the capillary rheometry analysis, Figure 7 shows the flow curves of the devulcanized rubber as a function of shear rate. The results reveal that the flow characteristics of the samples were affected by microwaves. At higher shear rates, the increased exposure to microwaves makes the rubber more fluid, since the microwave radiation affected the rubber molecular structures, leading to the scission of the molecules and the decrease of its molar mass. Consequently, the shear viscosity was decreased, as reported by Scuracchio *et al*. [29]. All samples heated more than 5 min presented a pseudoplastic behavior, similar to a thermoplastic polymer. Regarding sample GTR5, the curve did not show linearity by reducing the shear viscosity at higher shear rates. Somehow, its high cross-link density (in comparison to the others) appears to have affected its viscosity. It is worth noting that sample GTR3 could not be analyzed, since it did not flow at high shear stresses and high temperatures due to its high cross-link density.

3.4. Morphological properties

Based on the texture changes after the devulcanization and mixture processes (Figure 1), the SEM analyses were performed. According to Figure 8,

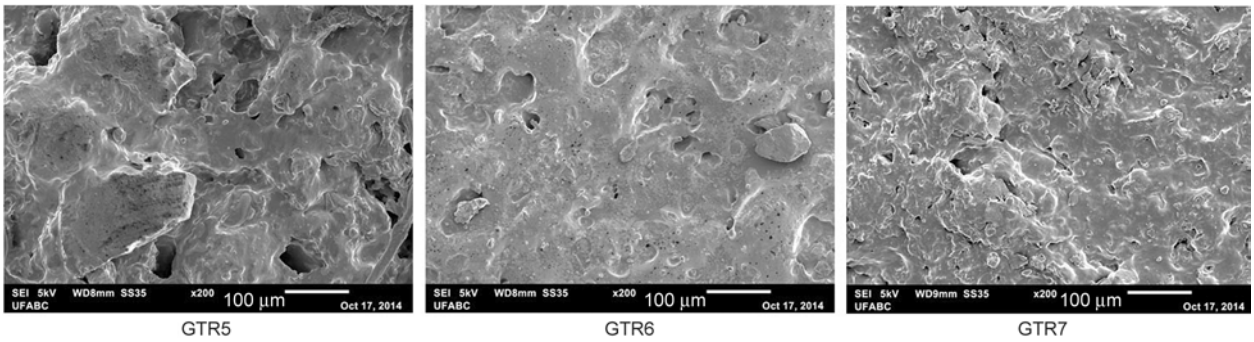

Figure 8. SEM of the surface sheets of the GTR5, GTR6 and GTR7 samples

the micrographs reveal differences amongst themselves regarding voids and particles. It is believed that as this rubber went through the roll mills, the sol phase could have wet the gel phase more effectively. Thus, the most devulcanized samples (GTR6 and GTR7), which have higher amount of the sol phase in their structures, exhibited smoother sheets with smaller voids. It was deducted that the wettability of the sol phase can be related to its fluidity when it is submitted to shear stress during the mixing process. On the other hand, GTR5 exhibited larger voids, indicating that this material possibly did not flow like the others. Also, this sample exhibited stiff particles (i.e cross-link fraction) that were not deformed under mechanical stress.

It should also be noted that GTR7 revealed the presence of some other small particles, which are carbonized materials from the thermo-oxidative degradation process. These data support the thermal analysis results, showing an increase of residual materials in the samples that received higher microwave exposures. The data are also in agreement with the results of rheological properties, since the viscosity of the samples tends to decrease with the increase of the exposure time of GTR to microwaves, increasing the rubber fluidity.

Additionally, phase images obtained from AFM (Figure 9) were used to provide information about the composition of the polymeric blends at nanoscale [43, 44]. Assuming that GTR is a blend composed by NR, SBR and carbon black (according to the previous results presented in this work), its morphology could be analyzed, where three phases were clearly distinguished by the different colors in the images.

Regarding the color scale, which represents the scale of hardness in the images, hard and soft segments can be seen in the mixture. Some studies have represented the dark domains as being the softer materials and the clear domains the harder ones [45, 46]. Similarly, in the present work the carbon black particles are represented by clearer domains. As this filler is the hardest phase found in the blends and as it has a specific shape and nanometric sizes [46], it was easy to single it out in the images. Consequently, the darkest and middle color areas are the NR and the SBR domains, respectively. Thus, the phase images (GTR5 → GTR7) show the consumption of the darker phase and the increase of the clearer phase with the increase of exposure time of GTR to microwaves, and in the same way an increase in the amount of carbon black domains can be also observed. These data validate the results obtained mainly from TGA analysis, where there was a reduction in the amount of the NR and the relative increase in the amount of carbon black and residual materials with higher

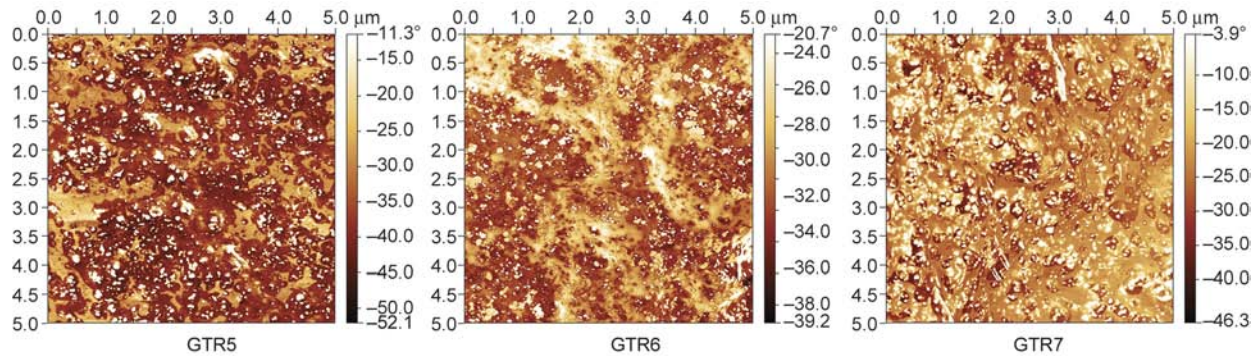

Figure 9. Tapping mode AFM phase images of the samples

exposure times. Although some studies have shown that SBR is softer than NR [46], it should be remembered that the NR molecular structures were changed with radiation, where their main chains and cross-links were broken, and it is possible that this allowed the NR to become softer.

Regarding the dispersion of carbon black particles in elastomeric blends, GTR5 showed peculiar results about the localization of these fillers in the elastomeric phases. It can be observed that in this sample the carbon black is located in the NR, and in samples GTR6 and GTR7 these particles were transferred to the SBR phase. Le *et al*. [47] showed that there are two factors that cause carbon black to remain in one of the phases: (1) the effect of the matrix viscosity, and (2) the polarity. The authors reported that although NR chains are more capable of wetting the carbon black, fillers migrate to the SBR over time due to chemical affinity. However, in this work, in addition to the fact that NR underwent degradation and was able to enhance its degree of wettability, its polarity also changed. These factors may have contributed to the preference for carbon black by NR. However, while the NR phases decreased with increasing exposure times, carbon black particles were being transferred from NR to the SBR phases.

Another peculiar result was seen in the GTR7. It appears that the devulcanized NR domains were deformed during mixing in the two-roll mill, even under small stresses, and they were oriented in the flow direction. The obtained morphology is very similar to droplet dispersion morphology, frequently seen in thermoplastic blends, as illustrated in Figure 10.

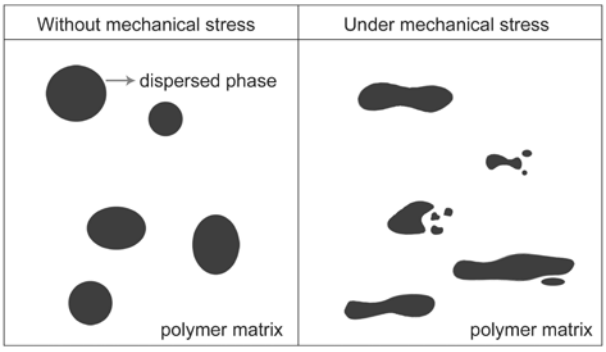

Figure 10. Illustration of the droplet dispersion morphology during melt-mixing of immiscible polymer blends. Deformation and breakup of dispersed phase in shear flow.

4. Conclusions

GTRv samples were devulcanized using different microwave exposure times. Long microwave exposure periods resulted in many structural changes, such as the decrease of the insoluble phase content (gel phase), breaking of chemical bonds (C=C and C–S) and increase in the fluidity of rubber. Even though the goal was achieved, the breaking of the main polymer chain also occurred. Substantial amounts of the NR chain were decomposed and broken during the treatment, and likewise there was an increase in the relative amount of carbon black and residual materials with the polymer degradation. However, this amount of carbon black led to the samples' enhanced thermostability and increased stiffness. The treatment proved to be efficient in the compatibilization of the elastomeric phases. Despite all structural changes, the devulcanized samples could not to be revulcanized during the rheological analyses. Regarding the analyses, it is very important to emphasize that the AFM technique proved to be an interesting and effective tool in monitoring changes in GTR using the devulcanization process. This technique revealed the morphology of the blends at nanoscale. The method enabled to observe the increasing wettability of the NR domain in the carbon black, and also its increasing fluidity in the blend, which was similar to a droplet dispersion (NR) in a continuous phase of the SBR.

Acknowledgements

The authors are grateful to the Universidade Federal do ABC (UFABC) and Braskem S.A. for financial support and UFABC and Brazilian Nanotechnology National Laboratory (LNNano) for assistance in this project. We specially thank the AFM staff for technical support.

References

[1] Adhikari B., De D., Maiti S.: Reclamation and recycling of waste rubber. Progress in Polymer Science, **25**, 909–948 (2000).
DOI: 10.1016/S0079-6700(00)00020-4

[2] Wolsky A. M., Gaines L. L.: Discarded tires: A potential source of hydrocarbons to displace petroleum. Resources and Energy, **3**, 195–206 (1981).
DOI: 10.1016/0165-0572(81)90023-2

[3] Celauro B., Celauro C., Lo Presti D., Bevilacqua A.: Definition of a laboratory optimization protocol for road bitumen improved with recycled tire rubber. Construction and Building Materials, **37**, 562–572 (2012).
DOI: 10.1016/j.conbuildmat.2012.07.034

[4] Guillamot F., Goujard L., Simard D., Boulangé L.: Influence of interface energy on compatibility between ground tyre rubber and bitumen used in asphalt pavement. Road Materials and Pavement Design, **14**, 372–383 (2013).
DOI: 10.1080/14680629.2013.796890

[5] Oh J. S., Ghose S., Isayev A. I.: Effects of ultrasonic treatment on unfilled butadiene rubber. Journal of Polymer Science Part B: Polymer Physics, **41**, 2959–2968 (2003).
DOI: 10.1002/polb.10606

[6] Scuracchio C. H., Bretas R. E. S., Isayev A. I.: Blends of PS with SBR devulcanized by ultrasound: Rheology and morphology. Journal of Elastomers and Plastics, **36**, 45–75 (2004).
DOI: 10.1177/0095244304039913

[7] Hassan M. M., Aly R. O., Abdel Aal S. E., El-Masry A. M., Fathy E. S.: Mechanochemical devulcanization and gamma irradiation of devulcanized waste rubber/high density polyethylene thermoplastic elastomer. Journal of Industrial and Engineering Chemistry, **19**, 1722–1729 (2013).
DOI: 10.1016/j.jiec.2013.02.012

[8] Hassan M. M., Badway N. A., Elnaggar M. Y., Hegazy E-S. A.: Thermo-mechanical properties of devulcanized rubber/high crystalline polypropylene blends modified by ionizing radiation. Journal of Industrial and Engineering Chemistry, **19**, 1241–1250 (2013).
DOI: 10.1016/j.jiec.2012.12.024

[9] Garcia P. S., Cruz S. A., Scuracchio C. H.: Composição para obtenção de blenda polimérica tenacificada, processo para a preparação da composição, blenda polimérica tenacificada, e, uso da mesma. BR 10 2014 021424 0, Brazil (2014).

[10] De S. K., Isayev A. I., Khait K.: Rubber recycling. CRC Press, New York (2005).

[11] Bandyopadhyay S., Agrawal S. L., Ameta R., Dasgupta S., Mukhopadhyay R., Deuri A. S., Ameta S. C., Ameta R.: An overview of rubber recycling. Progress in Rubber, Plastics and Recycling Technology, **24**, 73–112 (2008).

[12] Karger-Kocsis J., Mészáros L., Bárány T.: Ground tyre rubber (GTR) in thermoplastics, thermosets, and rubbers. Journal of Materials Science, **48**, 1–38 (2013).
DOI: 10.1007/s10853-012-6564-2

[13] Scuracchio C. H., Waki D. A., da Silva M. L. C. P.: Thermal analysis of ground tire rubber devulcanized by microwaves. Journal of Thermal Analysis and Calorimetry, **87**, 893–897 (2007).
DOI: 10.1007/s10973-005-7419-8

[14] Isayev A. I., Sujan B.: Nonisothermal vulcanization of devulcanized GRT with reversion type behavior. Journal of Elastomers and Plastics, **38**, 291–318 (2006).
DOI: 10.1177/0095244306067424

[15] Myhre M., MacKillop D. A.: Rubber recycling. Rubber Chemistry and Technology, **75**, 429–474 (2002).
DOI: 10.5254/1.3547678

[16] Myhre M., Saiwari S., Dierkes W., Noordermeer J.: Rubber recycling: Chemistry, processing, and applications. Rubber Chemistry and Technology, **85**, 408–449 (2012).
DOI: 10.5254/rct.12.87973

[17] Novotny D. S., Marsh R. L., Masters F., Tally D. N.: Microwave devulcanization of rubber. U.S. Patent US 4104205 A, USA (1978).

[18] Isayev A. I.: Recycling of rubbers. in 'Science and technology of rubber' (eds.: Mark J. E., Erman B., Eirich F. R.) Elsevier, New York, vol 3, 663–701 (2005).

[19] Hong Y. J., Jeong K. M., Saha P., Suh J., Kim J. K.: Processing and characterization of microwave and ultrasonically treated waste-EPDM/LDPE polymer composites. Polymer Engineering and Science, **55**, 533–540 (2015).
DOI: 10.1002/pen.23916

[20] Menéndez J. A., Arenillas A., Fidalgo B., Fernández Y., Zubizarreta L., Calvo E. G., Bermúdez J. M.: Microwave heating processes involving carbon materials. Fuel Processing Technology, **91**, 1–8 (2010).
DOI: 10.1016/j.fuproc.2009.08.021

[21] Kwon S. K., Ahn J. M., Kim G. H., Chun C. H., Hwang J. S., Lee J. H.: Microwave absorbing properties of carbon black/silicone rubber blend. Polymer Engineering and Science, **42**, 2165–2171 (2002).
DOI: 10.1002/pen.11106

[22] Yacubowicz J., Narkis M.: Dielectric behavior of carbon black filled polymer composites. Polymer Engineering and Science, **26**, 1568–1573 (1986).
DOI: 10.1002/pen.760262207

[23] Pistor V., Scuracchio C. H., Oliveira P. J., Fiorio R., Zattera A. J.: Devulcanization of ethylene-propylene-diene polymer residues by microwave – Influence of the presence of paraffinic oil. Polymer Engineering and Science, **51**, 697–703 (2011).
DOI: 10.1002/pen.21875

[24] Zanchet A., Carli L. N., Giovanela M., Brandalise R. N., Crespo J. S.: Use of styrene butadiene rubber industrial waste devulcanized by microwave in rubber composites for automotive application. Materials and Design, **39**, 437–443 (2012).
DOI: 10.1016/j.matdes.2012.03.014

[25] Hirayama D., Saron C.: Chemical modifications in styrene–butadiene rubber after microwave devulcanization. Industrial and Engineering Chemistry Research, **51**, 3975–3980 (2012).
DOI: 10.1021/ie202077g

[26] Paulo G. D., Hirayama D., Saron C.: Microwave devulcanization of waste rubber with inorganic salts and nitric acid. Advanced Materials Research, **418–420**, 1072–1075 (2012).
DOI: 10.4028/www.scientific.net/AMR.418-420.1072

[27] Pistor V., Ornaghi F. G., Fiorio R., Zattera A. J., Oliveira P. J., Scuracchio C. H.: Devulcanization of ethylene-propylene-diene polymer residues (EPDM-r) by microwaves (in Portuguese). Polímeros, **20**, 165–169 (2010).
DOI: 10.1590/S0104-14282010005000027

[28] Pistor V., Zattera A. J.: Degradation kinetics of ethylene propylene diene terpolymer residues devulcanized by microwaves. Journal of Elastomers and Plastics, **46**, 69–83 (2014).
DOI: 10.1177/0095244312462159

[29] Scuracchio C. H., Waki D. A., Bretas R. E. S.: Thermal and rheological characterization of ground tire rubber devulcanized by microwaves (in Portuguese). Polímeros, **16**, 46–52 (2006).
DOI: 10.1590/S0104-14282006000100011

[30] Zhang X., Lu C., Liang M.: Properties of natural rubber vulcanizates containing mechanochemically devulcanized ground tire rubber. Journal of Polymer Research, **16**, 411–419 (2009).
DOI: 10.1007/s10965-008-9243-x

[31] Tripathy A. R., Morin J. E., Williams D. E., Eyles S. J., Farris R. J.: A novel approach to improving the mechanical properties in recycled vulcanized natural rubber and its mechanism. Macromolecules, **35**, 4616–4627 (2002).
DOI: 10.1021/ma012110b

[32] Jiang G., Zhao S., Li W., Luo J., Wang Y., Zhou Q., Zhang C.: Microbial desulfurization of SBR ground rubber by *Sphingomonas sp*. and its utilization as filler in NR compounds. Polymers for Advanced Technologies, **22**, 2344–2351 (2011).
DOI: 10.1002/pat.1769

[33] Gunasekaran S., Natarajan R. K., Kala A.: FTIR spectra and mechanical strength analysis of some selected rubber derivatives. Spectrochimica Acta Part A: Molecular and Biomolecular Spectroscopy, **68**, 323–330 (2007).
DOI: 10.1016/j.saa.2006.11.039

[34] Mangili I., Collina E., Anzano M., Pitea D., Lasagni M.: Characterization and supercritical CO_2 devulcanization of cryo-ground tire rubber: Influence of devulcanization process on reclaimed material. Polymer Degradation and Stability, **102**, 15–24 (2014).
DOI: 10.1016/j.polymdegradstab.2014.02.017

[35] Fernández-Berridi M. J., González N., Mugica A., Bernicot C.: Pyrolysis-FTIR and TGA techniques as tools in the characterization of blends of natural rubber and SBR. Thermochimica Acta, **444**, 65–70 (2006).
DOI: 10.1016/j.tca.2006.02.027

[36] Mui E. L. K., Lee V. K. C., Cheung W. H., McKay G.: Kinetic modeling of waste tire carbonization. Energy and Fuels, **22**, 1650–1657 (2008).
DOI: 10.1021/ef700601g

[37] Yang J., Kaliaguine S., Roy C.: Improved quantitative determination of elastomers in tire rubber by kinetic simulation of DTG curves. Rubber Chemistry and Technology, **66**, 213–229 (1993).
DOI: 10.5254/1.3538307

[38] Chrissafis K., Paraskevopoulos K. M., Stavrev S. Y., Docoslis A., Vassiliou A., Bikiaris D. N.: Characterization and thermal degradation mechanism of isotactic polypropylene/carbon black nanocomposites. Thermochimica Acta, **465**, 6–17 (2007).
DOI: 10.1016/j.tca.2007.08.007

[39] Shih Y-F., Jeng R-J.: Carbon black-containing interpenetrating polymer networks based on unsaturated polyester/epoxyII. Thermal degradation behavior and kinetic analysis. Polymer Degradation and Stability, **77**, 67–76 (2002).
DOI: 10.1016/S0141-3910(02)00080-0

[40] Prasertsri S., Lagarde F., Rattanasom N., Sirisinha C., Daniel P.: Raman spectroscopy and thermal analysis of gum and silica-filled NR/SBR blends prepared from latex system. Polymer Testing, **32**, 852–861 (2013).
DOI: 10.1016/j.polymertesting.2013.04.007

[41] Levin V. Y., Kim S. H., Isayev A. I., Massey J., von Meerwall E.: Ultrasound devulcanization of sulfur vulcanized SBR: Crosslink density and molecular mobility. Rubber Chemistry and Technology, **69**, 104–114 (1996).
DOI: 10.5254/1.3538350

[42] Garcia P. S., Scuracchio C. H., Cruz S. A.: Effect of residual contaminants and of different types of extrusion processes on the rheological properties of the post-consumer polypropylene. Polymer Testing, **32**, 1237–1243 (2013).
DOI: 10.1016/j.polymertesting.2013.08.002

[43] Dikland H. G., Sheiko S. S., van der Does L., Möller M., Bantjes A.: A scanning force microscopy study on the morphology of elastomer-coagent blends. Polymer, **34**, 1773–1775 (1993).
DOI: 10.1016/0032-3861(93)90341-7

[44] de Sousa F. D. B., Scuracchio C. H.: The use of atomic force microscopy as an important technique to analyze the dispersion of nanometric fillers and morphology in nanocomposites and polymer blends based on elastomers. Polímeros, **24**, 661–672 (2014).
DOI: 10.1590/0104-1428.1648

[45] Le H. H., Sriharish M. N., Henning S., Klehm J., Menzel M., Frank W., Wießner S., Das A., Stöckelhuber K-W., Heinrich G., Radusch H-J.: Dispersion and distribution of carbon nanotubes in ternary rubber blends. Composites Science and Technology, **90**, 180–186 (2014).
DOI: 10.1016/j.compscitech.2013.11.008

[46] Jeon I. H., Kim H., Kim S. G.: Characterization of rubber micro-morphology by atomic force microscopy (AFM). Rubber Chemistry and Technology, **76**, 1–11 (2003).
DOI: 10.5254/1.3547733

[47] Le H. H., Ilisch S., Kasaliwal G. R., Radusch H-J.: Filler phase distribution in rubber blends characterized by thermogravimetric analysis of the rubber-filler gel. Rubber Chemistry and Technology, **81**, 767–781 (2008).
DOI: 10.5254/1.3548231

eXPRESS Polymer Letters Vol.9, No.11 (2015) 1027–1039
Available online at www.expresspolymlett.com
DOI: 10.3144/expresspolymlett.2015.92

Synthesis and property characterization of two novel side-chain isoindigo copolymers for polymer solar cells

X. Liu[1], *F. Wu*[1], *H. Guo*[1], *B. Zhao*[1,2], *S. Tan*[1,2*]

[1]College of Chemistry, and Key Laboratory of Environmentally Friendly Chemistry and Applications of Ministry of Education, Xiangtan University, 411105 Xiangtan, PR China
[2]Key Laboratory of Advanced Functional Polymeric Materials of College of Hunan Province, Key Laboratory of Polymeric Materials & Application Technology of Hunan Province, Xiangtan University, 411105 Xiangtan, PR China

Received 23 April 2015; accepted in revised form 28 June 2015

Abstract. Two novel side-chain conjugated polymers, **PTBT-TID** and **PTBT-TTID**, based on the new synthetic thiophene-benzne-thiophene (TBT) unit, side-chain isoindigo (ID) unit, and the introduced thiophene π-bridge, have been designed and synthesized. The photophysical, electrochemical and photovoltaic properties of the two polymers have been systematically investigated. The two polymers possess relatively good solubility as well as excellent thermal stability up to 380°C, and all of the polymer solar cell (PSC) devices based on the two polymers obtain high open circuit voltage (V_{oc}) of about 0.8 V. The polymer solar cells based on the polymer **PTBT-TID** show relatively higher efficiencies than the **PTBT-TTID**-based ones, due to the broader absorption spectrum, a relatively higher hole mobility, a lower HOMO (the highest occupied molecular orbital) energy level, a stronger IPCE (the incident photon to current conversion efficiency) response and a better microphase separation, Consequently, the device based on **PTBT-TID**:$PC_{61}BM$ (1:2, by weight) gives the best power conversion efficiency (PCE) of 2.04%, with a short-circuit current density (J_{sc}) of 5.39 mA·cm^{-2}, an open-circuit voltage (V_{oc}) of 0.83 V, and a fill factor (FF) of 0.45.

Keywords: *polymer synthesis, molecular engineering, isoindigo, thiophene bridge, polymer solar cells*

1. Introduction

Harvesting energy directly from sunlight using photovoltaic technology has been a key solution to the growing energy crisis. In recent years, polymer solar cells (PSCs) have attracted considerable attention due to their unique advantages, such as low cost, light weight, solution processibility, and flexibility of molecular design [1–3]. The bulk heterojunction (BHJ) structure, which is composed of a photoactive blend layer of a conjugated polymer donor and a fullerene derivative acceptor, sandwiched between an anode and a cathode (at least one of them should be transparent), is one of the most successful and useful architectures in PSCs [4–8]. Recently, great advances have been made in the development of high-efficiency photovoltaic materials and device structures, especially in multiple-junction tandem solar cell and ternary solar cells. In 2015, an efficient triple-junction tandem solar cell designed by Yusoff *et al*. got record-high power conversion efficiency (PCE) of 11.83% in PSCs [9]. On the other hand, ternary solar cells have attracted more and more attention due to the advantages to extend the absorption spectra of large-band-gap polymers to the near IR region and to enhance light harvesting in single-junction BHJ solar cells [10–14]. However, the PCEs of PSCs still need a further promotion to meet the prospective commercial application.

So far, one appropriate approach is to design alternating donor-acceptor (D-A) low-band-gap copoly-

*Corresponding author, e-mail: tanst2008@163.com

mers through the combination of various electron-rich (donors) and electron-deficient (acceptors) moieties as repeating units in the polymer backbone [15, 16]. Nevertheless, among all the existing D-A copolymers, although main chain D-A copolymers have witnessed great success for achieving highly efficient PSCs, they may suffer from lower hole mobility due to the influence of the acceptor units on the polymer main chain [17]. Thus, a new type of distinctive polymers with conjugated side chains or groups emerged, and they possess excellent features, such as a better overlap of absorption spectra with the solar spectrum, excellent solubility in common device processing solvent such as chlorobenzene (CB) or dichlorobenzene (DCB), and suitable miscibility with the fullerene acceptor ($PC_{61}BM$), thus the side-chain polymers have demonstrated prominent device performances in PSCs [18].

To further manipulate stereo-structure and photoelectronic properties of conjugated polymers, some π-conjugated bridges, especially thiophene or alkylthiophene units, are inserted between donor (D) and acceptor (A) moieties to produce new D-π-A conjugated copolymers. π-Conjugated bridges crucially impact the electronic structures of polymer main chains and the interactions between D and A units; therefore, they remarkably affect the stereostructure and consequently the photophysical, electrochemical, charge transport, and photovoltaic properties of D-π-A conjugated copolymers [19, 20].

Isoindigo (ID), which contains two strong electron-deficient lactam rings with a planar geometry, is a useful monomer for the design and synthesis of alternating D-A low-band-gap conjugated polymers for photovoltaic device applications [21, 22]. Many ID-based polymers exhibited intense and broad absorption, which is beneficial to achieving high photovoltaic performances in PSCs [23]. And the side-chain ID unit has been reported by our group for the first time, wherein the inverted device based on **PBDT-TID** obtained a high PCE of 6.51% [24].

Benzodithiophene (BDT) unit is widely used in photovoltaic devices because of its symmetrical planar conjugated structure and excellent photovoltaic performance. While in this manuscript, we introduced a new donor similar to the BDT unit, thiophene-2,5-bis((2-ethylhexyl)oxy)benzene-thiophene (TBT) unit, united with the side-chain ID unit, designing and synthesizing two novel side-chain polymers (**PTBT-TID** and **PTBT-TTID**), as shown in Figure 1. Unlike the BDT unit, benzene and thiophene moieties were connected by carbon-carbon single bond in TBT unit, which increased the torsion degree of donor unit, resulting in a lower HOMO (the highest occupied molecular orbital) energy level and then a higher open-circuit voltage (V_{oc}) value. And a side-chain ID unit was introduced as an acceptor unit to get broad absorption spectra and good photovoltaic performance. Additionally, a thiophene unit was applied as π-conjugated bridge to broaden the absorption spectra and adjust energy level. Next, the photophysical, electrochemical and photovoltaic properties of two polymers were systematically investigated.

2. Experimental section

2.1. Materials

All the chemicals were purchased from Alfa Aesar and Chem Greatwall Chemical Company (Wuhan, China) and used without further purification. Toluene and tetrahydrofuran (THF) were dried and distilled over sodium and benzophenone. N,N-Dimethylformamide (DMF) was dried over and distilled from CaH_2 under an atmosphere of dry nitrogen. Phosphorus oxychloride and 1,2-dichloroethane were atmospheric distillation. All other commercially available materials were used as received unless noted otherwise. 2,5-Dibromothiophene-3-carbaldehyde (**1**), tributyl(thiophen-2-yl)stannane (**2**), (E)-5-(1,1′- bis(2-ethylhexyl)-2,2′-dioxo-[3,3′-biindolinylidene]-6-yl) thiophene-2-carbaldehyde (**8**), (E)-6-(5-((E)-2-(2,5-dibromothiophen-3-yl)vinyl)thiophen-2-yl)-1,1'-bis(2-ethylhexyl)-[3,3′-biindolinylidene]-2,2′-dione (**M1**) and (5,5'-(2,5-bis((2-ethylhexyl)oxy)-1,4-phenylene) bis(thiophene-5,2-diyl))bis(trimethylstannane) (**M3**) were prepared according to literature procedures [24–26].

2.2. Synthesis

The synthetic routes and molecular structures of two polymers are shown in Figure 1. The detailed synthetic processes are as follows.

2.2.1. [2,2′:5′,2″-Terthiophene]-3′-carbaldehyde (3)

The compound 3 was synthesized by Stille coupling reaction. Compound **1** (6.00 g, 22.22 mmol) and compound **2** (24.85 g, 66.66 mmol) were dissolved in anhydrous toluene (120 mL) and deoxygenated with nitrogen for 15 min. $Pd(PPh_3)_4$ (230 mg, 0.67 mmol) was then added under nitrogen and the mixture was again flushed with nitrogen for 30 min. Then the

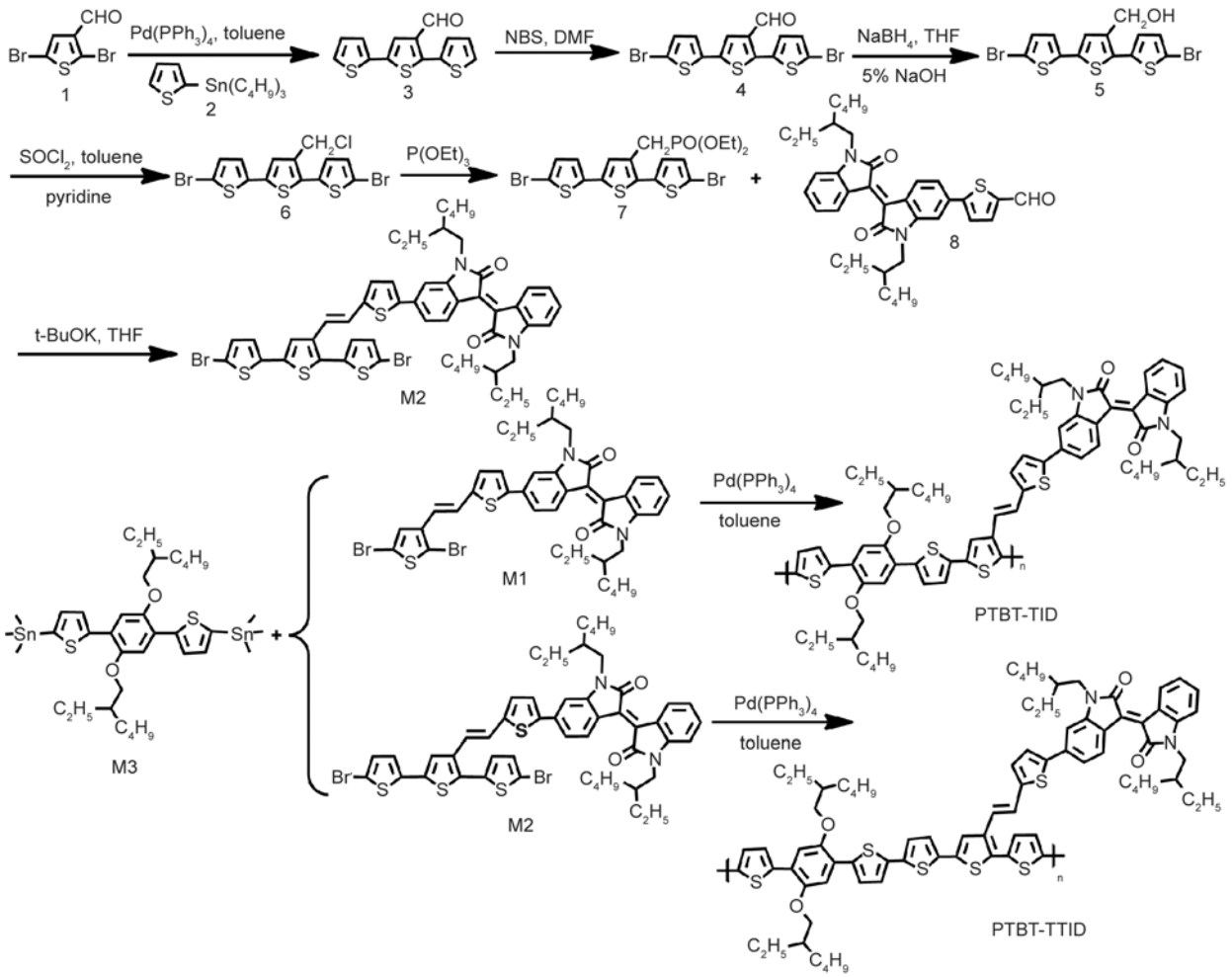

Figure 1. Synthetic routes and molecular structures of the two polymers **PTBT-TID** and **PTBT-TTID**

reaction mixture was stirred at 110°C for 2 days under nitrogen atmosphere. After cooled to room temperature, the mixture was poured into water (100 mL) and extracted with dichloromethane. The organic phase was washed with water and dried over anhydrous $MgSO_4$. After concentration, the crude product was purified on silica gel chromatography using a petroleum ether/dichloromethane mixture (1/1 by volume) as eluent to afford a yellow liquid (4.49 g, 73.2%). ^{1}H NMR ($CDCl_3$, 400 MHz, δ/ppm): 10.09 (s, 1H), 7.57 (s, 1H), 7.51–7.49 (d, 1H), 7.31–7.23 (m, 3H), 7.17–7.16 (d, 1H), 7.06–7.05 (d, 1H). GC-MS ($C_{13}H_8OS_3$) *m*/*z*: calcd for 276.4; found 276.9.

2.2.2. 5,5″-Dibromo-[2,2′:5′,2″-terthiophene]-3′-carbaldehyde (4)

Compound **3** (4.49 g, 16.25 mmol) was dissolved in DMF (50 mL). The mixture of N-bromosuccinimide (NBS) (5.79 g, 32.50 mmol) in DMF (30 mL) was added dropwise to the solution and the solution was stirred at 30°C till a large amount of yellow solid dissolved. Then, the solid was washed by methyl alcohol then dried in vacuum drying oven for one day to afford a light yellow liquid (6.80 g, 96.1%). ^{1}H NMR ($CDCl_3$, 400 MHz, δ/ppm): 10.02 (s, 1H), 7.48 (s, 1H), 7.13–7.12 (d, 1H), 7.09–7.08 (d, 1H), 7.02–7.01 (d, 1H), 6.97–6.96 (d, 1H). MALDI-TOF MS ($C_{13}H_6Br_2OS_3$) *m*/*z*: calcd for 434.190; found 433.867.

2.2.3. (5,5″-Dibromo-[2,2′:5′,2″-terthiophen]-3′-yl)methanol (5)

Compound **4** (3.00 g, 6.91 mmol) was dissolved in THF (80 mL), and the sodium borohydride (5.23 g, 138.19 mmol) dissolved in 5% sodium hydroxide solution (20 mL) was added dropwise. After that, the reaction mixture was stirred at room temperature for two hours. Then the mixture was extracted with CH_2Cl_2 and washed with salt water. The organic phase was dried over anhydrous $MgSO_4$ and the solvent was removed by rotary evaporation. The crude product was dried in vacuum drying oven for half an hour to afford a yellow solid (2.65 g, 87.9%)

without further purification. MALDI-TOF MS ($C_{13}H_8Br_2OS_3$) *m*/*z*: calcd for 436.210; found 435.834.

2.2.4. 5,5″-Dibromo-3′-(chloromethyl)-2,2′:5′,2″-terthiophene (6)

Under nitrogen atmosphere, to a solution of compound **5** (2.55 g, 5.83 mmol) and pyridine (2.9 mL, 35.01 mmol) in toluene (100 mL), anhydrous thionyl chloride (4.1 mL, 58.34 mmol) was added slowly at 0°C. Then the mixture was heated to 70°C for 24 h. After cooled to room temperature, the mixture was extracted with CH_2Cl_2 and washed with water. The organic phase was dried over anhydrous $MgSO_4$ and the solvent was removed by rotary evaporation. The crude product was purified on silica gel chromatography using petroleum ether as eluent to afford a yellow-green solid (1.03 g, 39.1%). ^{1}H NMR ($CDCl_3$, 400 MHz, δ/ppm): 7.14 (s, 1H), 7.11–7.10 (d, 1H), 7.06–7.05 (d, 1H), 7.02–7.01 (d, 1H), 6.96–6.95 (d, 1H), 4.64 (s, 2H). MALDI-TOF MS ($C_{13}H_7Br_2ClS_3$) *m*/*z*: calcd for 454.650; found 453.829.

2.2.5. Diethyl ((5,5″-dibromo-[2,2′:5′,2″-terthiophen]-3′-yl)methyl)phosphonate (7)

Compound **6** (0.77 g, 1.69 mmol) was dissolved in triethyl phosphite (40 mL). Then the reaction mixture was stirred at 160°C for one day under argon atmosphere. After cooled to room temperature, the redundant triethyl phosphite was removed by rotary evaporation. The crude product was purified on silica gel chromatography using a petroleum ether/ethyl acetate mixture (2/1 by volume) as eluent to afford a yellow-green oil (0.73 g, 77.7%). ^{1}H NMR ($CDCl_3$, 400 MHz, δ/ppm): 7.13 (s, 1H), 7.08–7.06 (d, 2H), 6.98–6.97 (d, 1H), 6.92 (s, 1H), 4.12–4.05 (m, 4H), 3.26 (s, 1H), 3.20 (s, 1H), 1.31–1.27 (t, 6H).

2.2.6. (E)-6-(5-((E)-2-(5,5″-dibromo-[2,2′:5',2″-terthiophen]-3′-yl)vinyl)thiophen-2-yl)-1,1′-bis(2-ethylhexyl)-[3,3′-biindolinylidene]-2,2′-dione (M2)

Compound **7** (0.70 g, 1.26 mmol) and compound **8** (0.75 g, 1.26 mmol) were dissolved in THF (15 mL) and the solution was stirred at room temperature for 30 min under nitrogen atmosphere. Then potassium tert-butoxide (0.21 g, 1.89 mmol) was dissolved in THF (25 mL) and added dropwise to the solution. The reaction mixture was stirred for 5 h at room temperature, and then heated to 50°C for twelve hours. After cooled to room temperature, water was added for quenching the reaction, and the aqueous layer was then extracted with CH_2Cl_2. The organic layer was washed with dilute aqueous HCl solution and dried over $MgSO_4$. Solvent was removed by rotary evaporation. The crude product was purified on silica gel chromatography using a petroleum ether/dichloromethane mixture (3:1 by volume) as eluent to get a dark red solid (0.12 g, 9.5%). ^{1}H NMR ($CDCl_3$, 400 MHz, δ/ppm): 9.21–9.15 (m, 2H), 7.38–7.31 (m, 4H), 7.18 (s, 1H), 7.14–7.13 (d, 3H), 7.08–7.06 (d, 1H), 7.03–6.94 (m, 4H), 6.78 (s, 1H), 3.75–3.69 (m, 4H), 1.89 (s, 2H), 1.43–1.28 (m, 16H), 1.02–0.91 (m, 12H). ^{13}C NMR (100 MHz, $CDCl_3$, δ/ppm): 168.54, 168.33, 145.76, 145.08, 143.34, 143.24, 137.39, 136.29, 135.45, 132.61, 132.58, 132.07, 130.78, 130.35, 129.74, 127.95, 127.25, 124.94, 124.43, 124.05, 122.08, 121.89, 121.17, 121.10, 118.99, 113.48, 111.86, 108.09, 104.60, 44.22, 44.10, 37.81, 37.66, 30.92, 30.82, 29.72, 28.87, 28.81, 24.33, 24.16, 23.10, 14.11, 14.08, 10.92, 10.74. MALDI-TOF MS ($C_{50}H_50Br_2N_2O_2S_4$) *m*/*z*: calcd for 999.010; found 999.106.

2.2.7. Polymerization for PTBT-TID

The monomer **M1** (97 mg, 0.12 mmol) and monomer **M3** (96 mg, 0.12 mmol) were dissolved in anhydrous toluene (5 mL) and deoxygenated with nitrogen for 15 min. $Pd(PPh_3)_4$ (6.7 mg, 0.006 mmol) was then added under nitrogen and the mixture was again flushed with nitrogen for 30 min. Then the reaction mixture was stirred at 110°C for 3 days under nitrogen atmosphere. Finally, the reaction mixture was cooled to room temperature and slowly added to methanol (150 mL). The precipitate was collected by filtration from methanol and further purified by Soxhlet extraction with methanol, acetone, petroleum ether, and chloroform in sequence. The chloroform fraction was evaporated by rotary evaporation. The final product was obtained as a black red solid (110 mg, 79.7%). ^{1}H NMR ($CDCl_3$, 400 MHz, δ/ppm): 9.16–9.11 (br, 4H), 7.76–6.74 (br, 16H), 4.14–4.08 (br, 4H), 3.71–3.64 (br, 4H), 1.97–1.95 (br, 4H), 1.78–1.30 (br, 32H), 0.91 (br, 24H). Anal. Calcd for $C_{72}H_{86}N_2O_4S_4$: C, 73.84; H, 7.35; N, 2.39; S, 10.94. Found: C, 73.44; H, 7.53; N, 2.39; S, 11.05. M_n = 25.7 KDa, PDI = 2.2.

2.2.8. Polymerization for PTBT-TTID

Following the similar method as **PTBT-TID**, **PTBT-TTID** was synthesized from monomer **M2** (99 mg, 0.099 mmol) and monomer **M3** (82 mg, 0.099 mmol), dried toluene (5 mL) and $Pd(PPh_3)_4$ (5.7 mg, 0.005 mmol). A black red solid was collected (120 mg, 88.9%). ^{1}H NMR ($CDCl_3$, 400 MHz, δ/ppm): 9.16–9.10 (br, 2H), 7.77–7.04 (br, 20H), 4.14–4.05 (br, 4H), 3.67–3.54 (br, 4H), 1.95–1.93 (br, 4H), 1.80–1.30 (br, 32H), 1.06–0.90 (br, 24H). Anal. Calcd for $C_{80}H_{90}N_2O_4S_6$: C, 71.96; H, 6.74; N, 2.09; S, 14.39. Found: C, 71.56; H, 6.96; N, 2.08; S, 14.45. M_n = 12.8 KDa, PDI = 1.7.

2.3. Instruments and characterizations

Nuclear magnetic resonance (NMR) spectra were measured with Bruker AVANCE 400 spectrometer. The elemental analysis was performed with an Elementar Vario EL III element analyzer for C, H, N, and S. MALDI-TOF mass spectrometric measurements were performed on Bruker Autoflex III. UV-Visible (UV-Vis) absorption spectra of the polymers were conducted on a Perkin-Elmer Lamada 25 UV-Vis-NIR spectrometer. The average molecular weight and polydispersity index (PDI) of the polymers were determined using Waters 1515 gel permeation chromatography (GPC) analysis with THF as eluent and polystyrene as standard. Thermogravimetric analysis (TGA) measurement was conducted on a Netzsch TG 209 analyzer under nitrogen at a heating rate of 20°C·min^{-1}. Electrochemical redox potentials were obtained by cyclic voltammetry (CV) using a three-electrode configuration and an electrochemistry workstation (ZAHNER ZENNIUM) at a scan rate of 50 mV·s^{-1}. CV was conducted on an electrochemistry workstation with the thin film on a Pt plate as the working electrode, Pt slice as the counter electrode, and Ag/AgCl electrode as the reference electrode. The supporting electrolyte is 0.1 M tetra-n-butylammonium hexafluorophosphate (Bu_4NPF_6) in anhydrous acetonitrile solution. All AFM measurements were performed on a Digital Instruments Enviro Scope in a tapping mode.

2.4. Fabrication and characterization of PSCs

The structure of the solar cells was indium tin oxide (ITO)/MoO_3(20 nm)/polymer:$PC_{61}BM$(~100 nm)/LiF(0.5 nm)/Al(100 nm). The PSC devices were fabricated with ITO glass as a positive electrode and LiF/Al as a negative electrode. The ITO glass was pre-cleaned and then modified by a thin layer of MoO_3, which was deposited on ITO surface by vacuum evaporation under 5·10^{-4} Pa. The photoactive layer was prepared by spin-coating a blend solution of polymer and $PC_{61}BM$ in CB on the surface of ITO/MoO_3 substrate. Then, the LiF/Al cathode was deposited on the polymer layer by vacuum evaporation under 5·10^{-4} Pa. The accurate area of every device is 3.8 mm^2, defined by the overlap of the ITO and metal electrode. The current density-voltage (*J–V*) curves were measured by a Keithley 2602 Source Meter under 100 mW·cm^{-2} standard AM 1.5G spectrum using a Sol 3A Oriel solar simulator. The incident light intensity was calibrated using a standard Si solar cell. The measurement of monochromatic incident photon-to-current conversion efficiency (IPCE) was performed using a Zolix Solar Cell Scan 100 QE/IPCE measurement system.

3. Results and discussion

3.1. Synthesis

The detailed synthetic routes of monomer **M2** and target copolymers were outlined in Figure 1. The compound **3** was synthesized by Stille coupling reaction. Compound **4** was gained by a bromination reaction. The compound **5** was obtained via a reduction reaction and subsequently transformed into compound **6** by a chlorination reaction. Compound **7** was synthesized by Arbuzov reaction. Then the monomer **M2** was obtained through Wittig-Horner reaction. Finally, two copolymers (**PTBT-TID** and **PTBT-TTID**) were synthesized by Stille coupling polymerization using Pd(0) as catalyst under nitrogen atmosphere. After the purification of the crude polymers to remove oligomeric materials by Soxhlet extraction with methanol, acetone, petroleum ether, and chloroform, the dark-red colored polymers were obtained. The structures of the monomers and copolymers were confirmed by ^{1}H NMR, ^{13}C NMR, and MALDI-TOF MS. The copolymers were found to have good solubility in most of the organic solvents such as chloroform, toluene, CB, and o-dichlorobenzene (ODCB) at room temperature. The number-average molecular weight (M_n) and polydispersity index (PDI) are 25.7 KDa and 2.2 for **PTBT-TID**, 12.8 KDa and 1.7 for **PTBT-TTID** (Table 1), determined by gel permeation chromatography (GPC) with THF as an eluent.

Table 1. Molecular weights and thermal properties of two copolymers

Copolymers	Yields [%]	M_n[a] [Kg·mol^{-1}]	M_w[b] [Kg·mol^{-1}]	PDI[c]	T_d[d] [°C]
PTBT-TID	79.7	25.7	57.0	2.2	381
PTBT-TTID	88.9	12.8	22.1	1.7	388

[a]Number-average molecular weight.
[b]Weight-average molecular weight.
[c]M_w/M_n.
[d]Decomposition temperature (5% weight loss) determined by thermal gravimetric analysis under nitrogen.

3.2. Thermal properties

The polymers were analyzed by thermal gravimetric analysis (TGA) and the results were summarized in Table 1. The polymers **PTBT-TID** and **PTBT-TTID** revealed high decomposition temperatures (T_d, 5% weight loss) of 381 and 388°C, respectively (Figure 2), indicating that the two polymers possessed excellent thermal and morphology stability, fully ensuring their application in PSCs.

3.3. Optical properties

The UV-Vis absorption spectra of the two copolymers **PTBT-TID** and **PTBT-TTID** in (a) diluted chloroform solutions (0.01 mg·mL^{-1}) and (b) solid films are shown in Figure 3, and the corresponding data are listed in Table 2. In diluted chloroform solution (Figure 3a), due to the overlap of the π-π* transition and intramolecular charge transfer (ICT) bands, both of the two copolymers showed one broad absorption band covering the wavelength range from 300 to 700 nm [27]. The maximum absorption wavelength (λ_{max}) of **PTBT-TID** and **PTBT-TTID** appeared at 475 and 481 nm, and the corresponding maximum molar extinction coefficients (ε) were $4.73 \cdot 10^4$ and $4.95 \cdot 10^4$ M^{-1}·cm^{-1}, respectively. Polymer **PTBT-TTID** exhibited a slight increase in ε with a positive impact on the short-circuit photocurrent density (J_{sc}). Generally, relatively larger ε value can enhance the J_{sc} [28], but the ε value of **PTBT-TTID** was only $0.22 \cdot 10^4$ M^{-1}·cm^{-1} larger than **PTBT-TID**. However, the absorption spectra of **PTBT-TID** were broader than that of **PTBT-TTID**, resulting in an apparently higher integrated current density in **PTBT-TID**-based device (see Figure 6a). As a result, **PTBT-TID** should get a higher J_{sc} than **PTBT-TTID**.

In addition, as shown in Figure 3b, the maximum absorption peaks in thin films were observed to approximately red-shift by 35 and 27 nm with respect to those in chloroform solution for **PTBT-TID** and

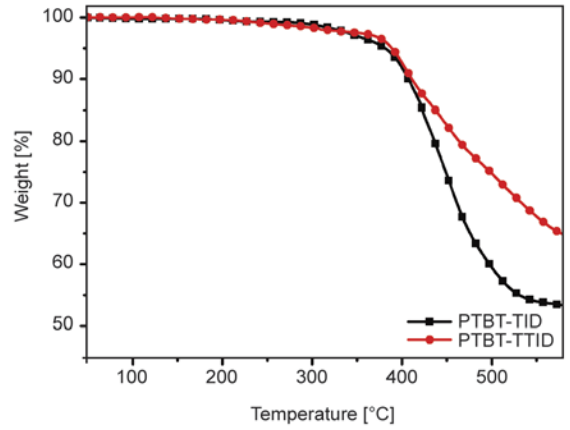

Figure 2. TGA curves of two copolymers with the scan rate of 20°C min^{-1}

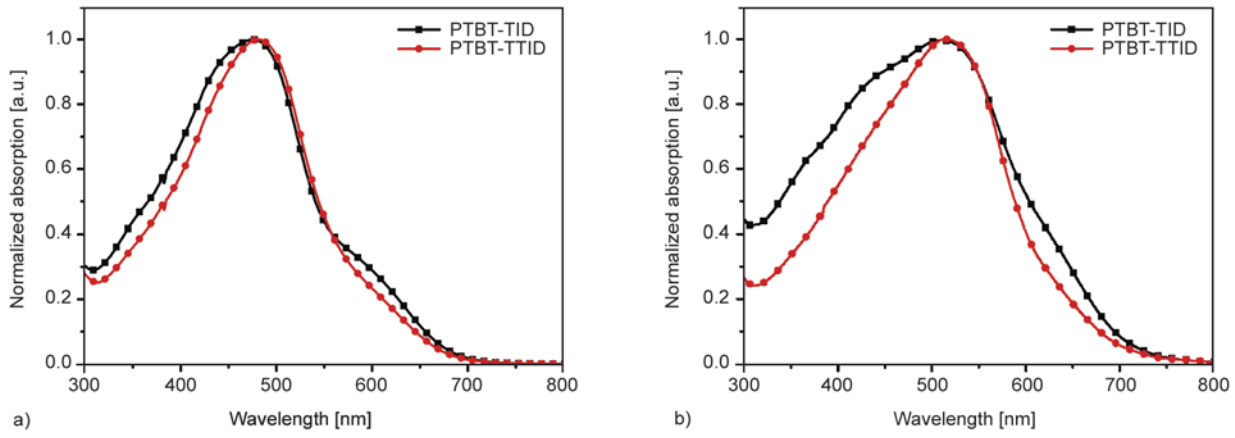

Figure 3. UV-Vis absorption spectra of two copolymers in (a) diluted chloroform solution and (b) thin films

Table 2. Optical and electrochemical properties of the two copolymers

Polymers	Solution $\lambda_{s,max}$[a] [nm]	Film $\lambda_{f,max}$[b] [nm]	E_g^{opt}[c] [eV]	HOMO[d] [eV]	LUMO[e] [eV]	E_g^{ec}[f] [eV]
PTBT-TID	475	510	1.79	–5.33	–3.59	1.74
PTBT-TTID	481	514	1.92	–5.22	–3.61	1.61

[a]Dilute chloroform solution.
[b]Thin film spin-cast from chloroform solution.
[c]Optical band gap determined from the onset of absorption in the solid state.
[d]HOMO = –e(E_{ox} + 4.22) [eV].
[e]LUMO = –e(E_{red} + 4.22) [eV].
[f]E_g^{ec} = – e(E_{HOMO} – E_{LUMO}) [eV].

PTBT-TTID, respectively, indicating the presence of aggregation or orderly π-π stacking in the solid state [29, 30]. Compared to **PTBT-TTID** film, **PTBT-TID** film showed a more red-shifted absorption peak than that in solution. Besides, **PTBT-TID** demonstrated a shoulder peak in the absorption range of 550–700 nm, while no apparent shoulder peak in the corresponding band could be observed for **PTBT-TTID**. These results indicated that **PTBT-TID** film formed a stronger molecular stacking than **PTBT-TTID** film [31], leading to an improved light absorption in long wavelength range. Simultaneously, it implied that **PTBT-TID** film would possess a higher hole-transporting ability. Thus, the polymer **PTBT-TID** should obtain a higher J_{sc} than **PTBT-TTID**. The optical band gaps (E_g^{opt}) calculated from the onset wavelengths of the film absorptions of **PTBT-TID** and **PTBT-TTID** were 1.79 and 1.92 eV, respectively.

3.4. Electrochemical properties

The highest occupied molecular orbital (HOMO) and lowest unoccupied molecular orbital (LUMO) energy levels of conjugated polymers are crucial for the application as photovoltaic materials in PSCs, and they can be measured from the onset oxidation and reduction potentials (E_{ox} and E_{red}) in the cyclic voltammograms of the polymers [32]. Figure 4 shows the cyclic voltammograms of two copolymer films. The results of the electrochemical properties are also summarized in Table 2. The cyclic voltammograms were recorded by using a Ag/AgCl reference electrode, which was calibrated against the redox potential of ferrocene/ferrocenium couple (Fc/Fc^+), whose energy level was assumed to be 4.8 eV below the vacuum level [19], and measured under the same condition as polymer sample to be 0.58 V. The corresponding HOMO and LUMO energy levels of polymers were calculated according to the equation: HOMO = –e(E_{ox} + 4.22) [eV], LUMO = –e(E_{red} + 4.22) [eV], where E_{ox} and E_{red} were the onset oxidation and reduction potential (vs. Ag/AgCl) of the two polymers, respectively.

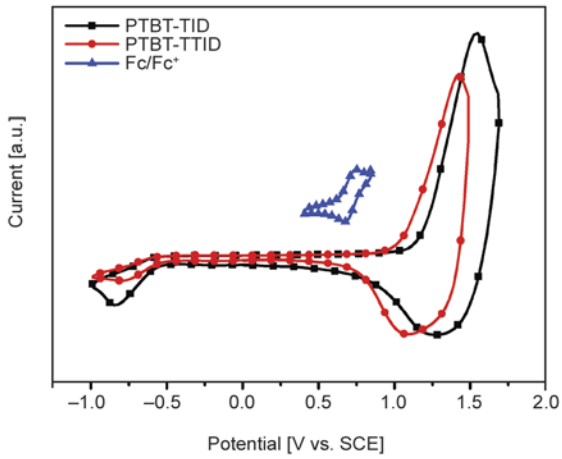

Figure 4. Cyclic voltammograms of the two copolymers

As shown in Table 2, E_{ox}/E_{red} of the two copolymers **PTBT-TID** and **PTBT-TTID** were 1.11/–0.63 and 1.00/–0.61 V, and the corresponding HOMO/LUMO energy levels were –5.33/–3.59 and –5.22/–3.61 eV, respectively. Both of the two copolymers exhibited lower HOMO energy levels than –5.20 eV, which was desirable for ambient stability to oxidation [33]. The deeper-lying HOMO energy level of **PTBT-TID** than **PTBT-TTID** showed that the PSC device based on **PTBT-TID** was expected to get better air stability [17] and higher V_{oc}. Their LUMO energy levels were above 0.3 eV higher than that of $PC_{61}BM$ (–4.02 eV), indicating sufficient driving force for electron transfer from polymer to $PC_{61}BM$ [34]. Therefore, the HOMO and LUMO energy levels of these two copolymers were suitable for their application as donor materials in PSCs. The electrochemical bang gaps (E_g^{ec}) of the two copolymers were estimated by the equation E_g^{ec} = –e(E_{HOMO} – E_{LUMO}) [eV] to be 1.74 and 1.61 eV, respectively.

The polymer **PTBT-TTID** possessed a higher-lying HOMO energy level due to the addition of thiophene units. Simultaneously, the LUMO energy levels of the two polymers were similar because of the same acceptor units. Therefore, the E_g^{ec} of **PTBT-TTID** was smaller than that of **PTBT-TID**. However, the E_g^{opt} of the former was larger than that of the later, which could be attributed to the different aggregation structure of these two polymers films. Usually, the E_g^{opt} of a conjugated polymer decreases with the increase of the molecular stacking in film [31, 35]. For example, the E_g^{opt} of the polymer P3 (1.70 eV) is largely smaller than its E_g^{ec} (2.11 eV) [36]. As mentioned before, **PTBT-TID** film possessed strong molecular stacking, so **PTBT-TID** film showed a small E_g^{opt}. While **PTBT-TTID** film possessed weak molecular stacking, so it showed a large E_g^{opt}. As a result, **PTBT-TID** film shows a smaller E_g^{opt} than that of **PTBT-TTID**.

3.5. Film morphology

To explore the effect of the morphology of active layers on the photovoltaic performances of the two copolymers, we investigated the surface morphologies of polymers/$PC_{61}BM$ (1/2, w/w) blends using an atomic force microscopy (AFM) in a tapping mode. As is well-known, the better morphology of the polymer could be beneficial for a higher fill factor (FF). Better morphology should include an ideal domain size of 10~20 nm of polymer and PCBM with an interpenetrating bicontinuous network, and both smaller (<10~20 nm) and larger (>10~20 nm) domain sizes of the blend films will limit charge transfer and separation [37]. Figure 5a, 5c demon-

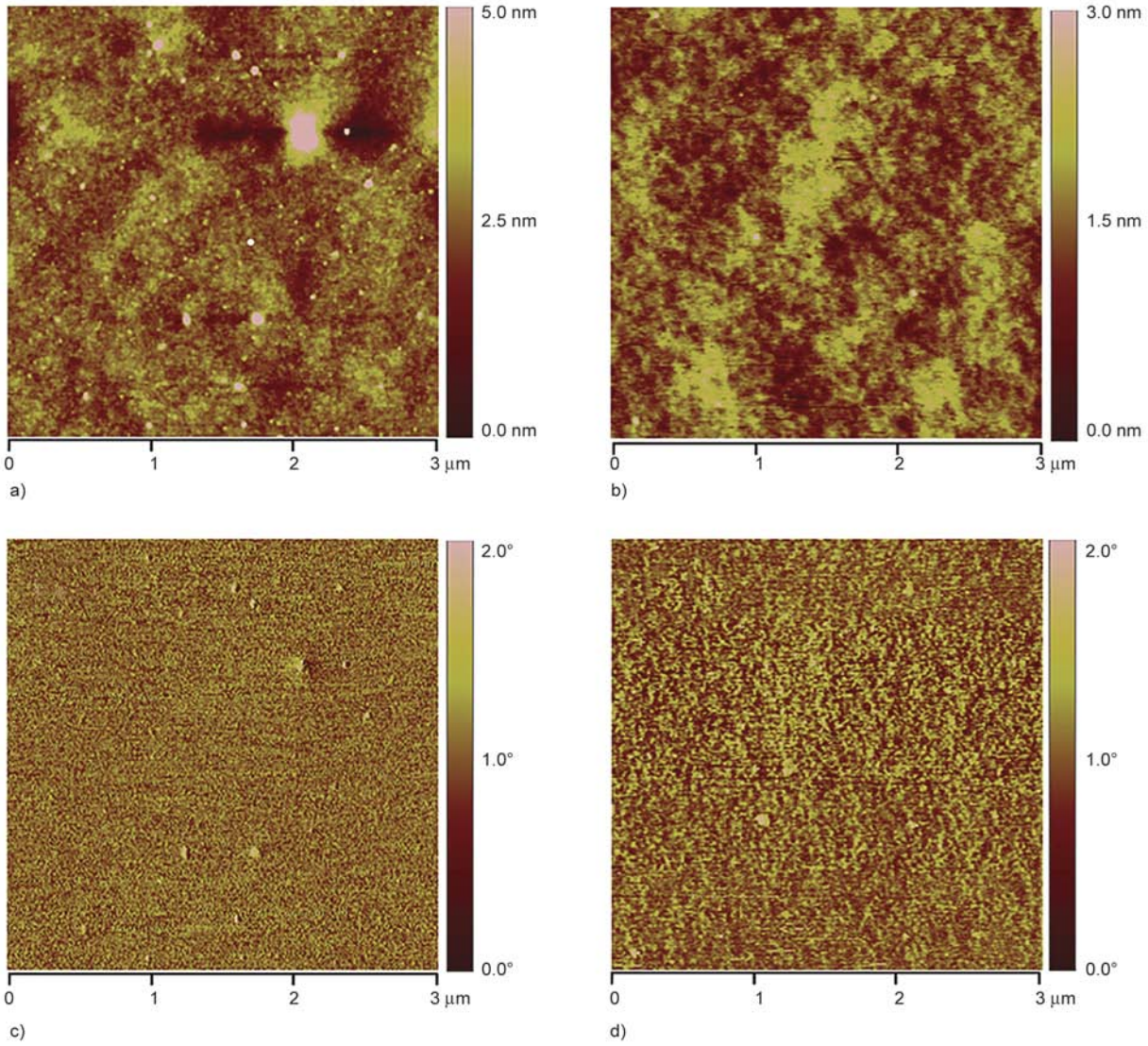

Figure 5. (a, b) AFM height images and (c, d) phase images (3×3 µm) of copolymers:$PC_{61}BM$ (1:2, w/w). (a), (c) for **PTBT-TID**. (b), (d) for **PTBT-TTID**.

strates the AFM height images and (Figure 5b, 5d) phase images of the active layer surfaces. The root-mean-square (rms) surface roughness for **PTBT-TID**/$PC_{61}BM$ and **PTBT-TTID**/$PC_{61}BM$ film was 0.695 and 0.348 nm, respectively. Generally, a rough surface might increase the heterojunction area and effectively reduce the charge-transport distance and at the same time provide a nano-scaled texture that further enhances internal light absorption [38, 39]. Thus, for the **PTBT-TID**/$PC_{61}BM$ film, the charge recombination at the interface was decreased which benefited the charge transport, resulting in a relatively high FF and photovoltaic performance. Furthermore, the suitable microphase separation of the **PTBT-TID**/$PC_{61}BM$ film could facilitate the diffusion and separation of excitons and charge transport, leading to a high J_{sc}, FF and PCE [40]. While the greater phase segregation of the **PTBT-TTID**/$PC_{61}BM$ blends presumably arose because of poor miscibility with the fullerene, causing a larger aggregation in film and the decrease in FF and PCE [41].

3.6. Hole mobility

In order to get a better understanding in the influence of charge carrier transport on photovoltaic performance, the hole mobility of the target copolymers was measured by using a space charge limit current (SCLC) method under the same condition. Hole-only devices were fabricated with the configuration of ITO/PEDOT:PSS (30 nm)/Polymer:$PC_{61}BM$/MoO_3 (10 nm)/Al (100 nm). And the corresponding data of the copolymers are summarized in Table 3. The calculated hole mobility of **PTBT-TID** and **PTBT-TTID** blend films was $3.0 \cdot 10^{-4}$ and $1.4 \cdot 10^{-4}$ $cm^2 \cdot V^{-1} \cdot s^{-1}$, respectively (Table 3). The relatively higher hole mobility of **PTBT-TID** than **PTBT-TTID** suggested that with the introduction of excessive thiophene units, the intermolecular charge transfer was blocked, resulting in a drop in charge transporting ability of **PTBT-TTID**. Meanwhile, this phenomenon presented that **PTBT-TID** could obtain a higher J_{sc} than **PTBT-TTID**.

3.7. Photovoltaic properties

To study the effect of new TBT donor and thiophene π-bridge on the photovoltaic properties of the two copolymers, BHJ PSCs with the same conventional device configuration of ITO/MoO_3 (20 nm)/polymer:$PC_{61}BM$/LiF (0.5 nm)/Al (100 nm) were fabricated. Figure 6a shows the incident photon to current conversion efficiency (IPCE) spectra, (Figure 6b) the current density-voltage (*J-V*) curves under the illumination of AM 1.5G, 100 $mW \cdot cm^{-2}$ and (Figure 6c) the *J-V* curves in the dark for the optimized PSC devices, respectively, with the detailed photovoltaic parameters summarized in Table 3.

We systematically investigated the performances of PSC devices based on these two copolymers under various conditions. Firstly, the blend ratios of **PTBT-TID**:$PC_{61}BM$ were optimized from 1:1, 1:2 to 1:3, and the optimized device prepared at a blend ratio of 1:2 exhibited the best PCE of 1.68%. Then we treated the active layers of **PTBT-TID**-based devices with different device-processing solvents from CB to ODCB. Generally, fast solvent evaporation conditions by relatively volatile CB induces less-ordered structure of the active layer, while the high-boiling solvent ODCB has a slower film-forming process, equal to the effect of solvent annealing, which is easy to form the photo-active layer with a better aggregation structure [42, 43]. Thus, the ODCB-processed device based on **PTBT-TID** got a better PCE of 2.04%. Moreover, to further optimize the device performance, 1,8-diiodooctane (DIO) as an additive was added, but no apparent improvement could be observed.

As shown in Figure 6a, the PSC device based on **PTBT-TID** exhibited a relatively strong IPCE response ranging from 350 to 500 nm with maximum IPCE value of 40% at 477 nm, while the IPCE

Table 3. Photovoltaic parameters of PSC devices based on two copolymers

Polymers	Thickness [nm]	D/A blend ratio	Solvent	J_{sc} [$mA \cdot cm^{-2}$]	V_{oc} [V]	FF	PCE_{max} (PCE_{ave}) [%]	$\mu_{h\ ave}$ [$cm^2 \cdot V^{-1} \cdot s^{-1}$]
PTBT-TID[a]	96	1:1	CB	4.45	0.81	0.37	1.34 (1.27±0.07)	
PTBT-TID[a]	98	1:2	CB	5.13	0.79	0.41	1.68 (1.59±0.10)	
PTBT-TID[a]	94	1:3	CB	4.74	0.84	0.38	1.49 (1.47±0.01)	
PTBT-TID[a]	88	1:2	ODCB	5.39	0.83	0.45	2.04 (2.02±0.01)	$3.0 \cdot 10^{-4}$
PTBT-TTID[a]	86	1:2	ODCB	4.47	0.79	0.39	1.36 (1.30±0.04)	$1.4 \cdot 10^{-4}$

The structure of fabricated devices: [a]ITO/MoO_3 (20 nm)/polymer:$PC_{61}BM$/LiF(0.5 nm)/Al(100 nm).

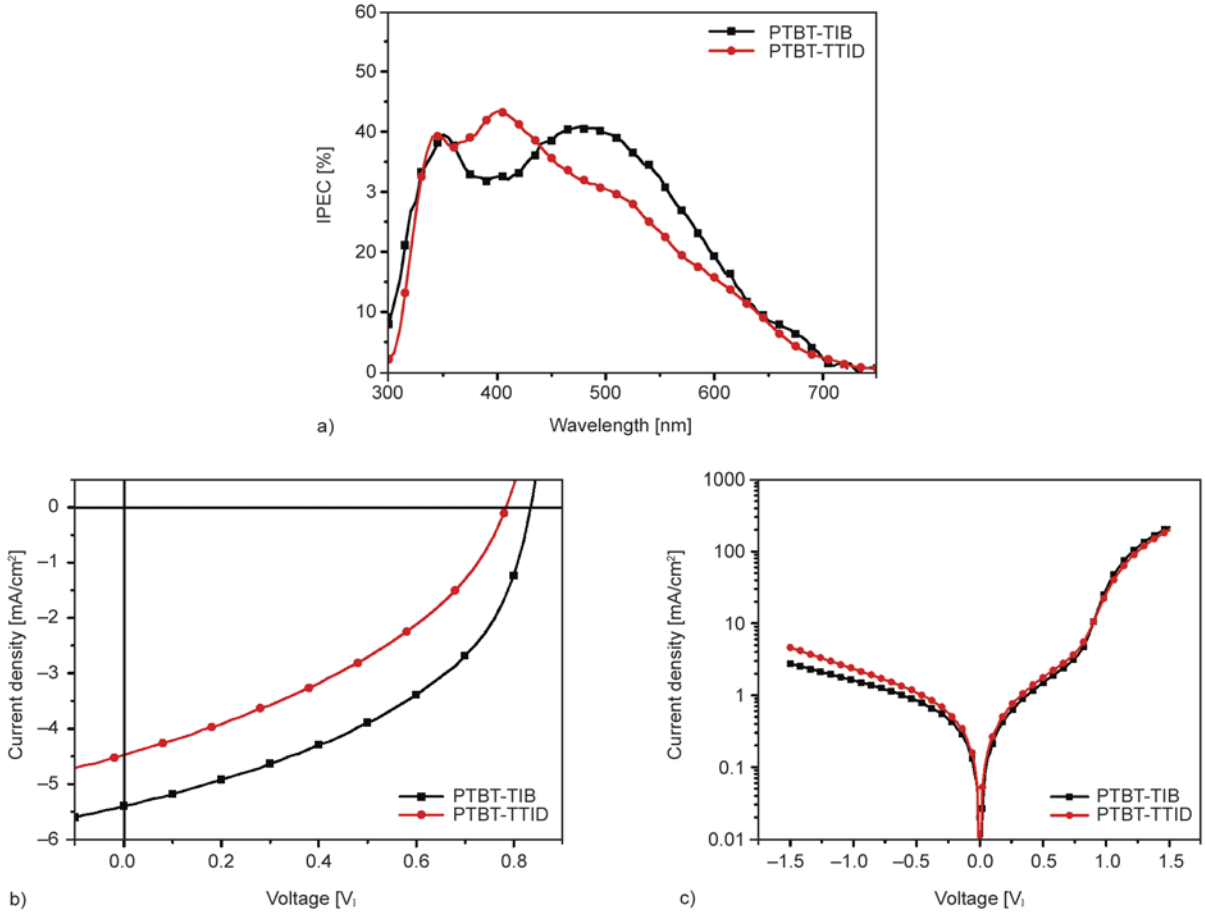

Figure 6. (a) IPCE curves, (b) *J-V* curves under the illumination of AM 1.5 G, 100 mW·cm^{-2} and (c) *J-V* curves in the dark for the optimized PSC devices based on the two copolymers

curve of PTBT-TTID-based device displayed an obvious falling tendency from the wavelength of 400 nm, indicating its narrow spectral response range and lower absorptivity in long wave. Although the absorption spectrum shapes and maximum absorption peak positions of **PTBT-TID** and **PTBT-TTID** films were very similar, **PTBT-TID** showed a broader absorption spectrum with respect to **PTBT-TTID**, which would benefit the IPCE response. Besides, IPCE is related to not only the absorption spectra in thin film, but also the electron transport. So there is often a difference between the IPCE curves and UV-Vis absorption spectra [44, 45]. These results were in good accordance with the J_{sc} variation obtained in *J-V* measurements (Figure 6b). From the dark *J-V* characteristics (Figure 6c), it was clear that the **PTBT-TID**-based device showed a lower leakage current (thus a higher shunt resistance) and a little smaller series resistance, resulting in a higher J_{sc} for **PTBT-TID-based** device when compared to the **PTBT-TTID-based** one [46].

Consequently, the PSC device based on **PTBT-TID** obtained a relatively higher PCE value of 2.04%, with a higher J_{sc} of 5.39 mA·cm^{-2}, a higher V_{oc} of 0.83 V, and a higher FF of 0.45. While the device based on **PTBT-TTID** only got the PCE of 1.36% on the same condition.

4. Conclusions

In a word, based on the new TBT unit and side-chain ID unit as well as the introduction of thiophene π-bridge, two novel side-chain conjugated copolymers **PTBT-TID** and **PTBT-TTID** were designed and synthesized. Both of these two copolymers exhibited good solubility and excellent thermal stability, and all of the PSC devices based on them obtained high V_{oc} values around 0.8 V. The addition of excessive thiophene units distorted the polymer backbone and then lowered the hole mobility of **PTBT-TTID**, resulting in a drop in PCE value. As a result, the device based on **PTBT-TID** showed the relatively higher J_{sc}, V_{oc} and FF values, which

resulted from a better overlap of the absorption spectrum with solar spectrum, a relatively higher hole mobility, a lower HOMO energy level, a stronger IPCE response and a better microphase separation, leading to a higher PCE of 2.04% than the device based on **PTBT-TTID** (1.36%) on the same measured condition. Although the PCEs of these two copolymers are not high, the copolymers **PTBT-TID** and **PTBT-TTID** have great potential application in ternary solar cells due to the good compatibility with the fullerene acceptor, resulting in the less phase separation of the active layers. And it can be expected to obtain more polymer materials with better photovoltaic performances through the further optimization and control of polymerization units in the future.

Acknowledgements

This work was supported by the National Natural Science Foundation of China (21474081), and Hunan Provincial Natural Science Foundation of China (13JJ2025).

References

[1] Li Y., Zou Y.: Conjugated polymer photovoltaic materials with broad absorption band and high charge carrier mobility. Advanced Materials, **20**, 2952–2958 (2008). DOI: 10.1002/adma.200800606

[2] Xu Q., Wang J., Chen S., Li W., Wang H.: Synthesis and characterization of naphthalene diimide polymers based on donor-acceptor system for polymer solar cells. Express Polymer Letters, **7**, 842–851 (2013). DOI: 10.3144/expresspolymlett.2013.81

[3] Yang J., Clark N., Long M., Xiong J., Jones D. J., Yang B., Zhou C.: Solution stability of active materials for organic photovoltaics. Solar Energy, **113**, 181–188 (2015). DOI: 10.1016/j.solener.2015.01.001

[4] Wang T. L., Shieh Y. T., Yang C. H., Ho T. H., Chen C. H.: Photovoltaic properties and annealing effects of a low bandgap copolymer containing dithienothiophene and benzothiadiazole units. Express Polymer Letters, **7**, 63–75 (2012). DOI: 10.3144/expresspolymlett.2013.6

[5] Zou Y., Najari A., Berrouard P., Beaupré S., Réda Aïch B., Tao Y., Leclerc M.: A thieno[3,4-*c*]pyrrole-4,6-dione-based copolymer for efficient solar cells. Journal of the American Chemical Society, **132**, 5330–5331 (2010). DOI: 10.1021/ja101888b

[6] Chu T-Y., Lu J., Beaupré E. S., Zhang Y., Pouliot J-R., Wakim S., Zhou J., Leclerc M., Li Z., Ding J., Tao Y.: Bulk heterojunction solar cells using thieno[3,4-c]pyrrole-4,6-dione and dithieno[3,2-b:2′,3′-*d*]silole copolymer with a power conversion efficiency of 7.3%. Journal of the American Chemical Society, **133**, 4250–4253 (2011). DOI: 10.1021/ja200314m

[7] Chang C-Y., Zuo L., Yip H-L., Li Y., Li C-Z., Hsu C-H., Cheng Y-J., Chen H., Jen A. K-Y.: A versatile fluoro-containing low-bandgap polymer for efficient semitransparent and tandem polymer solar cells. Advanced Functional Materials, **23**, 5084–5090 (2013). DOI: 10.1002/adfm201301557

[8] Lanzi M., Paganin L., Errani F.: Synthesis, characterization and photovoltaic properties of a new thiophene-based double-cable polymer with pendent fullerene group. Polymer, **53**, 2134–2145 (2012). DOI: 10.1016/j.polymer.2012.03.040

[9] Yusoff A. R. B. M., Kim D., Kim H. P., Shneider F. K., Da Silva W. J., Jang J.: A high efficiency solution processed polymer inverted triple-junction solar cell exhibiting a power conversion efficiency of 11.83%. Energy and Environmental Science, **8**, 303–316 (2015). DOI: 10.1039/C4EE03048F

[10] Yang Y. M., Chen W., Dou L., Chang W-H., Duan H-S., Bob B., Li G., Yang Y.: High-performance multiple-donor bulk heterojunction solar cells. Nature Photonics, **9**, 190–198 (2015). DOI: 10.1038/nphoton.2015.9

[11] An Q., Zhang F., Li L., Wang J., Zhang J., Zhou L., Tang W.: Improved efficiency of bulk heterojunction polymer solar cells by doping low-bandgap small molecules. ACS Applied Materials and Interfaces, **6**, 6537–6544 (2014). DOI: 10.1021/am500074s

[12] An Q., Zhang F., Li L., Wang J., Sun Q., Zhang J., Tang W., Deng Z.: Simultaneous improvement in short circuit current, open circuit voltage, and fill factor of polymer solar cells through ternary strategy. ACS Applied Materials and Interfaces, **7**, 3691–3698 (2015). DOI: 10.1021/acsami.5b00308

[13] An Q., Zhang F., Zhang J., Tang W., Wang Z., Li L., Xu Z., Teng F., Wang Y.: Enhanced performance of polymer solar cells through sensitization by a narrow band gap polymer. Solar Energy Materials and Solar Cells, **118**, 30–35 (2013). DOI: 10.1016/j.solmat.2013.07.050

[14] Ameri T., Khoram P., Min J., Brabec C. J.: Organic ternary solar cells: A review. Advanced Materials, **25**, 4245–4266 (2013). DOI: 10.1002/adma.201300623

[15] Pop F., Amacher A., Avarvari N., Ding J., Daku L. M. L., Hauser A., Koch M., Hauser J., Liu S., Decurtins S.: Tetrathiafulvalene-benzothiadiazoles as redox-tunable donor–acceptor systems: Synthesis and photophysical study. Chemistry – A European Journal, **19**, 2504–2514 (2013).
DOI: 10.1002/chem.201202742

[16] Deng P., Xiong J., Li S., Wu Y., Yang J., Zhang Q.: Random copolymers based on thieno[3,4-*c*]pyrrole-4,6-dione and isoindigo building blocks for polymer solar cells. Chinese Journal of Chemistry, **32**, 521–526 (2014).
DOI: 10.1002/cjoc.201400316

[17] Zhang Z-G., Liu Y-L., Yang Y., Hou K., Peng B., Zhao G., Zhang M., Guo X., Kang E., Li Y.: Alternating copolymers of carbazole and triphenylamine with conjugated side chain attaching acceptor groups: Synthesis and photovoltaic application. Macromolecules, **43**, 9376–9383 (2010).
DOI: 10.1021/ma101491c

[18] Hou J., Tan Z., Yan Y., He Y., Yang C., Li Y.: Synthesis and photovoltaic properties of two-dimensional conjugated polythiophenes with bi(thienylenevinylene) side chains. Journal of the American Chemical Society, **128**, 4911–4916 (2006).
DOI: 10.1021/ja060141m

[19] Bin H., Xiao L., Liu Y., Shen P., Li Y.: Effects of donor unit and π-bridge on photovoltaic properties of D–A copolymers based on benzo[1,2-*b*:4,5-*c*′]-dithiophene-4,8-dione acceptor unit. Journal of Polymer Science Part A: Polymer Chemistry, **52**, 1929–1940 (2014).
DOI: 10.1002/pola.27209

[20] Li Q., Zhong C., Huang J., Huang Z., Pei Z., Liu J., Qin J., Li Z.: Conjugated polymers with pyrrole as the conjugated bridge: Synthesis, characterization, and two-photon absorption properties. Journal of Physical Chemistry B, **115**, 8679–8685 (2011).
DOI: 10.1021/jp2015484

[21] Stalder R., Mei J., Reynolds J. R.: Isoindigo-based donor–acceptor conjugated polymers. Macromolecules, **43**, 8348–8352 (2010).
DOI: 10.1021/ma1018445

[22] Lei T., Cao Y., Fan Y., Liu C-J., Yuan S-C., Pei J.: High-performance air-stable organic field-effect transistors: Isoindigo-based conjugated polymers. Journal of the American Chemical Society, **133**, 6099–6101 (2011).
DOI: 10.1021/ja111066r

[23] Mahmood K., Liu Z-P., Li C., Lu Z., Fang T., Liu X., Zhou J., Lei T., Pei J., Bo Z.: Novel isoindigo-based conjugated polymers for solar cells and field effect transistors. Polymer Chemistry, **4**, 3563–3574 (2013).
DOI: 10.1039/c3py00341h

[24] Wang C., Zhao B., Cao Z., Shen P., Tan Z., Li X., Tan S.: Enhanced power conversion efficiencies in bulk heterojunction solar cells based on conjugated polymer with isoindigo side chain. Chemical Communications, **49**, 3857–3859 (2013).
DOI: 10.1039/c3cc40620b

[25] Gu Z., Tang P., Zhao B., Luo H., Guo X., Chen H., Yu G., Liu X., Shen P., Tan S.: Synthesis and photovoltaic properties of copolymers based on benzo[1,2-*b*:4,5-*b*′] dithiophene and thiophene with different conjugated side groups. Macromolecules, **45**, 2359–2366 (2012).
DOI: 10.1021/ma202399n

[26] Hou R., Zhao B., Wu F., Wang G., Shen T., Guo H., Zhang J., Chen H., Tan S.: Synthesis, characterization, and photovoltaic performance of the polymers based on thiophene-2,5-bis((2-ethylhexyl)oxy) benzene-thiophene. Organic Electronics, **20**, 142–149 (2015).
DOI: 10.1016/j.orgel.2015.02.011

[27] Patra D., Chiang C-C., Chen W-A., Wei K-I., Wu M-C., Chu C-W.: Solution-processed benzotrithiophene-based donor molecules for efficient bulk heterojunction solar cells. Journal of Materials Chemistry A, **1**, 7767–7774 (2013).
DOI: 10.1039/c3ta11544e

[28] Dong Y., Hu X., Duan C., Liu P., Liu S., Lan L., Chen D., Ying L., Su S., Gong X., Huang F., Cao Y.: A series of new medium-bandgap conjugated polymers based on naphtho[1,2-c:5,6-c]bis(2-octyl-[1,2,3]triazole) for high-performance polymer solar cells. Advanced Materials, **25**, 3683–3688 (2013).
DOI: 10.1002/adma.201301547

[29] Spano F. C., Silva C.: H- and J-aggregate behavior in polymeric semiconductors. Annual Review of Physical Chemistry, **65**, 477–500 (2014).
DOI: 10.1146/annurev-physchem-040513-103639

[30] Chang W-H., Gao J., Dou L., Chen C-C., Liu Y., Yang Y.: Side-chain tunability *via* triple component random copolymerization for better photovoltaic polymers. Advanced Energy Materials, **4**, 1300864/1–1300864/6 (2013).
DOI: 10.1002/aenm.201300864

[31] Shen P., Bin H., Zhang Y., Li Y.: Synthesis and optoelectronic properties of new D–A copolymers based on fluorinated benzothiadiazole and benzoselenadiazole. Polymer Chemistry, **5**, 567–577 (2014).
DOI: 10.1039/c3py00968h

[32] Pommerehne J., Vestweber H., Guss W., Mahrt R. F., Bässler H., Porsch M., Daub J.: Efficient two layer LEDs on a polymer blend basis. Advanced Materials, **7**, 551–554 (1995).
DOI: 10.1002/adma.19950070608

[33] Thompson B. C., Kim Y-G., Reynolds J. R.: Spectral broadening in MEH-PPV:PCBM-based photovoltaic devices *via* blending with a narrow band gap cyanovinylene–dioxythiophene polymer. Macromolecules, **38**, 5359–5362 (2005).
DOI: 10.1021/ma0505934

[34] Brédas J-L., Beljonne D., Coropceanu V., Cornil J.: Charge-transfer and energy-transfer processes in π-conjugated oligomers and polymers: A molecular picture. Chemical Reviews, **104**, 4971–5004 (2004). DOI: 10.1021/cr040084k

[35] Wang M., Hu X., Liu L., Duan C., Liu P., Ying L., Huang F., Cao Y.: Design and synthesis of copolymers of indacenodithiophene and naphtho[1,2-*c*:5,6-*c*]bis (1,2,5-thiadiazole) for polymer solar cells. Macromolecules, **46**, 3950–3958 (2013). DOI: 10.1021/ma400355w

[36] Wang N., Chen Z., Wei W., Jiang Z.: Fluorinated benzothiadiazole-based conjugated polymers for high-performance polymer solar cells without any processing additives or post-treatments. Journal of the American Chemical Society, **135**, 17060–17068 (2013). DOI: 10.1021/ja409881g

[37] Peng Q., Liu X., Qin Y., Zhou D., Xu J.: Thieno[3,4-b]pyrazine-based low bandgap photovoltaic copolymers: Turning the properties by different aza-heteroaromatic donors. Journal of Polymer Science Part A: Polymer Chemistry, **49**, 4458–4467 (2011). DOI: 10.1002/pola.24887

[38] Chang Y-T., Hsu S-L., Chen G-Y., Su M-H., Singh T. A., Diau E. W-G., Wei K.: Intramolecular donor–acceptor regioregular poly(3-hexylthiophene)s presenting octylphenanthrenyl-imidazole moieties exhibit enhanced charge transfer for heterojunction solar cell applications. Advanced Functional Materials, **18**, 2356–2365 (2008). DOI: 10.1002/adfm.200701150

[39] Li G., Shrotriya V., Huang J., Yao Y., Moriarty T., Emery K., Yang Y.: High-efficiency solution processable polymer photovoltaic cells by self-organization of polymer blends. Nature Materials, **4**, 864–868 (2005). DOI: 10.1038/nmat1500

[40] Shi Q., Fan H., Liu Y., Chen J., Ma L., Hu W., Shuai Z., Li Y., Zhan X.: Side chain engineering of copolymers based on bithiazole and benzodithiophene for enhanced photovoltaic performance. Macromolecules, **44**, 4230–4240 (2011). DOI: 10.1021/ma200576y

[41] Jiang J-M., Chen H-C., Lin H-K., Yu C-M., Lan S-C., Liu C-M., Wei K-H.: Conjugated random copolymers of benzodithiophene–benzooxadiazole–diketopyrrolopyrrole with full visible light absorption for bulk heterojunction solar cells. Polymer Chemistry, **4**, 5321–5328 (2013). DOI: 10.1039/C3PY00132F

[42] Chu C-W., Yang H., Hou W-J., Huang J., Li G., Yang Y.: Control of the nanoscale crystallinity and phase separation in polymer solar cells. Applied Physics Letters, **92**, 103306/1–103306/3 (2008). DOI: 10.1063/1.2891884

[43] Liu F., Gu Y., Wang C., Zhao W., Chen D., Briseno A. L., Russell T. P.: Efficient polymer solar cells based on a low bandgap semi-crystalline DPP polymer-PCBM blends. Advanced Materials, **24**, 3947–3951 (2012). DOI: 10.1002/adma.201200902

[44] Hasobe T., Imahori H., Fukuzumi S., Kamat P. V.: Light energy conversion using mixed molecular nanoclusters. porphyrin and C_{60} cluster films for efficient photocurrent generation. Journal of Physical Chemistry B, **107**, 12105–12112 (2003). DOI: 10.1021/jp035854v

[45] Tezuka N., Umeyama T., Matano Y., Shishido T., Kawasaki M., Nishi M., Hirao K., Lehtivuori H., Tkachenko N. V., Lemmetyinen H., Honsho Y., Seki S., Imahori H.: Good solvent effects of C_{70} cluster formations and their electron-transporting and photoelectrochemical properties. Journal of Physical Chemistry B, **114**, 14287–14297 (2010). DOI: 10.1021/jp911141s

[46] Savva A., Petraki F., Elefteriou P., Sygellou L., Voigt M., Giannouli M., Kennou S., Nelson J., Bradley D. D. C., Brabec C. J., Choulis S. A.: The effect of organic and metal oxide interfacial layers on the performance of inverted organic photovoltaics. Advanced Energy Materials, **3**, 391–398 (2013). DOI: 10.1002/aenm.201200317

eXPRESS Polymer Letters Vol.9, No.11 (2015) 1040–1051
Available online at www.expresspolymlett.com
DOI: 10.3144/expresspolymlett.2015.93

Mechanical performance of double gated injected metallic looking polypropylene parts

M. A. Costantino[1], *V. Pettarin*[1*], *A. J. Pontes*[2], *P. M. Frontini*[1]

[1]Institute of Materials Science & Technology (INTEMA) CONICET-University of Mar del Plata, Juan B. Justo 4302, B7608FDQ Mar del Plata, Argentina
[2]Institute for Polymers and Composites, IPC/I3N, Department of Polymer Engineering, University of Minho, Campus de Azurém, 4800-058 Guimaraes, Portugal

Received 20 February 2015; accepted in revised form 2 July 2015

Abstract. The metallic effect obtained by incorporation of metal particles in polymers by injection molding has the advantage of eliminating post-processing techniques reducing production cost and time. Nevertheless, undesired defects in the final appearance of parts are common. In this work PP/aluminum pigments were obtained by direct injection molding and the influence of metallic particles on the aesthetic, morphological and mechanical properties of the parts was assessed. Aesthetic aspects could be improved by manipulating processing conditions: high melt temperatures diminished differential shrinkage and made weld lines less noticeable. Also at high melt temperatures Al particles increased thermal conductivity of PP generating a thicker skin, which combined with an inherent gradient temperature and typical shear stresses developed during injection molding, induced the formation of β-PP phase. Mechanical performance of parts showed to be dependent on PP morphology. Distinct deformation behaviors were seen according to the presence of PP polymorph, β-PP counteracting the detrimental effect of not bonded Al flakes, and making PP-Al moldings to have similar toughness as PP moldings with the added value of metallic looking.

Keywords: *polymer composites, processing technologies, mechanical properties, fracture, morphology-performance relationship*

1. Introduction

New materials and new technologies have been developed to eliminate the existing gaps in terms of aesthetic products. Innovation, cost and weight reduction are some factors driving for the replacement of metals by plastics. Plastics continue to offer attractive solutions for design engineers. The metallic effects of the plastics came to revolutionize the automotive industry, packaging and appliances, replacing the metal by plastic in various components. Thus, attributing the quality and prestige of the metal and adding value to products [1].

The imitation of metal by plastic has increased notably through the addition of metallic pigments in thermoplastic materials. The composite obtained has the main advantage of eliminating post-processing operations. The mixtures made of thermoplastic polymers and metal fillers represent an important group of engineering materials with a wide range of applications including electric and thermal conduction, mechanical properties and aesthetic effects. Rusu *et al*. [2] studied the mechanical and thermal properties of HDPE/Zinc composites. They found an increase of thermal diffusivity and thermal conductivity and a decrease of mechanical properties. Gungor [3] investigated experimentally the effect of Fe powder (5, 10 and 15 vol%) on the physical and mechanical properties of HDPE and found that Fe

*Corresponding author, e-mail: pettarin@fi.mdp.edu.ar

particles reduced the yield and tensile strength, percentage of elongation and Izod impact strength (notched) of HDPE. Wang *et al*. [4] worked with PP filled with cooper particles and reported that the presence and size of the filler influence electrical and thermal properties.

Metal particles have different sizes and shapes. Those having a plate like shape promote the increase of reflected light in a specular way, increasing the luster and metallic appearance of surfaces [5]. The appearance of flow lines and welded lines caused by the orientation of the pigment flakes perpendicularly to the surface [6, 7] significantly affects the appearance of the injection molded part. Adjusting the processing conditions can minimize these defects. It has been pointed out that an increase in mold and injection temperatures causes the disorientation of flakes, which in turn, attenuates weld/flow lines. The changing of size and size distribution of metal particles are alternatives to minimize these defects. Park *et al*. [8] carried out experimental studies of ABS plus aluminum flakes using a Jeffery model to understand the orientation kinematics of pigment flakes during the injection molding process. They found that the flake orientation has a sandwich structure due to inhomogeneous shear rate along the thickness direction, besides at the weld line zone they saw a different orientation, which is the result of fountain flow and rapid cooling near the wall. Martins *et al*. [9] studied the influence of the metallic particles content and type on the aesthetic properties of weld lines in PP injected molded parts and found several types of undesired effects, such as weld lines and warpage that are dependent on the type and size of particles, on the load content and also on the processing conditions used. Santos *et al*. [10] studied the metallic pigments influence on the aesthetic and morphological properties of the PP injected parts finding that the particles are aligned perpendicularly to the surface causing a dark line in the region of the weld line. Simultaneously they observed a change in the skin thickness especially in the case of Al pigments.

When dealing with semicrystalline polymers such as PP, morphology is an important feature since it greatly affects performance of injected parts. The morphology of melt-crystallized polymers is known to be related to the fabrication technique. In compression molding, for example, where polymers crystallize from a quiescent melt, the morphology is spherulitic. In injection molding, polymers crystallize from a melt that has been exposed to flow, shear, and temperature variations. Also, a typical structure consisting of skin, shear layer and core develops. Due to the sudden cooling of the part in the cold mold walls, the skin is characterized by very high chain orientation. The shear layer appears between the skin and the core and is characterized by having an undeveloped spherulitic structure [11]. Finally, in the core, well developed spherulitic structure is observed. In PP parts, three basic crystalline forms of PP (α, β, γ) can be identified [12]. Among all crystal structures, the α-phase obtained under ordinary industrial processing conditions is the most stable. However, β-phase is occasionally observed during crystallization from melt. It can be obtained mainly by introducing specific nucleating agents in the melt using processing equipment such as extruders [13–15] incorporating an appropriate filler in micron and nanometer scale in the melt using internal mixers and extruders [16, 17], inducing temperature gradients [18] and by shear forces in controlled flow fields [19–21]. A toughness improvement is associated to β-PP, being attributed to the development of a more perfect crystalline structure, with higher continuity of the amorphous phase and more connecting bridges between individual crystallites than a material containing solely α-crystallites [22]; and to the occurrence of a β-α transformation during loading which is accompanied with volume contraction in respect to the related crystallographic densities [23].

Aluminum pigments have not been favored in the past for injection molded PP parts for several reasons. If they were used as powders there was always the concern that they could present a hazard. Aluminum pigments cause flow lines in injection molded parts which in most cases can not be tolerated. Even though new technologies have been developed to improve the use of metallic pigments in polymers, there is still no deep analysis of the effect of the addition of these particles in the morphological and mechanical performance of PP injected parts.

Melt temperature and mold temperature affect the temperature gradient and shear rate, two variables which are inherent to the injection-molding process and which are expected to influence crystallization and polypropylene morphology [24]. Viana *et al*. [25] identified the significant processing variables affecting the development of the morphological parameters. They found out that the morphology

(level of molecular orientation and degree of crystallinity) is mostly governed by the melt temperature and the degree of crystallinity of the core is essentially dominated by the mould temperature. Demiray *et al*. [26] studied the relationship between processing conditions and skin–core morphology of PP. They concluded that the melt temperature is the most important variable affecting the skin layer thickness and spherulite size distribution.

In this work double gated PP and PP/Al moldings were prepared varying melt and mold temperatures, as identified as the most influencing processing parameters. A complete characterization is therefore reported, which includes an aesthetical analysis, morphological evaluation and mechanical and fracture characterization. The influence of singularities induced by flow pattern such as weld lines and the injection gates on the arrangement of mechanical performance in the molding was also explored.

2. Experimental

2.1. Materials and processing

Polypropylene (PP) copolymer powder from ICORENE with specific gravity of 0.9 g/cm^3 and a melt flow index of 13 g/10 min (190°C, 2.16 kg), was used in this study. The pigment used was Silberline 21075 aluminum flake particles of 75 microns provided by Poliversal S.A. which consists of 70% nominal weight of Al particles and 30% nominal weight of carrier, and is compatible with a wide range of thermoplastics. The mixture of metallic particles with PP was done in a rotary drum, using 2 wt% of metal particles; this content based on previous results [9]. Rheological performance of materials was evaluated in an Anton Paar rheometer, Physica MCR-301, and it was verified that PP behavior was not influenced by the presence of Al flakes (Figure 1).

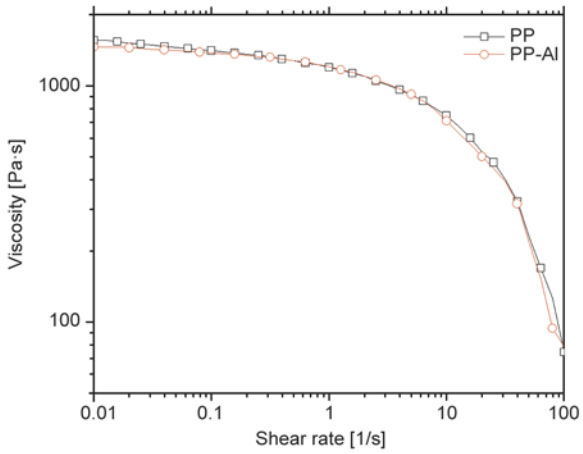

Figure 1. Rheological curves of PP and PP-Al as determined in a plate-cone configuration at 220°C

Table 1. Design of processing programme

Condition	T_{inj} [°C]	T_{mould} [°C]
1	190	25
2	190	40
3	190	55
4	190	70
5	220	70
6	220	55
7	220	40
8	220	25
9	250	25
10	250	40
11	250	55
12	250	70

Two gated boxes of dimensions: 152 mm width, 73 mm length, 16 mm height and 1,6 mm thick were processed in an injection molding machine Ferromatik-Milacron K85 (injection speed = 60 mm/s; injection pressure = 45 bar; injection time = 1 s; packing pressure = 35 bar; packing speed = 30 mms/s; packing time = 5 s; cooling time = 20 s; cycle time = 34 s). To determine the influence of processing conditions on morphology and therefore in performance of moldings, injection temperature (T_{inj}) and mould temperature (T_{mold}) were varied following Table 1.

2.2. Part features and defects

The shrinkage (S) of moldings was measured on a minimum of three specimens for each condition and in four different zones of the samples: three measurements in the width and one in the length. Measurements were done after 24 hours of parts processing with a digital caliper. Parts were stored in controlled temperature and humidity conditions. Shrinkage was determined using the following Equation (1):

$$S_L = \frac{l_M - l}{l_M} \text{ and } S_W = \frac{w_M - w}{w_M} \quad (1)$$

where l and w refers to the length and width of the part; l_M and w_M represents the mould cavity dimensions.

Also the superficial distribution of Al particles in PP moldings was observed with an optical metallographic microscope Olympus PMG3. Reflected light micrographs were analyzed with Software 'Image Pro Plus' and superficial percentage of Al particles

was obtained from a minimum of three specimens for each condition.

2.3. Mechanical performance

Mechanical performance of the moldings was evaluated at different locations of the boxes to evaluate the influence of in-homogeneities. Performance was evaluated by means of the stress intensity factor (K_{Ic}) plus the propagation value of the strain energy release rate (G_{cp}) at quasi-static conditions, and trough biaxial impact resistance (I_{bt}) under impact conditions.

Fracture tests were carried out on mode I double edge-notched tensile specimens (DENT) cut from the moldings (nominal width, W, of 30 mm, nominal crack to depth ratio, a/W, of 0.5, and nominal length, S, of 70 mm), at a crosshead speed of 2 mm/min and room temperature in an Instron 4467 universal testing machine. Sharp notches were introduced by scalpel-sliding a razor blade having an on-edge tip radius of 13 μm with a Ceast Notchvis notching machine. In order to assess influence of the weld lines in fracture, DENT samples were cut from different places of the moldings, away from weld lines, and samples including weld lines with angle between 45 and 78°, as depicted in Figure 2.

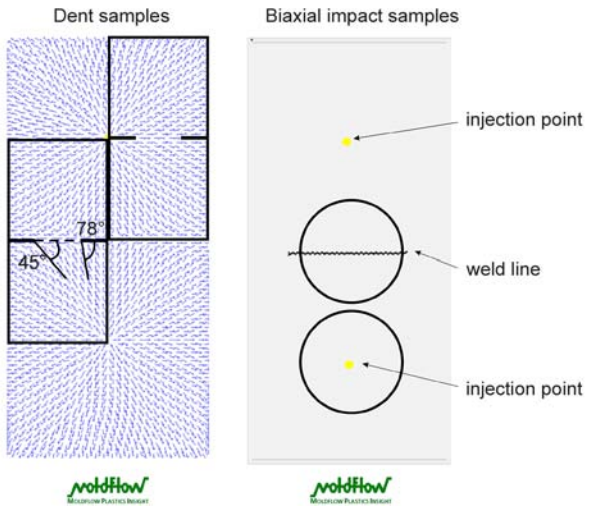

Figure 2. Location of samples cut from moldings for mechanical tests. Weld line location and flow direction in the skin were assessed using Moldflow®.

K_{Ic} was evaluated at 5% non-linearity [27]. The load at crack initiation F_q was determined as the intercept between the load curve and the $C + 5\%$ compliance line, C being the initial compliance of the load–displacement curve. The stress intensity factor at initiation, K_{Iq} was then determined by Equation (2):

$$K_{Iq} = \frac{F_q}{B\sqrt{\frac{W}{2}}} f\left(\frac{a}{W}\right) \tag{2}$$

where B is the thickness of the sample, W is the width of the sample, a is the length of the notch, and $f(a/W)$ is the function of the notch to width that for DENT samples is given by Equation (3):

$$f\left(\frac{a}{W}\right) = \frac{\sqrt{\frac{\pi a}{2W}}}{\sqrt{1-\frac{a}{W}}}\left[1.122 - 0.561\left(\frac{a}{W}\right) - 0.205\left(\frac{a}{W}\right)^2 + 0.471\left(\frac{a}{W}\right)^3 + 0.19\left(\frac{a}{W}\right)^4\right] \tag{3}$$

G_{cp} was estimated from the total fracture energy, Utot, according to Equation (4) [28]:

$$G_{cp} = \frac{U}{B(W-a)} \tag{4}$$

Biaxial impact performance was evaluated according to ASTM D 3763-93 procedure in two locations of the pieces (on and out of weld line) (Figure 2) using an instrumented Ceast Fractovis 6787 falling weight equipment. The specimens were clamped between two steel plates with a circular opening of 40 mm in diameter and tested at 3.5 m/s and room temperature. The biaxial impact resistance, (I_{bt}) was calculated as the total energy to break the sample (total area over the force-displacement curve) divided thickness. Biaxial impact tests are tests on representative samples, rather than measurements of basic material properties on standard test pieces, which give a realistic view of in service impact situations – being closer to real life conditions – with the additional advantage that they provide a convenient method of studying changes induced by flow in molded part performance [29, 30].

Fracture surfaces of broken samples were analyzed using a JEOL JSM-6460LV scanning electron microscope (SEM) at an accelerating voltage of 20 kV. Samples were sputter coated with a thin layer of gold before they were observed.

3. Results

3.1. Part features and defects

Injected parts presented the typical skin-shear layer-core structure of injected moldings (Figure 3). PP/Al skin thickness was larger than the one of PP moldings. This is due to the higher thermal conductivity of aluminum pigment which has been shown to increase the thermal conductivity of PP composites [31], providing a faster cooling rate and consequently an increase of the skin thickness.

Metallic pigments offer silver effects on the polymeric matrix, as can be observed in Figure 4. There are visual defects on the injection molded boxes with metallic particles directly related to the final quality of the moldings. The most noticeable ones are: the appearance of weld lines, flow lines and warpage.

A good dispersion of Al particles was observed away from flow and weld lines by reflection optical microscopy (see in Figure 4 Optical reflection). Also a

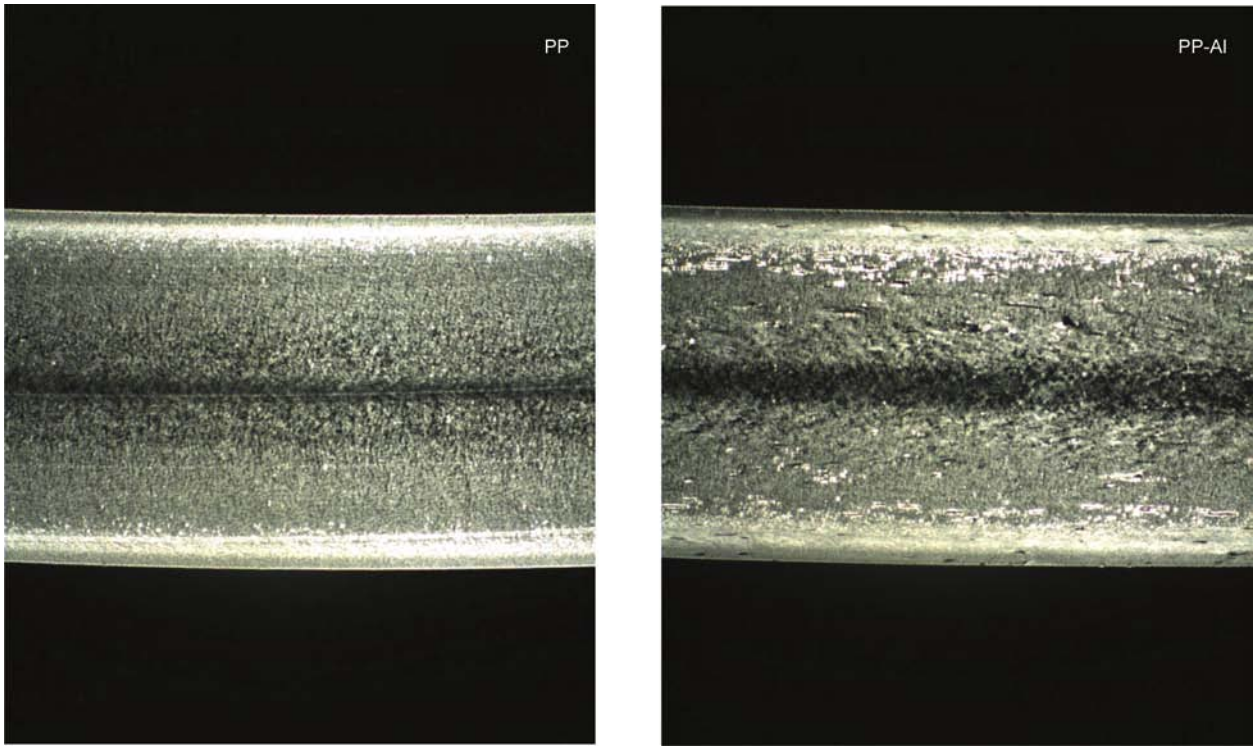

Figure 3. Trough the thickness cross-polarized optical transmission microscopies of PP and PP/Al

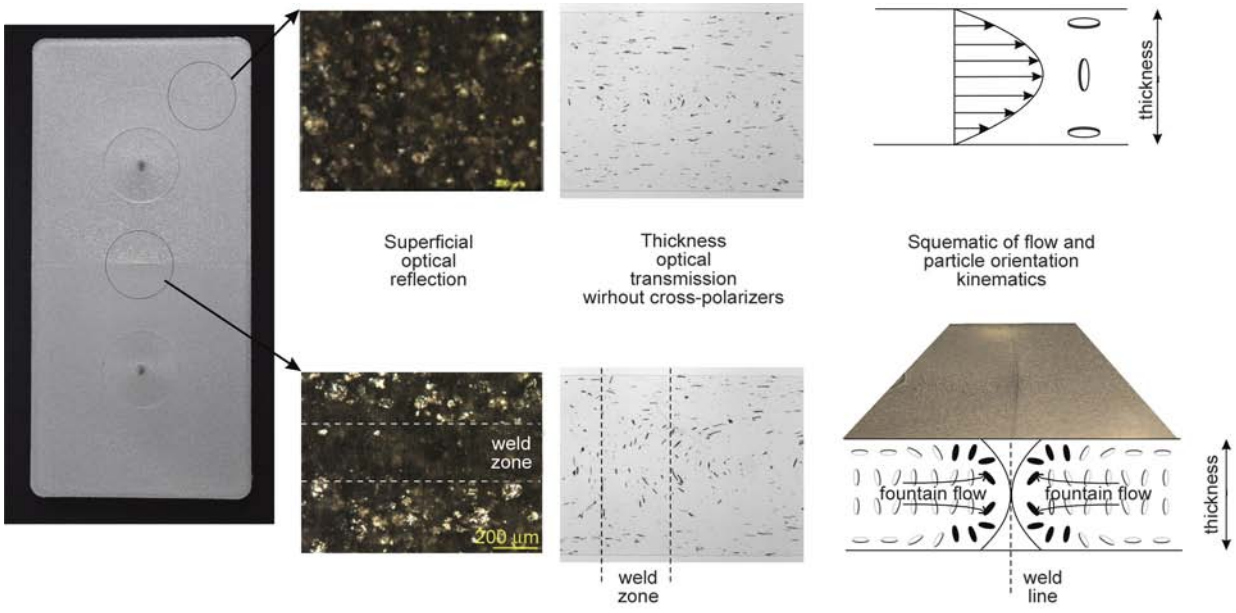

Figure 4. Optical microscopy results (reflection and transmission) with schematic of flow and particle orientation kinematics

beneficial orientation was observed, i.e. flakes with reflecting surface parallel to part surface. All samples presented a good dispersion and orientation of pigment away from injection points and weld lines. However, at weld lines a lower amount of reflecting particles was observed in the surface (6 vs 22% away from weld line). Weld lines and flow lines became visible due to the incorporation of Al pigment in PP matrix. These observations can be explained taking into account the particles anisotropy and orientation. Particles in the core are perpendicular to the plane of the surface (Figure 4, optical transmission). In injection molding, with a symmetric velocity profile in the midplane of the thickness, the bigest shear rate occur in the skin layer (near to the mold wall) while the core is characterized by a low shear rate. Jeffery model is a model which describes the kinematics of single ellipsoidal particle suspended in a viscous liquid [32]. This model applied to a disc (where $0 < L/D << 1$) describes that the orientation vector (normal to the disc) tends to align perpendicular to shear strain (see in Figure 4 the scheme). The melt front differs from the rest of the flow because its flow field has three-dimensional characteristics, namely the fountain-flow, which has a velocity component in the thickness direction driving the flakes at the core layer to move to the skin layer. If we have two meeting fountain flows, they result in a local region near the surface with a non parallel to the surface plane flake orientation (see scheme and micrographs in Figure 4). If the mold temperature is low and the solidification of the polymer takes place quickly, the surface orientation becomes frozen-in without any further reorientation. Thus particles remain perpendicular to the plane of the surface, and a dark line appears [8, 9].

Injection and mold temperatures influenced shrinkage. Shrinkage indexes of both PP and PP/Al pieces diminished with the increase of T_{inj} (see Figure 5). Moreover, shrinkage indexes of PP/Al pieces were lower than those of PP pieces, indicating higher quality of final pieces.

3.2. Mechanical performance

Quasi-static fracture performance of pieces depended not only on the presence or absence of Al particles, but also on the location of the samples.

At weld lines PP samples exhibited stress whitening and some plastic deformation prior to unstable failure, while PP/Al failed in a brittle manner, both following the weld line (Figure 6). In spite of differences in propagation values, i.e. GCP, fracture toughness K_{Ic} of PP and PP/Al samples at the weld line were similar indicating that weld lines were predominant in fracture leading the crack growth (Table 2).

Away from weld lines, fracture behavior of PP and PP-Al were similar: a non-lineal behavior with crack stable propagation and large plastic deformation was observed for all samples (Figure 7). As in samples at weld lines, K_{Ic} values were similar and differences were observed for GCP propagation values, PP pieces being a little more ductile than PP-Al moldings. Also, maximum load attained by PP-Al was

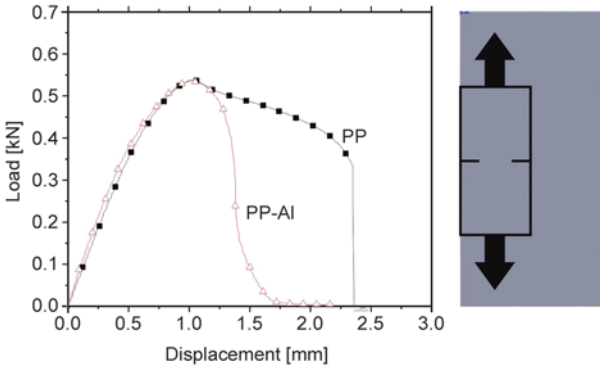

Figure 6. Typical load-displacement fracture curves at weld line for PP and PP-Al

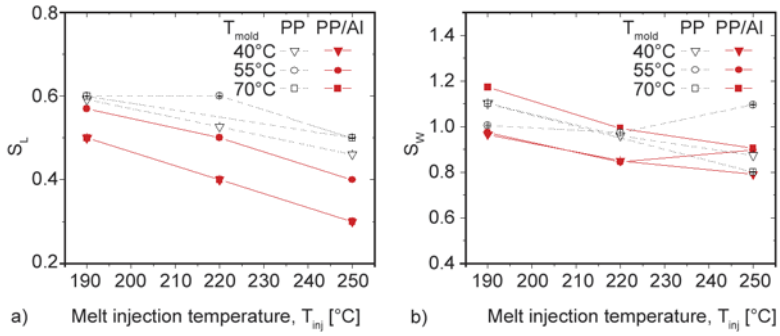

Figure 5. (a) Length and (b) width shrinkage indexes for PP and PP-Al moldings as a function of injection temperature and mold temperature

Table 2. Mechanical and fracture parameters of boxes

Test	Parameter		PP	PP-Al
Fracture	At weld line	K_{Ic} [MPa·m$^{1/2}$]	2.3	2.1
		G_{cp} [kJ/m^2]	44.1	24.3
	Away from weld line	K_{Ic} [MPa·m$^{1/2}$]	2.0	2.0
		G_{cp} [kJ/m^2]	87	75
Impact	$U_{biaxial}$ [J/mm] Near inj point	C-1	6.7	2.8
		C-2	7.1	4.1
	$U_{biaxial}$ [J/mm] At weld line	C-1	7.8	3.5
		C-2	8.1	3.7

lower than for PP samples. An important distinct feature is the difference observed in the shape of the developed plastic zones in PP and PP-Al pieces: plastic zones of PP pieces were diamond shaped while PP-Al pieces developed elliptic plastic zones (see pictures obtained *in-situ* in Figure 7). Moreover, differences in propagation mode were observed in post-mortem SEM of fracture surfaces. Skin and core behavior were very different, the core presenting larger plastic deformation. PP-Al injected samples presented more tearing in the core than PP moldings. It was also observed that Al particles acted as stress concentrators being not bonded to PP (Figure 8).

Due to the observed plastic behavior, fracture tests can be analyzed following the essential work of fracture (EWF) methodology, which considers the overall energy (W_f) necessary to fracture a notched specimen as made of two components: an essential one (W_e), to create new surfaces in the so-called fracture process zone, and the non-essential work (W_p) dissipated for the plastic deformation of the surrounding area, the process zone. Accordingly, the specific work, w_f, can be written as the sum of two terms, as shown by Equation (5):

$$w_f = w_e + \varphi w_p l \tag{5}$$

w_e and $\varphi w_p l$ are the essential and non-essential work respectively, φ being a shape factor and l the length of the uncracked specimen width (ligament length). By performing a series of experiments on notched specimens with different ligament length l, an over-

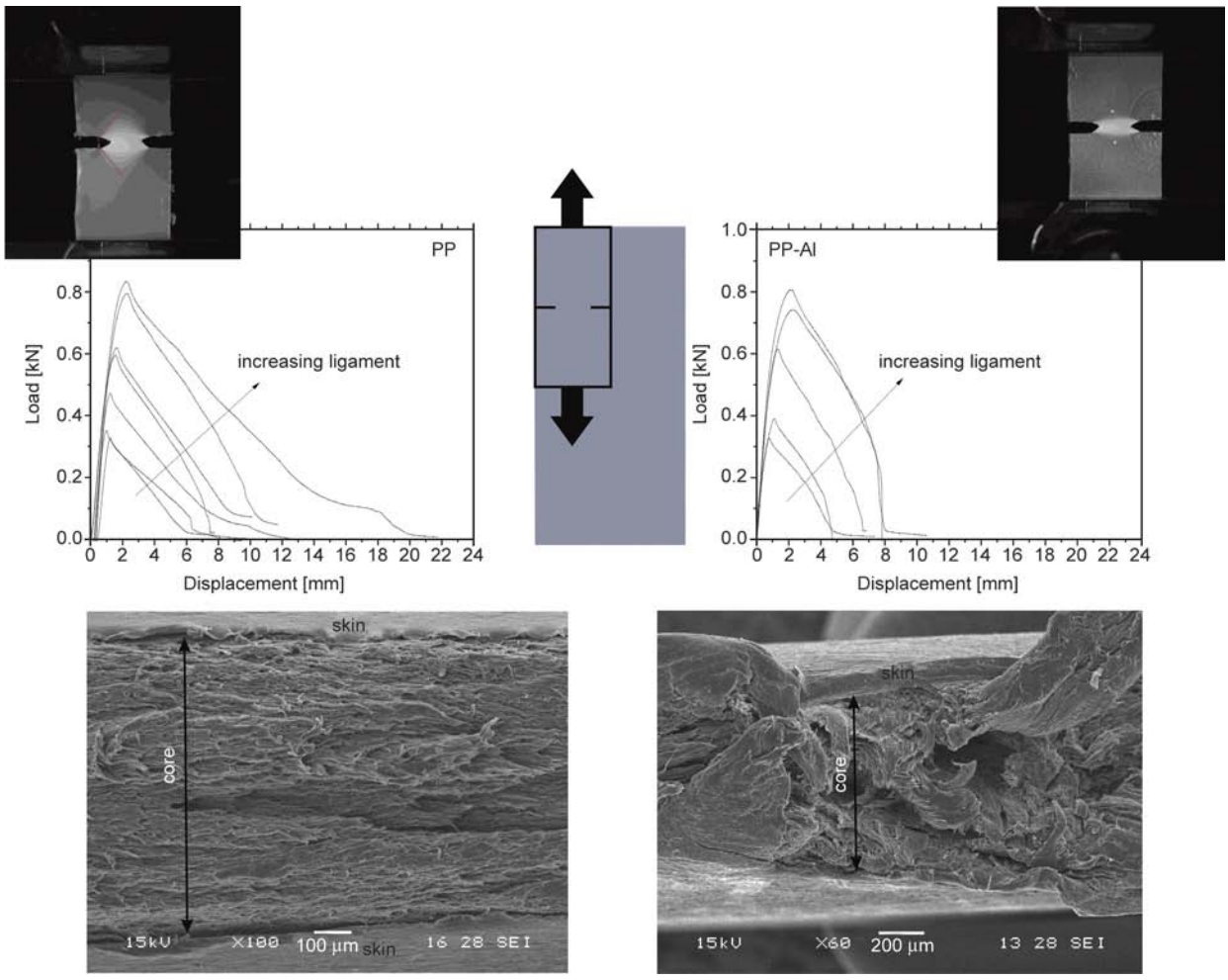

Figure 7. Typical load-displacement fracture curves away from weld line for PP and PP-Al. Developed plastic zones as seen *in-situ* and SEM micrographs of post-mortem fracture surfaces are also shown.

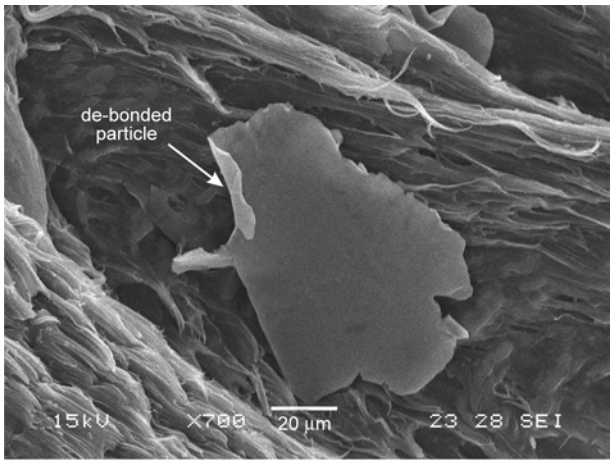

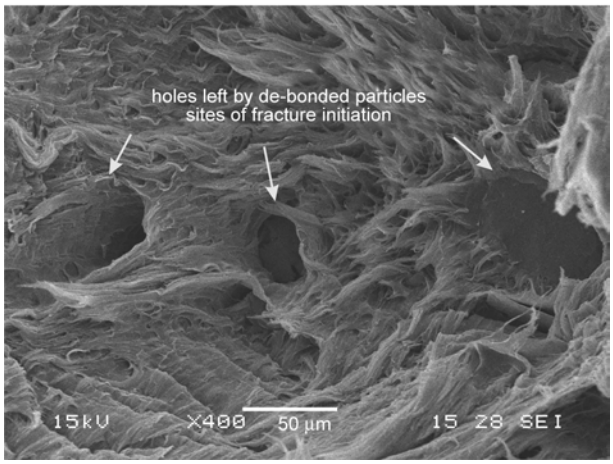

Figure 8. SEM micrographs of post-mortem fracture surfaces of PP-Al in which a de-bonded Al flake is clearly seen into deformed PP (a); and holes left by de-bonded particles are evidenced (b). It is clear from micrograph that these holes were points of fracture initiation.

all specific work w_f vs. l curve can be obtained in which we and $\varphi w_p l$ are the intercept and slope of a linear interpolation of the data. This analysis is shown in Figure 9. Consistently, initiation values (w_e) were

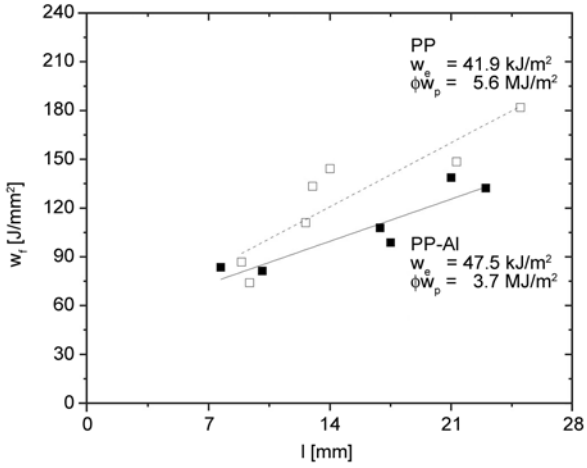

Figure 9. EWF plots

very similar, and some differences were seen in propagation stage (φw_p). To quantify them, the shape factor φ was determined – according to the EWF protocol [33] – by using the relation between h (plastic zone height, measured from cross-polarized photos as the examples in Figure 7) and l (for diamond plastic zone shape $\varphi = \pi h/(2l)$ and for elliptical plastic zone $\varphi = \pi h/(4l)$). φ values of 1.24 and 0.23 were obtained for PP (diamond) and PP-Al (ellipse) respectively. From these values and φw_p that emerged from the linear interpolation of w_f data (intercept), w_p (specific energy absorption per unit volume) equal to 4.51 and 16.01 MJ/m^3 were estimated for PP and PP-Al respectively. These values indicate that much more energy is involved in the propagation of a crack in the PP of PP-Al samples than in the PP of neat PP samples.

Typical behavior of PP and PP-Al samples under biaxial impact loads at the weld line is shown in Figure 10. PP presented a semi ductile behavior with

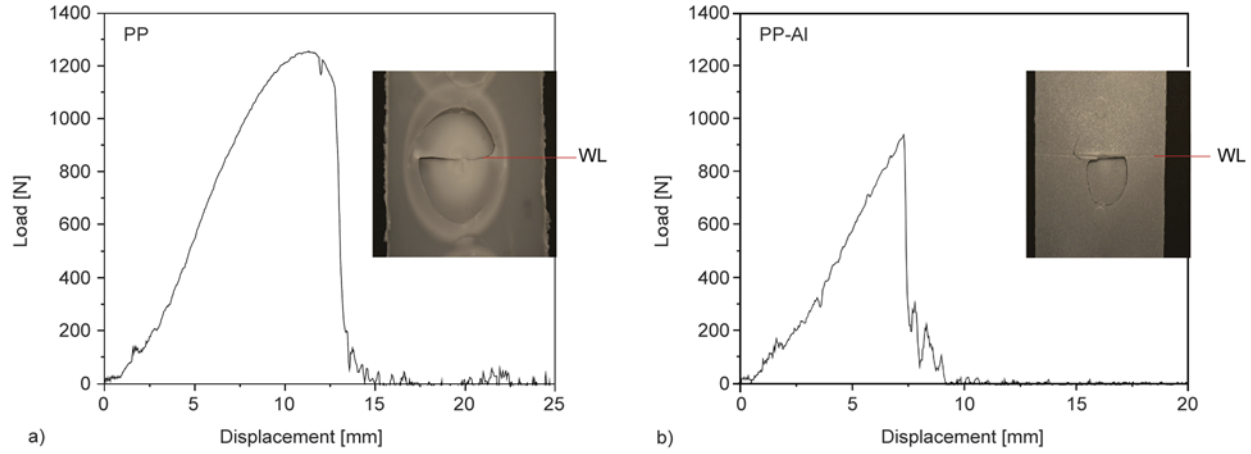

Figure 10. Typical behavior under biaxial impact at the weld line for (a) PP and (b) PP-Al moldings

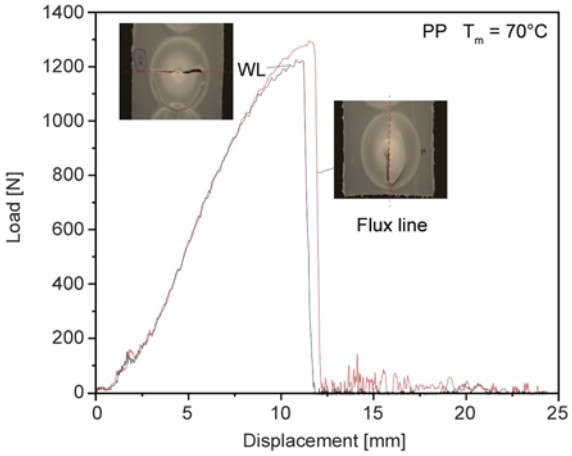

Figure 11. Comparison of behavior under biaxial impact at the weld line and near injection point (PP samples)

stress whitening before failure, while PP-Al exhibited a completely brittle failure. It is noticeable that as in quasi-static fracture tests, all samples (PP and PP-Al) failed following the weld line, i.e. it acted as a strong stress raiser defect. When samples were impacted at location near injection point a similar failure was observed, but now following flux lines. In Figure 11 a comparison between tests performed at the weld line and near injection point is shown. It was concluded that both weld lines and flux lines acted as stress raisers.

4. Discussion

Differences found in the fracture behavior and developed plastic zones in fracture samples suggested some micro-structural difference in PP induced by Al flakes. Therefore an analysis of the samples' morphology was done.

X-ray diffraction (XRD) was performed with a Phillips X'PERT MPD diffractometer in reflection mode (Cu Kα radiation λ = 1.5418 Å, generator voltage 40 kV, current 40 mA, sample to detector distance 240 mm) to observe the PP structure in the skin and the core. The metallic pigment induced noticeable differences in the skin's PP morphology (Figure 12). Unexpectedly, the commercial pigment promoted the formation of β-PP (increase in (300) reflection (Figure 12a), decreasing crystallinity (decrease of reflections intensity). The fraction of β-phase in the crystalline phase of polypropylene was calculated by using the Turner Jones *et al*. [34] relation (Equation (6)):

$$K_\beta = \frac{I_{300}^{\beta}}{I_{300}^{\beta} + I_{110}^{\alpha} + I_{040}^{\alpha} + I_{130}^{\alpha}} \quad (6)$$

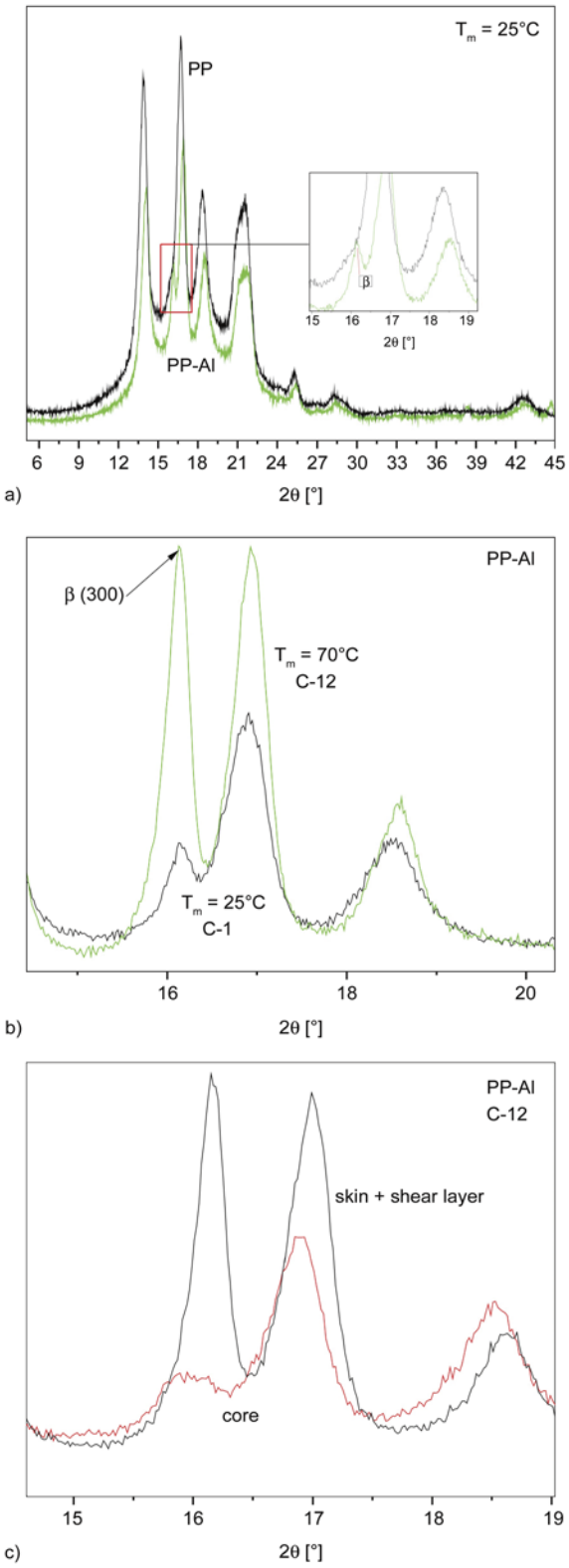

Figure 12. DRX curves of PP and PP/Al moldings. (a) condition 1 (b) processed at different temperatures (c) comparison between skin and core of PP-Al molding processed at condition 12

where in a generic sense I_{abc}^{i} is the intensity of the (*abc*) crystal growing plane for each phase *i*. Mold temperature greatly influenced PP microstructure:

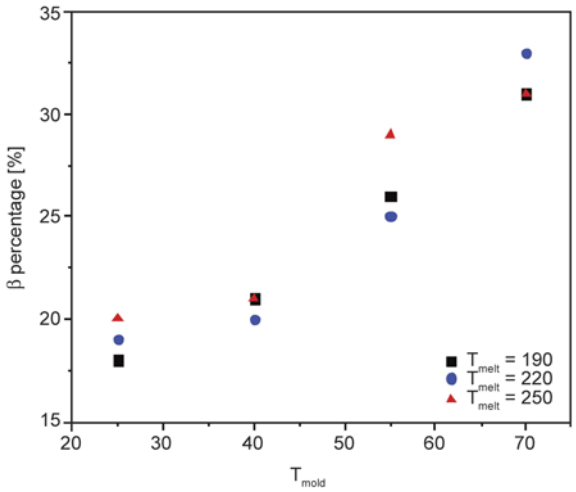

Figure 13. β-PP polymorph content in PP-Al samples for all processing conditions

Table 3. β content (K_β) in skin of samples of processing condition 12

Sample	K_β in weld line	K_β in bulk
PP	0.11	0.19
PP-Al	0.30	0.34

increasing temperature in 45°C duplicated the percentage of β-PP in both PP and PP/Al moldings (Figure12b and 13). It was also found that melt temperature does not influence the microstructure (Figure 13). An important finding is that there was a profile of β content trough the samples (Table 3 presents results for processing condition 12 as an example). K_β was lower in weld lines than away from them. Also big differences in K_β were found between skin and core. The influence of mold temperature on K_β is more pronounced in the close vicinity of the mold wall, i.e. in the specimens' skin: the 300 diffraction maximum of β-phase decreases from the skin to the core (see Figure 12c). For example, K_β diminished from 0.34 to 0.16 as moving from the skin to the core in PP-Al boxes away from weld lines. This fact can be easily explained remembering that while the skin solidifies nearly at the same temperature as mold temperature, the core crystallizes at notably higher temperature, which results in lower crystallinity changes.

The question to answer here is why Al pigment promotes β-polymorph if it is known to not being a nucleating agent for this polymorph in PP. Crystallization in a temperature gradient or in sheared melt, typical of injection molding, encourages the development of the β-phase in commercial non nucleated PP. But these conditions are present also in PP moldings. So, what is the effect of Al pigment? It is known that the growth rate of β spherulites is up to 70% faster than that of α-spherulites when conditions for β nucleation are provided [35] and this rate presents a maximum at approximately 120°C [36]. When cooling is fast, the crystallization of β form is favored. In fact Turner Jones *et al*. [34] produced large amounts of the β form quenching a sample very rapidly to below 130°C. Al pigment, which increased the thermal conductivity of PP composites [31], provided a faster cooling rate of the skin and therefore conditions for β-PP crystals to grow. It seems that the addition of Al flakes that increase the cooling rate combined with the high shear stresses of injection molding induced the formation of the β-PP.

According to these findings, differences in developed plastic zones in fracture tests can be explained by the differences in polymorphic phase: α-PP develops a diamond shaped plastic zone and β-PP develops an elliptic plastic zone [37]. Also, differences in plastic behavior of skin and core are due in part by the presence of β-PP, which is more ductile and tough than α-PP [37, 38]. Even though β-PP is tougher and more ductile, Al particles acted as stress concentrators. In other words, the occurrence of β-PP in PP-Al moldings may counteract in part the diminishment of PP toughness induce by Al flakes. Under impact conditions, these benefits of the β phase are mostly inhibited by solicitation mode (biaxial), and the processing defects (flow lines and weld lines) prevailed.

5. Conclusions

The addition of Al particles in PP matrix has influence on the aesthetical, morphological and mechanical properties of injection molded parts. The metallic looking effect is easily obtained when these particles are used, at low weight percentages (max 2%). However, several types of undesired effects appear, such as weld lines and warpage that are dependent on the processing conditions used.

In terms of aesthetics effects, high melt temperatures diminish differential shrinkage and welding lines are less noticeable, indicating that aesthetic aspects could be improved by manipulating processing conditions. Weld lines appeared wider and diffuser with increasing melt temperature.

Morphology analysis showed a distinction between PP and PP-Al molded parts. Al particles increased thermal conductivity of PP generating a thicker skin,

which combined with an inherent gradient temperature and typical shear stresses developed during injection molding, induced the formation of β-PP phase. This effect was found to be dependent of processing conditions: higher melt temperature induced higher β-PP content.

Mechanical performance of parts showed to be dependent on PP morphology. Under quasi-static loading conditions plastic zones of PP samples were diamond shaped (typical of α-PP) while PP-Al pieces developed elliptic plastic zones (typical of β-PP). Also, differences in propagation mode were observed in SEM. The occurrence of β-PP in PP-Al moldings counteracts the detrimental effect of not bonded Al flakes, and PP-Al moldings have similar toughness as PP moldings, under triaxial quasi-static loading conditions.

However, under biaxial impact loading these beneficial effects of β polymorph are inhibited, and the defects induced by Al flakes orientation and their poor adhesion to the PP matrix prevailed lowering toughness.

Acknowledgements

Authors would like to thank CONICET, ANPCyT and UNMdP for financial support.

References

[1] Wheeler I.: Metallic pigments in polymers. Rapra, Shawbury (1999).

[2] Rusu M., Sofian N., Rusu D.: Mechanical and thermal properties of zinc powder filled high density polyethylene composites. Polymer Testing, **20**, 409–417 (2001). DOI: 10.1016/S0142-9418(00)00051-9

[3] Gungor A.: The physical and mechanical properties of polymer composites filled with Fe-powder. Journal of Applied Polymer Science, **99**, 2438–2442 (2006). DOI: 10.1002/app.22637

[4] Luyt A. S., Molefi J. A., Krump H.: Thermal, mechanical and electrical properties of copper powder filled low-density and linear low-density polyethylene composites. Polymer Degradation and Stability, **91**, 1629–1636 (2006). DOI: 10.1016/j.polymdegradstab.2005.09.014

[5] Bunge H.: Metallic looking plastics with new silver and colored aluminum pigments. in 'Annual Technical Conference – ANTEC, Atlanta, USA' 2586–2588 (1998).

[6] Kobayashi Y., Teramoto G., Kanai T.: The unique flow of polypropylene at the weld line behind an obstacle in injection molding. Polymer Engineering and Science, **51**, 526–531 (2011). DOI: 10.1002/pen.21841

[7] Harris R. M.: Coloring technology for plastics. William Andrew Publishing, New York (1999).

[8] Park J. M., Jeong S. J., Park S. J.: Flake orientation in injection molding of pigmented thermoplastics. Journal of Manufacturing Science and Engineering, **134**, 014501/1–014501/4 (2012). DOI: 10.1115/1.4005309

[9] Martins C., Pontes A., Santos I.: On the effect of metallic particles on the performance of injection molded PP plastic parts. in 'Proceedings of International Conference on Polymers and Moulds Innovations, Ghent, Belgium' 375–382 (2012).

[10] Santos I., Pontes A., Martins C.: Morphological aspects of injection-molded polypropylene with metallic pigments. in 'ANTEC 2013 Conference Proceedings, Cincinnati, USA' p.5 (2013).

[11] Liu G., Edward G.: Correlation between morphology distribution of injection molded polypropylene and processing history identified by numerical simulation. Journal of Injection Molding Technology, **5**, 133–140 (2001).

[12] Lotz B., Wittmann J. C., Lovinger A. J.: Structure and morphology of poly(propylenes): A molecular analysis. Polymer, **37**, 4979–4992 (1996). DOI: 10.1016/0032-3861(96)00370-9

[13] Jacoby P., Bersted B. H., Kissel W. J., Smith C. E.: Studies on the β-crystalline form of isotactic polypropylene. Journal of Polymer Science Part B: Polymer Physics, **24**, 461–491 (1986). DOI: 10.1002/polb.1986.090240301

[14] Shi G., Zhang X.: Effect of β-nucleator content on the crystallization and melting behaviour of β-crystalline phase polypropylene. Thermochimica Acta, **205**, 235–243 (1992). DOI: 10.1016/0040-6031(92)85265-W

[15] Tjong S. C., Shen J. S., Li R. K. Y.: Mechanical behavior of injection molded β-crystalline phase polypropylene. Polymer Engineering and Science, **36**, 100–105 (1996). DOI: 10.1002/pen.10390

[16] Liu J., Wei X., Guo Q.: The β-crystalline form of wollastonite-filled polypropylene. Journal of Applied Polymer Science, **41**, 2829–2835 (1990). DOI: 10.1002/app.1990.070411125

[17] Medellín-Rodríguez F. J., Mata-Padilla J. M., Hsiao B. S., Waldo-Mendoza M. A., Ramírez-Vargas E., Sánchez-Valdes S.: The effect of nanoclays on the nucleation, crystallization, and melting mechanisms of isotactic polypropylene. Polymer Engineering and Science, **47**, 1889–1897 (2007). DOI: 10.1002/pen.20902

[18] Lovinger A. J., Chua J. O., Gryte C. C.: Studies on the α and β forms of isotactic polypropylene by crystallization in a temperature gradient. Journal of Polymer Science: Polymer Physics Edition, **15**, 641–656 (1977). DOI: 10.1002/pol.1977.180150405

[19] Dragaun H., Hubeny H., Muschik H.: Shear-induced β-form crystallization in isotactic polypropylene. Journal of Polymer Science: Polymer Physics Edition, **15**, 1779–1789 (1977).
DOI: 10.1002/pol.1977.180151008

[20] Somani R. H., Hsiao B. S., Nogales A., Fruitwala H., Srinivas S., Tsou A. H.: Structure development during shear flow induced crystallization of i-PP: *In situ* wide-angle X-ray diffraction study. Macromolecules, **34**, 5902–5909 (2001).
DOI: 10.1021/ma0106191

[21] Farah M., Bretas R. E. S.: Characterization of i-PP shear-induced crystallization layers developed in a slit die. Journal of Applied Polymer Science, **91**, 3528–3541 (2004).
DOI: 10.1002/app.13576

[22] Kotek J., Raab M., Baldrian J., Grellmann W.: The effect of specific β-nucleation on morphology and mechanical behavior of isotactic polypropylene. Journal of Applied Polymer Science, **85**, 1174–1184 (2002).
DOI: 10.1002/app.10701

[23] Karger-Kocsis J., Varga J.: Effects of β-α transformation on the static and dynamic tensile behavior of isotactic polypropylene. Journal of Applied Polymer Science, **62**, 291–300 (1996).
DOI: 10.1002/(SICI)1097-4628(19961010)62:2<291::AID-APP4>3.0.CO;2-S

[24] Fitchmun D. R., Mencik Z.: Morphology of injection-molded polypropylene. Journal of Polymer Science: Polymer Physics Edition, **11**, 951–971 (1973).
DOI: 10.1002/pol.1973.180110512

[25] Viana J. C., Cunha A. M., Billon N.: The thermomechanical environment and the microstructure of an injection moulded polypropylene copolymer. Polymer, **43**, 4185–4196 (2002).
DOI: 10.1016/S0032-3861(02)00253-7

[26] Demiray M., Isayev A.: Effect of processing conditions on crystallinity and microstructure of injection moldings of polypropylenes of various molecular weights. in 'SPE ANTEC '96 Conference proceedings, Indianapolis, USA' 1576–1580 (1996).

[27] Williams J.: K_c and G_c at slow speeds for polymers. in 'Fracture mechanics testing methods for polymers, adhesives and composites' (eds.: Moore D. R., Williams J. G., Pavan A.) Elsevier, Amsterdam, Vol 28, 11–26 (2001).
DOI: 10.1016/S1566-1369(01)80025-X

[28] Adams M. J., Williams D., Williams J. G.: The use of linear elastic fracture mechanics for particulate solids. Journal of Materials Science, **24**, 1772–1776 (1989).
DOI: 10.1007/BF01105704

[29] Cunha A., Pouzada A. S., Crawford R. J.: A study of the impact behaviour of injection moulded polypropylene using two different modes of testing. Plastics Rubber and Composites Processing and Applications, **18**, 79–90 (1992).

[30] Viana J., Cunha A. M., Billon N.: The tensile behaviour of an injection-moulded propylene–ethylene copolymer: The effect of the local thermomechanical processing conditions. Polymer International, **43**, 159–166 (1997).
DOI: 10.1002/(SICI)1097-0126(199706)43:2<159::AID-PI720>3.0.CO;2-X

[31] Boudenne A., Ibos L., Fois M., Gehin E., Majeste J-C.: Thermophysical properties of polypropylene/aluminum composites. Journal of Polymer Science Part B: Polymer Physics, **42**, 722–732 (2004).
DOI: 10.1002/polb.10713

[32] Rawson K. W., Allan P. S., Bevis M. J.: Controlled orientation of reflective pigment and optical property characterization of injection-molded polypropylene. Polymer Engineering and Science, **39**, 177–189 (1999).
DOI: 10.1002/pen.11406

[33] Clutton E.: Essential work of fracture. in 'Fracture mechanics testing methods for polymers, adhesives and composites' (eds.: Moore D. R., Williams J. G., Pavan A.) Elsevier, Amsterdam, Vol 28, 177–195 (2001).
DOI: 10.1016/S1566-1369(01)80033-9

[34] Turner Jones A., Aizlewood J. M., Beckett D. R.: Crystalline forms of isotactic polypropylene. Die Makromolekulare Chemie, **75**, 134–158 (1964).
DOI: 10.1002/macp.1964.020750113

[35] Bviickner S., Meille S.: Polymorphism in crystalline polypropylene. in 'Polypropylene' (Ed.: Karger-Kocsis J.) Kluwer, Dodrecht, 606–614 (1999).

[36] von Leugering H. J., Kirsch G.: Beeinflussung der Kristallstruktur von isotaktischem Polypropylen durch Kristallisation aus orientierten Schmelzen (in German). Die Angewandte Makromolekulare Chemie, **33**, 17–23 (1973).
DOI: 10.1002/apmc.1973.050330102

[37] Karger-Kocsis J.: How does 'phase transformation toughening' work in semicrystalline polymers? Polymer Engineering and Science, **36**, 203–210 (1996).
DOI: 10.1002/pen.10403

[38] Chen H. B., Karger-Kocsis J., Wu J. S., Varga J.: Fracture toughness of α- and β-phase polypropylene homopolymers and random- and block-copolymers. Polymer, **43**, 6505–6514 (2002).
DOI: 10.1016/S0032-3861(02)00590-6